The Dissertation Committee for Alireza Shahin Certifies that this is the approved version of the following dissertation:

Detection of Production-Induced Time-Lapse Signatures by Geophysical (Seismic and CSEM) Measurements

Committee:

Paul L. Stoffa, Co-Supervisor

Robert H. Tatham, Co-Supervisor

Mrinal K. Sen

John A. Goff

Brackin A. Smith

Detection of Production-Induced Time-Lapse Signatures by Geophysical (Seismic and CSEM) Measurements

by

Alireza Shahin, B.S.; M.S.

Dissertation

Presented to the Faculty of the Graduate School of

The University of Texas at Austin

in Partial Fulfillment

of the Requirements

for the Degree of

Doctor of Philosophy

The University of Texas at Austin

May 2011

Dedication

With love to my parents and my wife

Acknowledgements

I would like to express my most appreciation to my supervisor, Professor Paul L. Stoffa for constant guidance and constructive criticism during my entire research work. With no doubt, this work was impossible without his encouragement and support. I also want to thank my co-supervisor, Professor Robert H. Tatham, for his many enlightening suggestions leading to make several parts of this work happen. I extend my appreciation to my committee members, Dr. Mrinal K. Sen, Dr. John A. Goff, and Dr. Brackin A. Smith for their comments and suggestions. I would appreciate several other professors and researchers including Diana Sava, Kyle Spikes, Sergey Fomel, Kerry Key, Carlos Verdin, Larry Lake, Jack Dvorkin, William Galloway, William Fisher, and Jerry Lucia for helping at various parts of this work. I also gratefully acknowledge several friends at Jackson School of geosciences and petroleum& geosystems engineering departments of the University of Texas at Austin for help and support during my research. Finally, I would like to appreciate Jackson School of Geosciences and sponsors of EDGER forum for financial support.

Detection of Production-Induced Time-Lapse Signatures by Geophysical (Seismic and CSEM) Measurements

Publication No._____

Alireza Shahin, PhD

The University of Texas at Austin, 2011

Supervisor: Paul L. Stoffa

Co-supervisor: Robert H. Tatham

While geophysical reservoir characterization has been an area of research for the last three decades, geophysical reservoir monitoring, time-lapse studies, have recently become an important geophysical application. Generally speaking, the main target is to detect, estimate, and discriminate the changes in subsurface rock properties due to production. This research develops various sensitivity and feasibility analyses to investigate the effects of production-induced time-lapse changes on geophysical measurements including seismic and controlled-source electromagnetic (CSEM) data. For doing so, a realistic reservoir model is numerically simulated based on a prograding near-shore sandstone reservoir. To account for the spatial distribution of petrophysical properties, an effective porosity model is first simulated by Gaussian geostatistics. Dispersed clay and dual water models are then efficiently combined with other well-

known theoretical and experimental petrophysical correlations to consistently simulate reservoir model parameters. Next, the constructed reservoir model is subjected to numerical simulation of multi-phase fluid flow to replicate a waterflooding scenario of a black oil reservoir and to predict the spatial distributions of fluid pressure and saturation. A modified Archie's equation for shaly sandstones is utilized to simulate rock resistivity. Finally, a geologically consistent stress-sensitive rock physics model, combined with the modified Gassmann theory for shaly sandstones, is utilized to simulate seismic elastic parameters. As a result, the comprehensive petro-electro-elastic model developed in this dissertation can be efficiently utilized in sensitivity and feasibility analyses of seismic/CSEM data with respect to petrophysical properties and, ultimately, applied to reservoir characterization and monitoring research.

Using the resistivity models, a base and two monitor time-lapse CSEM surveys are simulated via accurate numerical algorithms. 2.5D CSEM modeling demonstrates that a detectable time-lapse signal after 5 years and a strong time-lapse signal after 10 years of waterflooding are attainable with the careful application of currently available CSEM technology.

To simulate seismic waves, I employ different seismic modeling algorithms, one-dimensional (1D) acoustic and elastic ray tracing, 1D full elastic reflectivity, 2D split-step Fourier plane-wave (SFPW), and 2D stagger grid explicit finite difference (FD). My analyses demonstrate that acoustic modeling of an elastic medium is a good approximation up to ray parameter (p) equal to 0.2 sec/km. However, at p=0.3 sec/km, differences between elastic and acoustic wave propagation is the more dominant effect compared to internal multiples. Here, converted waves are also generated with significant amplitudes compared to primaries and internal multiples.

I also show that time-lapse modeling of the reservoir using SFPW approach is very fast compared to FD, 100 times faster for my case here. It is capable of handling higher frequencies than FD. It provides an accurate image of the waterflooding process comparable to FD. Consequently, it is a powerful alternative for time-lapse seismic modeling.

I conclude that both seismic and CSEM data have adequate but different sensitivities to changes in reservoir properties and therefore have the potential to quantitatively map production-induced time-lapse changes.

Table of Contents

List of Tables xii

List of Figures xiii

List of Figures xiii

Chapter one: Introduction 1

1.1 Problem statement and literature review 1

1.2 Research objectives 8

1.3 Dissertation outline 9

Chapter two: Reservoir modeling and rock physics analysis 11

2.1 Introduction 11

2.2 Background and formulation 13

2.3 Constructing a synthetic reservoir model 18

2.3.1 Geological reservoir model 18

2.3.2 Petrophysics model 19

2.3.3 Reservoir simulation 21

2.3.4 Rock and fluid physics model 23

2.4 time-lapse rock-fluid physics templates 30

2.5 Summary and conclusions 35

Chapter three: Multi-component time-lapse seismic: on saturation-pressure discrimination and statistical detectability of fluid flow 64

3.1 Introduction 64

3.2 Background and formulation 65

3.3 Methodology 70

3.4 Synthetic example 72

3.5 Summary and conclusions 78

Chapter four: Derivative-bases sensitivity analysis: a viable tool in reservoir geophysics....94
4.1 Introduction....94
4.2 Background and formulation....94
4.3 Methodology....95
4.3.1 Sensitivity Analysis of MC Seismic Traveltimes....95
4.3.2 Sensitivity Analysis of MC Seismic RCs....97
4.4 Summary and conclusions....99

Chapter five: Accuracy required in seismic modeling to detect production-induced time-lapse signals....105
5.1 Introduction....105
5.2 Background and formulation....107
5.2.1 Approximate seismic modeling methods....109
5.2.2 Analytical seismic modeling methods....110
5.2.3 Direct or purely numerical seismic modeling methods....110
5.2.4 Hybrid seismic modeling methods....112
5.3 Constructing a synthetic petro-elastic reservoir model....113
5.3.1 Geological reservoir model....113
5.3.2 Petrophysics model....114
5.3.3 Reservoir simulation....115
5.3.4 Rock and fluid physics model....116
5.4 Seismic modeling....118
5.4.1 One-dimensional seismic modeling....118
5.4.2 2D seismic modeling....125
5.5 Summary and conclusions....131

Chapter six: Petro-electric modeling aimed to simulate CSEM data for reservoir characterization and monitoring....161
6.1 Introduction....161
6.2 Background and formulation....162
6.3 Constructing a synthetic reservoir model....165
6.3.1 Geological reservoir model....165

6.3.2 Petrophysics model 166
6.3.3 Reservoir simulation 167
6.3.4 Rock and fluid physics model 170
6.4 CSEM modeling 174
6.4.1 One-dimensional CSEM modeling 174
6.4.2 2.5D CSEM modeling 177
6.5 Summary and conclusions 180
Chapter seven: Conclusions, recommendations, and future work 205
Appendix A: Equations for the petro-elastic model developed in chapter two ...212
Appendix B: Equations for the sensitivity analysis developed in chapter three ..215
Appendix C: Equations for the petro-electric model developed in chapter six ...217
References 219
Vita 232

List of Tables

Table 2.1: Facies petrophysical properties associated with the synthetic reservoir model.....37

Table 2.2: Density and elastic properties of minerals associated with the synthetic reservoir model. 37

Table 3.1: Characteristics of three synthetic reservoir units used in this study. 81

Table 3.2: Density and elastic properties of minerals associated with the synthetic reservoirs. 82

Table 4.1: The rock and fluid properties used in the examples. 101

Table 5.1: Geometry of different pre-stack traces simulated by 1D and 2D plane-wave seismic modeling techniques 133

Table 6.1: Facies petrophysical properties associated with the synthetic reservoir model.....182

List of Figures

Figure 2.1: 3D distribution of effective porosity model (Christie and Blunt, 2001) associated with synthetic geologic model used for the numerical simulation of seismic and multi-phase fluid-flow. The model is described on a regular Cartesian grid. The model size is 220*60*35 cells in X (east-west), Y (north-south), and Z (depth) directions, respectively (top panel). The grid size defining the cells is 10*10*10 meters, so model dimension is 2200m*600m*350m (bottom panel). 38

Figure 2.2: Three directional cross-sections of 3D effective porosity model in Figure 2.1.....40

Figure 2.3: Map view of petrophysical facies A, B, and C overlaid on 2D distribution of effective porosity model. Grid numbers are used to show reservoir dimensions in two horizontal directions. 41

Figure 2.4: Petrophysics model. Panel a shows the dispersed clay model for porosity reduction due to increasing of clay. Panel b dispalys horizontal permeability versus shale content. Panel c is permeability vs. effective porosity. In panels a,b, and c, three colors are associated with three facies A(in blue) representing fine-grined sandstone, B(in green) associated with medium-grained sandstone, and C(in red) corrosponding to course-grained sandstone. Black dots in panels b and c are projected reservoir points . Panel d shows fluid saturations, vs. shale content , effective water saturation (Swe), oil saturation (So), caly-bound water saturation (Swb), and total water satuation (Swt).....42

Figure 2.7: The capillary pressures data, the relative permeability curves, and PVT properties of reservoir fluids. FVF stands for Formation Volume Factor. 46
Figure 2.9 Surface reservoir simulation outputs, i.e., production data, for a period of 10 years of waterflooding to enhance oil recovery. 48
Figure 2.10: Density, bulk modulus, and seismic P-wave velocity for the reservoir fluids. Batzle-Wang 1992 empirical relationships have been used to transform PVT properties of oil-gas-water. Note that bubble point pressure is 2000 psi. 49
Figure 2.11: Petro-elastic model evaluated at reservoir condition. 50
Figure 2.12: Effects of water saturation (first row) and pore pressure (second row) on density and elastic parameters of reservoir rock. 51
Figure 2.13: Various crossplots of elastic parameters for a wet sandy shale, a shaly water saturated sand, and a shaly oil-saturated sand all computed at the same effective pressure. 52
Figure 2.14: [Vp/Vs vs. AI] crossplots computed at the initial state of reservoir (t0) and before waterflooding. Each crossplot is color-coded with different petrophysical properties including effective porosity, shale content, effective water saturation, and pore pressure.....53
Figure 2.15: [Vp/Vs vs. AI] crossplots computed after six years (t06) of waterflooding. Each crossplot is color-coded with different petrophysical properties including effective porosity, shale content, effective water saturation, and pore pressure.....54

Figure 2.16: [SI vs. AI] crossplots computed at the initial state of reservoir (t0) and before waterflooding. Each crossplot is color-coded with different petrophysical properties including effective porosity, shale content, effective water saturation, and pore pressure.....55
Figure 2.17: [SI vs. AI] crossplots computed after six years (t06) of waterflooding. Each crossplot is color-coded with different petrophysical properties including effective porosity, shale content, effective water saturation, and pore pressure. 56
Figure 2.18: [MR vs. LR] crossplots computed at the initial state of reservoir (t0) and before waterflooding. Each crossplot is color-coded with different petrophysical properties including effective porosity, shale content, effective water saturation, and pore pressure.....57
Figure 2.19: [MR vs. LR] crossplots computed after six years (t06) of waterflooding. Each crossplot is color-coded with different petrophysical properties including effective porosity, shale content, effective water saturation, and pore pressure. 58
Figure 2.20: Time-lapse changes (t06-t01) in fluid pressure and saturation and the associated changes in elastic parameters. X and Y axes are the same for all panels and they are reservoir length and width in meters, respectively. Each panel is color-coded for the corrosponding attribute. Here, changes in AI and SI for base survey (after 1 year of waterflooding t01) is subtracted from those of monitor survey (after 6 years of waterflooding t06), and then normalized using those of base survey (t01). 59

Figure 2.21: Sensitivity analysis of elastic parameters to changes in fluid saturation and pore pressure. X and Y axes are the same for all panles and they are change in water saturation and change in pore pressure(in psi), respectively. Each panel is color-coded for the corrosponding attribute. 60

Figure 2.22: Dynamic or time-lapse crossplots associated with production-induced time-lapse changes illustrated in Figure 2.20. The colorbar indicated on the top left crossplot is true for all three crossplots in the top row and it shows change in effective water saturation (Swe) in percent. The colorbar indicated on the lower left crossplot is true for all three crossplots in the bottom row and it shows change in pore pressure (Pp) in percent.....61

Figure 2.23: Dynamic or time-lapse crossplots associated with production-induced time-lapse changes. The colorbar indicated on the top of each crossplot shows change in effective water saturation (Swe) in percent. X and Y axes are the same for all panels and they are change in acoustic and shear impedances, respectively. Each panel is titled with the corrosponding time-lapse scenario, e.g., panel (a) indicated with t04-t03 means changes in AI and SI for base survey (after 3 years of waterflooding t03) is subtracted from those of monitor survey (after 4 years of waterflooding t04), and then normalized using those of base survey(t03). 62

Figure 2.24: Dynamic or time-lapse crossplots associated with production-induced time-lapse changes. The colorbar indicated on the top of each crossplot shows change in pore pressure (Pp) in percent. X and Y axes are the same for all panels and they are change in acoustic and shear impedances, respectively. Each panel is titled with the corrosponding time-lapse model, e.g., panel (a) indicated with t04-t03 means changes in AI and SI for base survey (after 3 years of waterflooding t03) is subtracted from those of monitor survey (after 4 years of waterflooding t04), and then normalized using those of base survey(t03). 63

Figure 3.1: Rock physics models (P-wave and S-wave velocities versus porosity) adopted for this study. Continuous and dashed black lines are modified Hashin-Strikman upper bounds (Stiff sand model, Gal et al. 1998) for P&S-wave velocities, respectively. Reservoir A is located on these bounds with 10% porosity. Continuous and dashed blue lines are modified Hashin-Strikman lower bounds (Dvorkin and Nur, 1996) for P&S-wave velocities, respectively. Reservoir C is located on these bounds with 30% porosity. Continuous and dashed red lines are the average of upper (UB) and lower (LB) bounds and called middle bounds (MB). Reservoir B is positioned on these bounds with 20% porosity.83

Figure 3.2: Seismic P-wave velocity for the reservoir fluids. Batzle-Wang 1992 empirical relationships have been used to transform PVT properties of oil-gas-water. Note that bubble point pressure is 2000 psi.....84

Figure 3.3: Effects of water saturation (upper panel) and pore pressure (lower panel) on density, P&S-wave velocities of the reservoir rocks. Continuous and dashed lines indicate P&S-wave velocities, respectively. Upper bounds (UB) are shown in black, lower bounds (LB) in blue, and middle bounds (MB) in red. 85

Figure 3.4: Reservoir A: Joint effects of changes in water saturation and pore pressure on Multi-Component (MC) seismic traveltimes (first row) and Reflection Coefficients, RCs, (second row). dTpp, dTps, and dTss are the changes in MC traveltimes for conventional P-P, converted P-SV, and pure SH-SH seismic reflectivity data. dRpp, dRps, and dRss indicate the associated changes in MC RCs. 86

Figure 3.5: Reservoir B: Joint effects of changes in water saturation and pore pressure on Multi-Component (MC) seismic traveltimes (first row) and Reflection Coefficients, RCs, (second row). dTpp, dTps, and dTss are the changes in MC traveltimes for conventional P-P, converted P-SV, and pure SH-SH seismic reflectivity data. dRpp, dRps, and dRss indicate the associated changes in MC RCs. 87

Figure 3.6: Reservoir C: Joint effects of changes in water saturation and pore pressure on Multi-Component (MC) seismic traveltimes (first row) and Reflection Coefficients, RCs, (second row). dTpp, dTps, and dTss are the changes in MC traveltimes for conventional P-P, converted P-SV, and pure SH-SH seismic reflectivity data. dRpp, dRps, and dRss indicate the associated changes in MC RCs. 88

Figure 3.8: Single probability density function (PDF) for the RCs on the left column and for traveltimes on the right column. Three rows in this figure from top to bottom correspond to reservoir A, B, and C, respectively.....90

Figure 3.9: Joint probability density function (JPDF), the associated marginal single PDFs, the joint cumulative distribution function (JCDF), and the corresponding single CDF of reservoir C and only for P-P seismic data. 91

Figure 3.10: Single probability detectors (SPDs) for RCs on the left and for traveltimes on the right column. Three rows in this figure from top to bottom correspond to reservoir A, B, and C, respectively.....92

Figure 3.11: Joint probability detectors (JPDs) for three synthetic reservoirs. Three rows in this figure from top to bottom correspond to reservoir A, B, and C, respectively. Horizontal axes on these plots are the absolute (positive) values of changes in seismic traveltimes. Vertical axes are absolute values of changes in seismic RCs. All panels are color-coded with probability values ranged from 0 to 1. Note that the higher changes in time-lapse signals, the lower probability. 93

Figure 4.1: Sensitivities of MC seismic traveltimes vs. incident angle to water saturation (a), and to pore pressure (b). Sensitivity of P-P traveltime (Tpp) is shown in blue, P-SV (Tps) in green, and SH-SH (Tss) in red. Panels (c) and (d) display the sensitivities of traveltimes at zero offset for different saturations and pressures. 102

Figure 4.2: Sensitivities of MC seismic RCs (P-P (a), P-SV(b), and SH-SH (c) to contrast in P&S-wave velocities, in density, and Poission ratios at OWC. Sensitivity curves are displayed for contrast in P-wave velocity (in blue), contrast in S-wave velosity (in green), contrast in density (in red), and Poisson's ratios for both media (Pr1 for top layer in black, and Pr2 for bottom layer in ligh blue).....103

Figure 4.3: Sensitivities of MC seismic RCs to water saturation (a and c for reservoir top and OWC, respectively) and to pore pressure (b and d for reservoir top and OWC, respectively). Sensitivity of P-P (Rpp) is shown in blue, P-SV (Rps) in green, and SH-SH (Rss) in red. 104

Figure 5.1: 3D distribution of effective porosity model (Christie and Blunt, 2001) associated with synthetic geologic model used for the numerical simulation of seismic and multi-phase fluid-flow. The model is described on a regular Cartesian grid. The model size is 220*60*35 cells in X (east-west), Y (north-south), and Z (depth) directions, respectively. The grid size defining the cells is 10*10*10 meters, so the model dimension is 2200m*600m*350m. 134

Figure 5.2: Petrophysics model. Panel a shows the dispersed clay model for porosity reduction due to increasing of clay. Panel b dispalys horizontal permeability versus shale content. Panel c is permeability vs. effective porosity. In panels a,b, and c, three colors are associated with three facies A(in blue), B(in green), and C(in red). Black dots in panels b and c are projected reservoir points . Panel d shows fluid saturations vs. shale content. Swe, So, Swb, and Swt are effective water saturation, oil saturation, caly bound water saturation, and total water saturation, respectively. 135

Figure 5.3: Distribution of petrophysical properties for a 2D cross-section in the middle of the 3D reservoir. X and Y axes are the same for all panels and they are reservoir length and thickness in meters, respectively. Each panel is color-coded for the corresponding attribute. 136

Figure 5.4: Time-lapse normalized percentage changes in effective water saturation, Sw, (top row), pore pressure, Pp, (2^{nd} row from top), and the associated changes in seismic acoustic impedance, AI, (3^{rd} row from top) and shear impedance, SI, (bottom row) between base survey and monitor survey after 5 years of waterflooding (left column), between monitor survey after 5 years and monitor survey after 10 years (middle column), and between base survey and monitor survey after 10 years (right column). X and Y axes are the same for all panels and they are reservoir length and thickness in meters, respectively. Each panel is color-coded for the corresponding attribute. 137

Figure 5.5: Petro-elastic model embedded into a 1D background elastic model simulating surrounding offshore sedimentary basin. The background model has dimensions of 600×1×300 in length, width, and depth respectively. The grid size is the same as reservoir model 10×10×10 m^3. The first one kilometer of the model is sea water. Reservoir was injected at depth 2000 m of the background model and sandwiched between an ash and salt layers at top and bottom, respectively. The edges of the reservoir were smoothed to better blend with the background model.138

Figure 5.6: Plane-wave response of the 1D locally model in the middle of 2D reservoir for base survey (T0). The response was simulated by full elastic reflectivity algorithm for flat frequency of 0 to 75 Hz. Markers on the seismic data shows significant events associated with 2D model in Figure 5.5. No gain is applied to the data. For display purpose a band-pass filter of 5 to 65 Hz is applied. 139

Figure 5.7: Normalized derivative of a Gaussian wavelet with a peak frequency of 35 Hz convolved with 1D and 2D plane-wave seismic data and used, as a source, to simulate 2D finite difference data. 140

Figure 5.8: The scaling scheme used to tune 1D plane-wave seismic data computed from various algorithms. 141

Figure 5.9: 1D plane-wave responses of the base survey (T0) at ray parameter (p=0 sec/km) computed by different seismic modeling methods. 142

Figure 5.10: Residuals of 1D plane-wave responses of the base survey (T0) at ray parameter (p=0 sec/km) computed by different seismic modeling methods. 143

Figure 5.11: Residuals of 1D plane-wave responses of the base survey (T0) at ray parameter (p=0.1 sec/km) computed by different seismic modeling methods. 144
Figure 5.12: Residuals of 1D plane-wave responses of the base survey (T0) at ray parameter (p=0.2 sec/km) computed by different seismic modeling methods. 145
Figure 5.13: Residuals of 1D plane-wave responses of the base survey (T0) at ray parameter (p=0.3 sec/km) computed by different seismic modeling methods. 146
Figure 5.14: 1D plane-wave responses of the time-lapse (T5-T0), base survey is subtracted from monitor survey after 5 years of waterflooding, at ray parameter (p=0 sec/km) computed by different seismic modeling methods. 147
Figure 5.15: The residuals of 1D plane-wave responses of the time-lapse (T5-T0), base survey is subtracted from monitor survey after 5 years of waterflooding, at ray parameter (p=0 sec/km) computed by different seismic modeling methods. 148
Figure 5.16: The residuals of 1D plane-wave responses of the time-lapse (T5-T0), base survey is subtracted from monitor survey after 5 years of waterflooding, at ray parameter (p=0.1 sec/km) computed by different seismic modeling methods. 149
Figure 5.17: The residuals of 1D plane-wave responses of the time-lapse (T5-T0), base survey is subtracted from monitor survey after 5 years of waterflooding, at ray parameter (p=0.2 sec/km) computed by different seismic modeling methods. 150

Figure 5.18: The residuals of 1D plane-wave responses of the time-lapse (T5-T0), base survey is subtracted from monitor survey after 5 years of waterflooding, at ray parameter (p=0.3 sec/km) computed by different seismic modeling methods. 151
Figure 5.19: A pseudo FORTRAN code for Split-step Fourier plane-wave (SFPW) seismic modeling. 153
Figure 5.20: Plane-wave responses for base survey (T0) and time-lapse (T10-T0), associated with the base and the monitor survey after ten years of water flooding, at p= 0 sec/km. The first and the third panel are associated with 1D modeling and the second and forth panels are 2D modeling computed by SFPW algorithm. 154
Figure 5.21: Plane-wave responses for base survey (T0), at p= 0 sec/km, without (first panel) and with (second panel) internal multiples. The third panel shows the residual of the first two panels, highlighting the internal multiples. 155
Figure 5.22: Plane-wave responses for time-lapse (T10-T0), associated with the base and the monitor survey after ten years of water flooding, at p= 0 sec/km, without (first panel) and with (second panel) internal multiples. The third panel shows the residual of the first two panels, highlighting the internal multiples. 156
Figure 5.23: Finite difference shot gather located in the middle of 2D reservoir for base survey (T0). Pressure wavefield is displayed. Markers on the seismic data shows significant events associated with 2D model in Figure 5.5. For display purpose AGC of length 500 ms and band-pass filter of 5 to 65 Hz is applied. 157

Figure 5.24: Finite difference OBS gather located in the middle of 2D reservoir for base survey (T0). Horizontal velocity wavefield is displayed. Markers on the seismic data shows significant events associated with 2D model in Figure 5.5. For display purpose AGC of length 500 ms and band-pass filter of 5 to 65 Hz is applied. 158

Figure 6.1: 3D distribution of effective porosity model (Christie and Blunt, 2001) associated with synthetic geologic model used for the numerical simulation of seismic and multi-phase fluid-flow. The model is described on a regular Cartesian grid. The model size is 220*60*35 cells in X (east-west), Y (north-south), and Z (depth) directions, respectively (top panel). The grid size defining the cells is 10*10*10 meters, so the model dimension is 2200m*600m*350m (bottom panel). 183

Figure 6.2: Three directional cross-sections of 3D effective porosity model in Figure 2.1.....185

Figure 6.3: Map view of petrophysical facies A, B, and C overlaid on 2D distribution of effective porosity model. Grid numbers are used to show reservoir dimensions in two horizontal directions. 186

Figure 6.4: Petrophysics model. Panel a shows the dispersed clay model for porosity reduction due to increasing of clay. Panel b dispalys horizontal permeability versus shale content. Panel c is permeability vs. effective porosity. In panels a,b, and c, three colors are associated with three facies A(in blue), B(in green), and C(in red). Black dots in panels b and c are projected reservoir points . Panel d shows fluid saturations vs. shale content. Swe, So, Swb, and Swt are effective water saturation, oil saturation, caly bound water saturation, and total water saturation, respectively. 187

Figure 6.7: The capillary pressures data, the relative permeability curves, and PVT properties of reservoir fluids. FVF stands for Formation Volume Factor. 191

Figure 6.9 Surface reservoir simulation outputs, i.e., production data, for a period of 10 years of waterflooding to enhance oil recovery. 193

Figure 6.10 Rock physics model displaying the effects of porosity (Panel a), saturation (Panel b), and joint porosity-saturation (Panel c) on rock resistivity. 194

Figure 6.11 Comparison of seismic and CSEM rock physics model in terms of time-lapse signal due to changes in effective water saturation. Elastic parameters including P-wave velocity (Vp), S-wave velocity (Vs), and density (Rho) are less affected than rock resistivity (Rt). 195

Figure 6.12: Resistivity logs extracted from the middle of the 2D reservoir for base survey (in blue), the first monitor survey after 5 years of water flooding (dashed red), and the second monitor survey after 10 years of waterflooding (dashed black). 196

Figure 6.13: Time-lapse percentage changes in effective water saturation and the associated changes in electrical resistivity and seismic acoustic impedance for the first monitor survey(left column) and the second monitor survey(right column) after five and 10 years of water flooding, respectively. X and Y axes are the same for all panels and they are reservoir length and thickness in meters, respectively. Each panel is color-coded for the corresponding attribute. As mentioned in text, a minus sign is applied on the resistivity to have a consistent color display for flood geometry between saturation, acoustic impedance, and resistivity models. 197

Figure 6.14: 1D CSEM data associated with the base survey (t0) illustrated in Figure 6.12. The absolute amplitude (left column) and phase (right column) of the electric and magnetic fields for a single frequency of 0.25 Hz are simulated on sea-floor detectors. The horizontal axis is the same for all panels and it is range or offset between transmitter and receivers in meters. Each panel is labeled for the corresponding transmitter's orientation and color legends show three field components associated with each transmitter.....198

Figure 6.15: 1D CSEM time-lapse changes in response to waterflooding after 10 years between the base survey (t0) and monitor survey (t10) illustrated in Figure 6.12. The amplitude ratio in percent (left column) and phase difference in degree (right column) of the electric and magnetic fields for a single frequency of 0.25 Hz are simulated on sea-floor detectors. The horizontal axis is the same for all panels and it is range or offset between transmitter and receivers in meters. Each panel is labeled for the corresponding transmitter's orientation and color legends show three field components associated with each transmitter.....199

Figure 6.16: 1D-CSEM time-lapse changes in response to waterflooding after 5 years (solid lines) and 10 years (dashed lines). Inline transmitter is employed and inline electric (in red), crossline magnetic (in blue), and vertical electric (in green) fields simulated for a single frequency of 0.25 Hz. The top panel is the amplitude ratio (in percent), and the bottom panel is the phase difference (in degree) between base and monitor surveys. The horizontal axis is range or offset between transmitter and receivers in meters.....200

Figure 6.17: Frequency analysis for 1D CSEM time-lapse changes due to waterflooding after 5 and 10 years in solid and dashed line, respectively. The amplitude ratio in percent (left column) and phase difference in degree (right column) of the inline electric (in red) and crossline magnetic (in blue) field components for inline transmitter of 0.25 Hz frequency are displayed. The horizontal axis is the same for all panels and it is range or offset between transmitter and receivers in meters.201

Figure 6.18: The coarse starting grid (a) and the final refined gird (b) created by triangular meshing over the 2D reservoir model embedded into 1D background.....202

Figure 6.19: 2.5D CSEM time-lapse response of crossline magnetic field in midpoint-offset geometry. From top, the first and the second panels are related to the amplitude ratio (%) and the phase difference (degree) after 5 years of waterflooding, respectively. Third and fourth panels correspond to the amplitude ratio (%) and the phase difference (degree) after 10 years of waterflooding, respectively. The contour lines in all panels are the field amplitude (log10) of the base survey and show that the anomalies are present above the present day receiver noise floor of 10^{-18} T/Am..203

Figure 6.20: 2.5D CSEM time-lapse response of inline electric field in midpoint-offset geometry. From top, the first and the second panels are related to the amplitude ratio (%) and the phase difference (degree) after 5 years of waterflooding, respectively. Third and fourth panels correspond to the amplitude ratio (%) and the phase difference (degree) after 10 years of waterflooding, respectively. The contour lines in all panels are the field amplitude (log10) of the base survey and show that the anomalies are present above the present day receiver noise floor of 10^{-15} V/Am^2.204

Chapter one: Introduction

1.1 PROBLEM STATEMENT AND LITERATURE REVIEW

Exploration and development of any hydrocarbon reservoir consists of different phases including reservoir delineation, characterization, production, and monitoring. During these stages various sources of information (well logs, core analyses, production and seismic data) are integrated to construct a realistic three dimensional subsurface geological reservoir model which can reliably predict past and future production of the reservoir. In order to generate such a predictive reservoir model, spatial and temporal distributions of petrophysical properties of the reservoir comprising porosity, directional permeability, shale content, water saturation, pore pressure, etc. need to be estimated away from the well locations. The petrophysical properties are generally well defined with high vertical resolution at a few sparse well locations, but they are often unknown between and beyond the wells. In contrast, seismic data are very well distributed volumetrically in a dense surface grid covering the entire reservoir model. This is the greatest advantage of seismic data, which makes it the most reliable source of information beyond the well locations. Relatively low vertical resolution, low signal to noise ratio, weak tie between seismic and well logs, and low sensitivity to fluid within low porosity stiff rocks are limitations to the successful use of seismic data, and make its applications to the reservoir problem very challenging. The question is how to best obtain petrophysical properties from seismic data.

Conventional P-P Seismic data have been used to infer elastic parameters, e.g., P-wave velocity, S-wave velocity, and bulk density, via seismic elastic inversion (e.g., Smith and Gidlow, 1987; Stoffa and Sen 1992; Buland and Omre, 2003, etc). Seismic data can also be used to classify lithology and fluid clusters via various cross-plotting

techniques. Various forms of cross-plotting methods have been addressed by several authors. In these methods, pre-stack seismic data are inverted to elastic parameters, e.g., P-wave and S-wave velocities and density or acoustic and shear impedances (Fatti et al. 1994). Next, cross-plots of the original inverted elastic parameters or their derivatives to other elastic parameters, e.g., shear impedance vs. acoustic impedance, $\lambda\rho$ vs. $\mu\rho$ (Goodway et al. 1997), and elastic impedance vs. acoustic impedance (Connolly 1999), are made. Similarly, elastic parameters derived from well logs are cross-plotted and color-coded with other discriminatory well logs such as shale fraction and porosity. The well log analysis allows one to distinguish lithology and fluid classes which will guide the classification of the seismic cube. Finally, lithology and fluid clusters are back-projected from the cross-plot domain to the seismic cube.

Time-lapse seismic data consist of two or more repeated seismic surveys recorded at different calendar times over a depleting reservoir in primary, secondary, or even tertiary recovery phases. The main target of time-lapse seismic is to detect, discriminate, and estimate the changes in subsurface rock and fluid properties due to production, so ultimate recovery can be optimized. Important industrial applications are as follows:

- Identifications of flood fronts, preferential pathways, thief zones, and flow barriers, i.e. seals, by-passed pay and infill target definition, leading to better understanding of tectonic and depositional environment involved in the reservoir under study (Qualitative seismic time-lapse interpretation) .
- Discrimination of saturation and pressure changes from changes in seismic attributes (Quantitative seismic time-lapse interpretation).
- Updating of the reservoir flow model in order to have realistic reservoir production forecasts (Seismic reservoir history matching).

As summarized above and depending on ambiguities in the description of the reservoir architecture, the quality of seismic data and economic considerations for the field under study, seismic time-lapse interpretation can be performed in different levels. The most common approach is the qualitative interpretation of changes in seismic observations, e.g., amplitude, traveltime, etc., and association of the changes in the seismic attributes to changes in reservoir parameters, e.g., porosity, saturation, pressure, temperature, etc. The qualitative interpretation of time-lapse seismic data has been addressed by numerous workers, e.g. Cooper et al. (1999), Lumley et al. (1999), Marsh et al. (2001), Rutledal et al. (2001), Behrens et al. (2002), and various papers in Parker et al. (2003).

The more advanced methodology is to quantitatively interpret or invert changes in seismic observations or derived seismic attributes to changes in fluid saturation and pressure. This technique has been addressed by several authors in the literature. Some workers make use of inverted elastic parameters, e.g., acoustic and shear impedance changes, to indirectly estimate pressure and saturation changes (e.g., Tura and Lumley, 1999, Cole et al. 2002, Lumley 2003, Lafet et al. 2009). Other techniques have been proposed to directly invert time-lapse seismic data for fluid saturation and pressure changes. For example, Landrø (2001) and Landrø et al. (2003) directly inverted time-lapse seismic data for saturation and pressure changes based on an approximate rock physics model and a linearized form of reflection coefficients. Other authors (e.g., Angelov, 2004) made improvements based on Landrø's method. Veire et al. (2006) presented a stochastic inversion method to discriminate pressure and saturation changes directly from P-P time-lapse AVO data. MacBeth et al. (2006) developed a first order linear formula relating changes in any pair of seismic attributes to changes in fluid pressure and saturation.

The most recent application of time-lapse seismic is referred to as seismic reservoir history matching, 4D history matching, or reservoir history matching constrained by time-lapse seismic data. This state-of-the-art technology is a multi-disciplinary approach to integrate well logs, core analyses, production data, and time-lapse seismic reflectivity data. Reservoir modeling and simulation, petro-elastic rock and fluid modeling, and seismic wave propagation modeling are some of the disciplines involved in this technique. Several case studies, e.g., Walker et al. (2006) in the Andrew, Valhall, and Harding fields in the North Sea, have demonstrated that joint history matching of seismic and production data leads to a positive impact on the estimated reservoir parameters relative to estimates obtained from production history matching alone. This is due to the additional spatial knowledge contained in time-lapse seismic data.

In all above technologies, detecting small changes in seismic traveltimes and amplitudes is the key to successfully imaging the changes in reservoir properties. Seismic data as recorded are not just composed of primary arrivals with elastic reflection coefficients: also included will be internal multiples, converted waves, diffractions, etc. The question for this study, are these other arrivals significant enough to interfere with an analysis based solely on primary reflection coefficients. In responding to this question, here I briefly explain the current state of seismic modeling as a fundamental tool to investigate the effect of changes in reservoir properties on seismic data.

Seismic modeling simulates the propagation of elastic waves in a specified medium. There are several seismic modeling algorithms in seismology and they can be classified from various points of view. Accuracy, speed, and the range of wave phenomena that one seismic modeling algorithm can model, e.g., primary reflectors, multiples, converted waves, diffractions, head waves, critical reflections, etc., are some of

the important factors in classifying seismic modeling approaches. Currently, various approximate and hybrid seismic modeling algorithms are addressed in time-lapse modeling. Many papers address this concept by simulating a single seismic modeling for the overburden and conducting a set of repeated computations of seismic waveforms at the reservoir zone aimed at simulating the corresponding base and monitor surveys. Lecomte (1996), Gjotdal et al. (1998), and Hokstad et al. (1998) combined ray tracing in the overburden with repeated finite-difference (FD) seismic modeling in the reservoir zone. Robertson and Chapman (2000) deployed a similar approach by applying FD seismic modeling in both the overburden and target to allow for strongly scattering heterogeneities of the entire model. Kirchner and Shapiro (2001) used FD to simulate wave propagation in the overburden and employed Born perturbation theory to compute the production-induced changes in time-lapse seismograms.

In the seismic section of this dissertation, I first develop a petro-elastic model (See chapter 2 for details) and use seismic modeling techniques with different degrees of accuracy, including: 1D acoustic with and without internal multiples, 1D elastic without internal multiples, 1D full elastic reflectivity, split-steep Fourier plane-wave (SFPW), and staggered grid explicit FD. Next, I investigate the reservoir-scale effects of internal multiples, acoustic vs. elastic, the effect of converted waves, dimension of wave propagation (2D vs. 1D), and diffractions on time-lapse signatures. In addition, I demonstrate that the time-lapse response simulated with SFPW is closely correlated with the FD response but considerably faster to compute. Having superior speed to FD, the ability to model higher frequencies than FD, and yet comparable with FD and better than standard ray-based modeling, SFPW is the preferred method for reservoir characterization and monitoring workflows.

Controlled-source electromagnetic (CSEM) surveying has been recently applied to petroleum exploration as a direct hydrocarbon detector. The contrast between the electrical conductivity of hydrocarbon-saturated reservoir rocks and the surrounding water-saturated rocks leads to an anomaly in measured magnetic and electric fields emitted in the vicinity of the sea floor by dipole electrical transmitters and recorded at ocean bottom receivers. Various successful applications have been addressed by several authors (e.g., Ellingsrud et al. 2002; Eidesmo et al. 2002).

Time-lapse CSEM data consists of two or more repeated surveys recorded at different calendar times over a depleting reservoir. The main objective is to detect and estimate production-induced time-lapse changes in subsurface rock properties. In doing so, changes in observations, i.e., the amplitude and phase of magnetic and electric fields, or inverted attributes, e.g., rock resistivity, are often associated with changes in fluid saturation assuming a non-compacting isothermal reservoir. This technique has been addressed by several authors in the literature.

Wright et al. (2002) presented time-lapse transient EM surveys over a shallow underground gas storage reservoir with high porosity and showed that the data are repeatable enough to detect the reservoir and monitor the moving of gas-water content due to gas injection and/or extraction in summer and winter, respectively. Lien and Mannseth (2008) conducted a feasibility study of time-lapse CSEM data to monitor the waterflooding of an oil reservoir. Utilizing 3D integral equation modeling, they found that time-lapse signals exhibit detectable changes even in the presence of measurement errors. Orange et al. (2009) further expanded the work by Lien and Mannseth (2008) by utilizing a 2D finite element modeling to simulate time-lapse CSEM data in response to several simplified waterflooding scenarios, including lateral and bottom flooding, and partial depletion. Through a set of 2D modeling studies, they showed that a data

repeatability of 1-2% is required to detect the small time-lapse signals. Zach et al. (2009) conducted 3D time-lapse modeling by perturbing conductivity over a large reservoir (10*10 km^2) and reported anomalies of 30% to 50% changes in relative amplitudes of base and monitor surveys. They mentioned that these relatively strong time-lapse signals as well as different shapes of fronts can be monitored considering 5% repeatability for time-lapse surveys. Black et al. (2009) modeled time-lapse CSEM response over a realistic geologic model for a simplified flood geometry without fluid flow simulation and rock physics modeling. They showed that marine CSEM data are able to locate the position of the oil-water contact if the field is normalized by the background, bathymetry, and salt dome effects.

No reservoir simulation and rock physics modeling were performed in the above-mentioned studies; instead, they all consider direct perturbation of electrical-conductivity. In 2009, PGS (Petroleum Geo-Services) published a time-domain EM repeatability experiment over the North Sea Harding field. Fluid flow simulation and resistivity modeling by Archie's equation for clay-free sandstone were combined by integral equation modeling to simulate EM data. They concluded that the production-induced time-lapse changes in reservoir resistivity would be observable provided that a signal to noise ratio of greater than 100, i.e., 40dB, is obtained (Ziolkowski et al. 2010).

In the CSEM section of this dissertation, I first generate a 2D geological reservoir model showing the realistic spatial distribution of petrophysical parameters. Fluid flow simulation and a geologically consistent rock physics model are then employed to convert the petrophysical properties of the shaly sandstone to electrical resistivity. The representative time-dependent resistivity model developed here shows the accurate front geometry during a waterflooding to enhance oil recovery. To simulate the surrounding rocks, I embed the reservoir within a 1D background resistivity model correlated with a

P-wave velocity log. Finally, I numerically acquire 1D and 2.5D time-lapse CSEM data over the reservoir to assess the value of EM data in monitoring of a waterflooding scenario. To the best of my knowledge, no such comprehensive study has been reported in the open technical literature.

1.2 RESEARCH OBJECTIVES

The main objective of this dissertation is to perform various sensitivity and feasibility analyses to investigate the effects of production-induced time-lapse changes on geophysical measurements, including seismic and CSEM data. For doing so, a realistic reservoir model is numerically simulated based on a prograding near-shore sandstone reservoir. Next, the constructed reservoir model is subjected to numerical simulation of multi-phase fluid flow to replicate a waterflooding scenario of a black oil reservoir and to predict the spatial distributions of fluid pressure and saturation. A modified Archie's equation for shaly sandstones is utilized to simulate rock resistivity. Finally, a geologically consistent stress-sensitive rock physics model, combined with the modified Gassmann theory for shaly sandstones, is utilized to simulate seismic elastic parameters. Using the resistivity models, a base and two monitor time-lapse CSEM surveys are simulated via accurate numerical algorithms. 2.5D CSEM modeling demonstrates that a detectable time-lapse signal after 5 years and a strong time-lapse signal after 10 years of waterflooding are attainable with the careful application of currently available CSEM technology.

To simulate seismic waves, I employ different seismic modeling algorithms, one-dimensional (1D) acoustic and elastic ray tracing, 1D full elastic reflectivity, 2D split-step Fourier plane-wave (SFPW), and 2D stagger grid explicit FD. My analyses demonstrate that acoustic modeling of an elastic medium is a good approximation up to

ray parameter (p) equal to 0.2 sec/km. However, at p=0.3 sec/km, differences between elastic and acoustic wave propagation is the more dominant effect compared to internal multiples. Here, converted waves are also generated with significant amplitudes compared to primaries and internal multiples.

1.3 DISSERTATION OUTLINE

This dissertation is divided to seven chapters. After the current chapter, the second chapter is devoted to describing the depositional system of the reservoir used for this study, petrophysical modeling, fluid flow simulation, and rock physics modeling. This systematic trend aims at constructing a geological reservoir model with a meaningful spatial distribution of petrophysical properties. The final reservoir model is launched to a reservoir simulator to predict the distributions of water saturation and pore pressure as a result of water flooding. Then, static and dynamic reservoir parameters provide the necessary input for the rock physics model in which reservoir parameters are converted to seismic elastic parameters. At the end of the chapter, time-lapse rock-fluid physics templates are introduced and evaluated for the current reservoir.

The third chapter of this dissertation develops a methodology called seismic time-lapse crossplot to directly transfer changes in MC seismic traveltimes and reflection coefficients to changes in saturation and pressure. I also deploy a statistical method to determine whether or not a reservoir would be a candidate for a future MC seismic time-lapse prospect. This task can be done based on the quality of available seismic data and using a statistical representation of the data in seismic time-lapse crossplots.

The fourth chapter consists of analytical and numerical methods to compute the sensitivity of MC seismic attributes, e.g., seismic reflectivity amplitude and traveltime, with respect to petrophysical properties including porosity, shale content, water

saturation, and pore pressure. The sensitivity analyses shed light on which petrophysical properties can be directly retrieved from seismic data.

The fifth chapter describes various techniques to simulate seismic wave propagation in subsurface media. In summary, approximate, analytical, and purely numerical seismic modeling methods are presented. Then, ray tracing 1D synthetic seismic, reflectivity 1D synthetic seismic, split-step Fourier plane-wave, and stagger grid finite difference 3C-2D pre-stack seismic gathers have been generated over the reservoir under study. Finally, various comparisons are made among different seismic modeling approaches in terms of the detectability of fluid flow within the reservoir.

The sixth chapter is devoted to a feasibility study on time-lapse CSEM. A poorly consolidated shaly sandstone reservoir model is simulated and subjected to numerical simulation of multi-phase fluid flow to replicate a waterflooding scenario. A modified Archie's equation for shaly sandstones is then utilized to simulate rock resistivity. The petro-electric model developed in this chapter can be efficiently utilized in sensitivity analyses of CSEM data to petrophysical properties and, ultimately, applied to reservoir characterization and monitoring research. As an example, I present a time-lapse frequency domain CSEM feasibility study over the 2D reservoir model embedded in a 1D background resistivity model. Finally marine 2.5D CSEM data are simulated and the corresponding data is analyzed in terms of the detectability of time-lapse signals using the current CSEM technology.

The seventh chapter summarizes the overall conclusions of this dissertation and proposes recommendations for future work.

Chapter two: Reservoir modeling and rock physics analysis

This chapter is devoted to describing the depositional system of the reservoir under study, petrophysical modeling, fluid flow simulation, and rock physics modeling. This development aims at constructing a geological reservoir model with a meaningful spatial distribution of petrophysical properties. The reservoir model is launched into a reservoir simulator to predict the spatial distributions of water saturation and pore pressure due to an active water flood scenario. Then, computed static and dynamic reservoir properties provide the necessary input parameters for rock physics modeling through which reservoir properties are converted to seismic elastic parameters. At the end of this chapter, time-lapse rock-fluid physics templates are introduced and evaluated for the current reservoir conditions. Using the constructed synthetic reservoir model, a comparison is made to investigate the discriminatory power of different cross-plotting scenarios in terms of distinguishing the changes in saturation and pore pressure in a typical time-lapse seismic study. The same reservoir model created here will be used later in chapters 5 and 7 where repeated seismic vintages will be generated and inverted to seismic elastic parameters and petrophysical properties.

2.1 INTRODUCTION

This chapter appraises the ultimate ability of inverted time-lapse seismic data to discriminate the changes in fluid saturation and pore pressure. To do so, I simulate a poorly consolidated shaly sandstone reservoir model based on a prograding near-shore depositional environment. To account for spatial distribution of petrophysical properties, an effective porosity model is first simulated by Gaussian geostatistics. Dispersed clay and dual water models are then efficiently combined with other well-known theoretical and experimental petrophysical correlations to consistently simulate reservoir model

parameters including total porosity, directional permeabilities, shale content, initial water situation and pore pressure.

Next, the constructed reservoir model is subjected to numerical simulation of multi-phase fluid flow. A commercial reservoir simulator is employed to predict the spatial distributions of pore pressure and water saturation due to water injection into a black oil reservoir containing two phases: water and live oil.

A geologically-consistent stress-sensitive rock physics model, followed with modified Biot-Gassmann fluid substitution for shaly sandstones, is then utilized to simulate the inverted seismic elastic parameters. As a result, the comprehensive petro-elastic model developed in this chapter can be efficiently utilized in sensitivity analyses of seismic elastic parameters to petrophysical properties and, ultimately, applied to seismic reservoir characterization and monitoring research. As an example, I present a sensitivity analysis of seismic attributes and their crossplotting as a tool to discriminate the effect of pressure and saturation in a time-lapse seismic study. Various forms of seismic attributes are derived from the basic seismic attributes, i.e., P-wave velocity (Vp), S-wave velocity (Vs), density (Rho), Acoustic Impedance (AI) and Shear Impedance (SI), and then are cross-plotted to compare the discriminatory power of different cross-plotting scenarios in terms of distinguishing the changes in saturation and pore pressure. The imposed production conditions create variant states of pressure increase, pressure decrease, constant pressure, and water saturation increase in ten distinct calendar time intervals; therefore, opportunities exist to analyze various scenarios for changes in the corresponding elastic seismic attributes.

Sensitivity analysis demonstrates that well-known LMR (Lambda-Mu-Rho), i.e., [$\lambda\rho$ (LR) vs. ($\mu\rho$) MR] is the most convenient way to discriminate changes in saturation and pressure, and commonly used crossplots, e.g., [AI vs. SI] or [velocity ratio (Vp/Vs)

vs., AI], have less discriminatory power than that of LMR. The overall trend of LMR and [AI, SI] crossplots are similar, but LMR has wider ranges in both axes. However, [AI, SI] are the original and the most stable seismic attributes with the least amount of noise. The noise level in other derived seismic attributes, e.g., LMR and Vp/Vs, is amplified and make the use of the corresponding crossplots less practical. Consequently, cross-plotting of [AI, SI] should be the most conservative and stable way to quantitatively separate saturation and pressure changes. It is also shown that the saturation and pressure patterns are detectable in most of the time-lapse scenarios, however; saturation pattern is more likely detectable because the percentage in pressure change is often lower than that of the saturation change. Imperfections in saturation and pressure patterns exit in various forms and they can be explained by interaction of saturation and pressure, diffusive nature of pressure, and rapid change in pressure due to the production operations.

2.2 BACKGROUND AND FORMULATION

Seismic reflection data have been used to infer lithology and fluid from subsurface rocks. Various seismic attributes can be extracted from seismic volumes in order to qualitatively, semi-quantitatively, and quantitatively perform seismic litho-fluid facies classifications. Pattern recognition techniques, multivariate statistical methods, Bayesian classification, and neural networks have been utilized to map litho-fluid facies from seismic data. In most cases, authors have addressed cross-plotting of seismic attributes to classify seismic volumes into distinct litho-cubes. For example, Macrides et al. (2000) used supervised and unsupervised statistical pattern recognition technique to classify seismic volumes via cross-plotting of seismic attributes computed from seismic traces within reservoir intervals. Amplitude versus offset (AVO) is the other commonly used technique making use of cross-plotting of intercept and gradient of the amplitudes of

pre-stack seismic angle gather data to qualitatively infer litho-fluid clusters (Castagna and Backus 1999).

In general, classification techniques based on the seismic observations and/or seismic attributes can be unreliable due to wavelet and tuning effects. To overcome this problem, inverted seismic parameters, e.g., Rho, Vp, Vs, AI, and SI extracted from pre-stack seismic data have been used in most recent applications. In doing so, cross-plots of the original inverted parameters or their derivatives to other elastic parameters, e.g., [$\lambda\rho$ (LR) vs. ($\mu\rho$) MR] (Goodway et al. 1997), and [Elastic Impedance (EI) vs. AI] (Connolly 1999), are made. Similarly, well log derived elastic parameters are cross-plotted and color-coded with other discriminatory well logs such as shale fraction and porosity. The well log analysis allows one to distinguish lithology and fluid classes which will guide the classification of the inverted seismic attributes in crossplot domains. Finally, lithology and fluid clusters are back projected from cross-plot domains to seismic volumes (Avseth et al. 2005).

A popular crossplotting technique is called the rock physics template (RPT). In RPT analysis, the depositional and diagenetic trend models are combined with a rock physics model and Gassmann fluid substitution to make predictive templates of elastic parameters, e.g., Poisson ratio versus acoustic impedance. Using the RPTs, one is able to distinguish the litho-fluid effects and to extract some of the petrophysical properties, e.g., total porosity and water saturation (Avseth et al. 2005). However, the RPTs are not universal and they need to be created for each individual petroleum basin.

Recently, statistical rock physics (Mukerji et al. 2001a) has been introduced to the geosciences community to address inherent uncertainties involved in simplified physical relationships between petro-elastic attributes. Statistical rock physics combined with

cross-plotting techniques has been performed to map probabilistic litho-fluid facies (Takahashi 1999, Avseth et al. 2001, and Mukerji et al. 2001b).

The summary above was given as a reference to the current state-of-the-art technology in classifying seismic volumes into fluid and rock facies. In this chapter, I investigate various cross-plots to see whether or not the concept of the crossplotting of inverted seismic attributes can be extended to classify time-lapse seismic signals. Time-lapse seismic data consists of two or more repeated seismic surveys recorded at different calendar times over a depleting reservoir in primary, secondary, or tertiary recovery phases.

Depending on ambiguities in the description of the reservoir architecture, quality of the seismic data, and economic consideration of the filed under study, seismic time-lapse interpretation can be performed in three different levels.

The first approach is the qualitative interpretation of changes in seismic observations, e.g., amplitude, traveltime, etc., and association of the changes in the seismic attributes to changes in reservoir parameters, e.g., porosity, saturation, pressure, temperature, etc. The qualitative interpretation of time-lapse seismic data has been addressed by numerous workers, e.g. Cooper et al. (1999), Lumley et al. (1999), Marsh et al. (2001), Rutledal et al. (2001), Behrens et al. (2002), and various papers in Parker et al. (2003). The main objective of this type of analysis is to indentify flood fronts, preferential pathways, thief zones, and flow barriers, by-passed pay and infill target. Most of the authors mentioned that these objectives have been achieved and time-lapse seismic data have a positive impact on field development.

The second and more advanced methodology is to semi-quantitatively or quantitatively interpret or invert changes in seismic observations to changes in fluid

saturation and pressure. This approach is the main topic of this chapter and will be discussed in detail.

The third and most recent application of time-lapse seismic is referred to as seismic reservoir history matching, 4D history matching, or reservoir history matching constrained by time-lapse seismic data. This currently state-of-the-art technology is a multi-disciplinary approach to integrate well logs, core analyses, production data, and time-lapse seismic reflectivity data aimed at updating reservoir model. Reservoir modeling and simulation, petro-elastic rock and fluid modeling, seismic wave propagation modeling, and joint inversion of measured seismic and production data, are some of disciplines involved in this technique. Several case studies, e.g., Walker et al. (2006) in the Andrew, Valhall, and Harding fields in the North Sea, have demonstrated that joint history matching of seismic and production data leads to a positive impact on the quality of the estimated reservoir parameters relative to estimates obtained from production history matching alone. This is due to the additional spatial knowledge contained in time-lapse seismic data. The main focus of this chapter is to separate the changes in fluid saturation and pressure using changes in seismic attributes due to time-dependent reservoir production. Subsequently, seismic reservoir history matching (not discussed here) will be explained in chapter seven.

The main goal of this chapter is to associate the changes in time-lapse seismic attributes to the changes in fluid saturation and pressure. This approach has been addressed by several authors in the literature. Some techniques have been proposed to directly invert or transfer time-lapse seismic data to fluid saturation and pressure changes. For example, Landrø (2001) and Landrø et al. (2003) directly inverted time-lapse seismic data for fluid saturation and pressure changes based on an approximate rock physics model and a linearized form of reflection coefficients. Other authors (e.g., Angelov,

2004) made improvements based on Landrø's method. Veire et al. (2006) presented a stochastic inversion method to discriminate pressure and saturation changes directly from P-P time-lapse AVO data. MacBeth et al. (2006) developed a first-order linear formula relating changes in any pair of seismic attributes to changes in pressure and saturation. Shahin et al. (2009) proposed seismic time-lapse crossplots to directly transfer changes in multicomponent seismic traveltimes and reflection coefficients to changes in fluid saturation and pressure. In their method, there is no inversion involved and no assumption for rock physics is necessary. However, the methodology is only appropriate for single layer reservoirs.

Some workers make use of inverted elastic parameters, e.g., AI and SI changes, to indirectly estimate pressure and saturation changes via cross-plotting methods. To summarize, Tura and Lumley (1999) estimated changes in saturation and pressure via cross-plotting of inverted AI and SI changes. Cole et al. (2002) proposed a grid search method to estimate pressure and saturation by forward modeling of rock and fluid physics. Lumley (2003) proposed a 4D seismic cross-plot inversion method using a coordinate transformation and calibration with well data to simultaneously estimate pressure and saturation changes. Andersen et al. (2006) and Andersen et al. (2009) proposed a dual cross-plotting technology for the seismic facies classification problem. First, a crossplot of the inverted seismic attributes, i.e., [Vp/Vs vs. AI], for the base survey is created and lithofacies are classified accordingly. Second, time-lapse effects are classified via cross-plotting of 4D seismic attributes, i.e., [Δ(Vp/Vs) vs. ΔAI], where Δ denotes a change in any parameter due to production between base and monitor surveys. From 4D crossplots, one can classify the seismic volume into different subsets associated with scenarios of changes in pore pressure and/or saturation. Finally, the lithofacies and

4D classes are combined via dual classification to reveal pure and combined 4D effects in pay zones.

Here I examine the sensitivity of various seismic attributes, simulated via rock physics model and Gassmann fluid substitution, with respect to pore pressure and water saturation. It is shown that [AI vs. SI] should be the most stable crossplot to quantitatively discriminate saturation and pressure changes. The petro-elastic model developed here is utilized to validate the sensitivity analysis results.

2.3 CONSTRUCTING A SYNTHETIC RESERVOIR MODEL

2.3.1 Geological reservoir model

A stacked sand-rich strandplain reservoir architecture has been considered in this study to simulate a realistic geological framework. Strandplains are mainly marine-dominated depositional systems generated by seaward accretion of successive, parallel beach ridges welded onto the subaerial coastal mainlands. They are inherently progradational features and present on wave-dominated microtidal coasts (Tyler and Ambrose 1986; Galloway and Hobday 1996). This sand-rich, beach-ridge reservoir architecture is originally deposited as a clay-free geobody. However, due to post-depositional diagenesis, dispersed clay is produced and it is the main factor reducing porosity and permeability of the reservoir. Figure 2.1 displays a three dimensional distribution of effective porosity generated using a Gaussian Simulation technique. This model, comparative solution project (Christie and Blunt, 2001), is a large geostatistical model widely used in research in reservoir simulation, seismic and controlled-source electromagnetic (CSEM) modeling, etc. (e.g., Liang et al. 2010). I select to work with top 35 layers of the model which are representative of Tarbert formation, a part of Brent sequence of middle Jurassic age and one of the major producers in North Sea. By

changing the grid size and imposing smoothness, I modified this model to meet the objectives of this research. Next, I assign geologically consistent petrophysics information and add facies characterization to develop a more realistic reservoir model comparable to complicated models in the petroleum industry. The model is described on a regular Cartesian grid. The model size is 220*60*35 in X (east-west), Y (north-south), and Z (depth) directions, respectively. The grid size is 10*10*10 meters, so the model dimensions are 2200m by 600m by350m. Figures 2.2 illustrate cross-sections of the porosity cube in different directions.

The reservoir consists of three facies (Figure 2.3). Facies A is a fine grained sandstone with mean grain size distribution of 80 μm. This facies simulates a low porous and permeable sandstone reservoir with high clay content. Facies C is a course grained sandstone with mean grain size distribution of 500 μm. This facies is associated with a sandstone with high porosity and permeability and low clay content. Facies B is a transition facies between facies A and C and corresponds to a medium grained sandstone with mean grain size distribution of 250 μm. A strong correlation between grain size and clay content is reported by several authors (e.g., Saner et al. 1996), so this knowledge has been accordingly incorporated into the model by assigning clay-dependent grain sizes to the three facies, i.e., the higher the clay content, the lower the mean grain size distribution.

2.3.2 Petrophysics model

The geological model described above is used as the basic model in which petrophysical properties are populated assuming a meaningful petrophysics model. A petrophysics model includes a set of the theoretical and experimental correlations among various sets of petrophysical properties. The model is required to be validated using

available well log and core data. Here, the effective porosity model is first generated using Gaussian geostatistics and shale content and total porosity models are then computed assuming a dispersed clay distribution (Thomas and Stieber 1975; Marion et al. 1992), (Figure 2.4a). Horizontal permeabilities in the X and Y directions are equal and calculated based on the extension of the dispersed clay model to permeability introduced by Revil and Cathles (1999) (Figure 2.4b and 2.4c). Permeability fields depend on porosity, shale content, grain size distribution, and the degree of cementation; thus facies A, B, and C are assigned different trends in permeability-shale content and permeability-porosity domains based on their grain sizes. The vertical permeability field is taken as 25% of the horizontal permeability field for the entire reservoir.

So far, the effective and total porosities, shale content, and directional permeabilities are modeled using geostatistics and theoretical correlations according to dispersed clay distribution. Next, I initialize the reservoir for water saturation and pore pressure. An experimental correlation (Uden et al. 2004; Spikes et al. 2007) between water saturation and shale content is combined with the dual water model (Best 1980; Dewan, 1983; Clavier, 1984) to compute clay bound water (Swb), effective water saturation (Swe), total water saturation (Swt), and oil saturation (So) (Figure 2.4d). Initial reservoir pore pressure is simulated assuming a linear hydrostatic gradient from the top to the bottom of the reservoir. Figure 2.5 summarizes the distribution of petrophysical properties for a 2D cross section in the middle of the 3D reservoir. Figure 2.6 shows the histogram of petrophysical properties for the entire reservoir volume. Table 2.1 shows the petrophysical properties of the three facies within the reservoir.

A complete set of dynamic and static reservoir parameters has been generated and will be used to launch a reservoir simulation and to predict time-dependent subsurface distributions of water saturation, pore pressure, and surface well production data.

2.3.3 Reservoir simulation

Fluid flow simulation combines three fundamental laws governing fluid motions in porous media. These laws are based on conservation of mass, momentum, and energy (Aziz and Settari 1976). In this research, a commercial finite difference reservoir simulator, Eclipse 100, is utilized to replicate a waterflood enhanced oil recovery on a black-oil 2D reservoir containing oil, soluble gas, and water. The reservoir has no water drive. In addition, because of the high pressure conditions, no gas is produced in the reservoir. Thus, prior to waterflooding solution gas is the only drive mechanism forcing oil to be produced. This drive is so weak that implementation of water injection is required to enhance oil recovery. The other reason for selecting a water-flood is to provide some insights into potential water-floods in deepwater reservoirs where seismic data are the main and sometimes the only source of data.

As discussed earlier in developing the petrophysical model, the effective porosity model was constructed via Gaussian simulation. The relationships among petrophysical properties including porosity, permeability, and shale content are theoretically derived assuming the dispersed clay distribution. Then an experimental correlation combined with the dual water theoretical model was employed to obtain the initial water saturation from shale content. Finally a linear hydrostatic pressure gradient was selected to initialize the reservoir pore pressure distribution. The same grid block dimensions used to generate the geological model, i.e. 10 by 10 square meters, were used to simulate fluid flow; hence mathematical upscaling was not necessary.

The capillary pressure data, the relative permeability curves, and PVT (pressure, volume, and temperature) properties of reservoir fluids are borrowed from Killough (1995) model (Figure 2.7), and slightly modified to meet research objectives. As shown on the capillary pressure and relative permeability curves, the value of water saturation at

which water starts to flow, i.e. irreducible water saturation, is 0.15 and the same condition for oil is called residual oil saturation, and equals 0.12. In practice, irreducible water saturation and the corresponding capillary pressures are strongly clay-dependent in shaly sandstones, but here to simplify modeling, I assume a single capillary pressure curve and that irreducible water saturation is constant for the entire reservoir. The pressure below which the dissolved gas releases from oil, i.e. bubble point, is 2000 psi.

For a period of 10 years, the waterflood schedule is simulated by using two injectors at the corners and one producer in the middle of the reservoir. In this period, saturations and pressures values for each reservoir grid block are exported after each year. Collecting this database allows one to analyze the sensitivity of the corresponding seismic elastic parameters to a wide range of changes in fluid saturation and pressure. Figure 2.8 shows the snapshots of water saturation and pore pressure distributions at initial reservoir state and after production at different calendar times. With the start of production/injection, oil is replaced by water near the injectors and a portion of mobile oil will be extracted by the producer. Increasing the time, more oil will be replaced with water, hence; more oil will be produced. In other words, behind the waterfronts, the water saturation is increasing monotonically towards the injectors, meaning more oil is gradually displaced as more water is injected. In addition, one can clearly see that the behavior of the pressure front is very different from that of the waterfront. Pressure has a wave motion-like behavior and propagates very fast, but water has a mass bulk movement and moves slowly.

Figure 2.9 illustrates surface reservoir simulation outputs, i.e., production data, for a period of 10 years throughout the reservoir life. Water injectors perforate the entire 350 meters of reservoir thickness and are set to a constant water rate of 400 STB/Day. The only producer located in the middle of reservoir also perforate the whole reservoir

thickness and is initially set to a constant oil rate of 750 STB/Day. The reservoir initially starts producing oil with a plateau of 750 STB/Day. During this period, volumetric average pressure of the reservoir increases from 3200 to 3920 psi. After 2650 days, this rate is not affordable for the reservoir, so production strategy is intentionally changed to a constant bottom hole pressure (BHP) of 2600 psi for the producer. From this point the oil rate will decrease and a significant pressure drop is observed. The reservoir always produces above the bubble point pressure, i.e., 2000 psi; consequently, no gas is produced within the reservoir. However, dissolved gas will be released from live oil at the surface and gas will be produced with a similar production trend as oil. A slight water production occurs from the beginning up to the 2000 days of production, but it increases significantly afterward. CPU time for running 10 years of simulation of the 2D reservoir is 240 seconds.

Constructing a realistic reservoir model with spatial variations of petrophysical properties and simulating varying scenarios for the changes in water saturation and pore pressure due to the designed waterflood, I will be able to compute the spatial distributions of seismic elastic parameters using the rock-fluid physics model described in the following section.

2.3.4 Rock and fluid physics model

Rock and fluid physics modeling is the link between quantitative seismic interpretation, geology, and reservoir petrophysics. Using rock physics modeling, one can transform the petrophysical properties of a reservoir to seismic elastic parameters (Avseth et al. 2005) which can be further used to simulate post-stack and pre-stack seismic reflectivity data using a forward seismic modeling algorithm. This process is an essential step in any seismic inversion project aimed at estimating petrophysical properties. In

seismic reservoir monitoring, rock physics also plays a significant role. In other words, the numerical simulation of fluid flow, rock physics modeling, and seismic forward modeling can be effectively combined to simulate seismic and production data and, ultimately, to predict the static and dynamic reservoir properties.

Experimental and theoretical rock physics models have been introduced into the open technical literature. Experimental rock physics models (e.g., Wood, 1941, Wyllie et al., 1958; Hamilton, 1979; Raymer et al., 1980; Castagna et al., 1985; Han et al., 1986) are often developed based on empirical correlations and validated only at specific basins in the world. Consequently they are not universal and can not be readily utilized on fields at different geographical locations (Marion et al 1992). On the other hand, theoretical rock physics models (e.g., Mindlin, 1949; Gassmann, 1951; Biot, 1956; Duffy and Mindlin, 1957; Geertsma, 1961; Marion et al. 1992; Dvorkin and Nur, 1996; Gal et al., 1999; Dvorkin and Gutierrez, 2002) are developed based on effective medium theory and can be generalized for different kinds of sediments as long as their basic assumptions are satisfied. Furthermore, theoretical models are of great importance for modeling purposes especially when real well and core data are not available to validate an empirical rock physics model. Consequently, I emphasize the relevant theoretical models consistent with the geology and petrophysics models considered in this research.

Porosity in clastic rocks is controlled by two main factors: sedimentation and diageneses. Sedimentation controls porosity variations due to changes in sorting and clay content. Diageneses controls porosity reduction due to pressure solution, compaction, and cementation (Avseth et al. 2005). Diagenetic trends in velocity-porosity domain, can often be described well using the modified Hashin-Shtrikman (HS) upper bound (Dvorkin and Nur, 1996; Gal et al. 1998). On the other hand, the depositional or sorting

trends can be described by a series of modified HS lower bounds (Dvorkin and Nur 1996).

In this research study, I use a simulated strandplain geological architecture filled with poorly consolidated shaly sandstone. As described in the petrophysics model, the clay distribution is dispersed, or pore-filling. The corresponding porosity-clay content model is introduced by Thomas and Stieber (1975). Marion et al. (1992) and Yin (1992) conducted several laboratory measurements and introduced a topological elastic model for sand-shale mixtures. In their model, clay is a part of the pore fluid; hence shear modulus of the mixture is not affected by increasing the clay content. Gassmann theory is then utilized to compute the velocity-porosity trends due to clay content variations. Dvorkin and Gutierrez (2002) presented an effective-medium theoretical model for a complete sandy shale and shaly sand sequence assuming pore-filling clay. The model shows similar trends to those observed by Marion-Yin. However, instead of using Gassmann theory, the Hashin-Shtrikman lower bound is utilized to compute velocity-porosity-clay content relationships. In addition, this model is stress-sensitive and includes the effect of pore pressure variations on velocities of the mixture. I select this rock physics model because it is comprehensive, and more importantly, is consistent with my geology and petrophysics models employed.

Fluid substitution is the rock physics technique of predicting how seismic velocities depend on pore fluids. At the heart of the fluid substitution is Biot-Gassmann‘s theory (Gassmann, 1951; Biot, 1956). This theory is one of the most stable tools in rock physics and has been widely used in the geoscientist community. However, the use of this theory is questionable in shaly sandstone, because clay bound water, i.e., immobile water, in shaly sandstones might prohibit instantaneous equilibrium throughout the pore space when rock is exposed to pore pressure fluctuations induced by a propagating wavefield

(Gurevich and Carcione 2000). To make Gassmann's equations applicable to shaly sandstone, Dvorkin et al. (2007) presented an alternative approach to use effective porosity and effective water saturation instead of their corresponding total values. In their method, a new definition for mineral fractions is derived based on an equivalent effective medium in which the porous wet shale is treated as part of the grain material. This alternative technique shows greater sensitivity of sediment with respect to fluid replacement compared to that of traditional Gassmann theory based on the total porosity. In this research, I employ this alternative Gassmann fluid substitution(See equations A. 18 and A.19 in appendix A).

An intermediate step in fluid substitution is to compute the elastic properties of pore fluids. When fluids are compressible, their densities and bulk moduli are functions of pore pressure. In addition, temperature and composition affect fluid bulk moduli and densities. Batzle and Wang (1992) established a set of empirical correlations which transform pore fluid properties from engineering to the geophysics domain. Here, these correlations are used to transform PVT (Pressure, Volume, and Temperature) measurements of oil-gas-water to density and bulk modulus.

To summarize, combining the Dvorkin-Gutierrez (2002) rock physics model, with the fluid physics model (Batzle & Wang, 1992), and using a modified Gassmann theory (Dvorkin et al., 2007), I will be able to observe the joint effects of various petrophysical properties including porosity, clay content, pore pressure, and fluid saturation on elastic seismic parameters including P-and S-wave velocities, and density. Consequently, the comprehensive petro-elastic model developed in this research can be efficiently utilized in sensitivity analysis of seismic elastic parameters to petrophysical properties and, ultimately, applied to seismic reservoir characterization and monitoring research. In this chapter, I present a sensitivity analysis of seismic attributes and the

crossplotting of these attributes as a tool to discriminate the effect of pressure and saturation in a time-lapse seismic study.

The corresponding petro-electric model for the reservoir can be efficiently simulated by combining the Thomas and Stieber (1975) petrophysics model, dual water rock physics model (Best, 1980; Dewan, 1983; Clavier, 1984), and the empirical equation of Arps (1953) to calculate the free and bound-water resistivity. The joint modeling of the elastic and electrical properties of reservoir rocks will lead to the consistent forward modeling algorithms for joint inversion of seismic and electromagnetic (EM) data. Further applications of using the petro-electric model will be presented in chapter six where a time-lapse frequency domain CSEM feasibility study over the 2D reservoir model is simulated to investigate the corresponding time-lapse signals (Shahin et al., 2010a).

Figure 2.10 displays transformations of PVT properties of oil-gas-water using the Batzle-Wang relationships to density, bulk modulus, and seismic P-wave velocity for the reservoir under study. The reservoir is at isothermal condition with a temperature of 37 ^{o}C. The concentration of NaCl in mobile water, i.e., irreducible and free water, and clay bound water is 70000 and 40000 ppm, respectively. As described in the reservoir simulation section (Figure 2.7), the discontinuity on the oil PVT properties at 2000 psi is related to the bubble point pressure. The same discontinuity in the bulk modulus (Kb), density (Rho), and P-wave velocity (Vp) illustrate the oil behavior at bubble point pressure.

Table 2.2 summarizes the elastic properties of minerals used in this study. Figure 2.11 illustrates the petro-elastic model evaluated at reservoir condition. In this figure, Panel (a) is a plot of density versus shale content. Panel (b) shows a plot of total porosity, Vp, and Vs versus shale content. Panel (c) is the rock physics model for a full water

saturated rock. On panel (c), the intermediate values of Vp and Vs on the right lower corner of the plot (point A colored in dark blue), are associated with clean sandstone. By increasing the shale content velocities increase because the pore-filling clay stiffens the rock moduli and density up to the critical clay concentration at which the entire effective porosity of the sand is filled with clay (point C colored in cyan). The highest velocities on the left upper corner are corresponding to critical clay concentration. After this point, both Vp and Vs decrease with introducing more clay until the point with highest clay content, i.e., pure shale, (point B colored in dark red). This phenomenon occurs because quartz grains are replaced with porous clay and lead to soften the rock. The observed V-shape in the petro-elastic domains is a well-know behavior of dispersed-clay distribution in the shaly sandstones. In other words, the discontinuity at the critical clay concentration point creates two different petro-elastic domains: shaly sandstone and sandy shale.

Figure 2.12 shows the effects of water saturation and pore pressure on seismic elastic parameters. Panel (a) is the plot of elastic parameters versus water saturation increasing due to the scheduled waterflood and computed at constant effective pressure. Since water bulk modulus and density are greater than those of oil, Vp, Rho and Vp/Vs increase when water saturation goes up, i.e. oil is replaced with water. In contrast, Vs decreases with increasing water saturation. This is only a density effect because shear modulus of the rock is unaffected by fluids based on the Bio-Gassmann theory. Panel (b) shows the relative and normalized values of changes in elastic parameters due to changes in water saturation. In descending order, Vp/Vs, Vp, Rho, and Vs show the corresponding changes of 16, 14, 5, and -2.5 in percents. Panel (c) is the plot of elastic parameters versus pore pressure variation due to the scheduled waterflood and computed at constant water saturation. Both Vp and Vs decrease with increasing pore pressure, however, Vs is more sensitive to pore pressure, therefore, Vp/Vs goes up. Density is almost insensitive to

pore pressure variations. Panel (d) shows the relative and normalized values of changes in elastic parameters due to changes in pore pressure. The interesting asymmetric trend demonstrates that elastic parameters are more sensitive to pore pressure increase than decrease. This suggests that in a time-lapse seismic study, pore pressure detection should be easier near the injector wells than producers. The normalized sensitivities of elastic parameters to pore pressure can be expressed in a descending order by Vs, Vp/Vs, Vp, and Rho, respectively.

The power of elastic parameters differs in discriminating litho-fluid facies from one another. Figure 2.13 summarizes various crossplots of elastic parameters for a wet sandy shale, a shaly water saturated sand, and a shaly oil-saturated sand all at the same effective pressure, i.e., overburden minus pore pressure. This type of crossplotting using a petro-elastic rock model is very instructive in terms of identifying the best crossplots to distinguish litho-fluid facies. For example, [LR/MR vs. LR] and [Vp/Vs vs. AI] crossplots should be the best lithology discriminators for the specific petro-elastic model used in this research. However, the presented results are not universal and I suggest conducting all crossplots at any specific field locations, comparing results, and then making a decision on optimum crossplot. As mentioned in the discussion of the petrophysics model, three petrophysical facies are located in the shaly sandstone domain and there is no sandy shale within the reservoir. Lithology discrimination is not the main concern here and this research focuses on discriminating fluid saturation and pressure in a time-lapse study. I assume that lithology doesn't change with production over time. Consequently in the next section, I will describe the joint and gradual effect of fluid saturation and pressure on seismic elastic parameters, evaluate the discriminatory power of various seismic elastic parameters based on a sensitivity analysis, and find the

optimum time-lapse crossplot to separate the effect of fluid saturation and pressure due to waterflooding into the black-oil reservoir.

2.4 TIME-LAPSE ROCK-FLUID PHYSICS TEMPLATES

In this research, any change in elastic parameters is considered as a function of changes in pore pressure and/or water saturation assuming a non-compacting isothermal reservoir, i.e., constant porosity, permeability, and temperature during production. As a result, I am interested in finding an optimum way to separate the effect of fluid saturation and pressure using known seismic attributes. Figure 2.14 shows a set of [Vp/Vs vs. AI] crossplots computed at the initial state of the reservoir (t0) and before production/injection. Each crossplot is color-coded with different petrophysical properties including effective porosity, shale content, effective water saturation, and pore pressure. Figure 2.15 is basically the same as Figure 2.14, but this time crossplots are calculated after 6 years (t06) of water flooding. Both figures clearly reflect the monotonic variations of static reservoir properties, i.e., porosity and shale content, and water saturation in some degree, subsequently separation of these properties is possible based on the seismic attributes guided by crossplotting of well-log derived elastic parameters color-coded with other discriminatory well logs such as shale fraction and porosity. This well-proved technique, called seismic facies classification described earlier, is a necessary step in seismic reservoir characterization to distinguish petrophysical facies (here facies A, B, and C) by crossplotting of seismic attributes. In contrast, it is hard to estimate pore pressure from each individual static crossplot computed at a single time step of waterflooding. Figure 2.16 and Figure 2.17 display [SI vs. AI] crossplots and Figure 2.18 and Figure 2.19 shows [LR vs. MR] crossplots with the same explanations as Figures 2.14 to 2.17. Again, separation of static reservoir parameters is possible, but

discrimination is poor for water saturation and almost impossible for pore pressure. Now, the key question is whether or not I can quantitatively separate changes in dynamic reservoir properties, i.e., water saturation and pore pressure, form dynamic crossplots, i.e., [Δ(Vp/Vs) vs. ΔAI], [ΔSI vs. ΔAI], and [ΔLR vs. ΔMR], where Δ denotes change in any parameter and which crossplot provides the best discrimination.

Figure 2.20 illustrate time-lapse changes in pore pressure and water saturation and the associated changes in elastic parameters. Here, changes in elastic parameters, saturation, and pressure for the base survey (after 1 year of waterflooding t01) is subtracted from those of the monitor survey (after 6 years of waterflooding t06) and then normalized using those of base survey, i.e., $\Delta\alpha = \frac{\alpha_{monitor} - \alpha_{base}}{\alpha_{base}} * 100$ where α denotes any elastic or petrophysics parameter. As observed, the percentage of change in pressure is lower than of that of the saturation. Furthermore, the pressure front propagates very fast, but the waterfront has a mass bulk movement and moves slowly. Interpretation of changes in elastic parameters is complicated because of the joint and often compensating effects of fluid saturation and pressure. For example, AI will increase by increasing water saturation near the injector at the reservoir corner, but AI will decrease when pore pressure increases in the vicinity of the same injector. Visually, some attributes, e.g., LR and Vp/Vs, are mainly sensitive to fluid saturation than pressure, but others, e.g., SI, Mu, MR, and Vs are significantly more affected by pressure than saturation. However, due to the joint effect of fluid saturation and pressure any visual judgment will be misleading. These observations encouraged authors to attempt a sensitivity analysis of seismic attributes to changes in fluid saturation and pressure. Basically, to separate the effect of fluid saturation and pressure, it is required to find and crossplot a pairs of attributes where

one is most sensitive to saturation and least sensitive to pressure and the other should behave in the opposite way (Shahin et al. 2010b).

Figure 2.21 displays the results of the sensitivity analysis. Each individual panel is color-coded with a specific elastic parameter and the color scales show the percentage of changes in corresponding elastic parameters. Horizontal and vertical axes for all panels are the changes in water saturation and pore pressure, respectively. Axes ranges are extracted from the reservoir simulation. As observed from the plots, density purely reflects the changes in water saturation, but it is hard to get reliable estimates of density from a three-term pre-stack seismic inversion unless near, middle, and offset data are accessible (Contreras et al. 2007 and Shahin et al. 2008). In descending order, LR, Lambda (L), bulk modulus (Kb), and EI are the main saturation detectors, whereas Mu, MR, Vs, and SI, are significantly more affected by pressure than saturation. Finally, Vp, AI, Vp/Vs, and L/M carry the joint effect of saturation and pressure. Subsequently [Vp/Vs vs. AI] and [L/M vs. AI] crossplots reflect this joint effect as a trend and are not able to provide discrimination as well as those of [LR vs. MR] and [SI vs. AI] crossplots. This fact can be easily concluded from Figure 2.22 where dynamic crossplots are illustrated for the time-lapse scenario displayed in Figure 2.20. Here, three crossplots of [Δ(Vp/Vs) vs. ΔAI], [ΔSI vs. ΔAI], and [ΔLR vs. ΔMR] are displayed. Similar to Figure 2.20, changes in elastic parameters, saturation, and pressure for the base survey is subtracted from those of a monitor survey, and then normalized using those of base survey. The first and second rows of this figure are color-coded with changes in effective water saturation and pore pressure, respectively. Crossplots in each row are associated with one color scale on the left side. It is clear from crossplots that pressure and saturation can be separated to some degree. The direction of saturation change is almost perpendicular to that of pressure change. The directions of separations are not

parallel to the horizontal or vertical axes. The linear trend in the [Δ(Vp/Vs) vs. ΔAI] crossplot is associated with the fact that both Vp/Vs and AI carry the joint effect of saturation and pressure. Therefore, the crossplots of these two attributes is not a good discriminator for saturation and pressure as confirmed by the sensitivity analysis results. In contrast, [LR vs. MR] and [SI vs. AI] crossplots show favorite and almost the same discriminatory powers. The range of numbers on the axes of the LMR crossplot is much broader than that of [SI vs. AI] crossplot. However, the scattering of points has the same shape as [SI vs. AI], i.e., no more value is added when transforming the original seismic attributes, i.e., SI and AI, to other attributes, i.e., LR and MR. Moreover, I must keep in mind that inversion noise will be amplified whenever I attempt to derive other attributes from the original seismic inversion attributes, so [SI vs. AI] not only is the most powerful discriminator, but also is the least noisy one.

As a result, the [SI vs. AI] crossplot is selected as the most favored discriminator of saturation and pressure in a time-lapse study and other derived attributes have less or the same discriminatory power as the [SI vs. AI] crossplot.

I focus attention now on the most favored pressure-saturation discriminator, i.e., [SI vs. AI], and evaluate it for various monitor and base surveys to see if the same optimistic results are valid. Figure 2.23 and Figure 2.24 illustrate [ΔSI vs. ΔAI] crossplots for various time-lapse scenarios. As before, changes in AI, SI, Swe, and Pp for the base survey are subtracted from those of monitor survey, and then normalized using those of the base survey. Panels in Figure 2.23 and Figure 2.24 are color-coded with percentage of changes in effective water saturation and pore pressure, respectively. Time-lapse states are selected in such a way that the most significant possible scenarios in terms of average pore pressure changes are covered. In other words, the following four

categories illustrated in Figure 2.9 have been considered in comparison of different time-lapse scenarios:

- Category (1): The first two years of reservoir life immediately after water flooding. In this period, average reservoir pore pressure increases with calendar time. If the initial reservoir state is called t0, then t01 and t02 are in this category and they are the reservoir states after two and three years of waterflooding.
- Category (2): In this period, average reservoir pore pressure is high and constant during two calendar years. T02, t03, and t04 are in this category.
- Category (3): In this period, average reservoir pore pressure has a significant drop due to production strategy. It takes two calendar years for the reservoir to reach a stable and constant low pressure level, i.e., category (4). T04, t05, and t06 are in category (3).
- Category (4): In this period, average reservoir pore pressure is low and constant during the last four years of waterflooding. T06, t07, t08, t09, and t10 are in this category.

As displayed in Figure 2.23, saturation patterns are well detected in most of the time-lapse scenarios. This is mainly because of the high percentage of change in water saturation, up to 100 percent, in most of the time-lapse scenarios. Off course, the pattern is not always monotonic and there are some points scattered between different colors. A typical example is panel l: [t02-t01]. In a few cases, some points are misplaced, e.g., narrow trends in upper right corner of crossplots for panels h and j. In these cases, the base and monitor surveys are located in category (3) and (4), respectively. As mentioned above, a significant pressure drop (up to -30 %) has occurred between these categories and the imperfection in saturation patterns might be related to this fact to some degree.

Pressure patterns in Figure 2.24 are also well detected in most of the time-lapse scenarios especially when there is a notable pressure change between the base and monitor surveys. As in the saturation patterns, imperfections exist in the pressure patterns. In addition, the interpretation of the pressure patterns is not as easy as the case for saturation pattern. As an example, a small pressure change (less than 1%) in panels a, b, and k are well detectable, but the same pressure change in panels c, d, e, and f are hardly visible. Panel a, b, and k are associated with low average pressure in category (4), but panels c, d, e, and f are related to high average pressure in category (2). This phenomenon can be explained by Figure 2.12 c showing that elastic parameters are more sensitive to pressure changes at high reservoir pressure than at low reservoir pressure states.

2.5 SUMMARY AND CONCLUSIONS

The geologically consistent petro-elastic model developed in this chapter explicitly relates petrophysical properties to elastic parameters. It can be generalized as a model for other geological scenarios and, ultimately, applied to quantitative seismic reservoir characterization and monitoring. In addition, this model is well-suited for resistivity modeling aimed to simulate CSEM data.

As an example of applications, a sensitivity analysis is performed, and its results are validated by the developed reservoir model. Sensitivity analysis demonstrates that [AI vs. SI] is the most useful crossplot to quantitatively separate saturation and pressure changes.

It is also shown that saturation patterns are detectable in most of the time-lapse scenarios because of the high percentage of change in water saturation, up to 100 percent. Pressure patterns are also well detected in most of the time-lapse scenarios in particular

when notable pressure changes exist between the base and monitor surveys. The percentage in pressure change is often lower than of that of the saturation change in my waterflooded reservoir. Consequently, saturation patterns are more likely to be detected than pressure patterns. However, this does not necessarily mean that pressure patterns in time-lapse scenarios with lower change in percentage of pressure are less predictable. As I demonstrated, a small pressure change (less than 1%) is well detectable in some scenarios but it is not visible in others depending on the reservoir pressure state.

I show that imperfections exist in both saturation and pressure patterns and they appear in different forms such as mix-scattering and misallocated points preventing monotonic patterns. Some factors causing this phenomenon are the interaction of saturation and pressure, diffusive nature of the pressure front, and rapid change in pressure due to the production operations. Imperfections in saturation patterns can be also addressed by a pressure factor. The behavior of the pressure front during the waterflooding is very different from that of the water front. The distinct pressure behavior results in rapid iso-pressure equilibrium and makes the pressure and saturation patterns less predictable.

In this study, I assume that reasonable estimates of acoustic and shear impedances are already obtained via an accurate pre-stack seismic inversion algorithm constrained by reliable a priori information from well logs, core data, etc. As is the case for any seismic study, limitations include seismic noise, thickness tuning, weak seismic-well tie, and stiff rocks with low porosity. In addition, repeatability in seismic data acquisition and processing, and the low density contrast between hydrocarbon and injected fluid can limit the success of any seismic time-lapse project.

Table 2.1: Facies petrophysical properties associated with the synthetic reservoir model.

Facies	Total porosity	Effective porosity	Shale volume	Water saturation	Mean grain size (micron)	Horizontal permeability (mD)
A	0.11–0.18	0.01–0.12	0.25–0.34	0.45–0.62	80	0.37–10
B	0.18–0.25	0.12–0.22	0.15–0.25	0.27–0.45	250	68–1400
C	0.25–0.37	0.22–0.37	0.0–0.15	0.15–0.27	500	6800–91000

Table 2.2: Density and elastic properties of minerals associated with the synthetic reservoir model.

Constituents	Density (g/cm^3)	Bulk modulus (GPa)	Shear modulus (GPa)	P-wave velocity (km/s)	S-wave velocity (km/s)
Quartz	2.65	37.0	44.0	6.008	4.0748
Clay	2.41	21.0	7.0	3.4222	1.6440

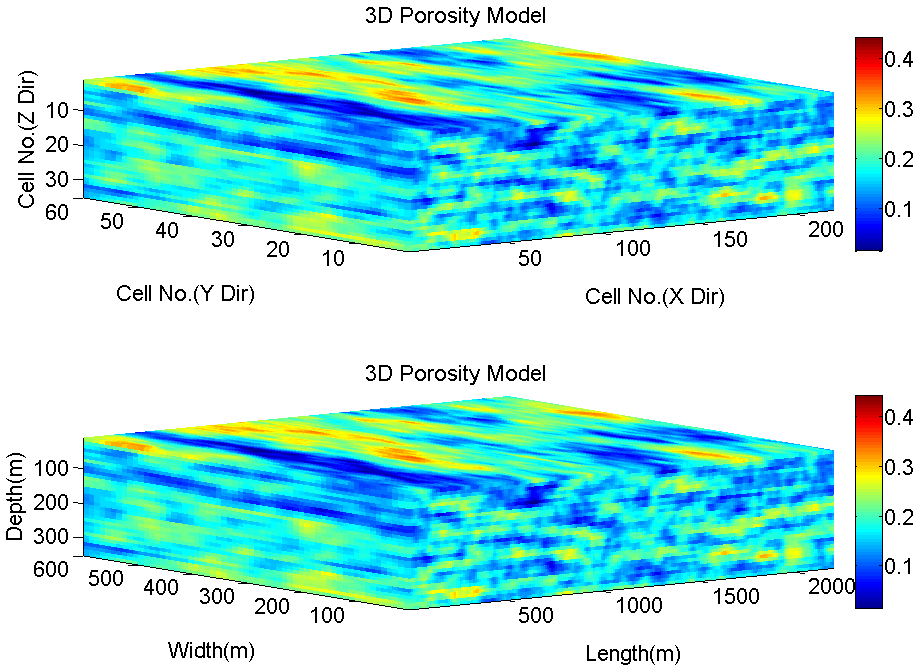

Figure 2.1: 3D distribution of effective porosity model (Christie and Blunt, 2001) associated with synthetic geologic model used for the numerical simulation of seismic and multi-phase fluid-flow. The model is described on a regular Cartesian grid. The model size is 220*60*35 cells in X (east-west), Y (north-south), and Z (depth) directions, respectively (top panel). The grid size defining the cells is 10*10*10 meters, so model dimension is 2200m*600m*350m (bottom panel).

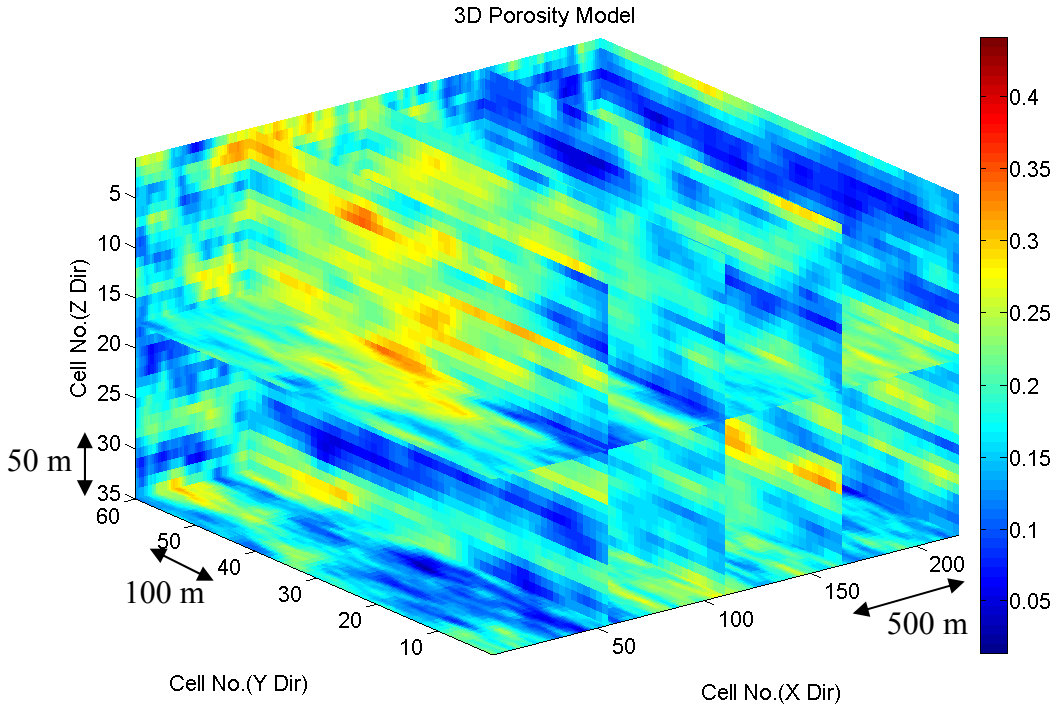
3D Porosity Model
Cell No.(Z Dir)
5
10
15
20
25
30
35
50 m
60
50
40
30
20
10
100 m
Cell No.(Y Dir)
50
100
150
200
500 m
Cell No.(X Dir)
0.4
0.35
0.3
0.25
0.2
0.15
0.1
0.05

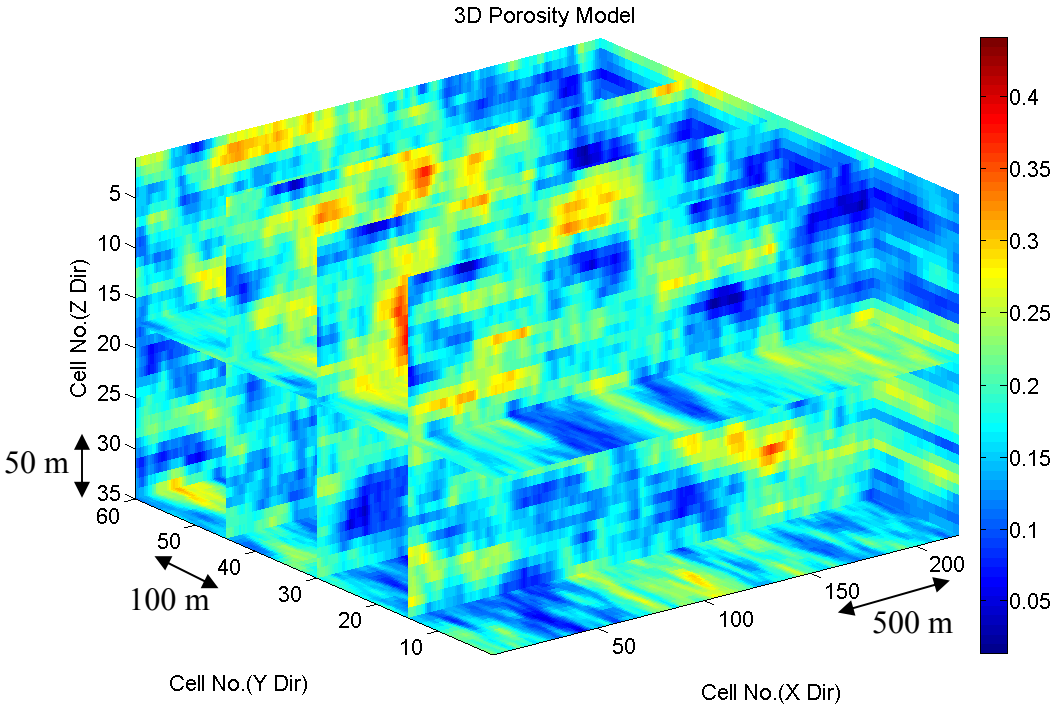
3D Porosity Model
Cell No.(Z Dir)
5
10
15
20
25
30
35
50 m
60
50
40
30
20
10
100 m
Cell No.(Y Dir)
50
100
150
200
500 m
Cell No.(X Dir)
0.4
0.35
0.3
0.25
0.2
0.15
0.1
0.05

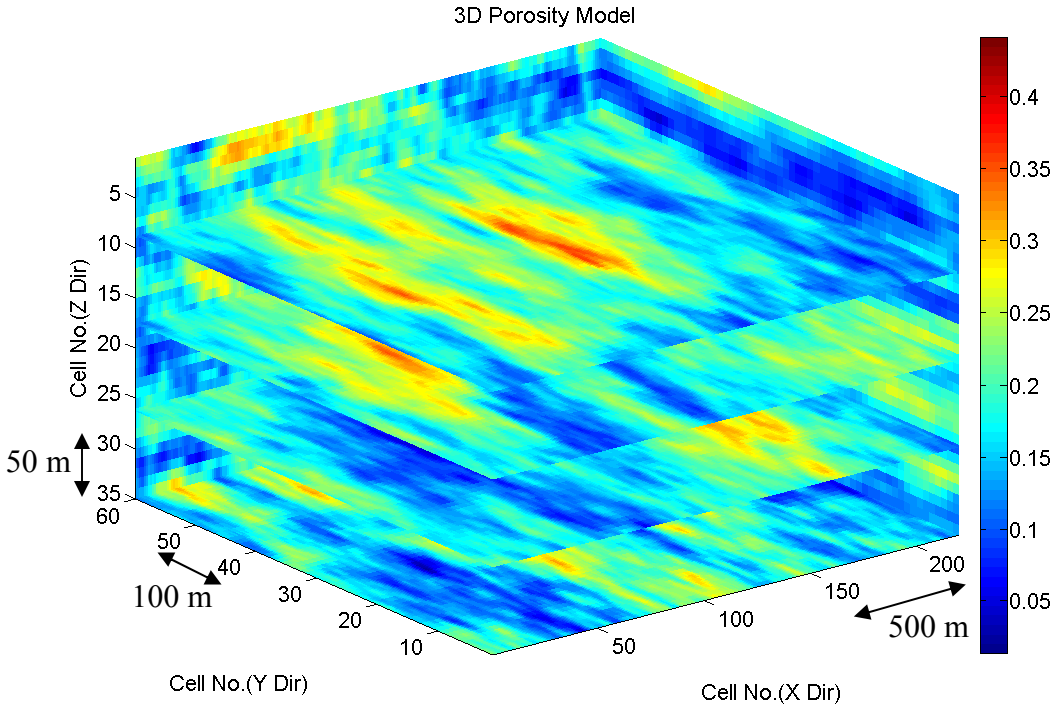

Figure 2.2: Three directional cross-sections of 3D effective porosity model in Figure 2.1.

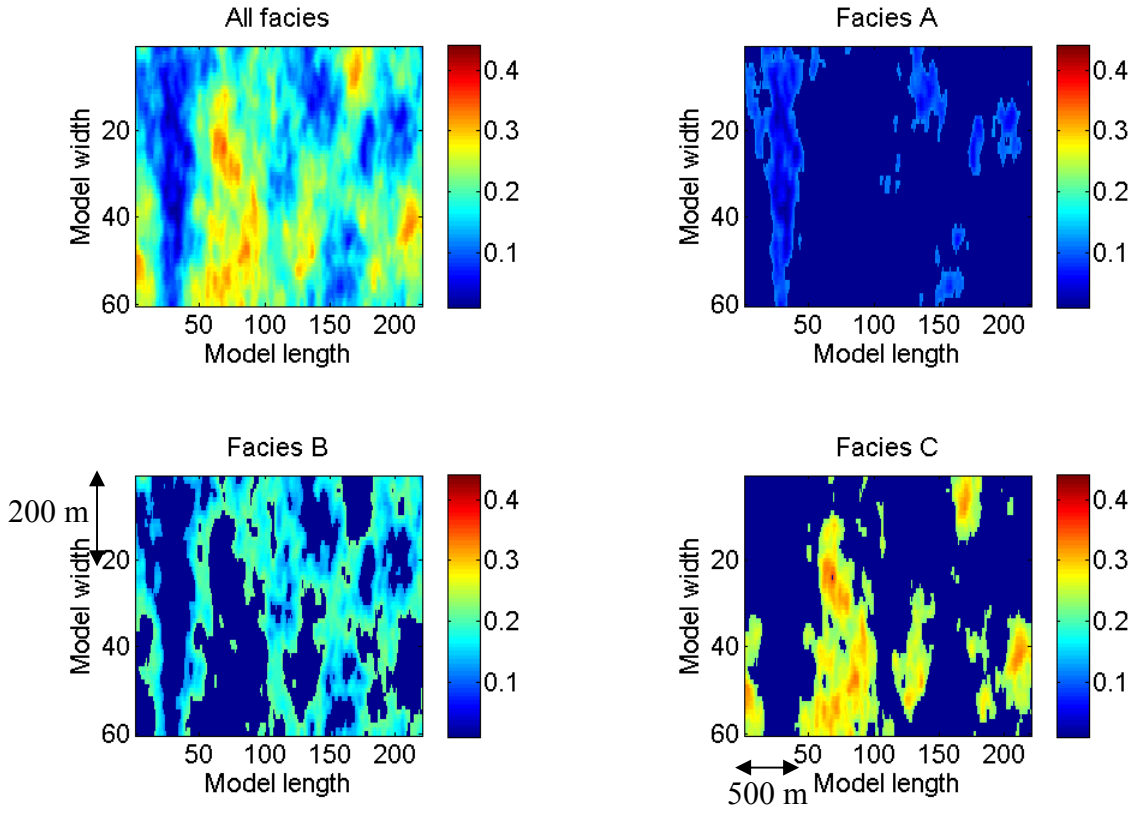

Figure 2.3: Map view of petrophysical facies A, B, and C overlaid on 2D distribution of effective porosity model. Grid numbers are used to show reservoir dimensions in two horizontal directions.

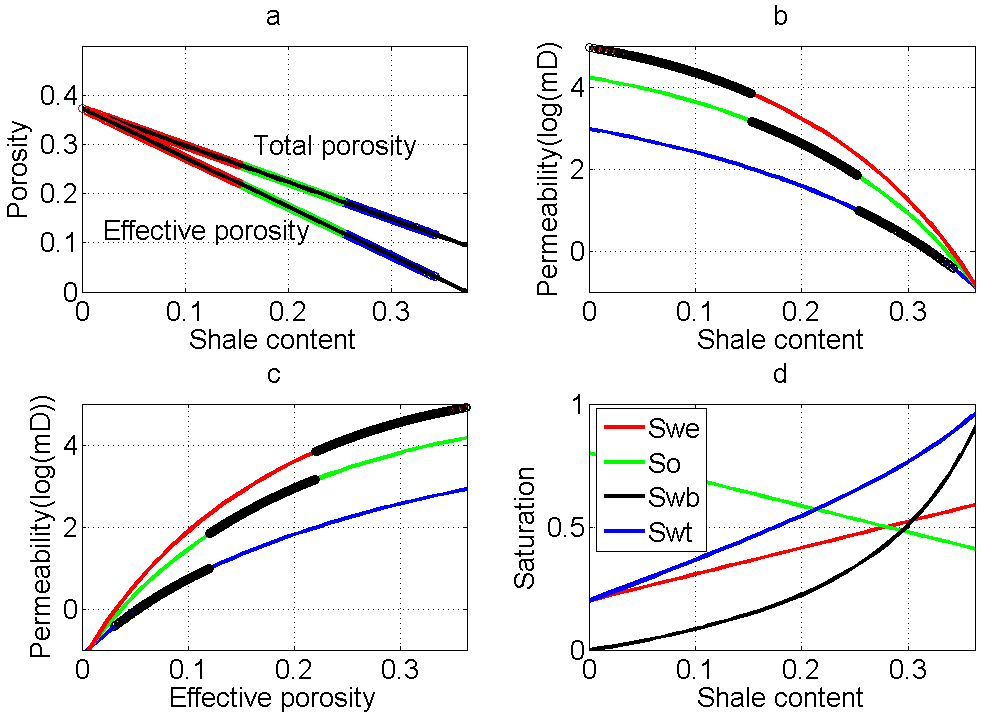

Figure 2.4: Petrophysics model. Panel a shows the dispersed clay model for porosity reduction due to increasing of clay. Panel b dispalys horizontal permeability versus shale content. Panel c is permeability vs. effective porosity. In panels a,b, and c, three colors are associated with three facies A(in blue) representing fine-grined sandstone, B(in green) associated with medium-grained sandstone, and C(in red) corrosponding to course-grained sandstone. Black dots in panels b and c are projected reservoir points . Panel d shows fluid saturations, vs. shale content , effective water saturation (Swe), oil saturation (So), caly-bound water saturation (Swb), and total water satuation (Swt).

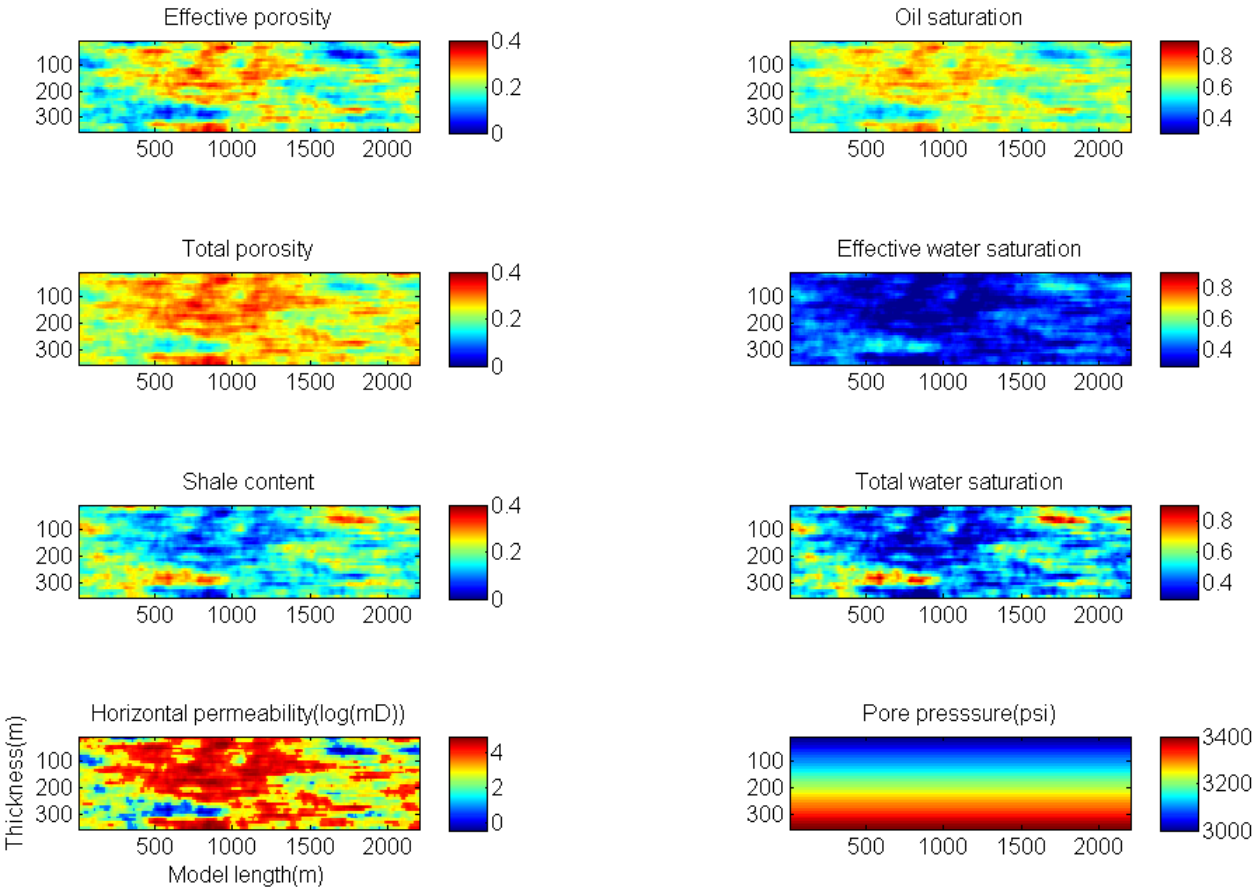

Figure 2.5: Distribution of petrophysical properties for a 2D cross-section in the middle of 3D reservoir.

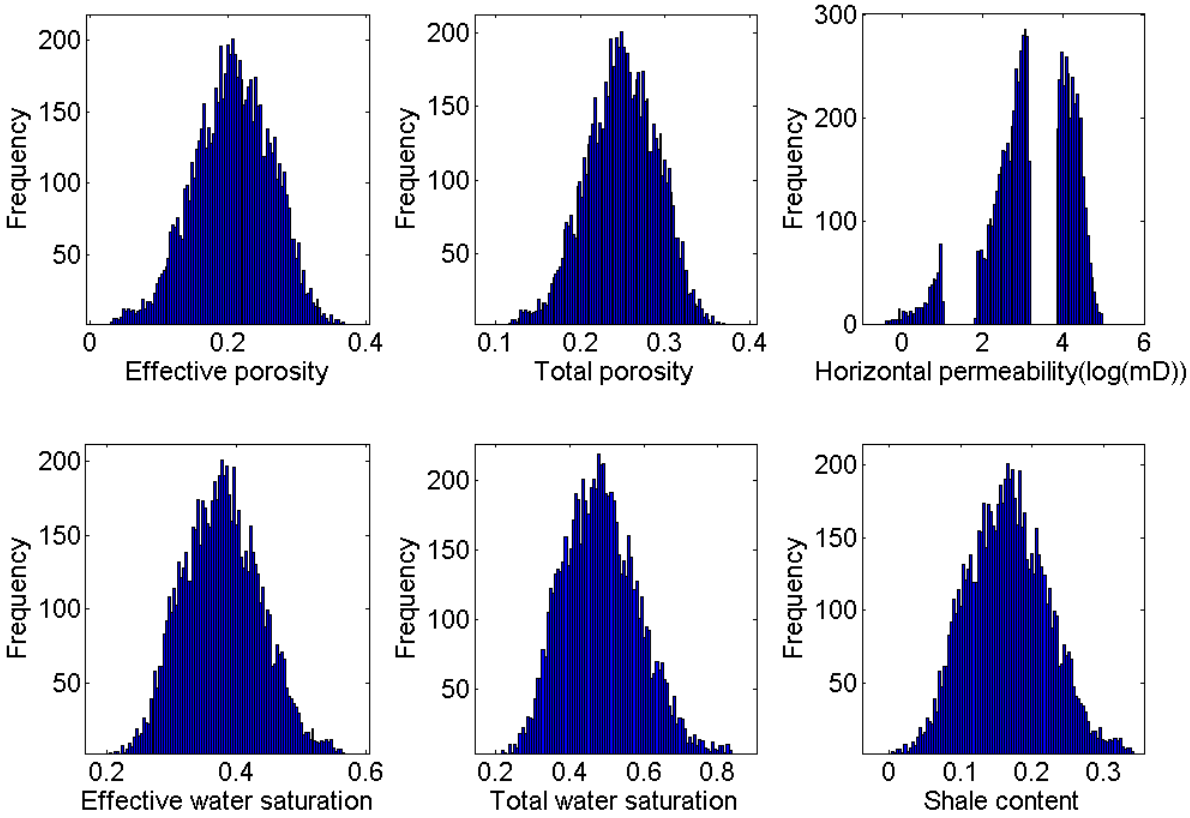

Figure 2.6: Histogram of petrophysical properties. Petrophysical facies are overlapped in all domains except in permeability domain where three distinct facies are separated.

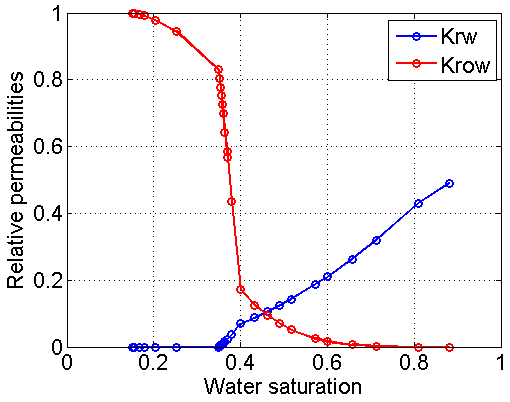
Krw
Krow
Relative permeabilities
Water saturation

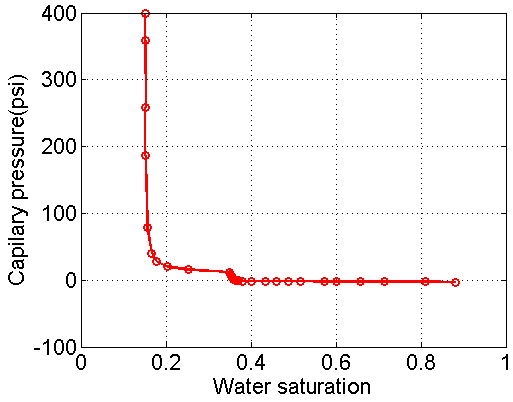
Capilary pressure(psi)
Water saturation

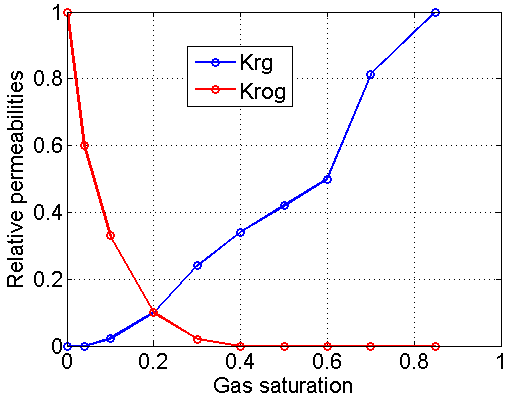
Krg
Krog
Relative permeabilities
Gas saturation

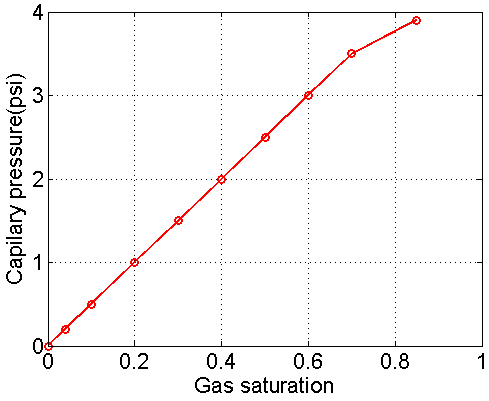
Capilary pressure(psi)
Gas saturation

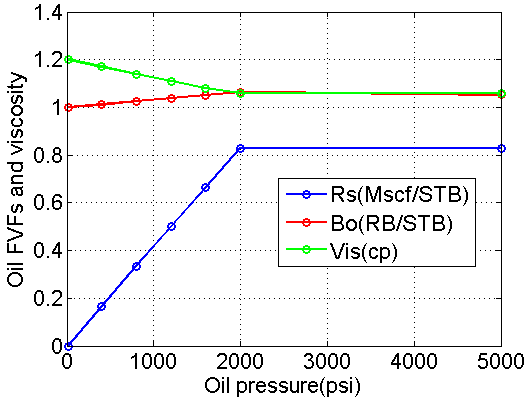
Rs(Mscf/STB)
Bo(RB/STB)
Vis(cp)
Oil FVFs and viscosity
Oil pressure(psi)

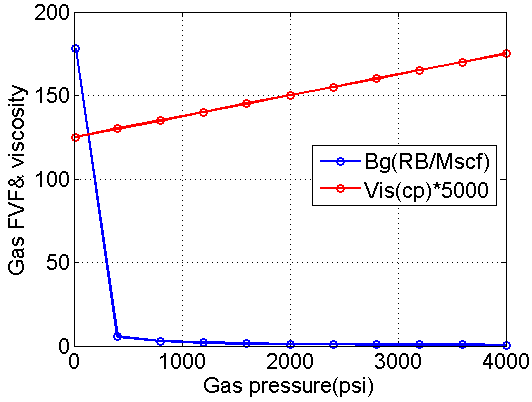
Bg(RB/Mscf)
Vis(cp)*5000
Gas FVF& viscosity
Gas pressure(psi)

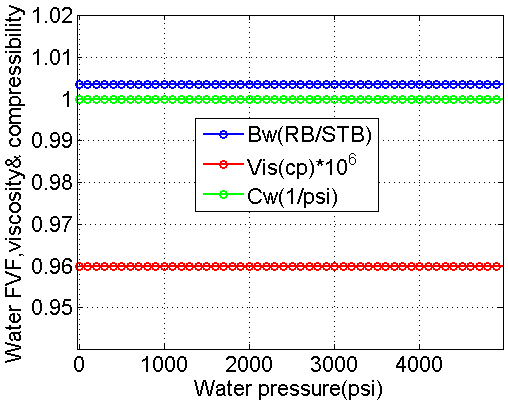

Figure 2.7: The capillary pressures data, the relative permeability curves, and PVT properties of reservoir fluids. FVF stands for Formation Volume Factor.

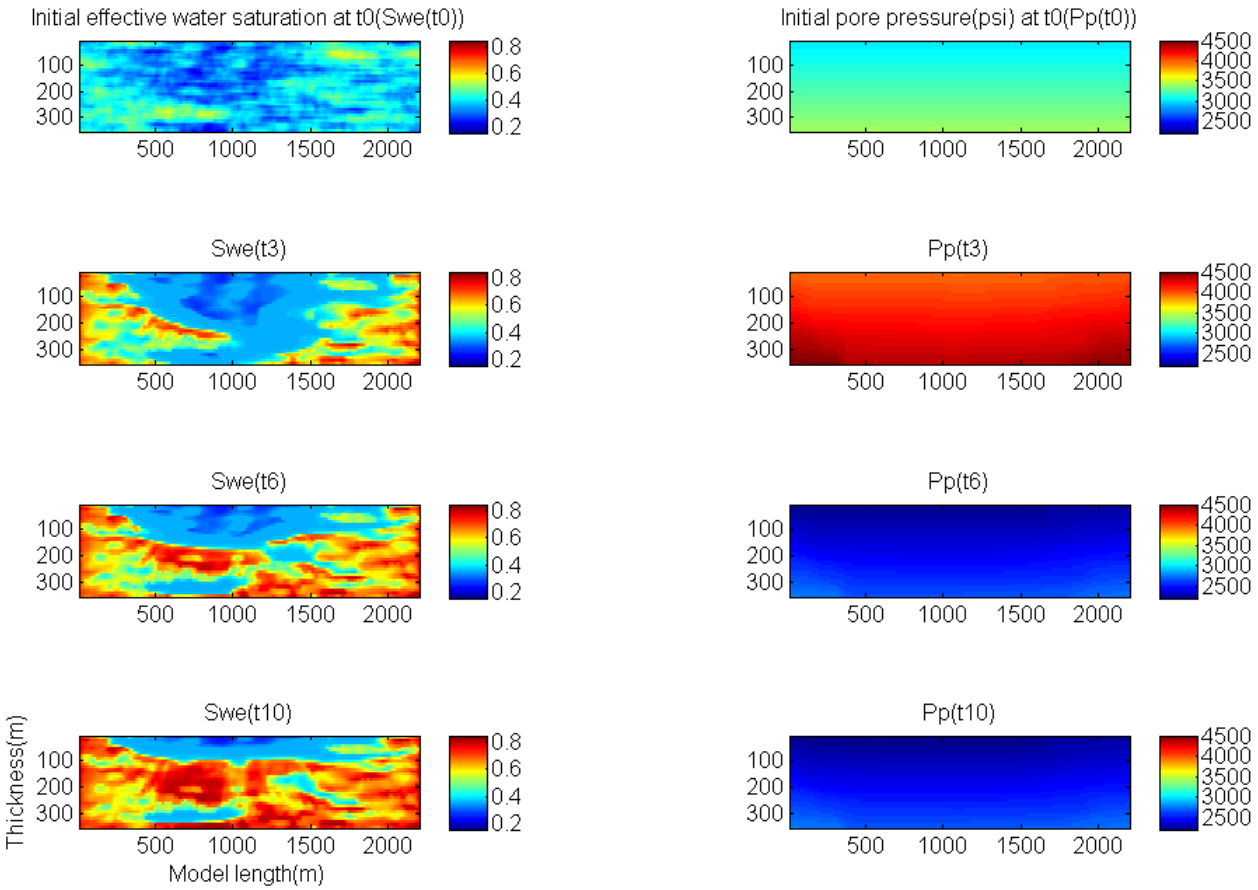

Figure 2.8: Snapshots of effective water saturation and pore pressure (psi) distributions at initial reservoir state (t0) and after production at different calendar times (three(t03), six (t06), and 10(t10) years).

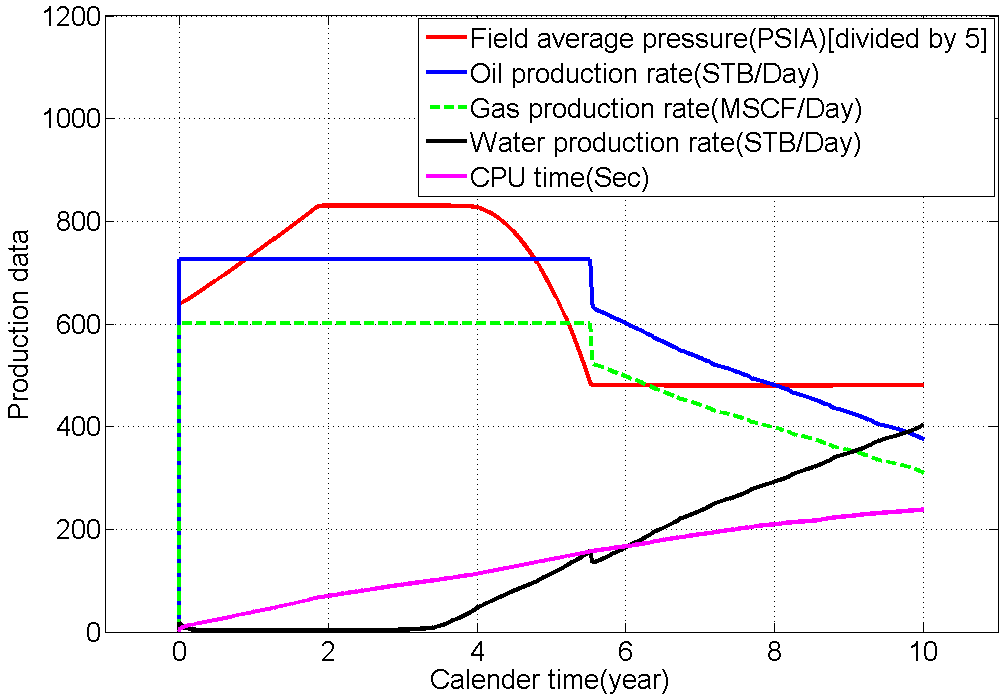

Figure 2.9 Surface reservoir simulation outputs, i.e., production data, for a period of 10 years of waterflooding to enhance oil recovery.

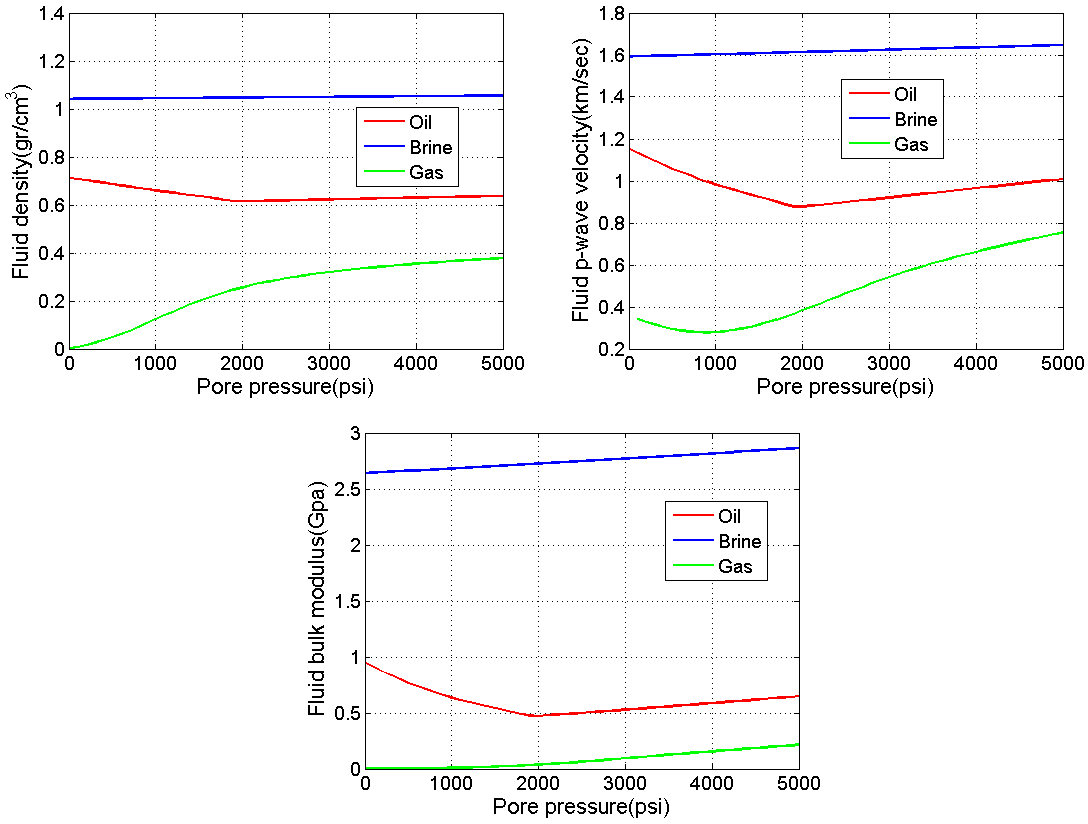

Figure 2.10: Density, bulk modulus, and seismic P-wave velocity for the reservoir fluids. Batzle-Wang 1992 empirical relationships have been used to transform PVT properties of oil-gas-water. Note that bubble point pressure is 2000 psi.

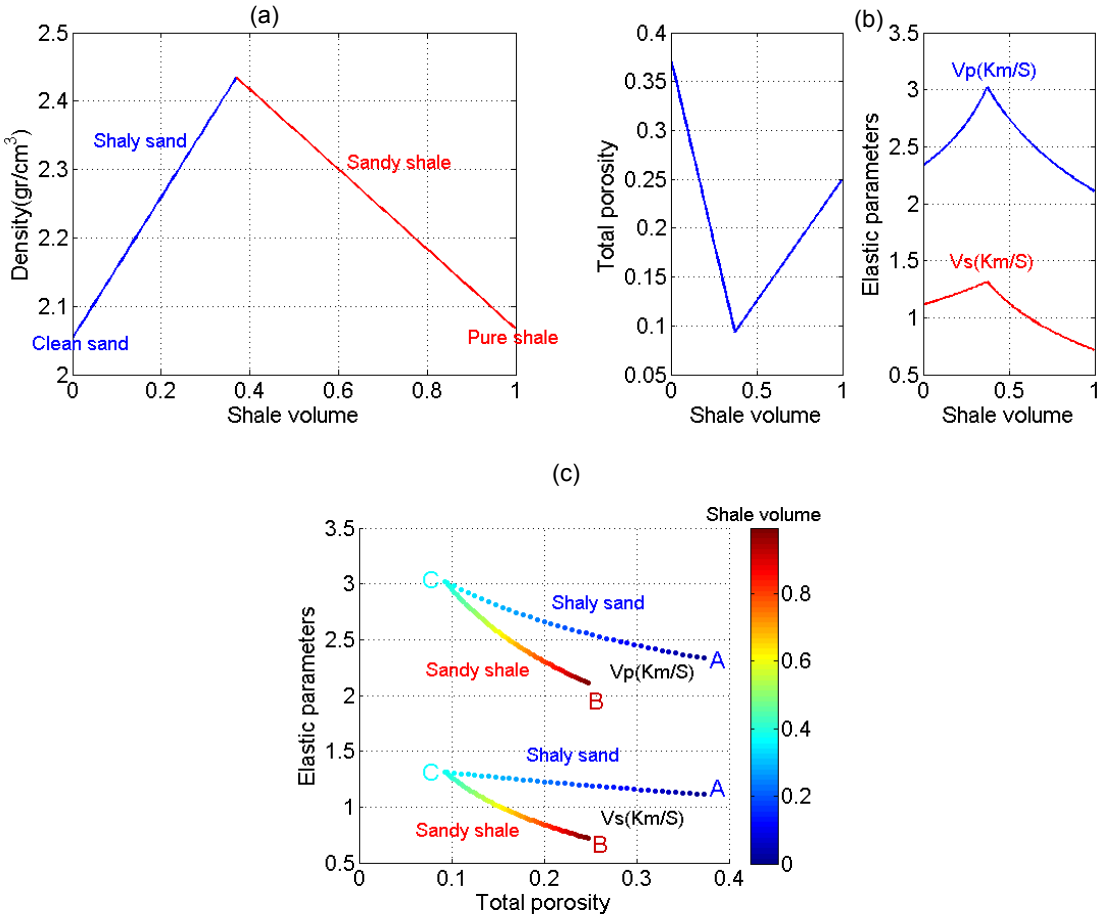

Figure 2.11: Petro-elastic model evaluated at reservoir condition.

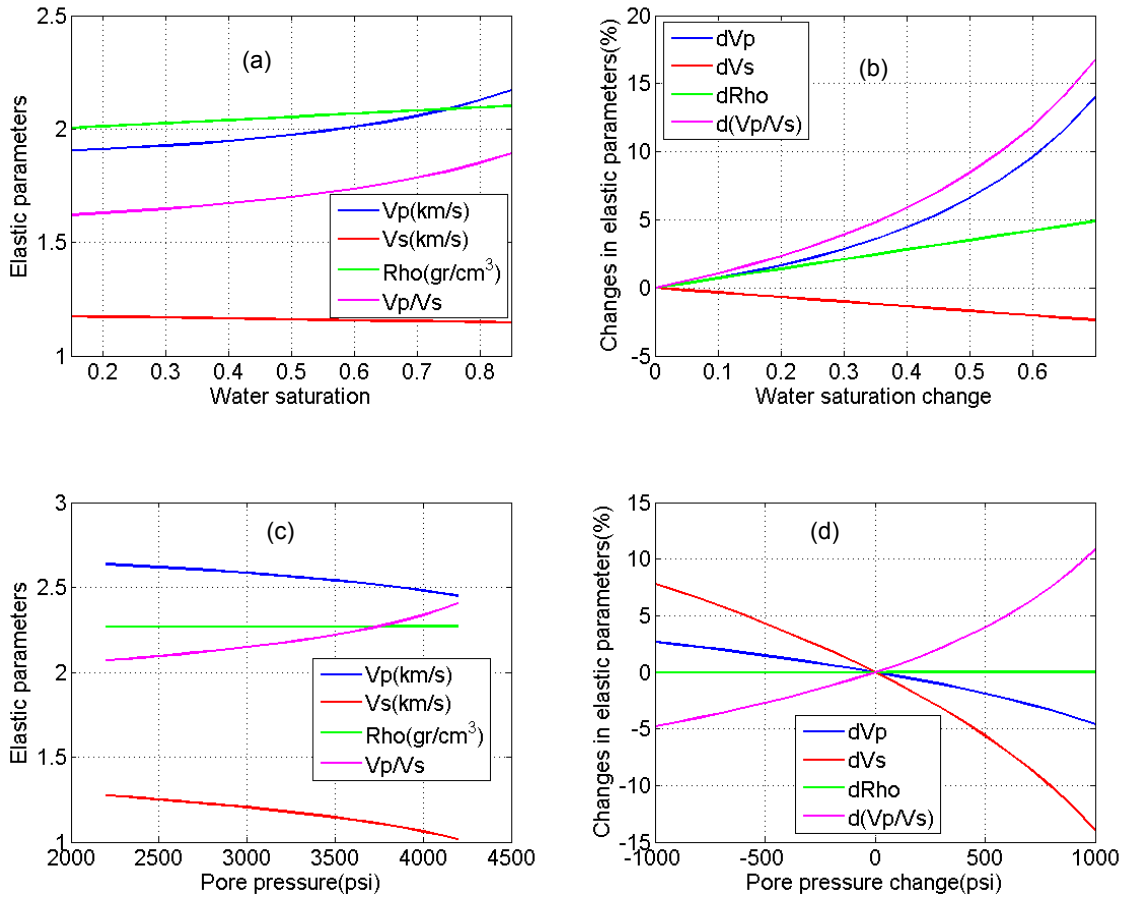

Figure 2.12: Effects of water saturation (first row) and pore pressure (second row) on density and elastic parameters of reservoir rock.

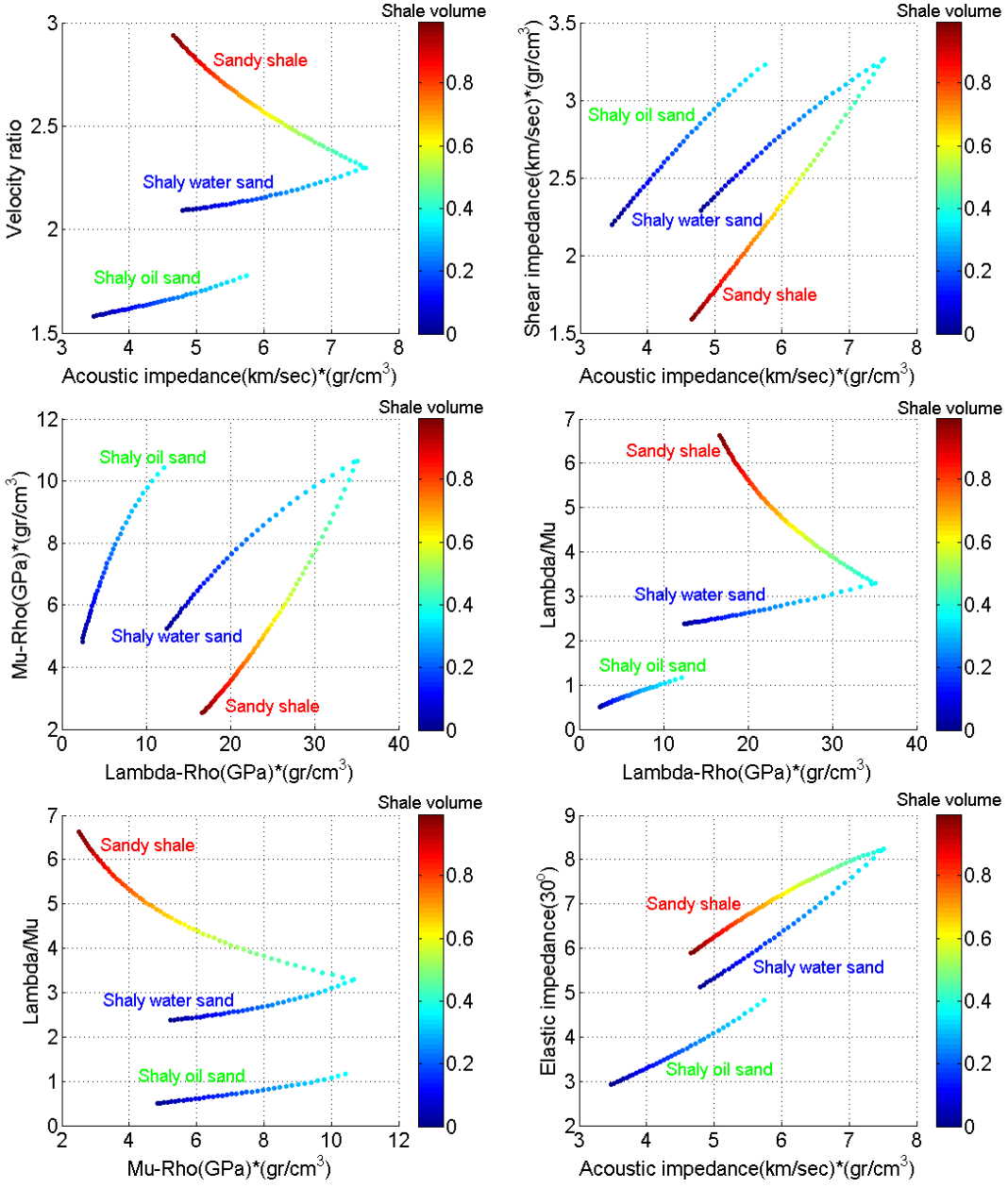

Figure 2.13: Various crossplots of elastic parameters for a wet sandy shale, a shaly water saturated sand, and a shaly oil-saturated sand all computed at the same effective pressure.

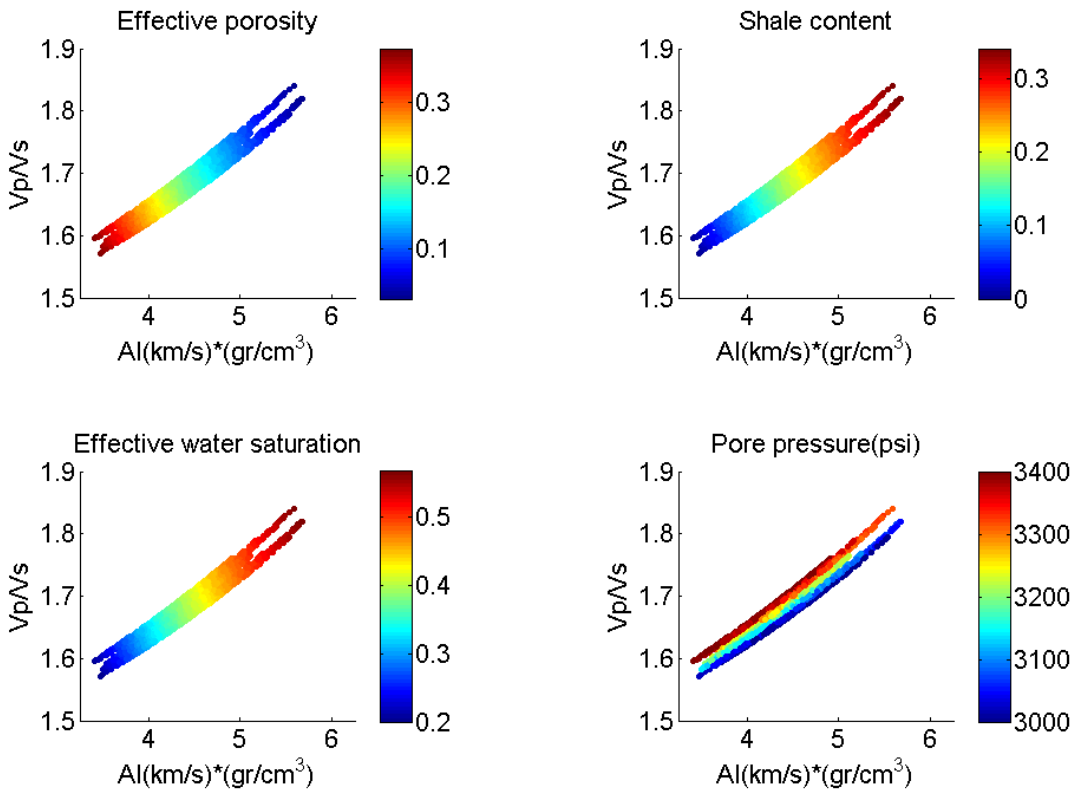

Figure 2.14: [Vp/Vs vs. AI] crossplots computed at the initial state of reservoir (t0) and before waterflooding. Each crossplot is color-coded with different petrophysical properties including effective porosity, shale content, effective water saturation, and pore pressure.

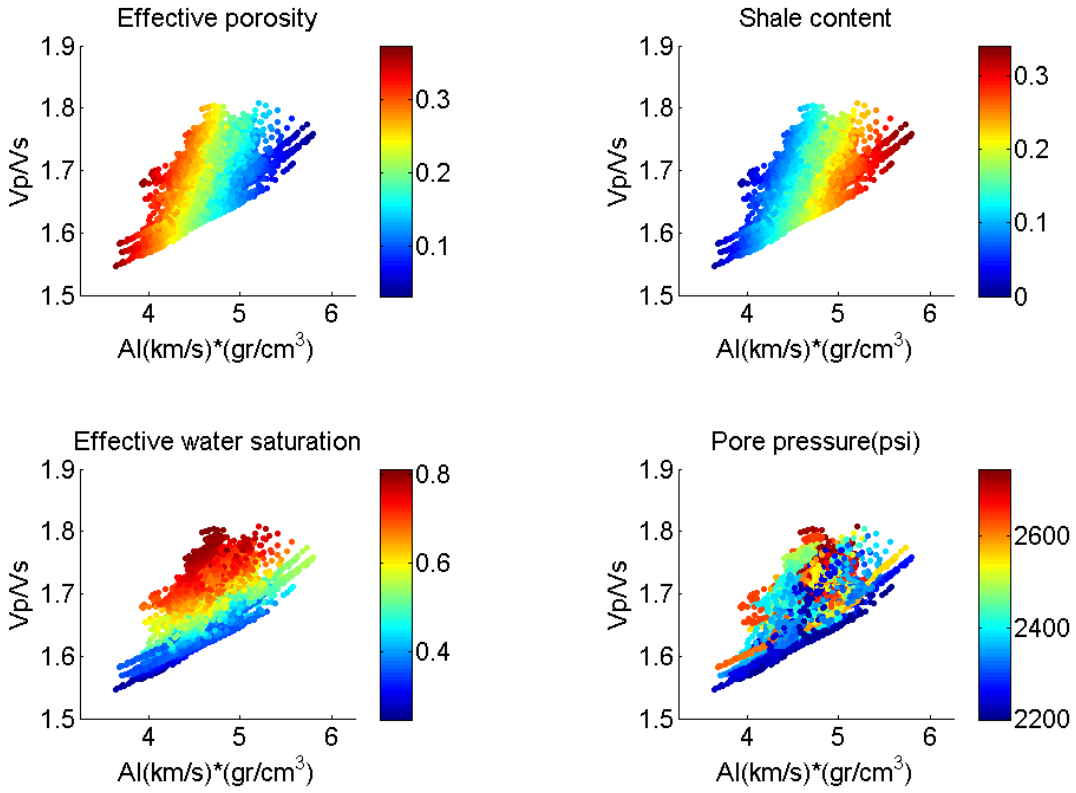

Figure 2.15: [Vp/Vs vs. AI] crossplots computed after six years (t06) of waterflooding. Each crossplot is color-coded with different petrophysical properties including effective porosity, shale content, effective water saturation, and pore pressure.

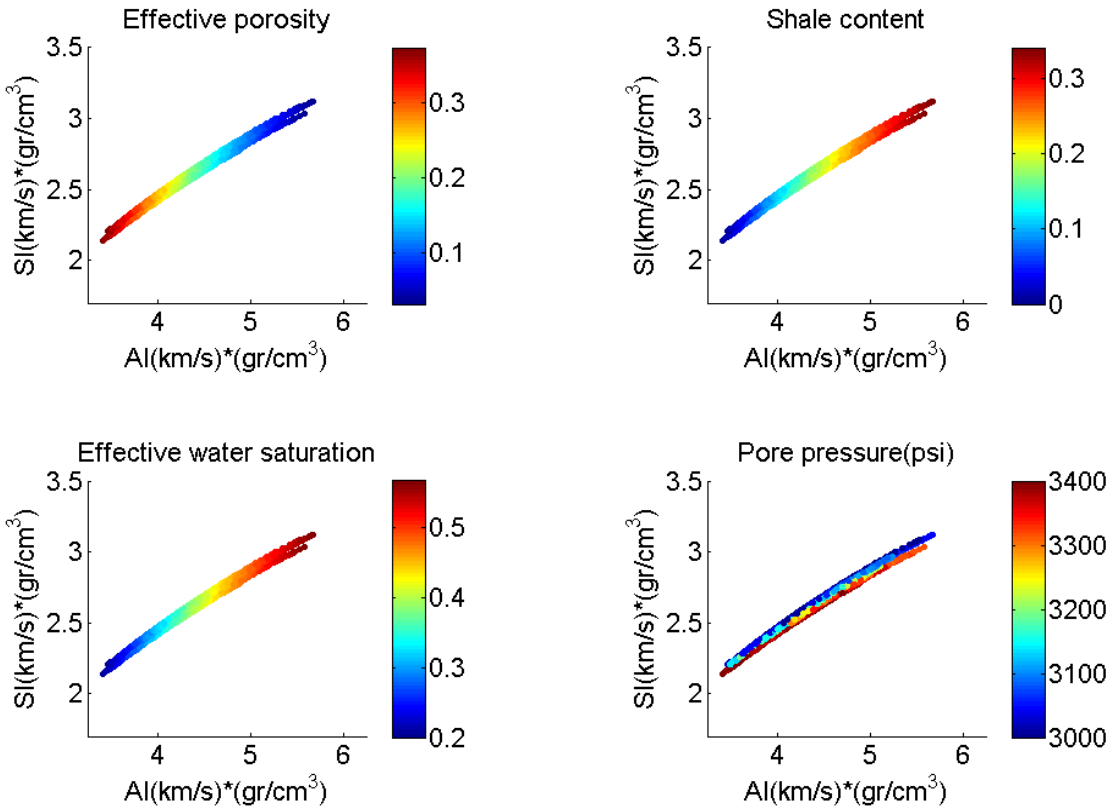

Figure 2.16: [SI vs. AI] crossplots computed at the initial state of reservoir (t0) and before waterflooding. Each crossplot is color-coded with different petrophysical properties including effective porosity, shale content, effective water saturation, and pore pressure.

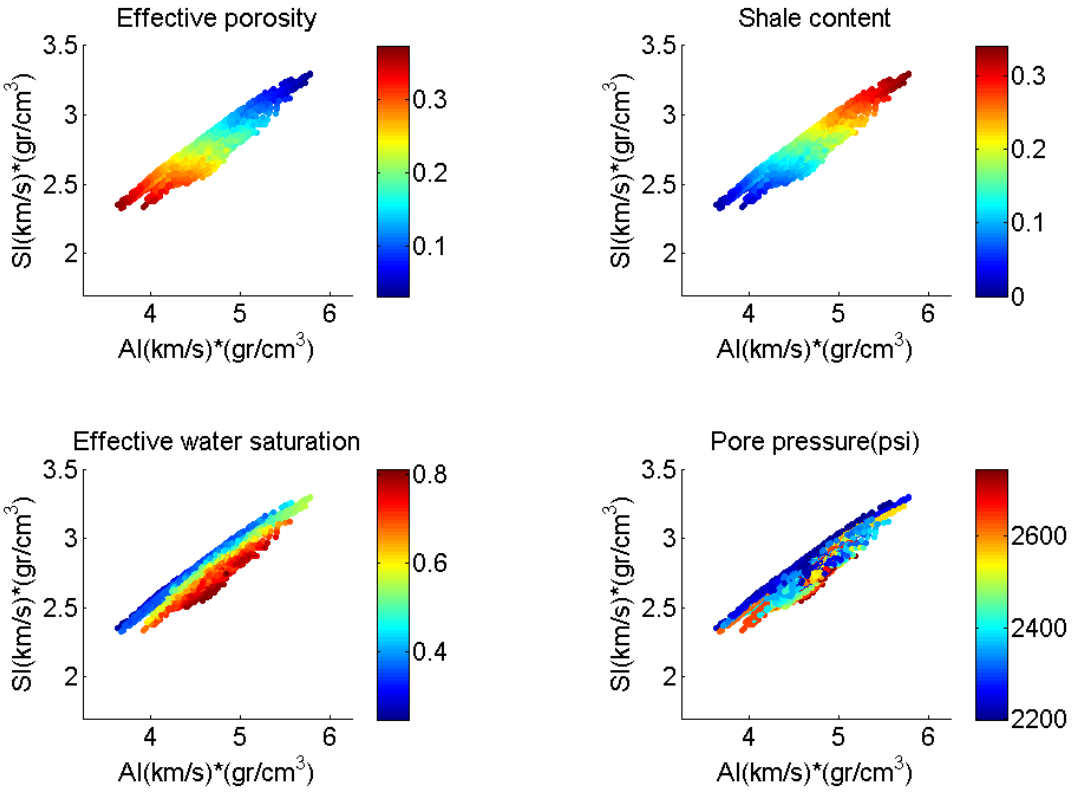

Figure 2.17: [SI vs. AI] crossplots computed after six years (t06) of waterflooding. Each crossplot is color-coded with different petrophysical properties including effective porosity, shale content, effective water saturation, and pore pressure.

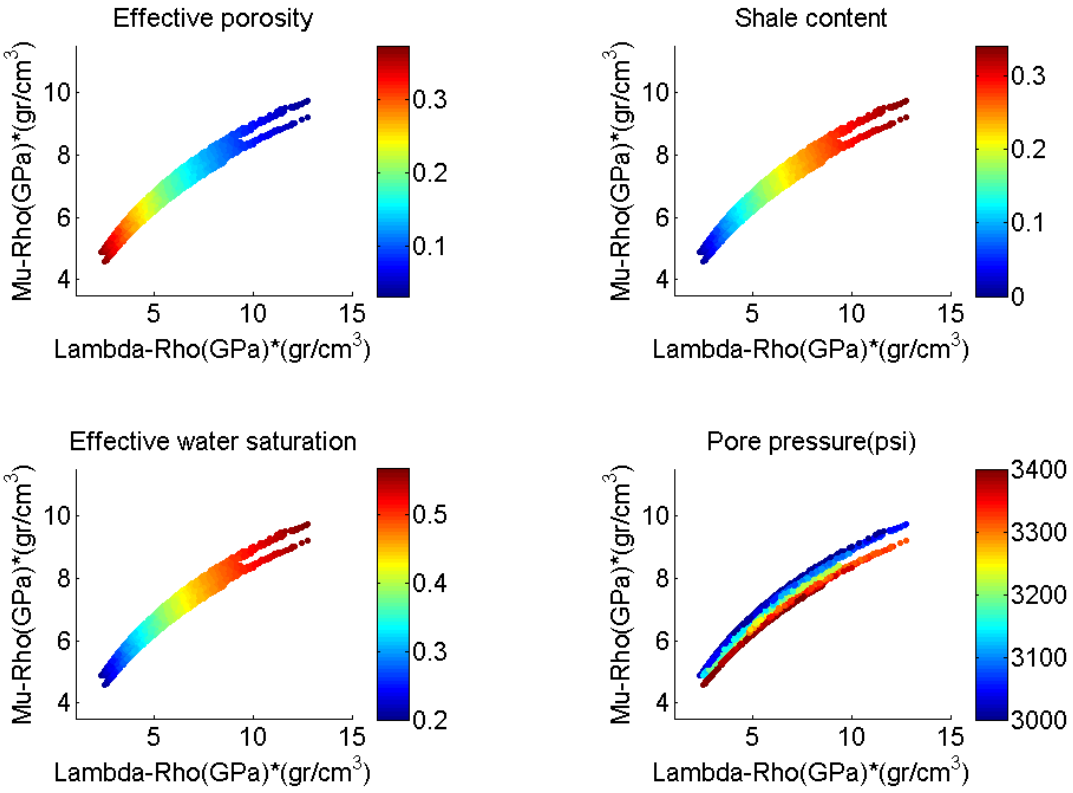

Figure 2.18: [MR vs. LR] crossplots computed at the initial state of reservoir (t0) and before waterflooding. Each crossplot is color-coded with different petrophysical properties including effective porosity, shale content, effective water saturation, and pore pressure.

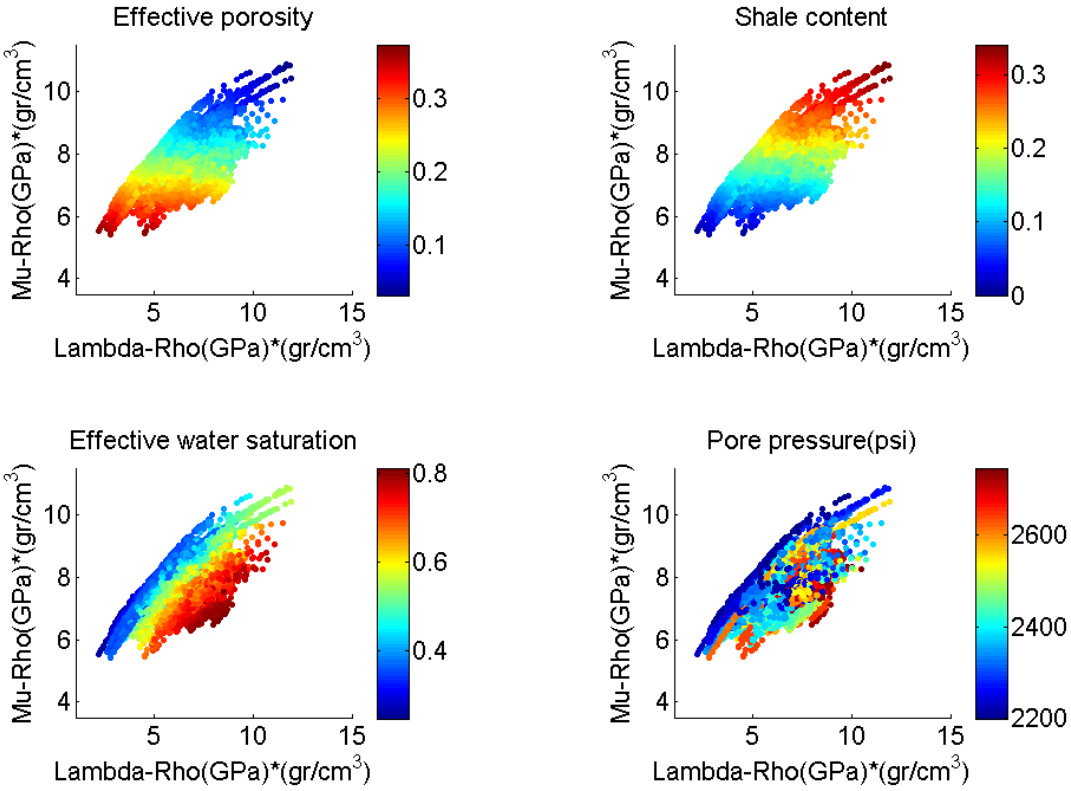

Figure 2.19: [MR vs. LR] crossplots computed after six years (t06) of waterflooding. Each crossplot is color-coded with different petrophysical properties including effective porosity, shale content, effective water saturation, and pore pressure.

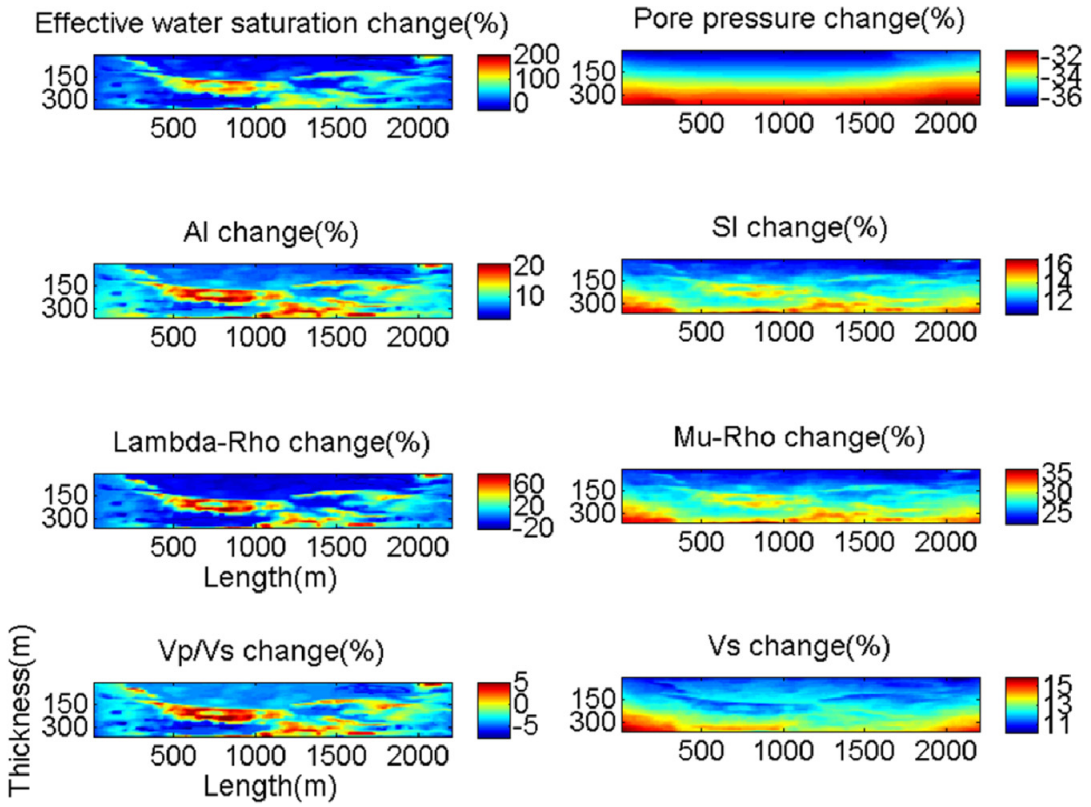

Figure 2.20: Time-lapse changes (t06-t01) in fluid pressure and saturation and the associated changes in elastic parameters. X and Y axes are the same for all panels and they are reservoir length and width in meters, respectively. Each panel is color-coded for the corrosponding attribute. Here, changes in AI and SI for base survey (after 1 year of waterflooding t01) is subtracted from those of monitor survey (after 6 years of waterflooding t06), and then normalized using those of base survey (t01).

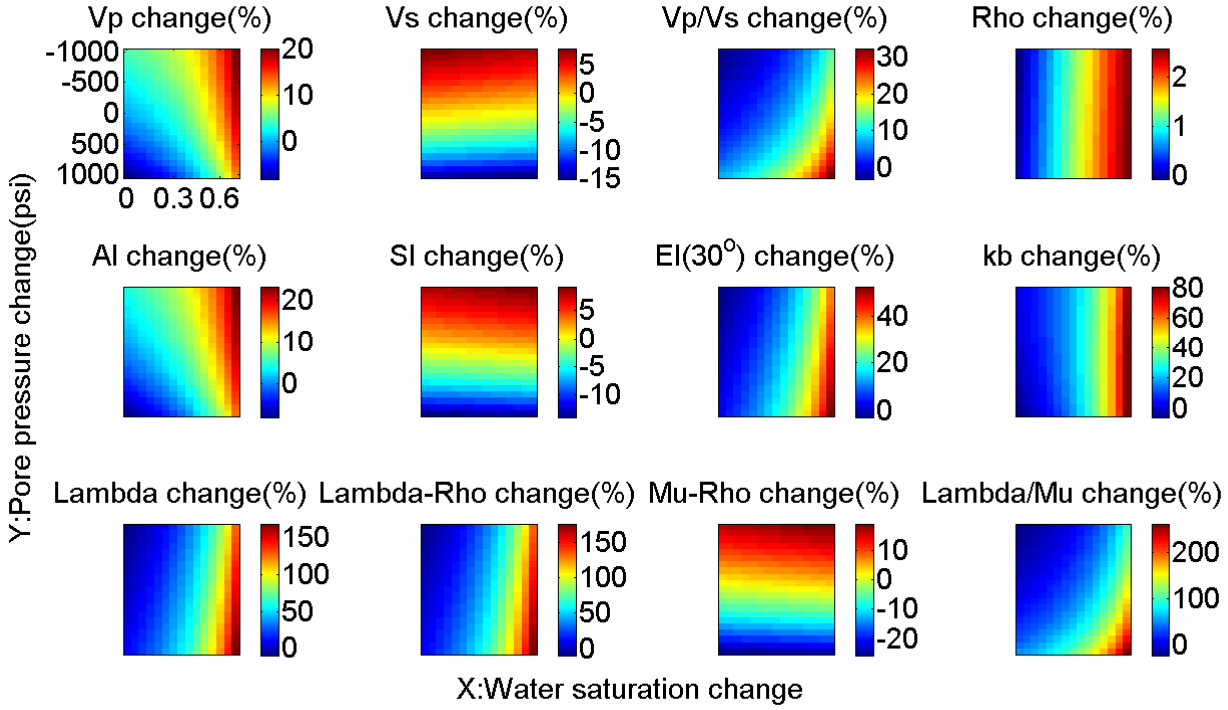

Figure 2.21: Sensitivity analysis of elastic parameters to changes in fluid saturation and pore pressure. X and Y axes are the same for all panles and they are change in water saturation and change in pore pressure(in psi), respectively. Each panel is color-coded for the corrosponding attribute.

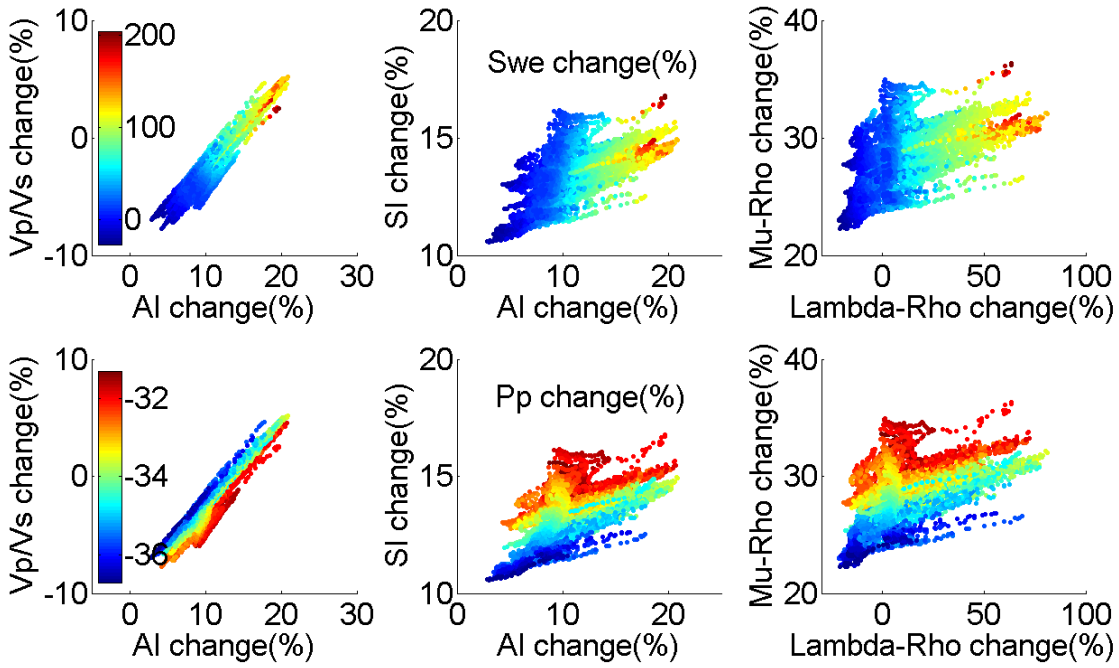

Figure 2.22: Dynamic or time-lapse crossplots associated with production-induced time-lapse changes illustrated in Figure 2.20. The colorbar indicated on the top left crossplot is true for all three crossplots in the top row and it shows change in effective water saturation (Swe) in percent. The colorbar indicated on the lower left crossplot is true for all three crossplots in the bottom row and it shows change in pore pressure (Pp) in percent.

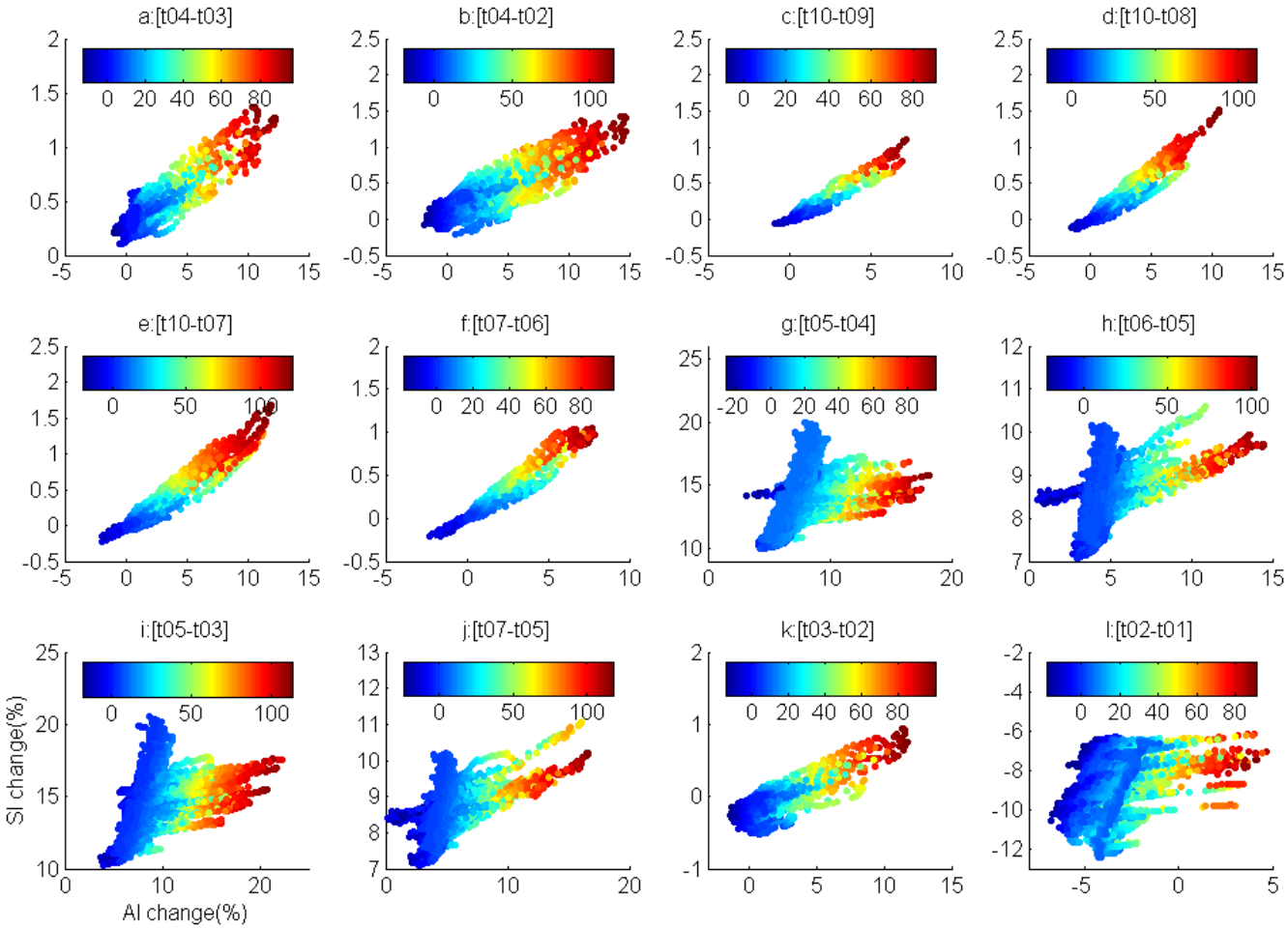

Figure 2.23: Dynamic or time-lapse crossplots associated with production-induced time-lapse changes. The colorbar indicated on the top of each crossplot shows change in effective water saturation (Swe) in percent. X and Y axes are the same for all panels and they are change in acoustic and shear impedances, respectively. Each panel is titled with the corrosponding time-lapse scenario, e.g., panel (a) indicated with t04-t03 means changes in AI and SI for base survey (after 3 years of waterflooding t03) is subtracted from those of monitor survey (after 4 years of waterflooding t04), and then normalized using those of base survey(t03).

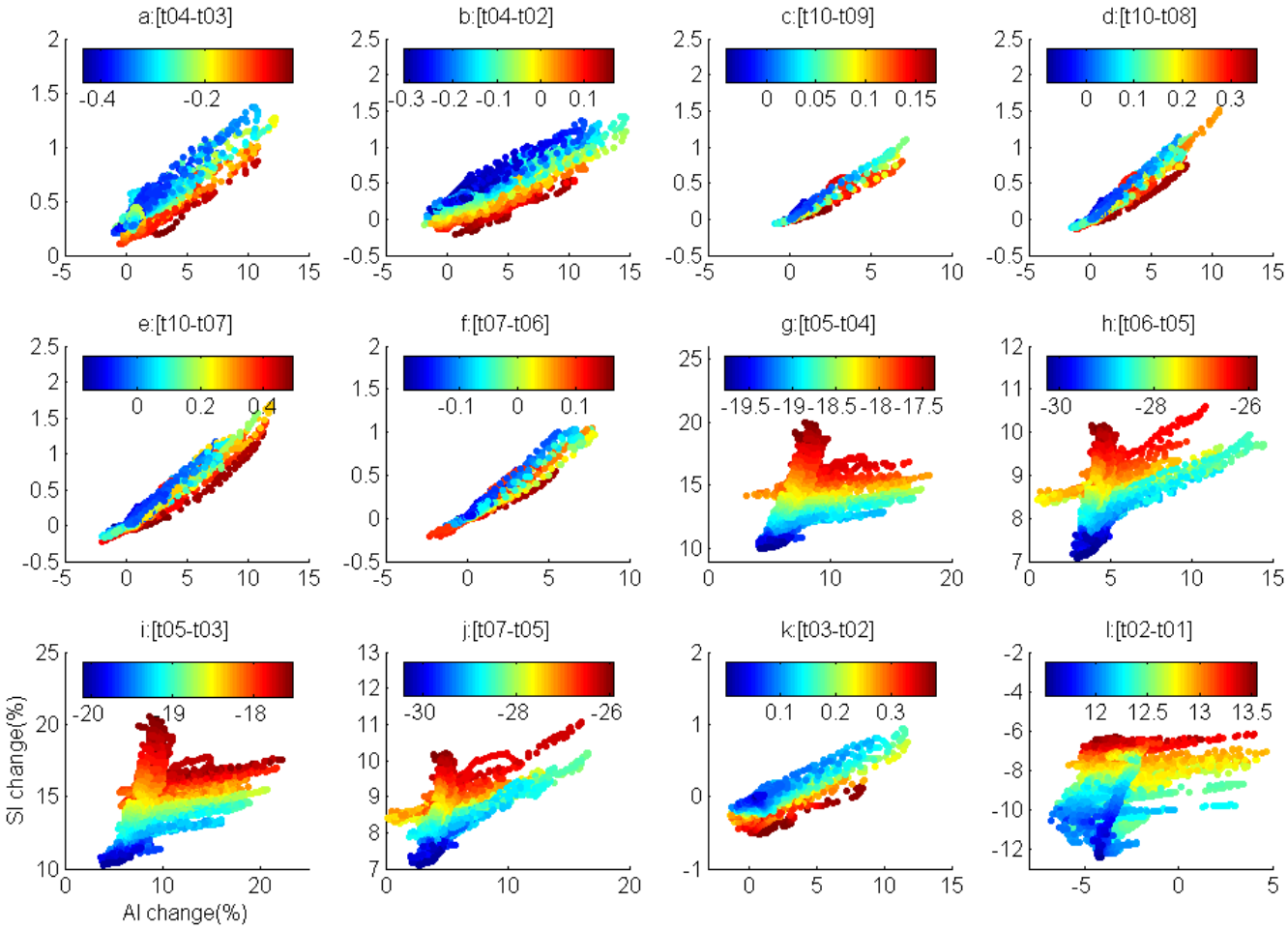

Figure 2.24: Dynamic or time-lapse crossplots associated with production-induced time-lapse changes. The colorbar indicated on the top of each crossplot shows change in pore pressure (Pp) in percent. X and Y axes are the same for all panels and they are change in acoustic and shear impedances, respectively. Each panel is titled with the corrosponding time-lapse model, e.g., panel (a) indicated with t04-t03 means changes in AI and SI for base survey (after 3 years of waterflooding t03) is subtracted from those of monitor survey (after 4 years of waterflooding t04), and then normalized using those of base survey(t03).

Chapter three: Multi-component time-lapse seismic: on saturation-pressure discrimination and statistical detectability of fluid flow

In this chapter, I investigate the detectability of the changes in fluid saturation and pressure using multi-component seismic measurements. Three different reservoir units associated with different degrees of consolidation and rock physics models are considered to analyze synthetic time-lapse seismic observations in response to water flooding into a black oil reservoir. First, the concept of time-lapse cross plot is presented. Next, I will show how one can separate the effect of water saturation from pore pressure using the time-lapse cross-plot. Finally, a statistical approach is developed to quantitatively predict the efficacy of multi-component seismic data in terms of detecting changes in fluid pressure and saturation.

3.1 INTRODUCTION

I evaluate the production-induced time-lapse response of three sandstone reservoirs corresponding to three rock physics models spanning a full range of common degrees of consolidation. For a range of water saturation and pore pressure, I compute multi-component (MC) seismic, i.e., conventional P-P, converted P-SV, and pure shear SH-SH, traveltimes through and reflection coefficients (RCs) at top of the sandstone reservoir embedded in a background shale.

Then, I compute changes in traveltimes and reflection coefficients with respect to a reference traveltime and RC calculated at reference saturation and pressure conditions. I plot changes in RCs versus changes in traveltimes. The corresponding time-lapse cross-plot shows interesting patterns for saturation and pressure changes and has the potential for quantitatively discriminating pressure and saturation changes.

Next, I deploy a statistical method to determine the efficacy of MC seismic in detecting production-induced time-lapse changes. The significant and representative data in time-lapse cross-plot allow one to statistically analyze the detectability of a known scenario of saturation and pressure changes using MC seismic attributes. Applying different thresholds for traveltimes and RCs, I construct single and joint probability detectors that help to compare the likelihood of detection of a known change in dynamic reservoir properties using different component of the seismic data. My analysis demonstrates that seismically detection of the changes in fluid saturation and pressure is significantly limited for a consolidated sandstone reservoirs. However, the detection is plausible for poorly to medium consolidated reservoirs in the presence of realistic seismic noise levels. In these cases, conventional P-P seismic data is dominant in amplitude change compared to converted P-SV and pure SH-SH seismic data. P-P data reflects changes in both fluid saturation and pore pressure. However, the main effect of P-P data is the saturation component than pressure. SH-SH seismic data capture most the pressure information using traveltimes of pre-stack data. P-SV seismic data is the weakest detector of changes in time-lapse amplitude, but its traveltime shows an intermediate detectability between P-P and SH-SH seismic data for changes in both fluid saturation and pressure.

3.2 BACKGROUND AND FORMULATION

Seismic reflection data have been used to estimate lithology and fluid of subsurface rocks. Various seismic attributes can be extracted from seismic volumes in order to qualitatively, semi-quantitatively, and quantitatively perform seismic litho-fluid facies classifications. Pattern recognition techniques, multivariate statistical methods, Bayesian classification, and neural networks have been utilized to map litho-fluid facies from seismic data. In most cases, authors have addressed cross-plotting of seismic

attributes to classify seismic volumes into distinct litho-cubes. For example, Macrides et al. (2000) used supervised and unsupervised statistical pattern recognition techniques to classify seismic volumes via cross-plotting of seismic attributes computed from seismic traces within reservoir intervals. Inverted seismic parameters, e.g., acoustic (AI) and shear impedances (SI), extracted from pre-stack seismic data can also be used to classify seismic volumes. In doing so, cross-plots of the inverted parameters are made. Similarly, elastic parameters derived from well log information are commonly cross-plotted and color-coded with other discriminatory well log-derived data such as shale fraction and porosity. The well log analysis allows one to distinguish lithology and fluid classes which will guide the classification of the inverted seismic attributes in crossplot domains. Finally, lithology and fluid clusters are back-projected from cross-plot domains to seismic volumes (Avseth et al. 2005).

The above summary is a review of the current state-of-the-art technology in classifying seismic volumes into fluid and rock facies. In this chapter, I first investigate the problem of classifying time-lapse signals to associated changes in saturation and pressure due to a waterflooding scenario. Next, I deploy a statistical method to determine the efficacy of MC seismic in detecting production-induced time-lapse changes. Afterward I present a summary of different approaches currently employed in the petroleum industry to investigate time-lapse data and then I focus on the crossplotting of time-lapse signals, which is the main focus of this chapter.

Time-lapse seismic data consist of two or more repeated seismic surveys recorded at different calendar times over a depleting reservoir in primary, secondary, or tertiary recovery phases. Seismic reservoir monitoring of a waterflooded reservoir is a challenging problem. Detecting small changes in seismic traveltimes and RCs due to changes in dynamic reservoir properties, i.e. water saturation and pore pressure may be

the key to success. Seismic waveform data contain two types of information: amplitude and traveltime. Amplitude is the convolution of RC series and a wavelet. RC responds to interface properties, i.e., contrasts in P and S-wave velocities and contrast in density between adjacent layers. On the other hand, seismic traveltime responds to interval properties, i.e., absolute values of P&S-wave velocities in the desired subsurface interval. These seismic attributes, RCs and traveltimes, are complicated functions of the elastic parameters of rocks. Elastic parameters are also related to the properties of the solid and fluid parts of the rocks, porosity, clay content, pressure, saturation, etc. through a set of complex and nonlinear equations defining rock physics models, e.g., Hertz-Mindlin (Mindlin, 1949) and Gassmann (1951) theories. Consequently, making any judgment about dynamic reservoir properties using seismic attributes is challenging and dependent on the rock physics model employed.

Depending on ambiguities in the description of the reservoir architecture, quality of the seismic data, and economic consideration of the field under study, seismic time-lapse interpretation can be performed at three different levels.

The first approach is the qualitative interpretation of changes in seismic observations, amplitude, traveltime, and an interpretive association of the changes in the seismic attributes to changes in reservoir parameters, e.g., porosity, saturation, pressure, temperature, etc. The qualitative interpretation of time-lapse seismic data has been addressed by numerous workers, e.g. Cooper et al. (1999), Lumley et al. (1999), Marsh et al. (2001), Rutledal et al. (2001), Behrens et al. (2002), and various papers in Parker et al. (2003). The primary objective of this type of analysis is to indentify flood fronts, preferential pathways, thief zones, and flow barriers, by-passed pay zones and infill drilling targets. Most of the authors mentioned that these objectives have been achieved and time-lapse seismic data have a positive impact on field development.

The second and more advanced methodology is to semi-quantitatively or quantitatively interpret or invert changes in seismic observations to changes in fluid saturation and pressure. This approach is the main topic of this chapter and is discussed in detail below.

The third and most recent application of time-lapse seismic is referred to as seismic reservoir history matching, 4D history matching, or reservoir history matching constrained by time-lapse seismic data. This currently evolving technology is a multi-disciplinary approach to integrate well logs, core analyses, production data, and time-lapse seismic reflectivity data aimed at updating a reservoir model. Reservoir modeling and simulation, petro-elastic rock and fluid modeling, seismic wave propagation modeling, and joint inversion of measured seismic and production data, are some of disciplines involved in this technique. Several case studies, e.g., Walker et al. (2006) in the Andrew, Valhall, and Harding fields in the North Sea, have demonstrated that joint history matching of seismic and production data leads to a positive impact on the quality of the estimated reservoir parameters relative to estimates obtained from production history matching alone. This is due to the additional spatial knowledge contained in time-lapse seismic data. The main focus of this chapter is to separate the changes in fluid saturation and pressure using changes in seismic attributes due to time-dependent reservoir production. Now, I focus on the main topic of this chapter to quantitatively associate the changes in time-lapse seismic observations, i.e. traveltime and amplitude, to the changes in fluid saturation and pressure. This approach has been addressed by several authors in the literature, so I briefly review the previous works.

Some workers make use of inverted elastic parameters, e.g., AI and SI changes, to indirectly estimate pressure and saturation changes via cross-plotting methods. To summarize, Tura and Lumley (1999) estimated changes in saturation and pressure via

cross-plotting of inverted AI and SI changes. Cole et al. (2002) proposed a grid search method to estimate pressure and saturation by forward modeling of rock and fluid physics. Lumley (2003) proposed a 4D seismic cross-plot inversion method using a coordinate transformation and calibration with well data to simultaneously estimate pressure and saturation changes. Andersen et al. (2006) and Andersen et al. (2009) proposed a dual cross-plotting technology for the seismic facies classification problem. First, a crossplot of the inverted seismic attributes, i.e., [Vp/Vs vs. AI], for the base survey is created and lithofacies are then classified accordingly. Second, time-lapse effects are classified via cross-plotting of 4D seismic attributes, i.e., [Δ(Vp/Vs) vs. ΔAI], where Δ denotes a change in any parameter due to production between base and monitor surveys. From 4D crossplots, one can classify the seismic volume into different subsets associated with scenarios of changes in pore pressure and/or saturation. Finally, the lithofacies and 4D classes are combined via dual classification to reveal pure and combined 4D effects in pay zones.

Some techniques have been proposed to directly invert or transfer time-lapse seismic data to fluid saturation and pressure changes. For example, Landrø (2001) and Landrø et al. (2003) directly inverted time-lapse seismic data for fluid saturation and pressure changes based on an approximate rock physics model and a linearized form of reflection coefficients. Other authors (e.g., Angelov, 2004) made improvements based on Landrø's method. Veire et al. (2006) presented a stochastic inversion method to discriminate pressure and saturation changes directly from P-P time-lapse AVO data. MacBeth et al. (2006) developed a first order linear formula relating changes in any pair of seismic attributes to changes in pressure and saturation.

As my first contribution to this work (Shahin et al. 2009), I introduce a methodology to make a MC seismic time-lapse crossplot. Then, I will show how one can

directly transfer changes in MC seismic traveltimes and reflection coefficients to changes in fluid saturation and pressure. In this method, there is no inversion involved. No assumption for rock physics is necessary. However, the methodology is only appropriate for single layer reservoirs. I further assume that water injection into a black oil reservoir is an isothermal process. In addition, I assume that changes in fluid saturation and pore pressure do not cause any mechanical compaction on the reservoir or the background shale.

Lumley et al. (1997) presented a method for assessing the technical risk of a P-P 4D seismic reservoir monitoring project in any production, reservoir and field conditions. They evaluated important reservoir and seismic parameters and assigned scores based on their experiences from various 4D seismic projects worldwide. After assigning scores, each individual reservoir will be a candidate for a future 4D project if it passes the 60% threshold of both reservoir and seismic scores of the ideal case. The method is fast and tested for different geographical fields. However, it is mainly based on experience and leads to a deterministic answer based on the 60 % rule. In addition, it is only for conventional P-P 4D projects, and not for P-SV and SH-SH surveys.

As a second contribution to this research, I develop a statistical detectability criterion using time-lapse cross-plots. This approach is able to estimate the likelihood of detecting a known production scenario using MC 4D seismic surveys. It can be easily tested for different reservoir types under various production conditions and leads to a probabilistic answer based on the quality of the available seismic data.

3.3 METHODOLOGY

In general, seismic reservoir monitoring results in a better understanding of flood fronts, preferential fluid migration, and flow barriers, followed by more effective

reservoir management. This task is often applicable after determining the static reservoir properties in the reservoir characterization stage. In other words, obtaining a reasonable static model including porosity, permeability, and lithology variations within the reservoir is an essential step before implementing seismic time-lapse analyses.

Assuming a well-defined initial static model, reservoir simulator can be run for a desirable production scenario. Then, the range of changes in dynamic reservoir properties, e.g., water saturation and pore pressure in a waterflooding scenario, can be recorded between two calendar times. Using the average static reservoir properties, i.e., constant values of porosity, reservoir thickness, clay content, etc., a simulated reservoir segment is generated. The simulated segment is a representative segment of the reservoir containing the average properties of the actual reservoir. My analysis is applied on this segment, but the same procedure can be implemented on different simulated segments, where their reservoir properties are perturbed properties of the representative segment.

The representative segment is embedded in background shale simulating the surrounding sedimentary rocks. Assigning the same scenarios of changes in saturation and pressure as the actual reservoir, one can calculate P and S-wave velocities and density of the reservoir segment using Gassmann's theory and a stress-sensitive rock physics model, e.g. modified Hashin-Strikman lower bound, (Dvorkin and Nur, 1996), calibrated with pressure-dependent core measurements. Next, I calculate MC seismic traveltimes within the reservoir either numerically, using ray tracing, or analytically assuming straight rays. In addition, I compute MC seismic RCs at the reservoir top. Then, I subtract an initial traveltime and RC, calculated for the reference pressure and saturation, from the above-calculated traveltimes and RCs, respectively. Then I plot changes in RCs at the top of the reservoir versus changes in traveltimes through the reservoir. The corresponding time-lapse cross-plot shows interesting patterns for

saturation and pressure changes and has the potential for quantitatively discriminating pressure and saturation changes.

In addition, the data in time-lapse cross-plot allow one to statistically analyze the detectability of a known scenario of saturation and pressure changes using MC seismic attributes. The single and joint Cumulative Distribution Function (CDF) for changes in MC seismic traveltimes and RCs provides a convenient way to obtain specific probabilities at desirable ranges of time-lapse attributes. Applying different thresholds for detectability of traveltimes and RCs, I construct single and joint probability detectors, called SPD and JPD, respectively. These detectors are effective tools that determine the likelihood of detecting the desirable ranges of changes in traveltimes and RCs for known changes in fluid saturation and pore pressure.

Finally, instructive forward modeling of this type for actual reservoirs will help to determine the detectability of dynamic reservoir properties using MC time-lapse seismic attributes. That is, repeating the above procedure for various simulated segments with different porosities, thicknesses, and clay contents, will give insight into the classification of various reservoir types or different parts of a laterally varying reservoir from a detectability point of view.

3.4 SYNTHETIC EXAMPLE

Three synthetic sandstone reservoir units embedded in background shale are considered to show the efficacy of the methodology presented in this chapter. Table 3.1 summarizes the characteristics of these reservoir units, A, B, and C. The reservoirs are composed of 80% quartz (Mavko et al., 1998) and 20% clay (Han, 1986). Table 3.2 shows the elastic properties of the minerals in the reservoirs.

Three reservoir units are located at different depths based on degrees of consolidations and the corresponding rock physics models are selected accordingly. Figure 3.1 displays the adopted rock physics models for this study. Reservoir A is consistent with the modified upper Hashin-Strikman (MUHS) bounds (continuous and dashed black lines for P& S-wave velocities versus porosity, respectively) with 10% porosity. Reservoir C is consistent with the modified lower Hashin-Strikman (MLHS) bounds (continuous and dashed blue lines for P& S-wave velocities versus porosity, respectively) with 30% porosity. Reservoir B with 20% porosity is positioned on velocity vs. porosity curves averaging the MUHS and MLHS bounds (continuous and dashed red lines for P& S-wave velocities, respectively). With these models, I span a wide range of sandstone reservoirs worldwide and evaluate the corresponding production-induced time-lapse signal. Porosity is depth dependent and reduces with increasing depth. Reservoir temperature, initial pore pressure, and overburden pressure are also depth dependent. A constant reservoir thickness of 100 meters is considered for all three reservoirs. Fluid properties are extracted from pressure, volume, temperature (PVT) data (Killough, 1995) and then transformed to seismic elastic parameters using Batzle and Wang's (1992) empirical correlations (Figure 3.2). Discontinuity on the oil P-wave velocity at 2000 psi is related to the bubble point pressure.

At initial production, I assume the reservoir is uniformly saturated with 50% brine (connate water) and 50% light oil. This will be the reference water saturation to calculate time-lapse attributes. Initial pore pressures differ for the three reservoirs depending on the depth at which each reservoir is located. A known scenario of changes in water saturation, -70% to +70% of the initial water saturation, and changes in pore pressure, -30% to +30% of the initial pore pressure, are intended to simulate a water-flooded black oil reservoir. Note that percentages of changes in pore pressure are relative values, i.e.,

the absolute values differ for pore pressure depending on initial pore pressure (Table 3.1). The assigned ranges of pore pressure variations are always above the bubble point pressure; consequently, no gas is produced within the reservoirs and light oil and brine water are the only liquid phases.

I use Biot-Gassmann‘s theory (Gassmann, 1951; Biot, 1956) to predict how seismic velocities depend on pore fluids. Stress-sensitive rock physics models are implemented to predict the pressure effect on seismic velocities. Figure 3.3 illustrates the effects of water saturation (first panel) and pore pressure (second panel) on density and elastic parameters of reservoir rocks. The first panel shows the relative and normalized values of changes in density and velocities due to changes in water saturation. It is computed at the constant effective pressure associated with each reservoir. It is clear that the lower bound is most sensitive to water saturation, the middle bound has the second rank, and the upper bound is the least sensitive one. Since water bulk modulus and density are greater than those of oil, P-wave velocity (Vp) and density (Rho) increase when water saturation goes up, i.e. oil is replaced with water. In contrast, S-wave velocity (Vs) decreases with increasing water saturation. This is only a density effect because the shear modulus of the rock is unaffected by fluids based on the Bio-Gassmann theory. The second panel shows the relative and normalized values of changes in seismic velocities due to changes in pore pressure. It is computed at constant initial water saturation associated with each reservoir. Similar to the first panel, lower bound is most sensitive to pore pressure, middle bound has the second rank, and upper bound is the least sensitive one. Both Vp and Vs decrease with increasing pore pressure. However, Vs is more sensitive to pore pressure than Vp. Density is almost insensitive to pore pressure variations (not shown here). The interesting asymmetric trend demonstrates that elastic parameters are more sensitive to pore pressure increase than decrease. This suggests that

in a time-lapse seismic study, pore pressure detection should be easier near the injector wells than producers.

Using all of the above reservoir properties, three reservoir units are generated and embedded in the background shale at different depths. The elastic properties of shale, i.e. density of 2.35 g/cc, P-wave velocity of 3.3 km/s, and S-wave velocity of 1.7 km/s, are extracted from Blangy (1994). MC seismic traveltimes (Tpp, Tps, and Tss) within the reservoir and RCs (RCpp, RCps, and RCss) at reservoir top are then calculated for the same percentage of changes in water saturation and pore pressure and for incident angles up to 20 degrees (Sub indices of pp, ps, and ss indicate conventional P-P, converted P-SV, and pure SH-SH seismic reflectivity data and will be used here after in the text and figures). Then, MC seismic traveltimes and RCs are subtracted from initial traveltimes and RCs computed at the reference water saturation and pore pressure for each individual reservoir.

Figures 3.4, 3.5, and 3.6 display the joint effect of changes in water saturation and pore pressure on MC seismic traveltimes and RCs for reservoir A, B, and C, respectively. The first row of each figure show the changes in traveltime and the second row show the corresponding changes in RCs. When comparing changes in traveltimes for reservoirs A, B, and C, one can state that the ranges of -10 to +20 millisecond (ms) for reservoir C are easily detectable, ranges of -4 to +3 ms for reservoir B are barely detectable, and ranges of -1 to +1 ms for reservoir A are not detectable. The same statement is true for the amplitude of time-lapse signals. A correlation exists between the changes in traveltimes and the associated changes in RCs. That is due to the changes in fluid saturation and pore pressure and this encourage authors to make crossplots of changes in RCs versus changes in traveltimes to explore this correlation in more detail. I also investigate if there is any

pattern to estimate and separate the effect of fluid saturation and pore pressure when only MC time-lapse traveltimes and RCs are available.

Figure 3.7 illustrates scatter plots for pairs of RCs changes versus traveltime changes computed for the reservoir C. The upper panel show a noise-free data set generated with large increment in water saturation and pore pressure changes. Incident angle varies between 0 to 20 degrees. By choosing such geometry, I can see some pattern in RCs and traveltimes. These patterns are associated with enforced patterns in water saturation and pore pressure changes. The origin, i.e., (0, 0), of this cross-plot corresponds to zero change in saturation and pressure. Two trends exist for saturation and pressure of P-P and SH-SH reflectivity data, but P-SV lacks these trends. This is due to fact that P-SV data has one way travel time through the reservoir with P-wave velocity and one way with S-wave velocity. The total traveltime is mainly affected with saturation in one path and with pressure in the other path, so separation is difficult for P-SV data using this kind of crossplotting. From the spread of points in the traveltime direction, it is evident that the value of traveltime for pressure detection is higher for SH-SH than that of P-P. However, spread of points in the RCs direction indicates that the value of RCs for saturation detection is higher for P-P than that of SH-SH.

One of the applications of time-lapse cross-plots is to quantitatively estimate and discriminate pressure and saturation changes from MC RCs and traveltime changes in a 4D project (upper panel in Figure 3.7). The other application is to statistically evaluate the cross-plot and to create criteria for detectability of a known production scenario using MC seismic measurements. To reach this goal, I first generate a set of noisy data set, contaminated with 10% Gaussian random noise, by choosing a small increment in water saturation and pore pressure. The representative data in time-lapse cross-plot (lower panel in Figure 3.7) allow one to statistically analyze the detectability of a known scenario of

saturation and pressure changes using MC seismic attributes. Next, I construct single and joint distributions functions for changes in RCs and traveltimes. Figure 3.8 displays the single probability density function (PDF) for the RCs on the left column and for traveltimes on the right column. Three rows in this figure from top to bottom correspond to reservoir A, B, and C, respectively. This figure summarizes the entire information hidden in previous figures and provides a concise and instructive manner to represent time-lapse signals. Figure 3.9 shows the joint probability density function (JPDF), the associated marginal single PDFs, the joint cumulative distribution function (JCDF), and the corresponding single CDF of reservoir C and only for P-P seismic data.

Having calculated the single CDF for time-lapse attributes (Figure 3.9), the probabilities of detecting certain symmetric ranges of time-lapse seismic attributes can be computed. Figure 3.10 illustrates single probability detectors (SPDs) for RCs on the left and for traveltimes on the right column. As an example for application of SPDs, assume that any changes in seismic traveltimes greater than plus minus 5ms are detectable based on the quality of the seismic data. For reservoir C, using the right lowermost panel of SPDs in Figure 3.11, the likelihood of having detectable traveltime for the specific production plan, will be 30, 40, and 65 percent, using P-P, P-SV, and SH-SH seismic data, respectively. By comparing SPDs of three reservoirs in Figure 3.11, one can determine that under specific conditions set for my reservoirs in this study, time-lapse signals for the reservoir A are not detectable, for reservoir B barely detectable, and for reservoir C more likely detectable.

In Figure 3.11, I color-plot the joint probabilities of detecting certain symmetric ranges of time-lapse seismic attributes and called them joint probability detectors (JPDs). Horizontal axes on these plots are the absolute (positive) values of changes in seismic traveltimes. Vertical axes are absolute values of changes in seismic RCs. As an example

for application of JPDs, assume that any changes in seismic traveltimes greater than plus minus 5ms, and any changes in seismic amplitude greater than plus minus 0.01 are detectable. For reservoir C, using the last row of JPDs in Figure 3.12, the likelihood of having jointly detectable traveltime and RCs for the specific production plan, will be 30, 15, and 50 percents, using P-P, P-SV, and SH-SH, respectively. In general, the higher changes in time-lapse signals, the lower probability.

Finally, evaluating various production plans with different reservoir properties will be an effective and a quantitative forward modeling approach to determine whether or not a reservoir is a candidate for acquiring MC 4D seismic data.

3.5 SUMMARY AND CONCLUSIONS

Time-lapse cross-plots of changes in MC RCs versus changes in traveltimes due to production show a separation between saturation and pressure and may have the capacity to quantitatively estimate and discriminate dynamic reservoir properties. In addition, I propose an effective statistical approach to estimate the detectability of a known production plan using MC seismic data. Time-lapse cross plot itself, single, and joint probability detectors help us to understand the efficacy of P-SV and SH-SH seismic time lapse data along with conventional P-P time-lapse reflectivity data.

The results of applying the proposed approach on three different synthetic reservoirs, consolidated, poorly consolidated and medium consolidated sandstones, are consistent with my intuition regarding the detectability of fluids within different reservoir types. This study suggests that fluid flow detection by seismic data is significantly limited for consolidated sandstone reservoirs. However, the detection is plausible for poorly to medium consolidated reservoirs in the present of realistic seismic noise level. In these cases, conventional P-P seismic data is dominant in amplitude change compared to

converted P-SV and pure SH-SH seismic data. P-P data reflects the changes in fluid saturation and pore pressure. However, the primary factor is the saturation effect. SH-SH seismic data are most sensitive to the pressure thorough traveltimes portion of pre-stack data. P-SV seismic data is the weakest detector in terms of time-lapse amplitude, but its traveltime shows an intermediate trend between P-P and SH-SH seismic data.

My observations suggest that in a waterflooding scenario, SH-SH and P-SV reflectivity data provide valuable information, if detectable changes in pore pressure accompany changes in water saturation. In contrast, P-SV and SH-SH reflectivity data are less valuable, if changes in water saturation within the reservoir are the only or dominant production-induced effects on seismic reflectivity data.

Several conclusions can be made by changing porosity, clay content, thickness, fluid type, fluid distribution type (Patchy and uniform), and production scenario. Different quality measures for the seismic data, such as improved time resolution may make detection more quantifiable further aiding my understanding of the benefits of time lapse seismic as reservoir properties change.

In this study I select three sandstone reservoirs with 100 meter thickness. Classification techniques based on the seismic observations can be unreliable due to wavelet and tuning effects in thin reservoir units. To overcome this problem, inverted seismic parameters, e.g., AI, and SI extracted from pre-stack seismic data for both base and monitor surveys can be employed to estimate and discriminate fluid saturation and pore pressure.

In general, as is the case for any seismic reservoir characterization study, limitations include seismic noise, thickness tuning, and stiff rocks with low porosity. In addition, repeatability in seismic data acquisition and processing, and the low density contrast between hydrocarbon and injected fluid can limit the success of any seismic

time-lapse project. Depth registration for MC seismic data has not been addressed in this study and I assume that depth registration for base and monitor surveys are already performed between all components of seismic reflectivity data.

The proposed methodology to estimate and discriminate saturation and pressure is only appropriate for single layer reservoirs. In multi-layer reservoirs, the cumulative effects of individual layers may prevent us from distinguishing patterns from one another. However, statistical detectability of fluid flow proposed in this study, can be generalized for any reservoir time-lapse study under various production scenarios.

Finally, I assume that water injection into black oil reservoirs is an isothermal process. In addition, I assume that changes in fluid saturation and pore pressure cause mechanical compaction neither on the reservoir nor on the background shale. This assumption is not valid for compacting reservoirs, e.g., a chalk reservoir in North Sea. Time-lapse amplitude at the top of such reservoirs is a function of two changes, changes in overburden due to mechanical compaction and changes in the reservoir itself. Similarly, time shifts in such a reservoir are associated with both mechanical compaction of the reservoir and changes in saturation-pressure.

Table 3.1: Characteristics of three synthetic reservoir units used in this study.

	Reservoir A	**Reservoir B**	**Reservoir C**
Degrees of consolidation	Consolidated sandstone	Medium-consolidated sandstone	Poorly-consolidated sandstone
Rock physics model	Stiff sand model or modifies Hashin-Strikman upper bound (Gal et al. 1998)	Average of upper and lower bound for reservoir A and C	Modifies Hashin-Strikman lower bound (Dvorkin and Nur 1996)
Porosity (%)	10	20	30
Critical porosity (%)	40	40	40
Depth (m)	3000	2200	1500
Thickness (m)	100	100	100
Temperature(^{o}C)	100	75	55
Salinity (PPM)	70000	70000	70000
Clay content (%)	20	20	20
Average contact number	6	6	6
Initial pore pressure (psi)	5000	4000	3000
Overburden pressure (psi)	10000	7000	5000
Effective pressure (psi)	5000	3000	2000
Change in initial pore pressure (psi)	-1500 to 1500	-1200 to 1200	-900 to 900
Initial water saturation	0.50	0.50	0.50
Change in initial water saturation	-0.35 to 0.35	-0.35 to 0.35	-0.35 to 0.35

Table 3.2: Density and elastic properties of minerals associated with the synthetic reservoirs.

Constituents	Density (g/cm^3)	Bulk modulus (GPa)	Shear modulus (GPa)	P-wave velocity (km/s)	S-wave velocity (km/s)
Quartz	2.65	37.0	44.0	6.008	4.0748
Clay	2.55	25.0	9.0	3.8092	1.8787

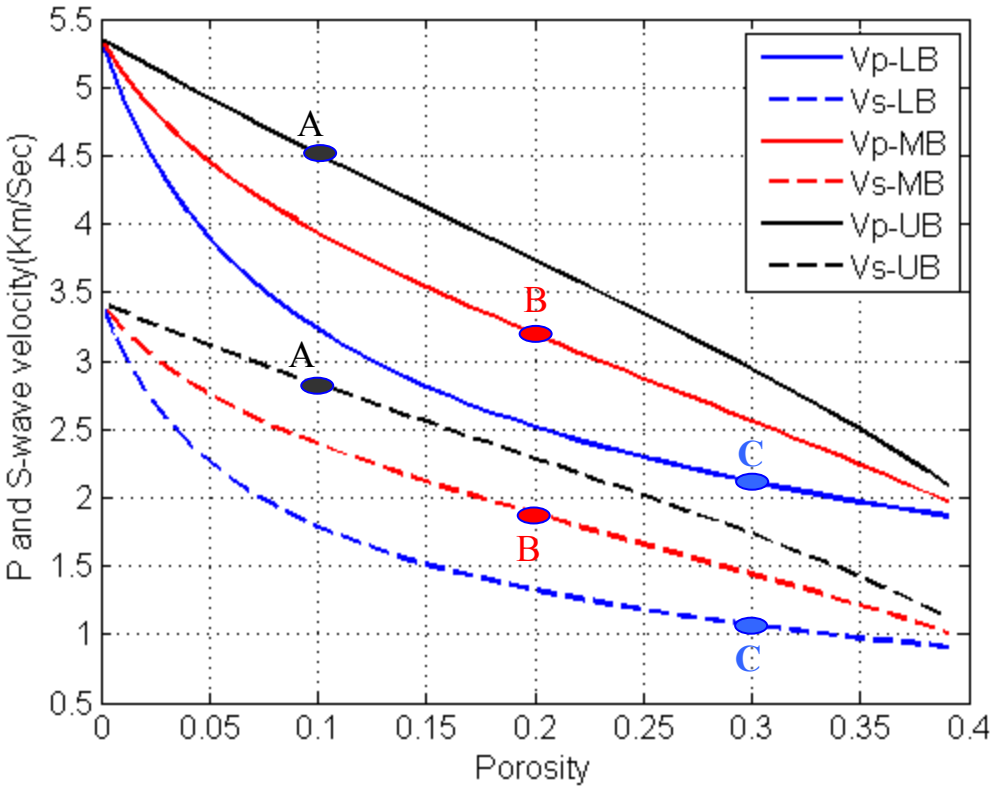

Figure 3.1: Rock physics models (P-wave and S-wave velocities versus porosity) adopted for this study. Continuous and dashed black lines are modified Hashin-Strikman upper bounds (Stiff sand model, Gal et al. 1998) for P&S-wave velocities, respectively. Reservoir A is located on these bounds with 10% porosity. Continuous and dashed blue lines are modified Hashin-Strikman lower bounds (Dvorkin and Nur, 1996) for P&S-wave velocities, respectively. Reservoir C is located on these bounds with 30% porosity. Continuous and dashed red lines are the average of upper (UB) and lower (LB) bounds and called middle bounds (MB). Reservoir B is positioned on these bounds with 20% porosity.

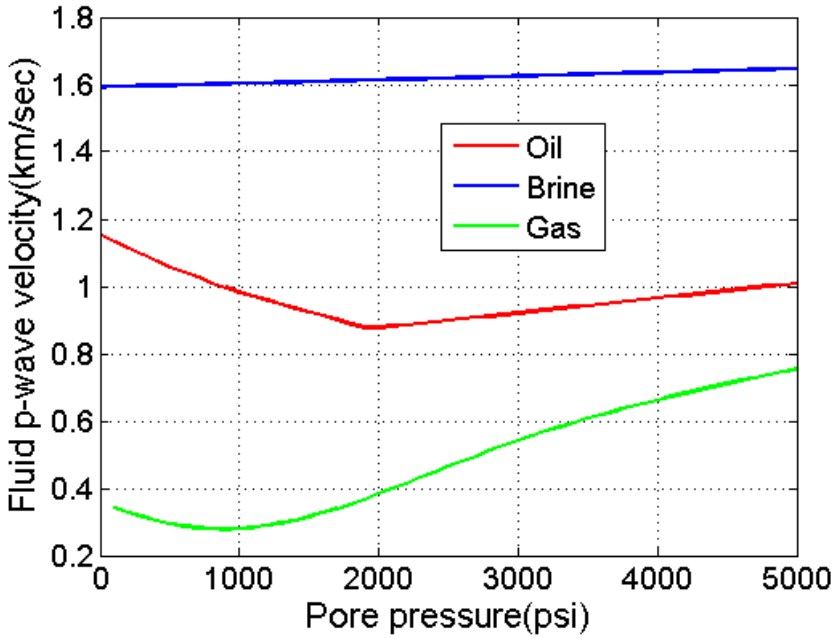

Figure 3.2: Seismic P-wave velocity for the reservoir fluids. Batzle-Wang 1992 empirical relationships have been used to transform PVT properties of oil-gas-water. Note that bubble point pressure is 2000 psi.

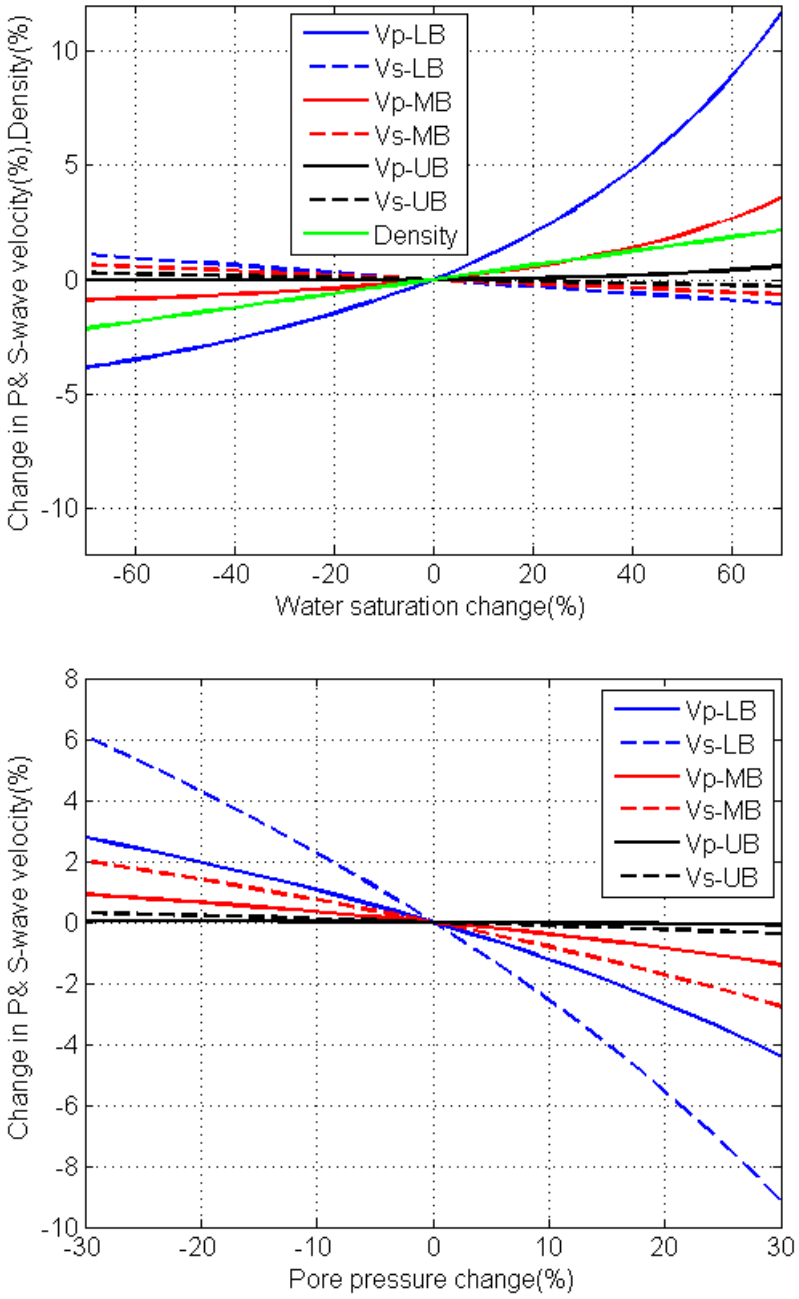

Figure 3.3: Effects of water saturation (upper panel) and pore pressure (lower panel) on density, P&S-wave velocities of the reservoir rocks. Continuous and dashed lines indicate P&S-wave velocities, respectively. Upper bounds (UB) are shown in black, lower bounds (LB) in blue, and middle bounds (MB) in red.

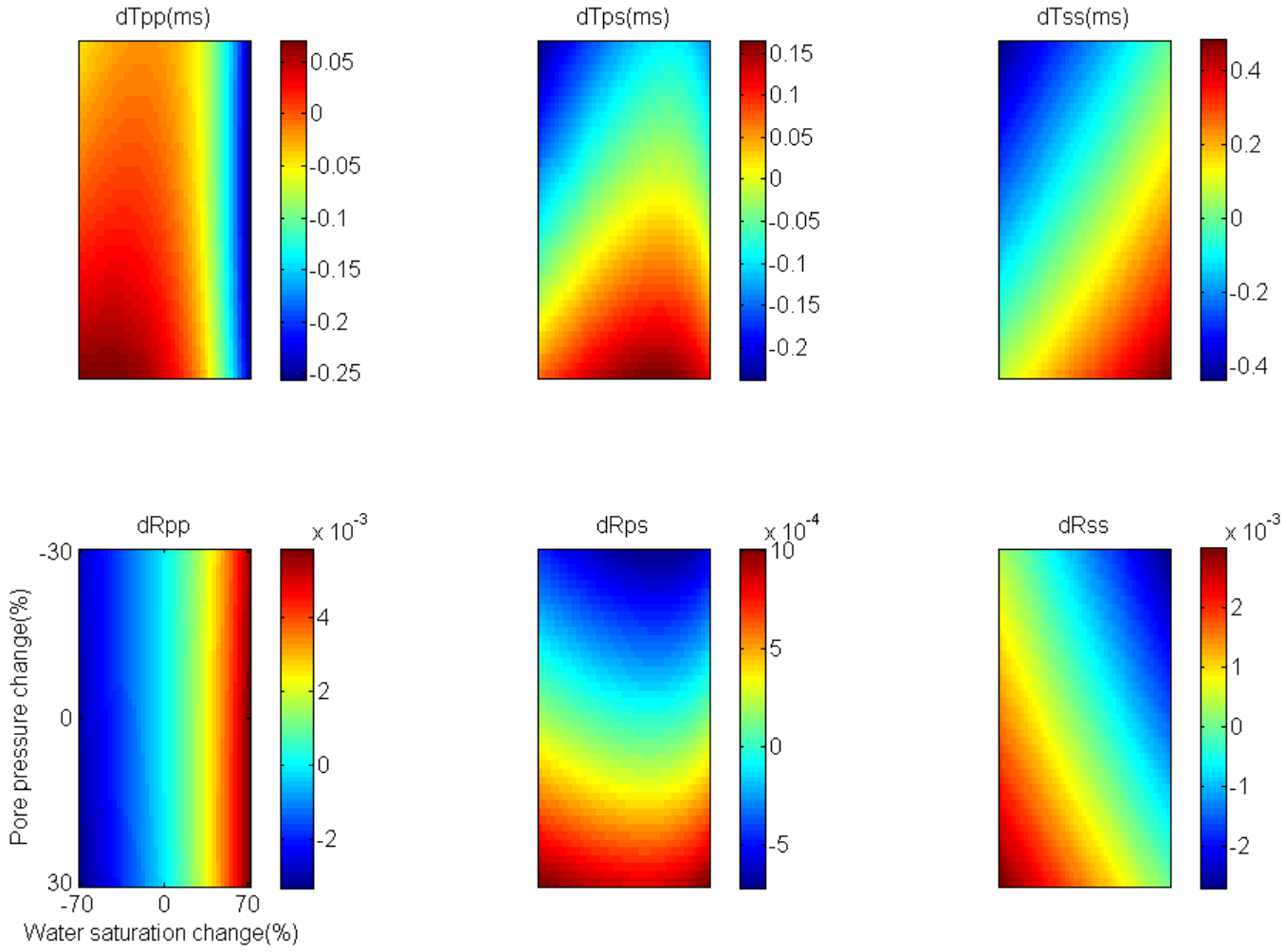

Figure 3.4: Reservoir A: Joint effects of changes in water saturation and pore pressure on Multi-Component (MC) seismic traveltimes (first row) and Reflection Coefficients, RCs, (second row). dTpp, dTps, and dTss are the changes in MC traveltimes for conventional P-P, converted P-SV, and pure SH-SH seismic reflectivity data. dRpp, dRps, and dRss indicate the associated changes in MC RCs.

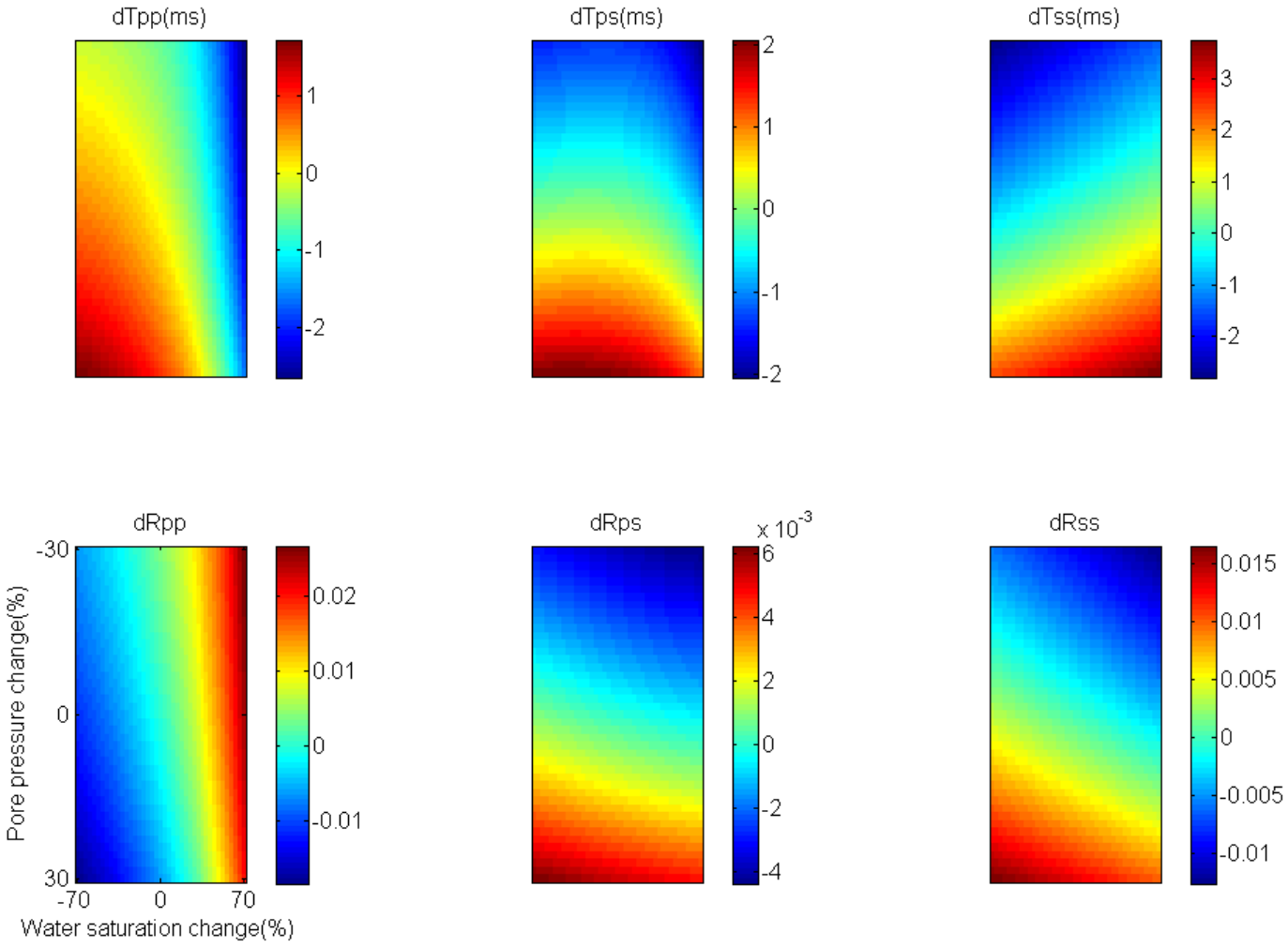

Figure 3.5: Reservoir B: Joint effects of changes in water saturation and pore pressure on Multi-Component (MC) seismic traveltimes (first row) and Reflection Coefficients, RCs, (second row). dTpp, dTps, and dTss are the changes in MC traveltimes for conventional P-P, converted P-SV, and pure SH-SH seismic reflectivity data. dRpp, dRps, and dRss indicate the associated changes in MC RCs.

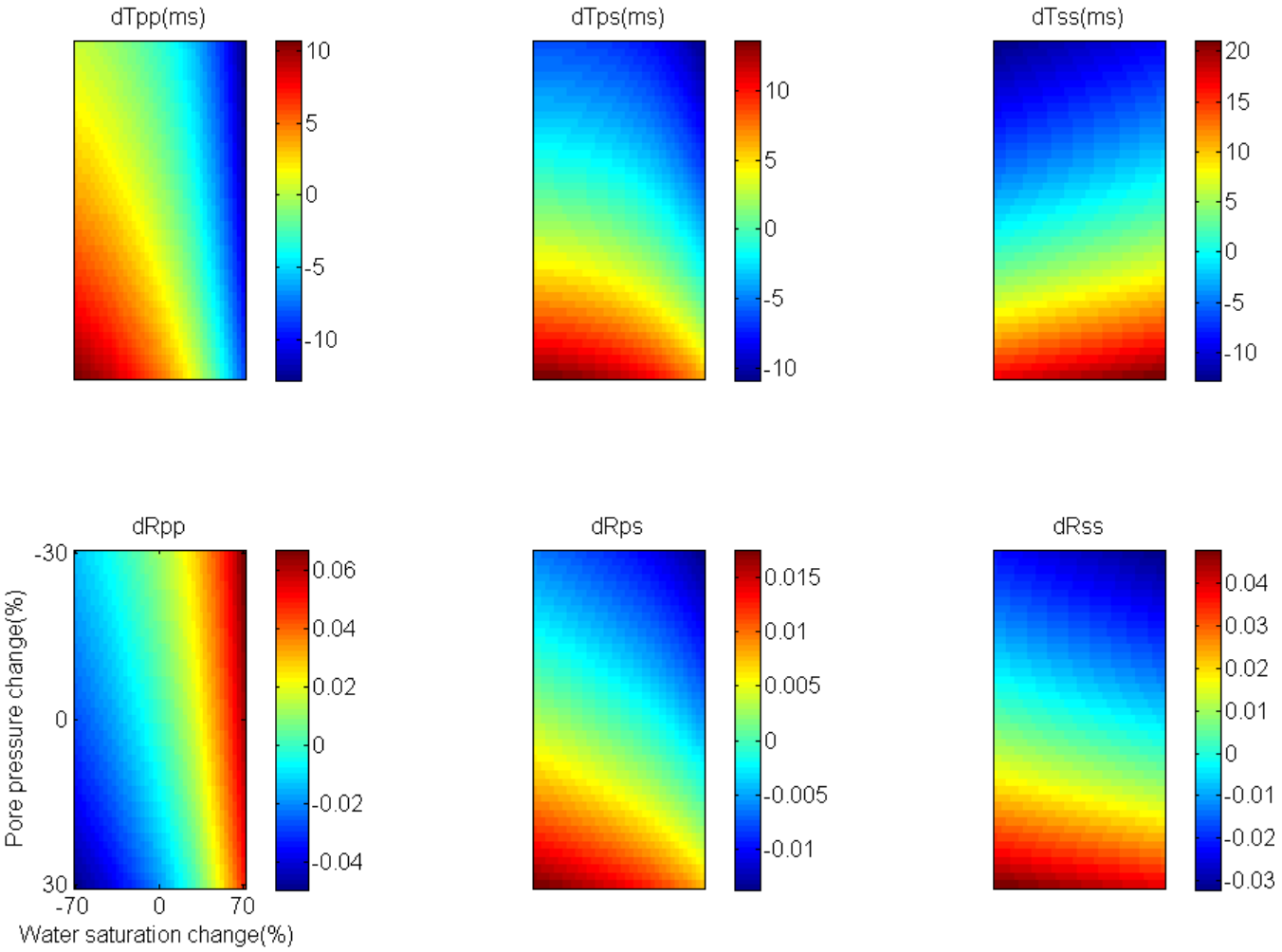

Figure 3.6: Reservoir C: Joint effects of changes in water saturation and pore pressure on Multi-Component (MC) seismic traveltimes (first row) and Reflection Coefficients, RCs, (second row). dTpp, dTps, and dTss are the changes in MC traveltimes for conventional P-P, converted P-SV, and pure SH-SH seismic reflectivity data. dRpp, dRps, and dRss indicate the associated changes in MC RCs.

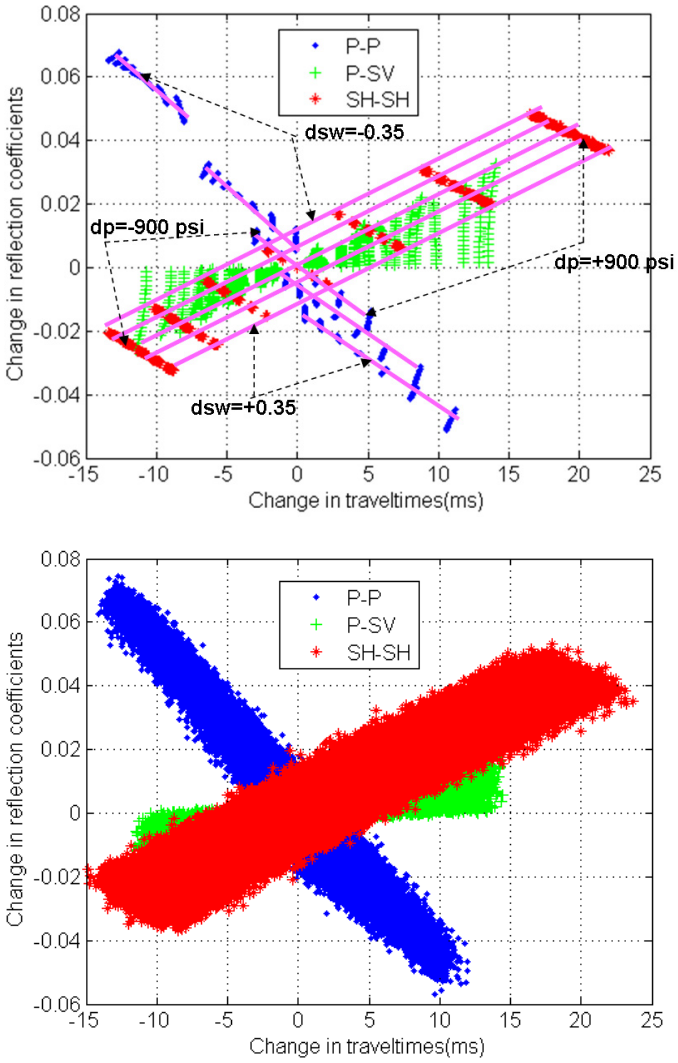

Figure 3.7: Cross-plots of changes in RCs versus changes in travel times (ms), for reservoir C. First panel is noise-free data set with large increment in water saturation (ranged from -0.35 to +0.35 by increment of 0.20) and pore pressure (ranged from -900 to +900 by increment of 300 psi). P-P cloud is shown in blue, P-SV in green, and SH-SH in red. Continuous pink lines indicate saturation patterns for changes of -0.35, -0.20, 0.0, +0.20, and +0.35 from bottom to top for P-P and from top to bottom for SH-SH. Black dashed arrows display the extreme values for two end members of -0.35 and +0.35. For pressure patterns, black dashed arrows display the extreme values for two end members of -900 and +900 psi from left to right for SH-SH and from top to bottom for P-P. Note that P-SV data lacks pattern for saturation and pressure. Second panel is contaminated data set with 10% random Gaussian noise and with small increment in water saturation (ranged from -0.35 to +0.35 by increment of 0.01) and pore pressure (ranged from -900 to +900 by increment of 5 psi).

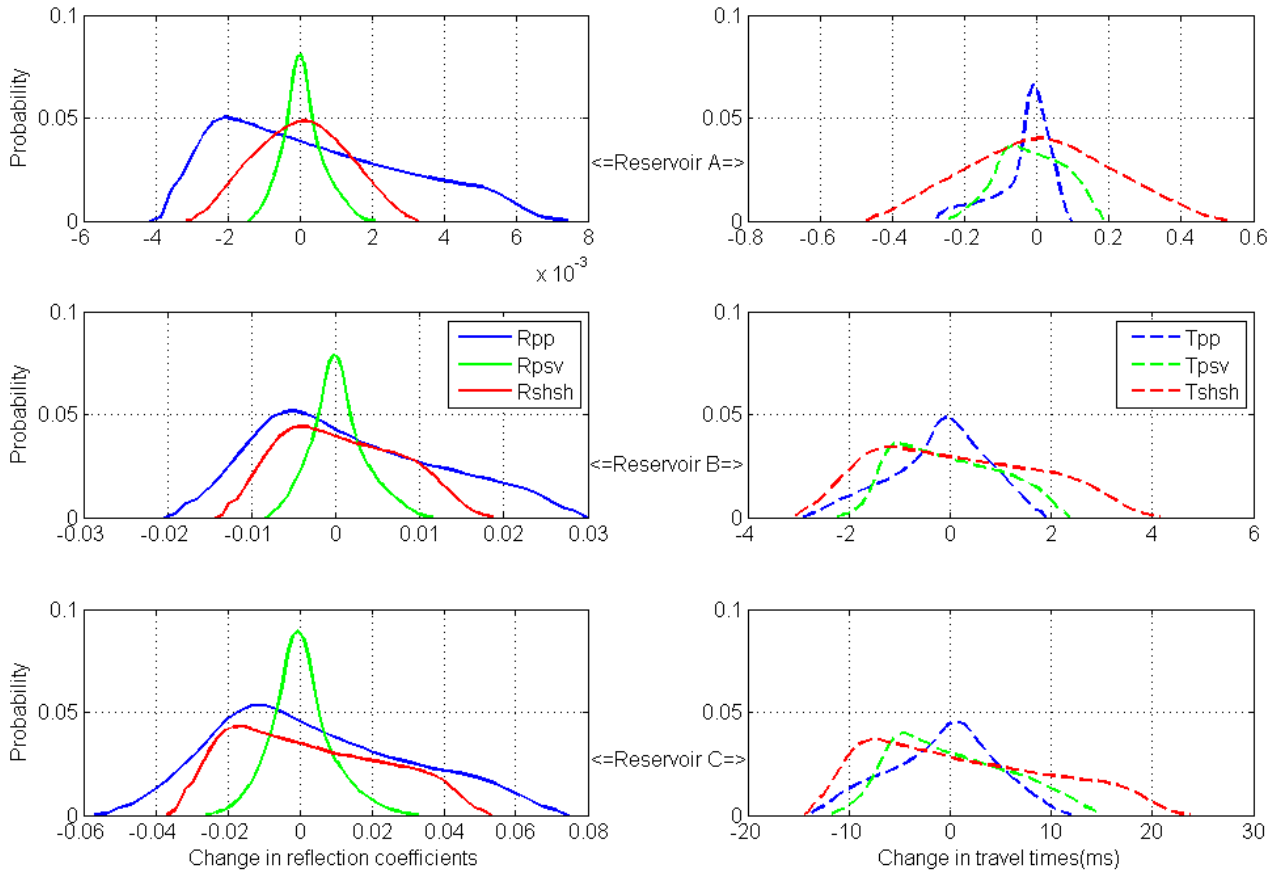

Figure 3.8: Single probability density function (PDF) for the RCs on the left column and for traveltimes on the right column. Three rows in this figure from top to bottom correspond to reservoir A, B, and C, respectively.

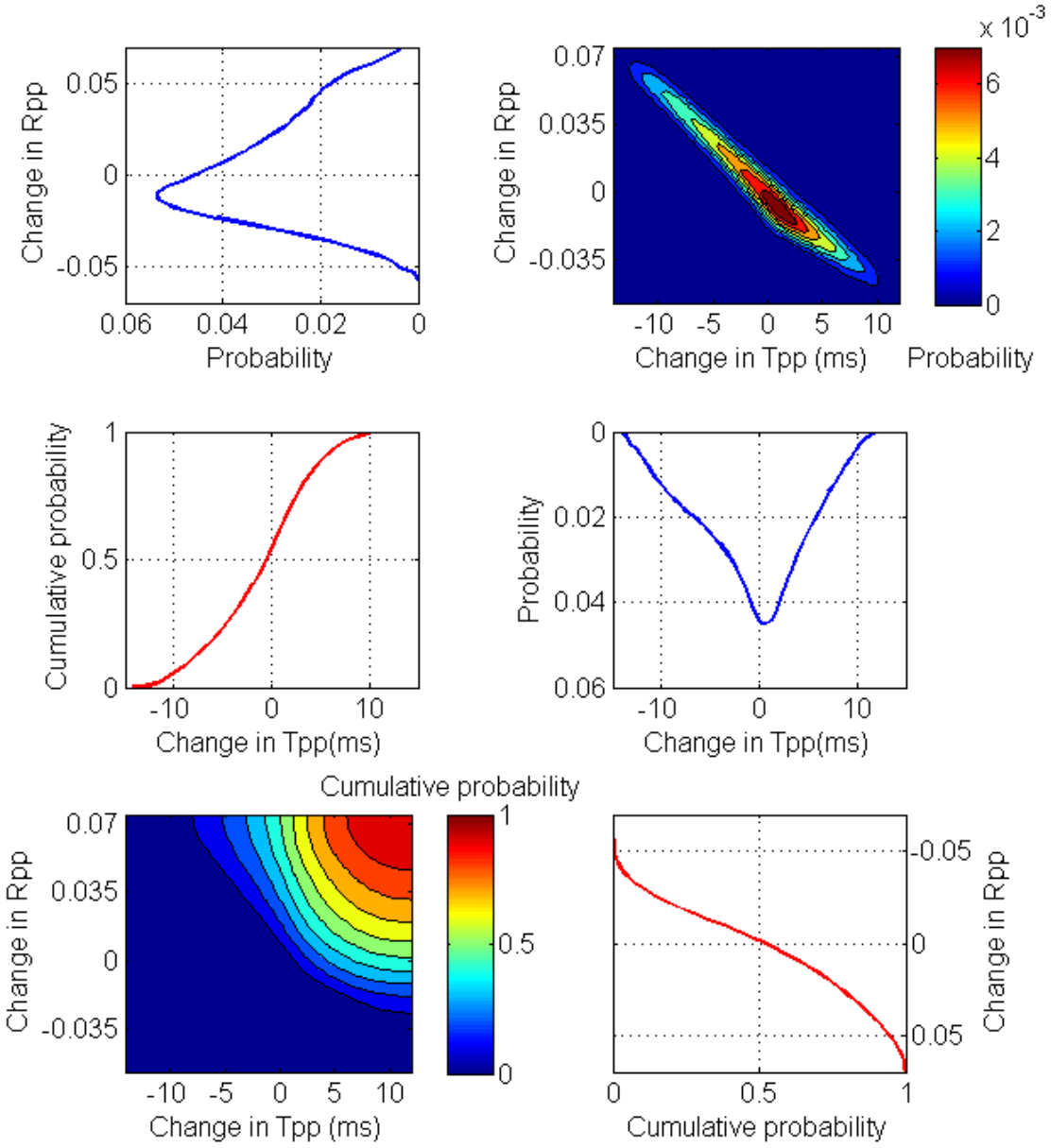

Figure 3.9: Joint probability density function (JPDF), the associated marginal single PDFs, the joint cumulative distribution function (JCDF), and the corresponding single CDF of reservoir C and only for P-P seismic data.

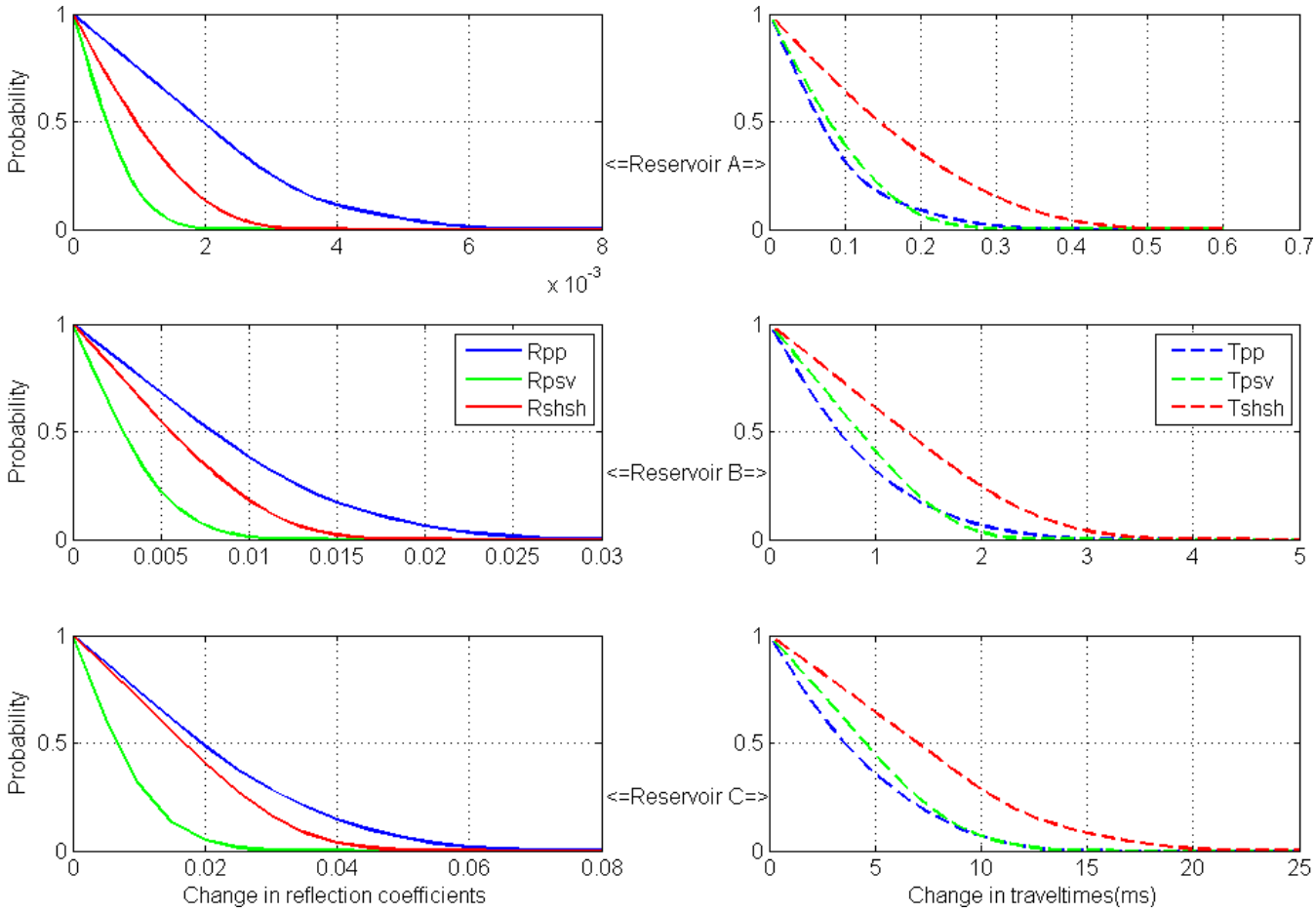

Figure 3.10: Single probability detectors (SPDs) for RCs on the left and for traveltimes on the right column. Three rows in this figure from top to bottom correspond to reservoir A, B, and C, respectively.

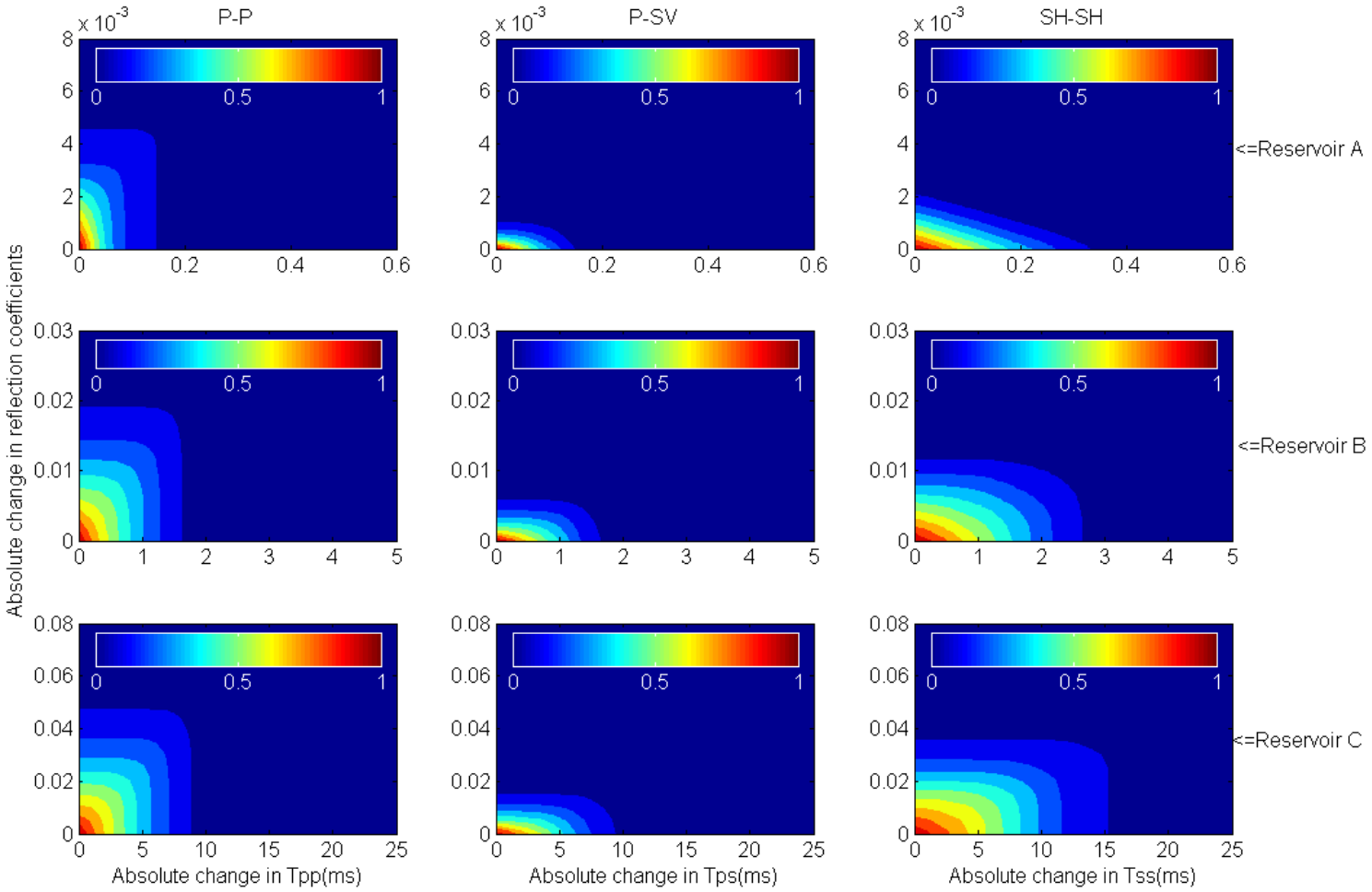

Figure 3.11: Joint probability detectors (JPDs) for three synthetic reservoirs. Three rows in this figure from top to bottom correspond to reservoir A, B, and C, respectively. Horizontal axes on these plots are the absolute (positive) values of changes in seismic traveltimes. Vertical axes are absolute values of changes in seismic RCs. All panels are color-coded with probability values ranged from 0 to 1. Note that the higher changes in time-lapse signals, the lower probability.

Chapter four: Derivative-bases sensitivity analysis: a viable tool in reservoir geophysics

4.1 INTRODUCTION

I analyze the sensitivity of multicomponent (MC) seismic (P-P, P-SV, and SH-SH) reflection coefficients (RCs) and traveltimes to water saturation and pore pressure variations by taking the appropriate partial derivatives. Applying this approach to a poorly consolidated sandstone reservoir partially saturated with light oil and brine, demonstrates that P-P traveltimes have the largest sensitivity to water saturation, but the least sensitivity to pore pressure. In contrast, SH-SH traveltimes have the least sensitivity to water saturation, and the most sensitivity to pressure. P-SV traveltimes have intermediate sensitivities to pressure and saturation, but are more affected by saturation than pressure. By analyzing the sensitivity of MC seismic RCs to water saturation at the reservoir top, i.e., shale over oil saturated sandstone, and at the oil-water contact (OWC), i.e., oil-saturated sandstone over brine-saturated sandstone, I find that the absolute value of amplitudes at all angles is greatest for P-P, smallest for P-SV, and intermediate for SH-SH. In addition, the absolute values of AVO (amplitude variation vs. offset) gradients at the reservoir top and OWC can be organized in descending order as (P-SV, SH-SH, PP) and (P-P, P-SV, SH-SH), respectively. For the sensitivity of both interfaces to pressure (the reservoir top and OWC), angle-dependent relations are also extracted.

4.2 BACKGROUND AND FORMULATION

Seismic reservoir monitoring of a waterflooded reservoir is a challenging problem. Detecting small changes in seismic traveltimes and RCs due to changes in dynamic reservoir properties, i.e., saturation and pressure, is the key to success. Seismic RCs respond to interface properties, i.e., contrasts in P and S-wave velocities and in density between adjacent layers. On the other hand, seismic traveltimes respond to the

reservoir interval properties. These seismic attributes are complicated functions of elastic parameters. Elastic parameters themselves are also related to the dynamic reservoir properties using rock physics model, e.g., Gassmann (1951) or Hertz-Mindlin (Mindlin, 1949) theories. Consequently, making any judgment about the sensitivity of the MC seismic attributes with respect to saturation and pressure is difficult and dependent on the rock physics model employed. In this paper, I consider the travel times and amplitudes for pre-stack MC seismic data and propose a quantitative approach to obtain their sensitivity to saturation and pressure at different offset ranges.

4.3 METHODOLOGY

4.3.1 Sensitivity Analysis of MC Seismic Traveltimes

In general, MC seismic traveltimes can be expressed as functions of P and S-wave velocities, interval thickness, and incident angle. P and S-wave velocities can then be related to saturation and pressure within the reservoir using rock physics equations. The following four steps summarize the calculation of the traveltime sensitivities: First, the partial derivatives of traveltimes with respect to P and S-wave velocities for a reservoir interval can be calculated either numerically using ray tracing, an Eikonal solver, or analytically assuming straight rays. Second, take the partial derivatives of the P and S-wave velocities relative to bulk and shear moduli, and density of the reservoir layer. Third, take the partial derivatives of the bulk and shear moduli, and density relative to saturation using Gassmann's theory and with respect to pressure using a stress-sensitive rock physics model, e.g. Modified Hashin Strikman lower bound, MHSLB, (Dvorkin and Nur, 1996), calibrated with pressure-dependent core measurements. Finally, combine these partial derivatives using the chain rule, to obtain full-derivatives of MC seismic traveltimes relative to saturation and pressure. It is also possible to do the entire process

of sensitivity analysis numerically. This can be done by setting up equations for MC traveltimes relative to pressure and saturation and then calculating the full derivatives numerically. My numerical results are consistent with my analytical ones, so here I only present the numerical results (See appendix B).

As an example, a poorly consolidated sandstone reservoir embedded in shale at depth 2100 meters is considered to show the sensitivity of MC seismic traveltimes to saturation and pressure. The 60 meters thick reservoir has a constant porosity of 25%. The reservoir is uniformly saturated with 20% brine (connate water) and 80% light oil. The reservoir model is composed of 80% quartz (Mavko et al., 1998) and 20% clay (Han, 1986). Fluid properties are extracted from PVT data (Killough, 1995) and then transformed to seismic elastic parameters using Batzle and Wang's (1992) empirical correlations. Table 4.1 summarizes the fluid and rock properties used in this example. Using the method summarized above, the full derivatives of MC seismic traveltimes relative to water saturation and pore pressure are derived and illustrated in Figure 4.1a and 4.1b. For the sensitivity of traveltimes to water saturation (Figure 4.1a) at given water saturation (20% brine), and pore pressure (32.27 MPa), P-P has the largest sensitivity with almost the same intercept and gradient with SH-SH but opposite signs. P-SV has zero sensitivity at near offsets, and negative sensitivity at middle and far offsets. For the sensitivity of traveltimes to pressure (Figure 4.1b), the intercept is greatest for SH-SH, smallest for P-P, and intermediate for P-SV. In addition, the value of traveltime gradients is greatest for SH-SH, smallest for P-SV, and intermediate for P-P. It is important to note that the values of sensitivities in Figure (4.1a and 4.1b) are pressure and saturation-dependent. That is, the presented values of sensitivities are only valid for the saturation and pressure values at which sensitivities are calculated. In fact, sensitivities versus incident angles at different values of saturation and pressure have the same trends

as Figure (4.1a and 4.1b) but different intercepts. Figure (4.1c and 4.1d) illustrate the sensitivities of traveltimes at zero offset for different saturations and pressures with respect to water saturation and pore pressure, respectively. P-P tarveltimes have the largest sensitivity to water saturation and its sensitivity is maximum (up to -21) at the largest values of water saturation and pore pressure. This phenomena for light oil (API=65) here, is associated with the well-known fact that P-P reflectivity data is not able to distinguish commercial concentrations of gas from noncommercial gas deposits. This maximum sensitivity point is also coincident with the locations around injector wells or waterfront for a water flooding scenario. The sensitivity of P-SV traveltimes to water saturation is less than that of P-P, but has a similar trend, i.e., the highest sensitivity is at the largest values of water saturation and pore pressure. SH-SH traveltimes have almost a constant sensitivity to water saturation at zero offset (Figure 4.1c). The sensitivities of traveltimes at zero offset to pore pressure have their peaks at the largest pore pressures, but they are not affected much by changing saturation (Figure 4.1d).

4.3.2 Sensitivity Analysis of MC Seismic RCs

MC seismic RCs can be defined from functions of contrasts in P and S-wave velocities, contrast in density, Poisson's ratios of the first and second media, and are also angle of incidence dependent (Rosa, 1976; Gomez and Tatham, 2007). These forms of reflection coefficient provide a convenient mathematical expression for taking the first derivatives of RCs. Calculations of the sensitivity of RCs can be summarized in the following four steps: First, take the first partial derivatives of the RCs relative to contrasts in P&S-wave velocities, contrasts in density, and Poisson's ratios. Second, calculate the partial derivatives of contrasts in P and S-wave velocities, contrast in density, and Poisson's ratios, relative to the bulk and shear moduli, and density of the two adjacent

media. The remaining steps are the same as those for the traveltimes sensitivity described above, and similar to traveltimes, the sensitivity analysis of RCs can be done numerically (See appendix B).

As an example, I select a reservoir which has two distinct parts. The top layer is uniformly saturated with 20% brine and 80% light oil. The bottom layer is uniformly saturated with 80% brine, and 20% light oil, called residual oil. The elastic properties of shale, i.e. density of 2.35 gm/cc, P-wave velocity of 3.3 km/s, and S-wave velocity of 1.7 km/s, are extracted from Blangy, 1994. Table 4.1 summarizes the fluid and rock properties used in this example. The partial derivatives of RCs relative to contrasts in elastic parameters were derived for the reservoir top, i.e., shale over oil-saturated sandstone, and for the OWC, i.e., oil saturated sandstone over brine-saturated sandstone. The results for reservoir top and OWC are very similar to each other, so I only present the results for the OWC (Figure 4.2a, 4.2b, and 4.2c). From these observations, I conclude that the far-offset range in both P-P and P-SV reflectivity data may provide valuable information regarding the density, which can help distinguish commercial gas concentration from non-commercial deposits. On the other hand, SH-SH reflectivity has the largest sensitivity to density for all offset ranges; consequently, pre-stack seismic inversion of SH-SH data can be a valuable source of density information.

Using the partial derivatives of the rock physics model and combining them with the partial derivatives of RCs, I perform the sensitivity analysis of RCs relative to water saturation and pore pressure. The results are presented in Figure 4.3a, 4.3b, 4.3c, and 4.3d. At the reservoir top (Figure 4.3a and 4.3b), P-P reflectivity has dominant sensitivity to water saturation for all offset ranges (Figure 4.3a). SH-SH and P-SV reflectivity data are very close to one another at middle and far offsets, but SH-SH has larger sensitivity at near offsets. In fact, the sensitivities of P-SV and SH-SH reflectivity data are quite small

compared to that of P-P reflectivity data. In this case, AVO gradients of reflectivity data can be classified in a descending order as P-SV, SH-SH, and P-P, respectively. For the sensitivity of RCs to pore pressure at reservoir top (Figure 4.3b), angle-dependent relations can be extracted as follows: for the incident angles of 0-20, 20-28, and greater than 28 degrees, the absolute values of amplitudes can be expressed in a descending order by (SH-SH, P-P, P-SV), (SH-SH, P-SV, P-P), and (P-SV, SH-SH, P-P), respectively. For the sensitivities of RCs at the OWC to water saturation, I observe similar results as at the reservoir top, but the P-P RC has larger sensitivity at larger offsets than that of the reservoir top (Figure 4.3c). The sensitivities of RCs at the OWC to pore pressure are strictly angle-dependent (Figure 4.3d). The sensitivities of RCs to saturation and pressure are also functions of saturation and pressure. In general, sensitivities of P-P and P-SV reflectivity to water saturation are maximum at higher water saturation, but the sensitivity of SH-SH reflectivity data to water saturation is almost constant when changing water saturation. In addition, the sensitivity of RCs to water saturation is not affected much by changes in pore pressure. On the other hand, the higher the pore pressure, the larger the sensitivities of RCs to pore pressure. In contrast, the sensitivity of RCs to pressure is not affected much by changes in water saturation.

4.4 SUMMARY AND CONCLUSIONS

In a water-flooding scenario, interactions between dynamic reservoir properties and their effects on seismic elastic parameters are complicated. I propose a quantitative approach to calculate the sensitivities of MC seismic attributes to saturation and pressure. This method improves my knowledge regarding MC AVO and TVO (traveltime vs. offset) for time-lapse seismic analyses.

The examples presented in the paper illustrate the sensitivities of MC seismic (P-P, P-SV, and SH-SH) traveltimes and RCs to water saturation and pore pressure. For the sensitivity of traveltimes to water saturation, the absolute intercept is greatest for P-P, smallest for P-SV, and intermediate for SH-SH. In addition, the absolute value of gradients is greatest for P-P, smallest for SH-SH, and intermediate for P-SV. For the sensitivity of traveltimes to pressure, the absolute intercept is greatest for SH-SH, smallest for P-P, and intermediate for P-SV. Here, the absolute value of gradients is greatest for SH-SH, smallest for P-SV, and intermediate for P-P.

By analyzing the sensitivity of RCs at the reservoir top and OWC to water saturation, I found that the absolute value of amplitudes at all angels is greatest for P-P, smallest for P-SV, and intermediate for SH-SH. In addition, the absolute values of AVO gradients at reservoir top and OWC can be expressed in a descending order by (P-SV, SH-SH, P-P) and (P-P, P-SV, SH-SH), respectively. For the sensitivity of both interfaces, reservoir top and OWC, to pressure angle-dependent relations are extracted. At reservoir top and for the incident angels of 0-20, 20-28, and greater than 28 degrees, the absolute values of amplitudes can be expressed in a descending order by (SH-SH, P-P, PSV), (SH-SH, P-SV, P-P), and (P-SV, SH-SH, P-P), respectively. At OWC, the sensitivities of RCs to pore pressure are strictly angle-dependent. My observations suggest that in a waterflooding scenario, SH-SH and P-SV reflectivity data provide valuable information at the reservoir top and OWC, if detectable changes in pore pressure accompany changes in water saturation. In contrast, P-SV and SH-SH reflectivity data are less valuable, if changes in water saturation within the reservoir are the only or dominant production-induced effects on seismic reflectivity data.

Table 4.1: The rock and fluid properties used in the examples.

Constituents	ρ(gr/cc)	K(GPa)	μ(GPa)
Quartz	2.65	37.0	44.0
Clay	25.0	9.0	2.55
Brine	1.05	2.84	0
Oil	0.57	0.41	0

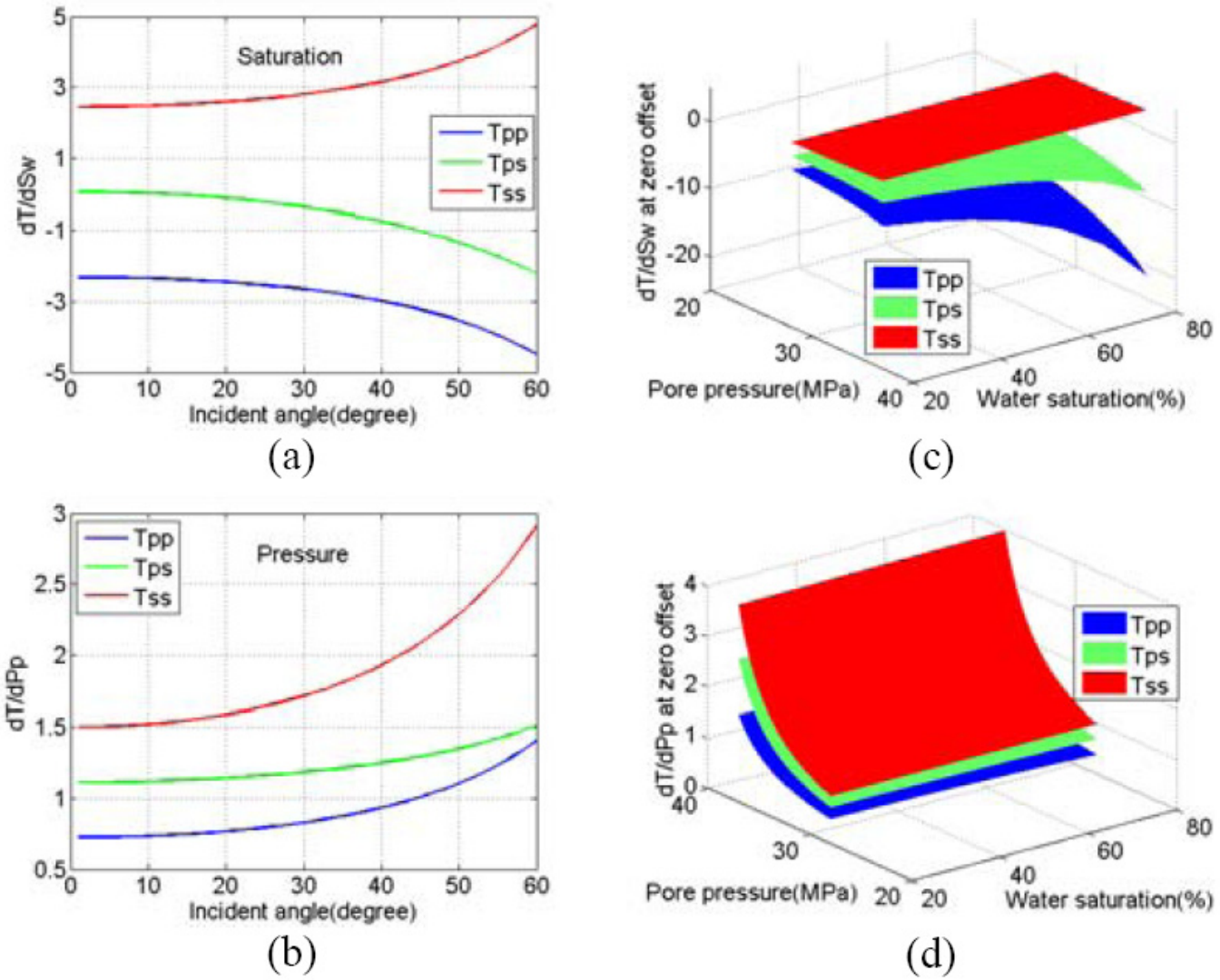

Figure 4.1: Sensitivities of MC seismic traveltimes vs. incident angle to water saturation (a), and to pore pressure (b). Sensitivity of P-P traveltime (Tpp) is shown in blue, P-SV (Tps) in green, and SH-SH (Tss) in red. Panels (c) and (d) display the sensitivities of traveltimes at zero offset for different saturations and pressures.

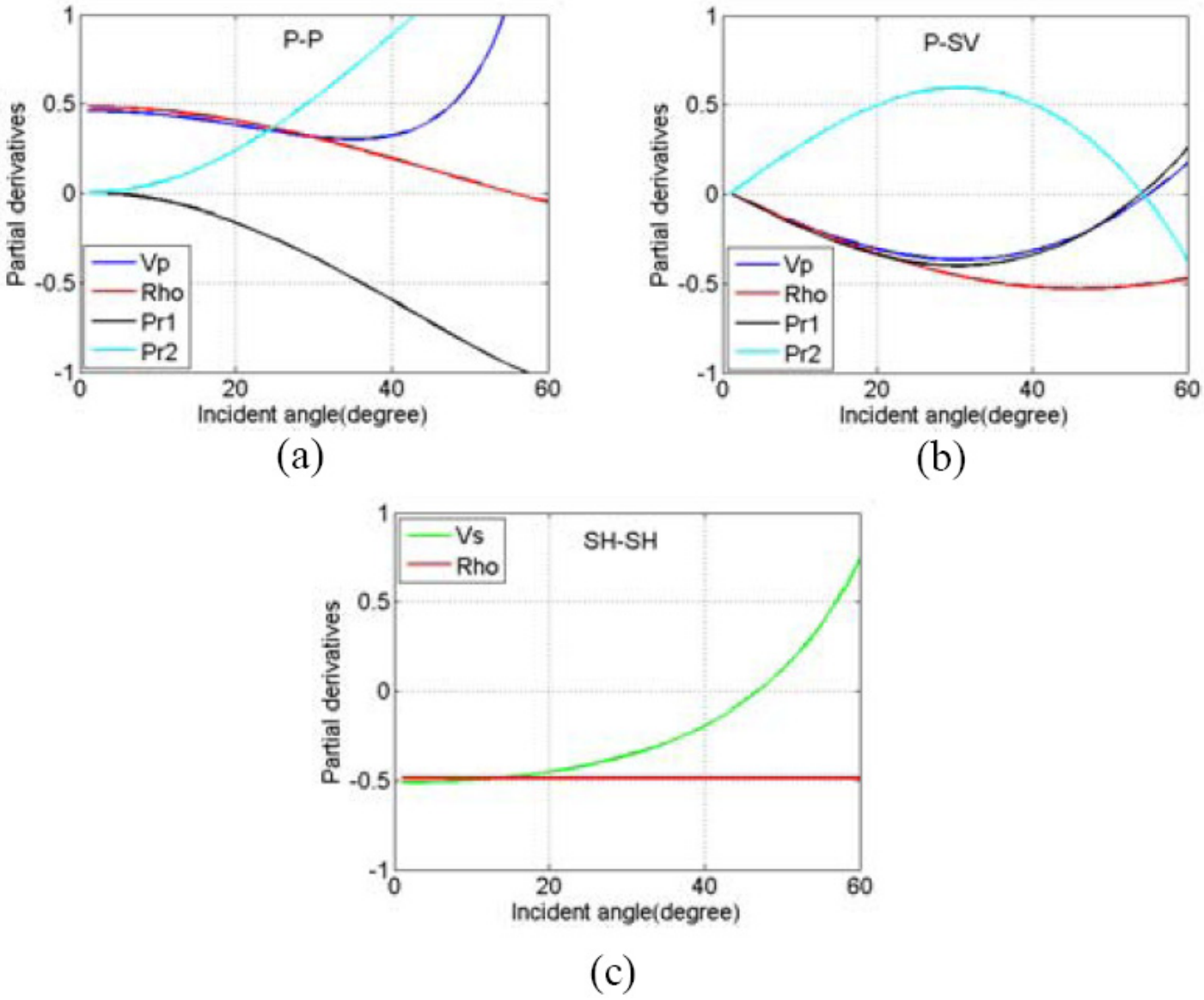

Figure 4.2: Sensitivities of MC seismic RCs (P-P (a), P-SV(b), and SH-SH (c) to contrast in P&S-wave velocities, in density, and Poission ratios at OWC. Sensitivity curves are displayed for contrast in P-wave velocity (in blue), contrast in S-wave velosity (in green), contrast in density (in red), and Poisson's ratios for both media (Pr1 for top layer in black, and Pr2 for bottom layer in ligh blue).

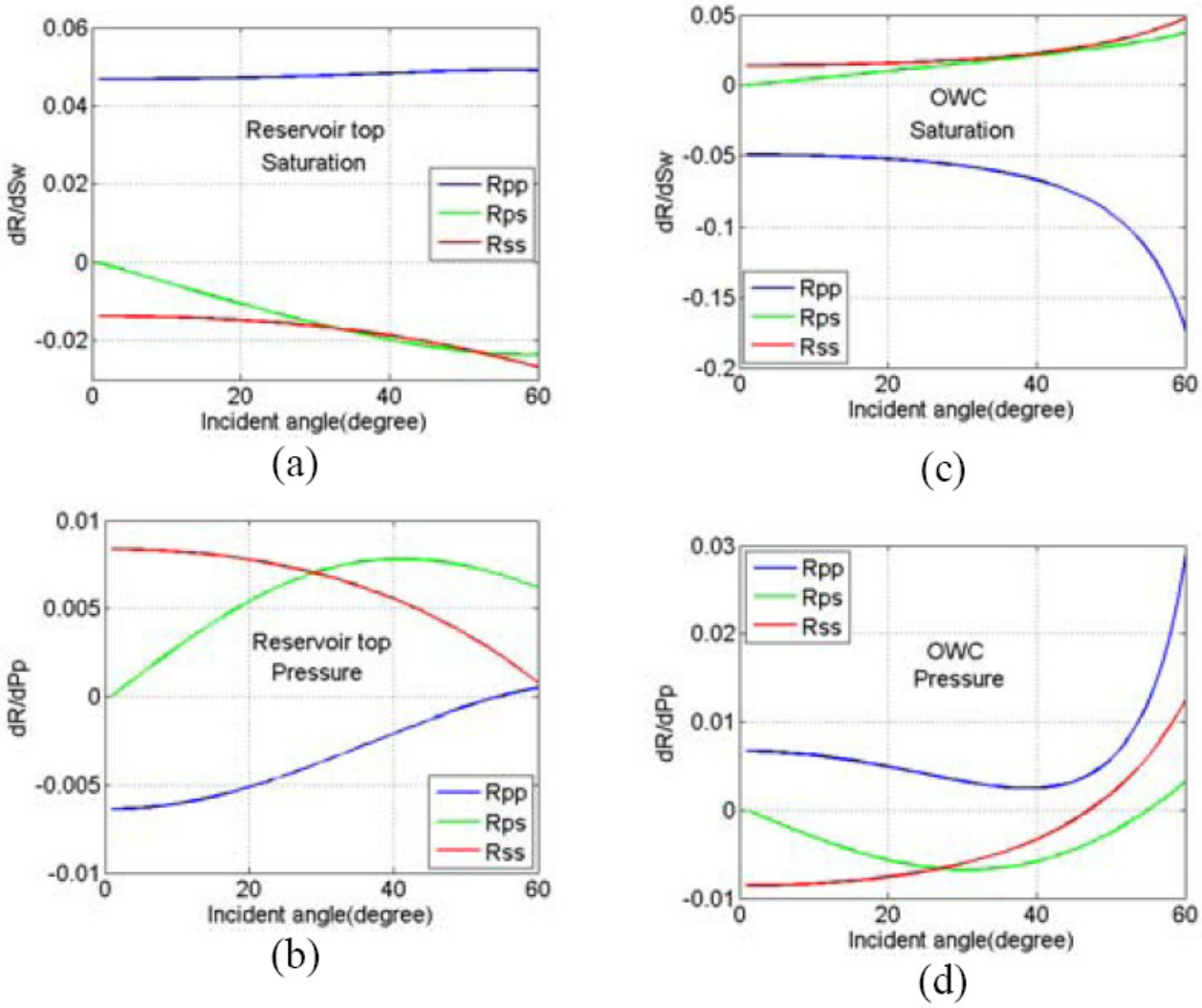

Figure 4.3: Sensitivities of MC seismic RCs to water saturation (a and c for reservoir top and OWC, respectively) and to pore pressure (b and d for reservoir top and OWC, respectively). Sensitivity of P-P (Rpp) is shown in blue, P-SV (Rps) in green, and SH-SH (Rss) in red.

Chapter five: Accuracy required in seismic modeling to detect production-induced time-lapse signals

This chapter is devoted to investigating the effect of different seismic modeling techniques in detecting changes in reservoir properties due to waterflooding. I construct a geological reservoir model with a meaningful spatial distribution of petrophysical properties. The reservoir model is then launched into a reservoir simulator to predict the spatial distributions of water saturation and pore pressure. Then, computed reservoir properties provide the necessary input parameters for rock physics model to generate seismic elastic parameters. The elastic model is inserted into a one-dimensional background elastic model. Finally, I employ different seismic modeling algorithms to simulate seismic wave propagation. A base and four monitor surveys are selected and the corresponding time-lapse signatures are analyzed.

5.1 INTRODUCTION

This chapter investigates the ability of different seismic modeling techniques to detect changes in reservoir properties due to waterflooding into a black oil reservoir. To do so, I simulate a poorly consolidated shaly sandstone reservoir model based on a prograding near-shore depositional environment. To account for the spatial distribution of petrophysical properties, an effective porosity model is first simulated by Gaussian geostatistics. Dispersed clay and dual water models are then efficiently combined with other well-known petrophysical correlations to consistently simulate the reservoirs.

Next, the constructed reservoir model is subjected to numerical simulation of multi-phase fluid flow to predict the spatial distributions of pore pressure and water saturation due to water injection into a black oil reservoir.

A geologically consistent stress-sensitive rock physics model, followed with modified Gassmann fluid substitution for shaly sandstones, is then utilized to simulate the seismic elastic parameters. Here, I insert the petro-elastic model into a one-dimensional background elastic model simulating the surrounding offshore sedimentary basin in which the reservoir was embedded. Finally, I employ different seismic modeling algorithms: one-dimensional (1D) acoustic and elastic ray tracing, 1D full elastic reflectivity, 2D split-step Fourier plane-wave (SFPW), and 2D stagger grid explicit finite difference, to simulate seismic waves propagated through the model and recorded at sea level and on the sea floor. A base and two monitor surveys associated with 5 and 10 years of waterflooding are selected and the corresponding time-lapse signatures are analyzed at different incident angles.

My analyses demonstrate that internal multiples behind the waterfront, flooded zones, partially subtract out in time-lapse differencing, so they are less significant in monitoring projects than that of reservoir characterization.

I also find that for time-lapse seismic modeling, acoustic modeling of an elastic medium is a good approximation up to ray parameter (p) equal to 0.2 sec/km or surface incident angle of 17 degrees. But, at p=0.3 sec/km (surface incident angle of 27 degrees), difference between elastic and acoustic wave propagation is the most dominant effect other than internal multiples and converted waves. Here, converted waves are generated with significant amplitudes compared to primaries and internal multiples.

I also find that time-lapse modeling of the reservoir using SFPW approach is computationally fast compared to FD, 100 times faster for my case here. It is capable of handling higher frequencies than FD. It provides an accurate image of the waterflooding process comparable to FD. Consequently, it is a powerful alternative for time-lapse seismic modeling.

5.2 BACKGROUND AND FORMULATION

In reservoir characterization, seismic reflectivity data have been extensively used to infer lithology and fluid characterization of subsurface rocks. More recently, time-lapse seismic surveying, repeated seismic surveys recorded at different calendar times over a depleting reservoir, is becoming one the most interesting applications for reservoir monitoring. The primary goal of time-lapse survey is to detect, estimate, and discriminate the changes in subsurface rock and fluid properties and ultimately to indentify flood fronts, preferential pathways, thief zones, and flow barriers, by-passed pay and infill targets. Depending on ambiguities in the description of the reservoir architecture, quality of the seismic data, and economic consideration of the subject field, seismic time-lapse interpretation can be performed at three different levels.

The first approach is the qualitative interpretation of changes in seismic observations, e.g., amplitude, traveltime, etc., and association of the changes in the seismic attributes to changes in reservoir parameters, e.g., porosity, saturation, pressure, temperature, etc. The qualitative interpretation of time-lapse seismic data has been addressed by numerous workers, Lumley et al. (1999), Marsh et al. (2001), and Behrens et al. (2002). Most of the authors mentioned that these objectives have been achieved and time-lapse seismic data have a positive impact on field development.

The more advanced methodology is to quantitatively interpret or invert changes in seismic observations and/or derived seismic attributes to changes in fluid saturation and pressure. This technique has been addressed by several authors in the literature. Some workers, e.g., Tura and Lumley (1999) and Cole et al. (2002), made use of inverted elastic parameters, e.g., acoustic and shear impedance changes, to indirectly estimate pressure and saturation changes. Others proposed schemes to directly invert time-lapse seismic data for fluid saturation and pressure changes (e.g., Landrø, 2001; Landrø et al.

2003; Angelov, 2004; Veire et al. 2006, and MacBeth et al. 2006). Shahin et al. (2009) proposed a methodology called seismic time-lapse crossplot to directly transfer changes in multicomponent seismic traveltimes and primary reflection coefficients to changes in saturation and pressure.

The third and most recent application of time-lapse seismic is referred to as seismic reservoir history matching. This currently state-of-the-art technology is a multi-disciplinary approach to integrate well logs, core analyses, production data, and time-lapse seismic reflectivity data aimed at updating reservoir model. Several case studies, e.g., Walker et al. (2006), have demonstrated that joint history matching of seismic and production data leads to a positive impact on the quality of the estimated reservoir parameters relative to estimates obtained from production history matching alone.

In all above technologies, detecting small changes in seismic traveltimes and amplitudes is the key to successfully imaging the changes in reservoir properties. Seismic data as recorded are not just composed of primary arrivals with elastic reflection coefficients: also included will be internal multiples, converted waves, diffractions, etc. The question for this study, are these other arrivals significant enough to interfere with an analysis based solely on primary reflection coefficients. In responding to this question, here I briefly explain the current state of seismic modeling as a fundamental tool to investigate the effect of changes in reservoir properties on seismic data.

Seismic modeling simulates the propagation of elastic waves in a specified medium. Application of seismic modeling in exploration seismology can be categorized into four main areas including seismic survey design and illumination studies, seismic data processing, interpretation, and inversion. In different applications and for the sake of simplicity, seismologists approximate inelastic, heterogeneous, anisotropic, and 3D earth

models with much more simpler models in dimension, e.g., 2D and 1D, and in properties, e.g., elastic, isotropic, and homogeneous.

There are several seismic modeling algorithms in seismology and they can be classified from various points of view. Accuracy, speed, and the range of wave phenomena that one seismic modeling algorithm can model, e.g., primary reflectors, multiples, converted waves, diffractions, head waves, critical reflections, etc., are some of the important factors in classifying seismic modeling approaches.

Currently, various approximate and hybrid seismic modeling algorithms are routinely used in academic and industrial projects. Here I summarize just a few of these methods.

5.2.1 Approximate seismic modeling methods

Ray theory is the cornerstone of many of the approximate methods. This theory consists of three fundamental parts including kinematic ray tracing, dynamic ray tracing, and polarization theory. Kinematic ray tracing describes the geometry and traveltimes of rays and wavefronts and it is governed by Snell's law. Dynamic ray tracing describes the geometrical spreading of rays and displacement magnitude. Finally, polarization theory describes the reflection and transmission coefficients, i.e., displacement direction, associated with interfaces in media (Chapman 2004). In approximate seismic modeling methods , these theories will be combined to simulate the propagation of elastic high-frequency, body waves or 'rays' approximately instead of solving the exact wave equation analytically or numerically. These methods are all well-proved to be computationally efficient and faster than most purely numerical methods, e.g., finite difference and finite element methods. One other salient features of the approximate method is their ability to isolate elementary waves, e.g. specific arrivals of reflected P-

and S-waves, multiples, etc. can be identified on synthetic seismograms. Nevertheless, they suffer from a lack of amplitude reliability when dealing with rapid changes in properties of the earth model. This is due to the fact that their formal validity criteria might be violated in complex geological models, e.g., sub-salt, gas cloud geology, and highly complex reservoir models of interest in time-lapse studies (Gjoystdal et al. 2007). Many other approaches have been proposed to overcome these difficulties by extending the standard ray theory: asymptotic or iterative ray theory, Maslov asymptotic ray theory, Quasi-isotropic ray theory, Born-scattering, Kirchhoff surface integral, Gaussian beam method (Cerveny 1982, Hill 1999), plane wave modeling (Stoffa et al. 2006). See Cerveny (2001) and Chapman (2004) for more references.

5.2.2 Analytical seismic modeling methods

Analytical methods solve the wave equations exactly for homogeneous and one-dimensional (1D) stratified media. In these methods, transformation of the wave equation is performed to reduce the partial differential equation to a set of first-order ordinary differential equations, solved using a propagator matrix method. The computation of propagator matrices generates a synthetic seismogram in a transformed domain, i.e., frequency-horizontal ray parameter. Finally, inverse transformation over ray parameter and frequency leads to the wavefield response of the stratified medium in the time-offset domain (See Kennett 1985 and Chapman 2004 for more detail). These algorithms are theoretically exact for 1D media because the multiples and mode-converted events are modeled.

5.2.3 Direct or purely numerical seismic modeling methods

To simulate the seismic response for an elastic complex earth model, one has to discretize the geological model into a finite number of grid points and then solve the

wave equation numerically. These methods have no restrictions on the spatial variation of the elastic properties being modeled and lead to very accurate results as long as sufficiently fine grids are employed (Carcione et al. 2002). However, these approaches are often computationally much more expensive than the approximate and analytical methods mentioned earlier; subsequently their usage is very specialized to complicated models, e.g., sub-salt and sub-basalt imaging, and detailed reservoir characterization and monitoring.

Recently, finite difference (FD) and finite element (FE) have become the main methods used to numerically simulate seismic data. FD methods, e.g., Levander (1988), are limited to regular grid implementations. On other hand, FE methods with flexible grid implementations, e.g. spatially variable triangular meshing, are more powerful than FD for including structural details. However, obtaining accurate results with flexible and fully unstructured triangular grids from FE methods is costly, especially for 3D structures mainly due to the representation of irregular grids in computer memory. In addition, geological interfaces are not well defined as engineering interfaces; subsequently, FE are best suited for engineering problem and FD is the method of choice for seismic wave propagation in exploration geophysics (Carcione et al. 2002).

In general, numerical artifacts, stability, and accuracy are the main concerns when discretizing wavefields via FD. To reduce the numerical artifacts, some researchers recommend computing the spatial derivatives of the wavefield using the pseudo-spectral Fourier (PSF) method (Chu and Stoffa, 2008). In addition to improve the accuracy of the derivative operators that are applied to the wavefields, PSF can be used on relatively coarser grids because it is accurate up to the nyquist frequency. This can help to save both disk and memory storage especially for 3D models.

The other numerical approximation of FD is to calculate the temporal or time derivatives of the wavefield. It is a common practice to calculate this part using the second order FD operator (Levander, 1988). This method is called explicit FD. It is also possible to calculate temporal derivatives of wavefield via Fourier transform, i.e., implicit FD. This technique leads to a linear system of equations which can be solved either directly by inverting a huge matrix of FD stencil or indirectly via iterative approaches. Recently, Stoffa and Pestana (2009) have introduced a new approach for marching in time for FD forward modeling. In this approach, wavefields can be advanced in time in one large time step and because of this capability is named Rapid Expansion Method (REM). They confirmed by numerical examples that the REM for time stepping combined with the PSF for the spatial derivatives leads to numerically stable results with less computational effort compared to a conventional FD time stepping method for the same level of accuracy.

5.2.4 Hybrid seismic modeling methods

Considering all the benefits and restrictions of these three seismic modeling (approximate, analytical, and numerical) methods, the next logical approach would be a hybrid approach providing fast and flexible modeling to handle complex geological models and having enough accuracy to be employed in seismic reservoir characterization and monitoring work flows.

Many papers address this concept for time-lapse seismic modeling by simulating a single seismic modeling for the overburden and conducting a set of repeated computations of seismic waveforms at the reservoir zone aimed at simulating the corresponding base and monitor surveys. Lecomte (1996), Gjotdal et al. (1998), and Hokstad et al. (1998) combined ray tracing in the overburden with repeated FD seismic

modeling in the reservoir zone. Robertson and Chapman (2000) deployed a similar approach by applying FD seismic modeling in both the overburden and target to allow for strongly scattering heterogeneities of the entire model. Kirchner and Shapiro (2001) used FD to simulate wave propagation in the overburden and employed Born perturbation theory to compute the production-induced changes in time-lapse seismograms.

Here, I employ a recently-developed petro-elastic model (See chapter 2 for details) and use seismic modeling techniques with different degrees of accuracy, including: 1D acoustic with and without internal multiples, 1D elastic without internal multiples, 1D full elastic reflectivity, SFPW(described below in section 5.4.2), and staggered grid explicit FD. Next, I investigate the reservoir-scale effects of internal multiples, acoustic vs. elastic, or the effect of converted waves, dimension of wave propagation (2D vs. 1D), and diffractions on time-lapse signatures. In addition, I demonstrate that the time-lapse response simulated with SFPW is closely correlated with the FD response but considerably faster to compute. Having superior speed to FD, the ability to model higher frequencies than FD, and yet comparable with FD and better than standard ray-based modeling, SFPW is the preferred method for reservoir characterization and monitoring workflows.

5.3 CONSTRUCTING A SYNTHETIC PETRO-ELASTIC RESERVOIR MODEL

5.3.1 Geological reservoir model

A stacked sand-rich strandplain reservoir architecture has been considered in this study to simulate a realistic geological framework. Strandplains are mainly marine-dominated depositional systems generated by seaward accretion of successive, parallel beach ridges welded onto the subaerial coastal mainlands. They are inherently progradational features and present on wave-dominated microtidal coasts (Tyler and

Ambrose 1986; Galloway and Hobday 1996). This sand-rich beach-ridge reservoir architecture is intended to be originally deposited as a clay-free geobody. However; due to post-depositional diagenesis, dispersed clay is produced and it is the main factor reducing porosity and permeability of the reservoir. Figure 5.1 displays a three dimensional distribution of effective porosity generated using a Gaussian Simulation technique. This model, called SPE comparative solution project, is a large geostatistical model widely used in research on upgridding and upscaling approaches (Christie and Blunt, 2001). I select the top 35 layers of the model which is representative of the Tarbert formation, a part of the Brent sequence of middle Jurassic age and one of the major producers in North Sea. By changing the grid size and imposing smoothness, I modify this model to meet the objectives of this research. Next, I will assign geologically consistent petrophysics information and add facies characterization to develop a more realistic reservoir model comparable to complicated models in the petroleum industry. The model is described on a regular Cartesian grid. The model size is 220*60*35 in X (east-west), Y (north-south), and Z (depth) directions, respectively. The grid size is 10*10*10 meters, so the model dimensions are 2200m by 600m by350m.

5.3.2 Petrophysics model

The geological model described above is used as the basic model in which petrophysical properties are populated assuming a meaningful petrophysics model. Here, the effective porosity model is first generated using Gaussian geostatistics and shale content and total porosity models are then computed assuming a dispersed clay distribution (Thomas and Stieber 1975; Marion et al. 1992), (Figure 5.2a). Horizontal permeabilities in the X and Y directions are equal and calculated based on the extension of the dispersed clay model to permeability introduced by Revil and Cathles 1999 (Figure

5.2b and 5.2c). Next, I should initialize the reservoir for water saturation and pore pressure. An experimental correlation (Uden et al. 2004; Spikes et al. 2007) between water saturation and shale content is combined with the dual water model (Best 1980; Dewan, 1983; Clavier, 1984) to compute clay bound water (Swb), effective water saturation (Swe), total water saturation (Swt), and oil saturation (So) (Figure 5.2d). Initial reservoir pore pressure is simulated assuming a linear hydrostatic gradient from the top to the bottom of the reservoir. Figure 5.3 summaries the distribution of petrophysical properties for a 2D cross section in the middle of the 3D reservoir.

5.3.3 Reservoir simulation

Fluid flow simulation combines three fundamental laws governing fluid motions in porous media. These laws are based on conservation of mass, momentum, and energy (Aziz and Settari 1976). In this research, a 2D cross section in the middle of the 3D reservoir is selected. Then, a commercial finite difference reservoir simulator, Eclipse 100, is utilized to replicate a waterflood enhanced oil recovery on a black-oil 2D reservoir containing oil, soluble gas, and water. The reservoir has no water drive. In addition, because of the high pressure conditions no gas is produced in the reservoir. Thus, prior to waterflooding solution gas is the only drive mechanism forcing oil to be produced. This drive is so weak that implementation of water injection is required to enhance oil recovery.

The same grid block dimensions used to generate the geological model, i.e. 10 by 10 square meters, are used to simulate fluid flow and seismic modeling; hence mathematical upscaling and/or downscaling was not necessary.

For a period of 10 years, the waterflood schedule is simulated by using two injectors at the corners and one producer in the middle of the reservoir. In this period,

saturations and pressures values for each reservoir grid block are exported after each year. Collecting this database allows us to analyze the sensitivity of the corresponding seismic data to a wide range of changes in fluid saturation and pressure.

5.3.4 Rock and fluid physics model

Rock and fluid physics modeling is the link between quantitative seismic interpretation, geology, and reservoir petrophysics. Using rock physics modeling, one can transform the petrophysical properties of a reservoir to seismic elastic parameters (Avseth et al. 2005) which can be further used to simulate seismic reflectivity data.

Combining the Dvorkin-Gutierrez rock physics model (2002), with the fluid physics model (Batzle & Wang 1992), and using a modified Gassmann theory (Dvorkin et al. 2007), I were able to observe the joint effects of various petrophysical properties on elastic seismic parameters including P-and S-wave velocities, and density. Consequently, the comprehensive petro-elastic model can be efficiently utilized in sensitivity analysis of seismic data to changes in reservoir properties due to production. See chapter two for details and further applications of the petro-elastic model.

Figure 5.4 shows the distribution time-lapse normalized percentage changes in effective water saturation, pore pressure, and the associated changes in seismic acoustic impedance (AI), and shear impedance (SI) between different base and monitor survey. Here, changes in elastic parameters, saturation, and pressure for the base survey (before waterflooding) are subtracted from those of the monitor survey (after waterflooding) and then normalized using those of the base survey, i.e., $\Delta\alpha = \frac{\alpha_{monitor} - \alpha_{base}}{\alpha_{base}} * 100$ where α denotes any elastic or petrophysical parameter. As observed, the percentage of change in pore pressure (Pp) is lower than of that of the water saturation (Sw). Furthermore, the pressure front propagates very fast, but the waterfront has a mass bulk movement and

moves slowly. Time-lapse associated with the first 5 years of waterflooding (left column), is mainly affected by saturation changes rather than pressure. On the other hand, two other time-lapses between monitor survey after 5 years and monitor survey after 10 years (middle column), and between base survey and monitor survey after 10 years (right column) are jointly affected with saturation and pressure. Due to the high sensitivity of AI to Sw based on the Gassmann theory, all time-lapses show a clear mapping between these two attributes. The same, but less clear, mapping can be observed between SI and Sw. This is because of low sensitivity of SI to Sw and it is mainly a density effect. Based on the rock physics model, I expect to see an obvious transformation between SI and Pp, but that is not the case here because of joint effect of Sw and Pp. In other words, the saturation effect masks the pressure effect. I might be able to follow the effect of Pp on SI, only in places of the reservoir that are least affected by Sw, e.g., lower left corner of the reservoir in left column (Time-lapse associated with the first 5 years of waterflooding). See chapter two for more detail on separation of saturation and pressure.

The corresponding petro-electric model for the reservoir can be efficiently simulated by combining the Thomas and Stieber petrophysics model (1975), dual water rock physics model (Best 1980; Dewan, 1983; Clavier, 1984), and Arps' empirical equation (Arps, 1953). The joint modeling of the elastic and electrical properties of reservoir rocks will lead to the consistent forward modeling algorithms for joint inversion of seismic and electromagnetic (EM) data. Further applications of using the petro-electric model will be presented in Chapter six where a time-lapse frequency domain CSEM (controlled-source EM) feasibility study over the 2D reservoir model is simulated (See Chapter six for detail).

5.4 SEISMIC MODELING

Here I explore the use of 1D and 2D seismic modeling and their effects on the time-lapse signatures associated with waterflooding into a black oil reservoir. To do so, the developed petro-elastic model are embedded into a 1D background elastic model simulating surrounding offshore sedimentary basin in which the reservoir is buried (Figure 5.5). The background model has dimensions of $600 \times 1 \times 300$ in length, width, and depth respectively. The grid size is the same as the reservoir model $10 \times 10 \times 10$ m^3. The first one kilometer of the model is sea water. The reservoir is injected at a depth of 2000 m of the background model and sandwiched between an ash and salt layers at top and bottom, respectively. These two markers help to track the reservoir on various seismic responses. The edges of the reservoir are smoothed by a linear interpolation scheme to better blend with the background model.

5.4.1 One-dimensional seismic modeling

The most widely used earth model in petroleum exploration is a horizontally-stratified model representing a typical sedimentary basin in which a reservoir is buried. The corresponding approach to computing the seismic response in such a media is called one-dimensional seismic forward modeling and is well studied in the open technical literature, e.g., Kennett (1985) and Chapman (2004).

In this chapter, I utilize 1D modeling approach to simulate pre-stack seismic data in the intercept time and horizontal ray parameter domain, called $\tau - p$. The first modeling approach is to simulate acoustic wave propagation without internal multiples. Here, the frequency domain is used to construct a primaries-only wavefield, i.e., acoustic P-P reflection coefficients, for all depth levels in the 1D model. The intercept times are calculated by 1D ray tracing. After collecting the wavefield at all desired frequencies for each ray parameter being simulated an inverse 1D Fourier transform over frequency is

applied to obtain the wavefield in intercept time. The outermost loop in the algorithm is over horizontal ray parameter (p), allowing us to generate data for all the ray parameters of interest.

The second modeling approach is to simulate acoustic wave propagation with internal multiples. Similar to the above method, the primary wavefield is simulated and internal multiples are also simulated by including a recursive term for each layer into the frequency domain equations (Kennett, 1985).

The third algorithm simulates elastic wave propagation without internal multiples. Here, full Zoeppritz equations to compute elastic P-P reflection coefficients and 1D ray tracing to calculate intercept times, are employed.

The ultimate 1D modeling option is to generate the full elastic reflectivity response of the stratified media. The corresponding seismic response is theoretically exact for 1D media because the internal multiples and mode-converted events are modeled (See Kennett, 1985 and Chapman, 2004 for more detail).

To simulate the production-induced seismic response of the reservoir, I implement a locally 1D modeling over the 2D reservoir models associated with a base and two monitor surveys after 5 and 10 years of waterflooding. As mentioned earlier, my 1D modeling methods generate seismic data in $\tau - p$ domain. Figure 5.6 displays plane-wave response of the 1D locally model in the middle of the 2D reservoir for the base survey (T0). The $\tau - p$ response is simulated by full elastic reflectivity algorithm for a flat frequency range of 0 to 75 Hz. Markers on the seismic data show significant events associated with 2D model in Figure 5.5. To evaluate the full range of pre-stack data, I select four ray parameters of 0.0, 0.10, 0.20, and 0.30 sec/km. These ray parameters are associated with different incident angles at sea level and at the reservoir top. Using 1D ray tracing equations, I also compute the corresponding intercept times, offsets, and

traveltimes for the selected ray parameters and up to the reservoir top. Table 5.1 summarizes the geometry of data to be selected for further analysis. For the rest of the analysis of 1D seismic responses of the reservoir, I will concentrate on a time window from reservoir top to bottom. This window has a fixed interval, but its starting level is ray parameter-dependent. This scheme allows one to analyze the raw seismic data without any seismic data processing, e.g., normal moveout correction; consequently, the time-lapse signatures will be preserved. This is important to compare time-lapse signature using various plane-wave seismic modeling in $\tau - p$ domain and also consistent with my further analysis in offset-traveltime domain for finite difference data to be discussed later. The 1D plane-wave seismic modeling is carried out for a flat frequency range of 0 to 75 Hz and recorded at all 600 horizontal grid positions (every 10 m) at sea level. Finally, a normalized derivative of a Gaussian wavelet with a peak frequency of 35 Hz is convolved with data (Figure 5.7). The same wavelet will be convolved with 2D plane-wave and used, as a source, to simulate 2D finite difference data to be discussed later.

Due to the fact that my 1D modeling algorithms are generated using different numerical methods, I expect to have slightly different amplitude scales. To overcome this problem I use the sea floor amplitude as a tuning parameter and scaled data accordingly. Form the physics of the seismic modeling, I expect to have the same response from 1D acoustic without multiples (called method 1DAp; A stands for Acoustic and p stands for primary) and 1D elastic without multiples (called method 1DEp; E stands for Elastic) at zero ray parameter. In addition 1D full elastic reflectivity algorithm (called method 1DEpmc; m, and c stand for internal multiples and converted waves, respectively) should converge to 1D acoustic with multiples (called method 1DApm) at p=0, because no converted wave is generated. Figure 5.8 illustrates the scaling scheme employed in this study for a single trace in the middle of the 2D reservoir. Method 1DEpmc perfectly

coincides on 1DAm for the entire survey (not shown here). However, this is not the case between 1DAp and 1DEp (the second panel in Figure 5.10). This is explained by the fact that I use a time-domain modeling, 1D ray tracing algorithm to compute 1DEp and a frequency domain method for 1DAp. In other words, numerical differences between these two algorithms lead to a minor difference between these two surveys, but this will not affect my analyses as long as I are aware of its existence.

Figure 5.9 shows the plane-wave responses of different modeling methods computed for base survey (T0) at p= 0 sec/km. I only display the reservoir zone in both temporal and lateral axes. The reservoir response looks very realistic with all the complicated structures inherent in actual petroleum reservoirs. This is mainly because of spatial distributions of and correlations between reservoir properties used in the developed petro-elastic model. Comparing both 1DAp and 1DEp, by introducing the internal multiples in 1DApm and 1DEpmc tends to attenuate primary amplitudes. As mentioned above, 1DEpmc data is scaled to 1DAm, so these two data sets are exactly the same for the entire base and monitor surveys at p= 0. The same statement is true for 1DEp and 1Dap. However, there are minor numerical differences between these two data sets as explained above.

To highlight the effects of internal multiples, acoustic versus elastic wave propagation, and converted waves, I will display the residual sections associate with different seismic modeling techniques. Figure 5.10 shows the residual between the plane-wave responses shown in Figure 5.9 for base survey (T0) at p= 0 sec/km. The first panel is the residual between 1DAp and 1DApm, and one can clearly see the internal multiples created in reservoir zone. Some of the coherent and linear ones may be generated due to contrast at reservoir top or even ash layer above the reservoir (See Figure 5.5). The minor ones may be generated due to the local big contrasts within the reservoir. The second

panel displays the residual between 1DEp and 1DAp, and as expected this is almost zero everywhere because no difference exists between elastic and acoustic wave propagation at p= 0. The third panel illustrates the residual between 1DEp and 1DEpmc. Similar to panel one, internal multiples are the residual, but this time they are computed by full elastic reflectivity algorithm. Similarities between panels 1 and 3 confirm that my modeling algorithms are consistent. The last panel in this figure indicates the effect of converted waves. This panel is computed from the residual of the first and third panel. The common terms in these two panels, primary and internal multiples subtract out, so the remainder can be a first order approximation of the converted waves, if any. I emphasize that this is only an approximation because internal multiples computed from 1DApm and 1DEpmc are not necessarily the same due to the internal multiples of converted waves not model by 1DApm. There is no converted wave at p= 0, so the last panel must be zero everywhere. This isn't the case here as mentioned earlier due to numerical error propagated from differences between two algorithms of 1DAp and 1DEp. Consequently, panels 2 and 4 are similar.

Figures 5.11 to 5.13 show the same kind of residual sections, as Figure 5.10, between plane-wave responses for base survey (T0) and for p= 0.1, 0.2, and 0.3 sec/km, respectively. The goal here is to investigate the effect of internal multiples, elastic vs. acoustic wave propagation, and converted waves at larger ray parameters. The same events on the p=0 section appear at earlier intercept times at larger ray parameter. This is because of elliptical trajectories in $\tau - p$ domain. In general, internal multiples, converted waves, and elastic effects are more observable at larger ray parameters, however; this is not a linear relationship. At p= 0.1 sec/km, elastic and acoustic wave propagation types are approximately similar to p=0. Converted waves are not generated. At p=0.2 sec/km, I start seeing some noticeable differences between elastic and acoustic

wave propagation. This effect is more significant than internal multiples in some parts of the reservoir, e.g., coherent peak event at upper right indicated in red. At p=0.3 sec/km, differences between elastic and acoustic wave propagation is the most dominant effect. Here, converted waves are generated with significant amplitudes compared to primaries and internal multiples. At p=0.2 and 0.3 sec/km, there are coherent horizontal events in the last panel. They are expected to be converted waves, but they are residual of internal multiples modeled by 1DEpmc but not modeled by 1DApm algorithm.

The above observations based on the simulating different seismic modeling for the base survey (T0), confirms that modeling of internal multiples matters in seismic reservoir characterization projects. They are small at p= 0 sec/km but nonetheless observable. The larger the ray parameter, the higher the amplitude of the internal multiples. The acoustic wave propagation is a good approximation to model a 1D elastic medium up to p=0.1 sec/ km. However, this assumption is not valid beyond p=0.1 sec/km. Finally, converted waves are rarely produced between p=0. and p=0.2 sec/km, so a primary plus multiples analysis only should be enough in this ray parameter range. Converted waves are significant beyond p=0.2 sec/km and their ignorance may seriously impact my analyses.

The key question for this study is whether or not the same statements are true in reservoir monitoring projects. In other words, can I show that internal multiples and converted waves are less important in time-lapse seismic modeling because they subtract out between the base and monitor survey, so a primary wavefield analysis should be enough. To investigate this hypothesis, I repeat the experiment for one set of time-lapse.

Figure 5.14 shows the plane-wave responses of different modeling methods computed for time-lapse (T5-T0), associated with the base and the monitor survey after five years of waterflooding, at p= 0 sec/km. By comparing to Figure 5.4, one can easily

track waterfront location and distinguish between the virgin areas and flooded zones at the back of waterfront. As expected, 1DAp and 1DEp are the same because there is no difference between acoustic and elastic wave propagation at p=0.0 sec/km. Also, 1DEpmc and 1DApm are similar because of the lack of converted waves at zero ray parameter.

Figures 5.15 to 5.18 show the residuals between time-lapse surveys computed by different seismic modeling algorithms for p=0.0, 0.1, 0.2, and 0.3 sec/km, respectively. In other words, a set of base and monitor surveys are first computed by, say, algorithm A, and then computed by algorithm B. If I subtract these two time-lapse surveys I should be able to track differences in fluid flow detection as simulated by various seismic modeling algorithms. Similar to the base survey in Figure 5.11 to 5.13, internal multiples, converted waves, and elastic effects are more observable at larger ray parameters. At p=0.0 sec/km, internal multiples in unflooded zones areas completely cancel out each other. Internal multiples in the back of waterfront, flooded zones, partially subtract out and they are less significant than those of the base survey in Figure 5.10. As discussed earlier, the second and third panels are supposed to be zero, but they are not due to numerical differences between algorithms 1DEp and 1DAp. At p= 0.1 sec/km, elastic and acoustic wave propagation types are approximately similar to p=0. Converted waves are not generated. At p=0.2 sec/km, I start seeing some noticeable differences between elastic and acoustic wave propagation. However, these differences are not as significant as the base survey in Figure 5.12. That is, for time-lapse, acoustic modeling of an elastic medium is good approximation up to p=0.2 sec/km. At p=0.3 sec/km, differences between elastic and acoustic wave propagation once again becomes the most dominant effect. Here, converted waves are generated with significant amplitudes compared to primaries and internal multiples.

I emphasize that all internal multiples, elastic vs. acoustic modeling and converted waves show time-lapse signatures at the back of the waterfront. These time-lapse signatures are less noticeable at p=0.0 and 0.1 sec/km, but they are significant beyond p=0.2 sec/km.

5.4.2 2D seismic modeling

One-dimensional seismic modeling is an accurate approach for modeling layered sedimentary basins. Many sedimentary basins, however, are so structurally complicated that they can not be modeled by 1D modeling algorithms. In addition to the complexity of overburden of the petroleum reservoirs, the fluid flow phenomena itself has a 3D nature, so seismic time-lapse modeling has to be carried out using 3D or at least 2D modeling algorithms and compared against 1D responses. By doing so, I can highlight the differences in modeling for time-lapse purposes. To address this problem, many forward modeling approaches, ray theory, integral equations, finite difference, finite element, etc., can be utilized to evaluate numerical approximations of wave equations (See Carcione et al. ,2002 for an overview on seismic modeling methods).

In this chapter, I utilize two seismic modeling techniques, a semi-analytical method based on plane-waves originally used in split-step Fourier migration (Stoffa et al. 1990) and a purely numerical approach, staggered grid explicit FD (Levander, 1988).

Stoffa et al. (1990) developed split-step Fourier migration to migrate zero-offset seismic data. The method is an extension of Gazdag's phase shift migration to handle lateral velocity variations. In their method, a 3D slowness model is first decomposed to a 1D, depth-dependent, mean slowness and a perturbation term representing the local variability of slowness. Downward continuation of the wavefield across each depth interval by performing a global phase shift using the mean slowness in the frequency-

wavenumber domain is followed by a local phase shift based on the slowness perturbation component in the frequency-space domain. The extension of this method to accommodate pre-stack seismic imaging is reported in open technical literature, e.g., Stoffa et al. (1990b), Tanis et al. (1998), etc. However, the use of this algorithm as a seismic forward modeling has not yet been published. Here in this chapter, I first explain the algorithm and then apply it on several 2D geological models associated with a base and two monitor surveys.

The Split-step Fourier plane-wave (SFPW) seismic modeling algorithm is described schematically in Figure 5.19. Initially full elastic reflection coefficients are computed for the geological model. For each depth interval and in space-frequency domain wavefield is updated by applying a local phase shift accounting for local variability of slowness component. Next, the wavefield is transformed into wavenumber domain where a global phase shift associated with mean slowness of the depth interval is performed in frequency-wavenumber. The wavefield is then back-transformed into space-frequency domain. After collecting all frequencies, the wavefield is transformed to intercept time. The entire process can be repeated to obtain the wavefield at different ray parameters allowing one to simulate pre-stack seismic data in the $\tau - p$ domain.

The salient features of SFPW are as follows:

- Full elastic P-P reflection coefficients are utilized in acoustic wave equation, leading to an accurate approximation of the wavefield in complex geological models with low to moderate lateral variations. Shear amplitude loss is accounted for by using the Zoeppritz equations to define the P-wave reflection coefficients.
- Computational time of SFPW is very low and it can simulate, in a reasonable time, seismic data over 2D and 3D geological models of

interest in petroleum industry. Modeling can be performed over a few ray parameters and over any desired frequency range, giving more flexibility and speed. In addition, it is naturally parallelizable over ray parameters and over frequencies. Finally, it is possible to move down to the target in one or several large steps using the average slowness of the corresponding depth interval. In marine seismic modeling, it is possible for example to model the water column in one large step.

- Internal and surface multiples can be either included or excluded from the computations.
- Diffractions are an internal part of the modeling, making SFPW a superior algorithm to locally 1D seismic modeling methods.
- Having superior speed to FD, and the ability to model higher frequencies than FD, SFPW is a good a candidate for seismic reservoir characterization and monitoring workflow.

I carry out 2D plane-wave seismic modeling using in-house SFPW code, called PW3D. To be consistent with 1D plane-wave modeling discussed earlier, a flat frequency range of 0 to 75 Hz is simulated and data were recorded at all 600 horizontal grid positions (every 10 m) at sea level at the top of 2D geological models associated with a base and two monitor surveys after 5 and 10 years of waterflooding. Finally, a normalized derivative of a Gaussian wavelet with a peak frequency of 35 Hz is convolved with the data (Figure 5.7). Similar to 1D analyses, four ray parameters of 0.0, 0.10, 0.20, and 0.30 sec/km are selected. These ray parameters are associated with different incident angles, intercept times, offsets, and consequently traveltimes for the reservoir top (Table 5.1).

Figure 5.20 shows the plane-wave responses for base survey (T0) and time-lapse (T10-T0), associated with the base and the monitor survey after ten years of water flooding, at p= 0 sec/km. The first and the third panel are associated with 1DEp modeling and the second and forth panels are computed by SFPW algorithm, called 2DEp. In this algorithm I can optionally include or exclude internal multiples. Here, to be consistent with 1DEp, I exclude internal multiples. 2DEp data is scaled to 1DEp by tuning the sea floor amplitude. The most obvious difference between 1D and 2D elastic modeling are the diffractions; they can be generated at reservoir edges and also at scatter points inside the reservoir. The diffractions contaminate the region outside the reservoir as well as inside; this is why the inside is so different from 1DEp. One may argue that migration of the 2DEp data results in 1DEp data. That may be the case, but it is out of scope of this study. Diffractions for the time-lapse partially subtract out, but not completely. This is because of the fact that diffractions for the base survey (T0) and monitor survey (T10) have some common parts, but they are a bit different as reservoir properties are different.

Figure 5.21 and Figure 5.22 show 2DEp (primaries) and 2DEpm (primaries and internal multiples) at p= 0 sec/km for base survey (T0) and time-lapse (T10-T0), respectively. One can easily see that internal multiples not only cancel out each other in the virgin areas, but also they subtract out in flooded zones, so they are not a problem in the time-lapse analysis for small ray parameters. However, as demonstrated in 1D analyses, the internal multiples will be more pronounced at larger ray parameters.

The final seismic modeling technique employed in this study is a purely numerical approach, staggered grid explicit finite difference, FD, (Levander, 1988). For this part, I utilize in-house code called FDPSV. A 2^{nd}-order operator in time and 4^{th}-order in space are used in a staggered grid scheme. The program will generate elastic waves for multiple source activations and the data can be collected for each source

activation at multiple receiving arrays each having multiple detectors. Vertical and horizontal velocity, tractions and pressure data can be recorded at each detector as required. This scheme makes it possible to acquire multi fold surface data and downhole data simultaneously and to simulate the shooting of a seismic line. Snapshots of the wavefield can also be generated to monitor the waves as they propagate through the medium.

The geological models associated with different production time steps, are tapered at the sides and the tops to attenuate artificial artifacts. In addition, models are extended at all sides to prevent backscattering waves from boundaries. For each geological model, 521 shots are acquired. Each shot position is evenly distributed at sea level located at the top of the models and spaced 10 meters apart, equal to grid size used in flow simulation. The pressure wavefield are recorded at 521 surface hydrophones at the sea level. Simultaneously, 521 OBS (Ocean Bottom Seismogram) at sea floor, one kilometer beneath the sea level, acquired vertical & horizontal velocity, and pressure wavefields. All receivers were evenly distributed across the sea level and sea floor and spaced 10 meters apart. To satisfy stability conditions given by $\alpha = \frac{C_{\max}\Delta t}{\Delta x} \le \frac{\sqrt{2}}{\pi}$, and considering $\Delta x = \Delta z = 10m$, $C_{\max} = 4600\, m/\sec$ for the salt layer beneath the reservoir, I employ $\alpha \le 0.2$ (as recommended by Kosloff and Baysal (1982)), which results in $\Delta t \le 0.4ms$. Having computed the sample rate $\Delta t = 0.4ms$, the maximum frequency to be recovered in seismic modeling without numerical dispersion, aliasing, is calculated using $f_{\max} \le \frac{C_{\min}}{2\Delta x}$ and taking $C_{\min} = 1500\, m/\sec$, water velocity at the top of the model. The computed $f_{\max} = 75Hz$ leads to choose the normalized derivative of a Gaussian wavelet with a peak frequency of 35 Hz, as a source (Figure 5.7).

Figures 5.23 and 5.24 illustrate finite difference response for a shot gather and an OBS gather, respectively, located in the middle of 2D reservoir for base survey (T0). Pressure wavefield on shot gather and horizontal velocity on OBS gather are displayed. Markers on the seismic data shows significant events associated with 2D model in Figure 5.5.

Figure 2.25 compares the 2D plane-wave response (2DEpm at p = 0.0 sec/km) and finite difference responses (2DEpmc) of the base survey (T0) at zero offset, x = 0.0 km. These two data sets are inherently different because FD data has a cylindrical spreading divergence, but 2DEPm doesn't. In addition, my FD operator is an approximation of the derivatives of the wavefield in time and space. Finally, numerical dispersion and artifacts, common drawbacks of FD methods, are the other main difference between the FD and SFPW data. Consequently, one interested in making these two data sets identical for quantitative comparison first needs to remove the 2D cylindrical spreading and correct FD to a true plane wave response by taking the appropriate plane wave transform of the FD data. In addition, I would need to use an FD operator accurate to the nyquist in space and time to get a response similar to the plane-wave algorithm. For an improved spatial response, one may consider pseudo-spectral Fourier (PSF) method (Chu and Stoffa, 2008) which helps to reduce numerical dispersion. These steps are out of scope of this study.

For my purposes I simply scale these two data sets by dividing each by its own maximum absolute value. This allows us to compare these data qualitatively. After scaling, most of the important features can be mapped between the two data sets. The main differences are in the arrival times and the dispersion in the FD data. The arrival times of the SFPW data is less accurate than FD because of the 1D with small later

variation assumption. But, the dispersion in the FD split most of events and seems to be the most serious problem for matching the two data sets.

Figure 2.26 compares the 2DEpm and 2DEpmc of the base survey (T0) at p=0.0 sec/km and for two monitor surveys associated with 5 and 10 years of waterflooding. As expected, due to subtraction the time-lapse response of SFPW and FD match better than the corresponding base surveys. This confirms that SFPW is able to model time-lapse responses of a complicated reservoir similar to the petro-elastic model very well and leads to comparable results as FD, but retains higher frequencies and is computationally much faster (a factor of 100 for my modeling).

5.5 SUMMARY AND CONCLUSIONS

The geologically consistent petro-elastic model employed here provide an opportunity to evaluate the effect of various seismic modeling techniques on a realistic reservoir model and investigate the corresponding time-lapse signatures due to waterflooding into a black oil reservoir. My analyses demonstrate that internal multiples in the back of waterfront, flooded zones, partially subtract out, so they are less significant in monitoring projects than reservoir characterizations.

I also find that for time-lapse seismic modeling, acoustic modeling of an elastic medium is a good approximation up to p=0.2 sec/km. In addition, at p=0.3 sec/km, differences between elastic and acoustic wave propagation is the most dominant effect. Here, converted waves are generated with significant amplitudes compared to primaries and internal multiples.

I also show that time-lapse modeling of the reservoir using SFPW approach is very fast compared to FD, 100 times faster for my case here and it is capable of handling higher frequencies than FD. It provides an accurate image of the waterflooding process

comparable to FD. Consequently, it is a powerful alternative for time-lapse seismic modeling.

Table 5.1: Geometry of different pre-stack traces simulated by 1D and 2D plane-wave seismic modeling techniques

	First trace	Second trace	Third trace	Forth trace
Ray parameter (sec/km)	0.0	0.10	0.20	0.30
Offset (km)	0.0	0.721	1.526	2.565
Incident angle at sea level (degree)	0.0	8.7	17.4	26.7
Incident angle at reservoir top (degree)	0.0	11.8	24.1	37.8
Intercept time (sec)	2.314	2.278	2.167	1.965
Traveltime (sec)	2.314	2.350	2.472	2.735

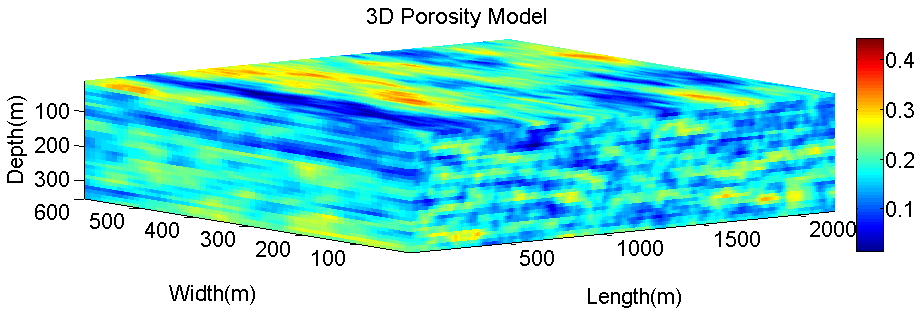

Figure 5.1: 3D distribution of effective porosity model (Christie and Blunt, 2001) associated with synthetic geologic model used for the numerical simulation of seismic and multi-phase fluid-flow. The model is described on a regular Cartesian grid. The model size is 220*60*35 cells in X (east-west), Y (north-south), and Z (depth) directions, respectively. The grid size defining the cells is 10*10*10 meters, so the model dimension is 2200m*600m*350m.

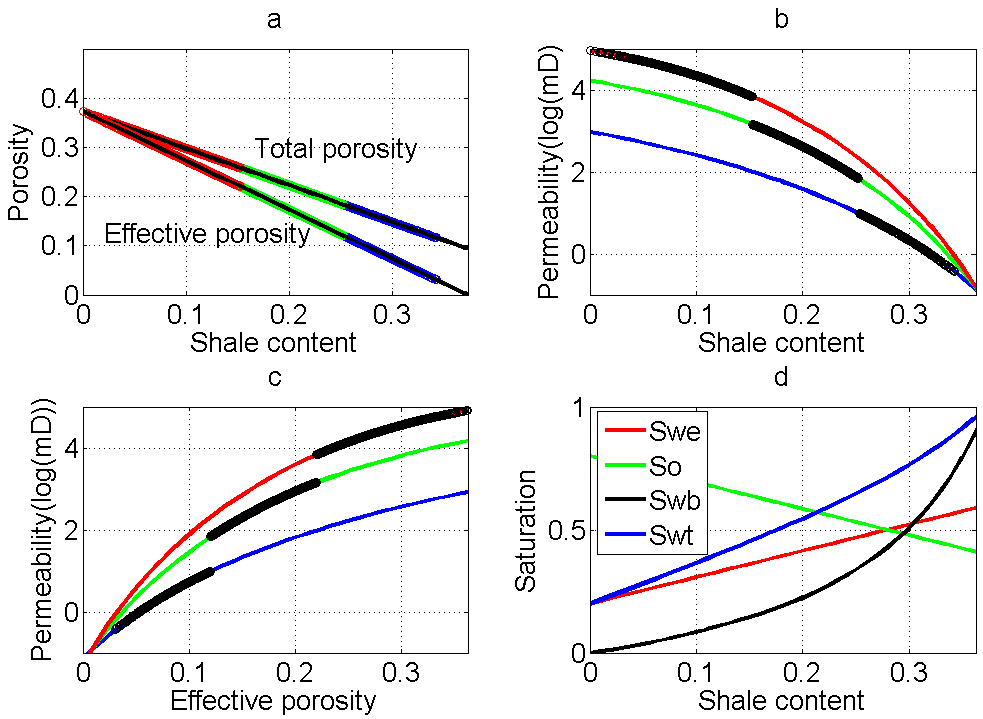

Figure 5.2: Petrophysics model. Panel a shows the dispersed clay model for porosity reduction due to increasing of clay. Panel b dispalys horizontal permeability versus shale content. Panel c is permeability vs. effective porosity. In panels a,b, and c, three colors are associated with three facies A(in blue), B(in green), and C(in red). Black dots in panels b and c are projected reservoir points . Panel d shows fluid saturations vs. shale content. Swe, So, Swb, and Swt are effective water saturation, oil saturation, caly bound water saturation, and total water saturation, respectively.

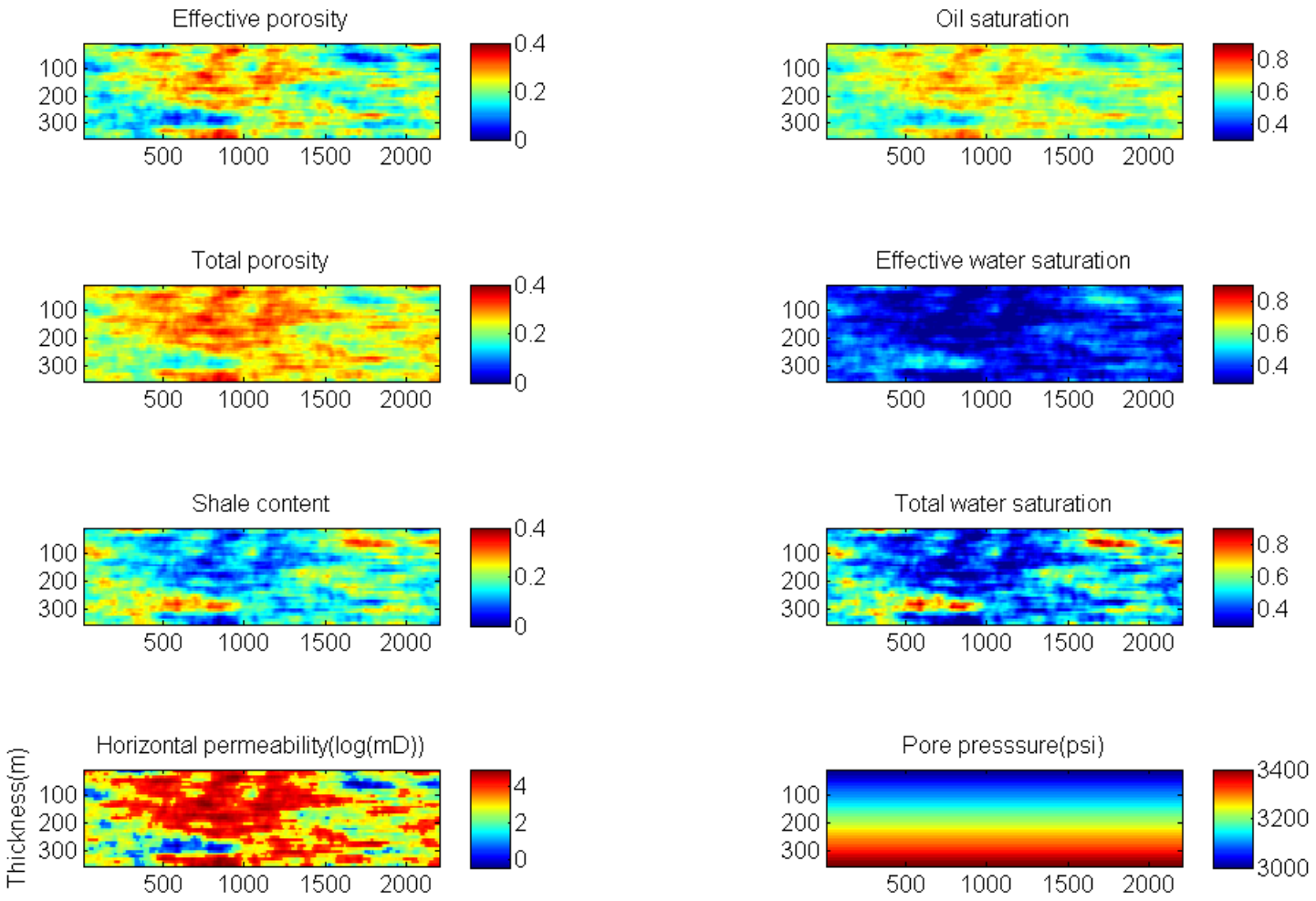

Figure 5.3: Distribution of petrophysical properties for a 2D cross-section in the middle of the 3D reservoir. X and Y axes are the same for all panels and they are reservoir length and thickness in meters, respectively. Each panel is color-coded for the corresponding attribute.

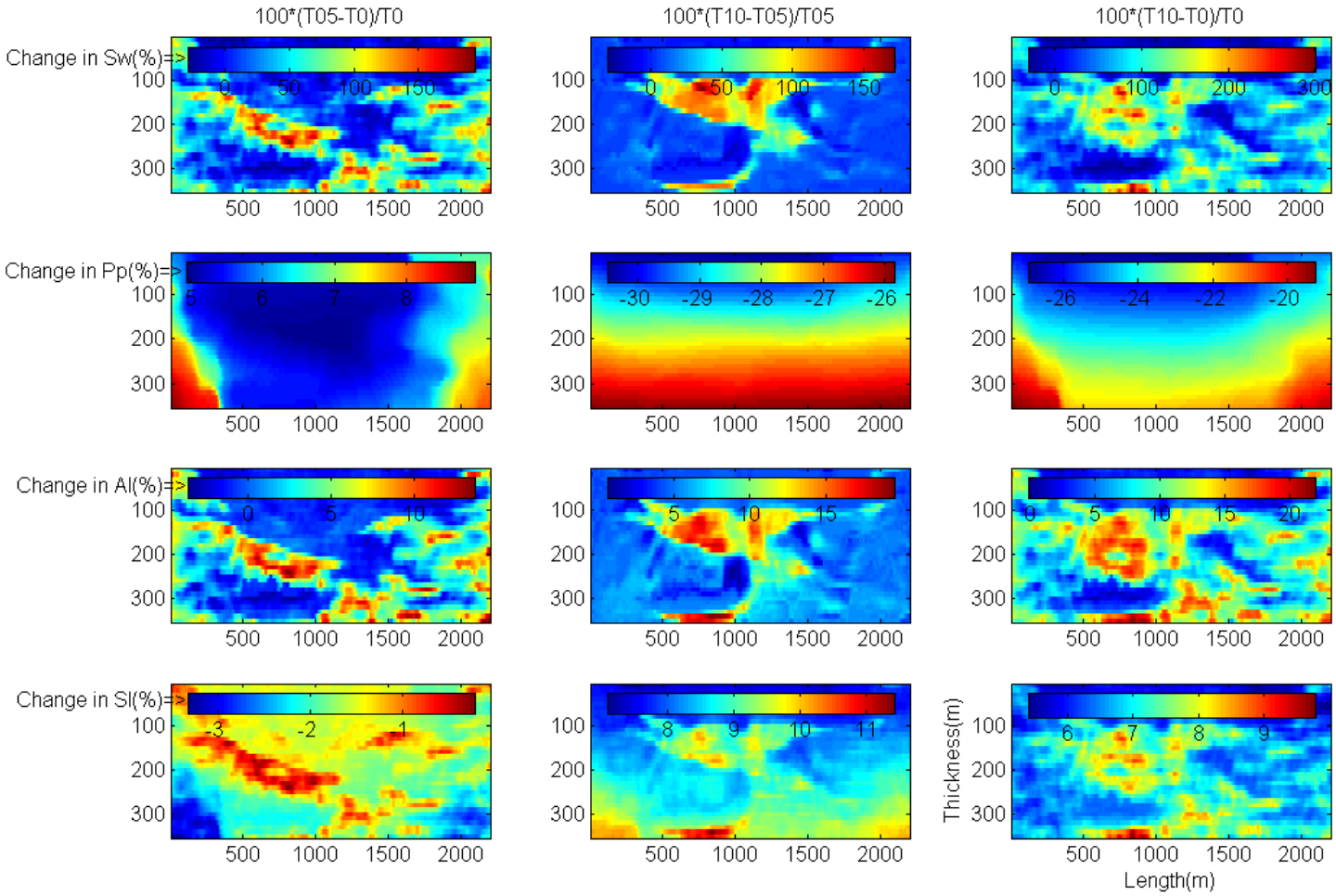

Figure 5.4: Time-lapse normalized percentage changes in effective water saturation, Sw, (top row), pore pressure, Pp, (2nd row from top), and the associated changes in seismic acoustic impedance, AI, (3rd row from top) and shear impedance, SI, (bottom row) between base survey and monitor survey after 5 years of waterflooding (left column), between monitor survey after 5 years and monitor survey after 10 years (middle column), and between base survey and monitor survey after 10 years (right column). X and Y axes are the same for all panels and they are reservoir length and thickness in meters, respectively. Each panel is color-coded for the corresponding attribute.

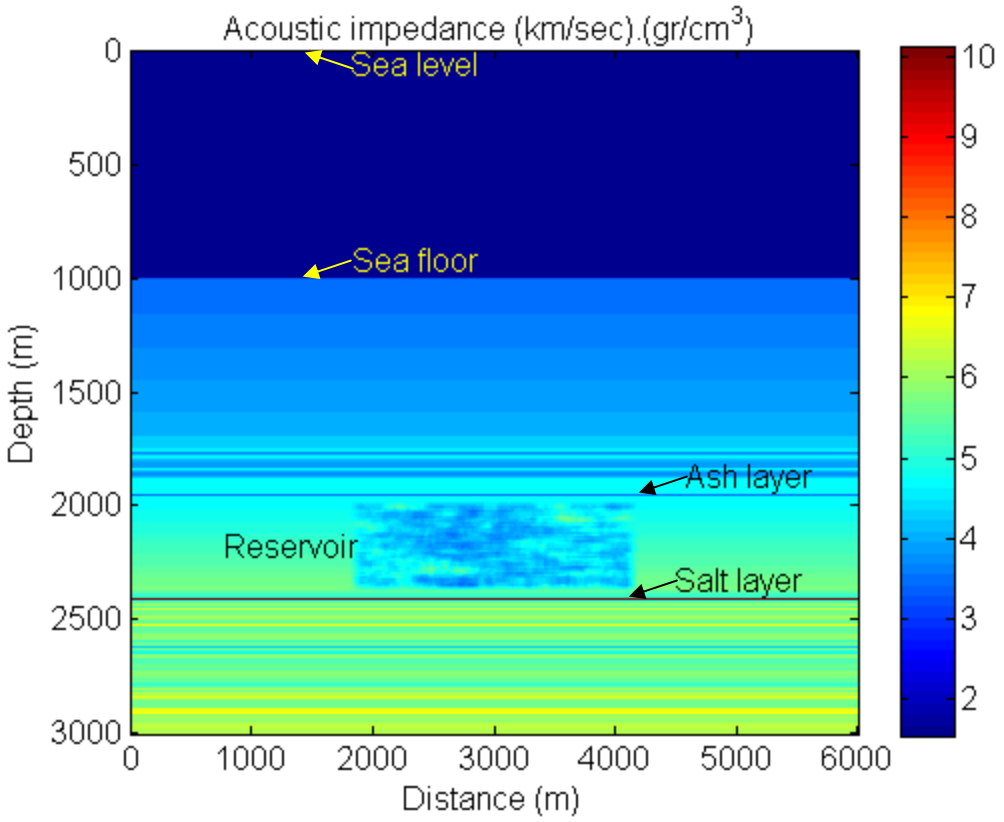

Figure 5.5: Petro-elastic model embedded into a 1D background elastic model simulating surrounding offshore sedimentary basin. The background model has dimensions of 600×1×300 in length, width, and depth respectively. The grid size is the same as reservoir model 10×10×10 m^3. The first one kilometer of the model is sea water. Reservoir was injected at depth 2000 m of the background model and sandwiched between an ash and salt layers at top and bottom, respectively. The edges of the reservoir were smoothed to better blend with the background model.

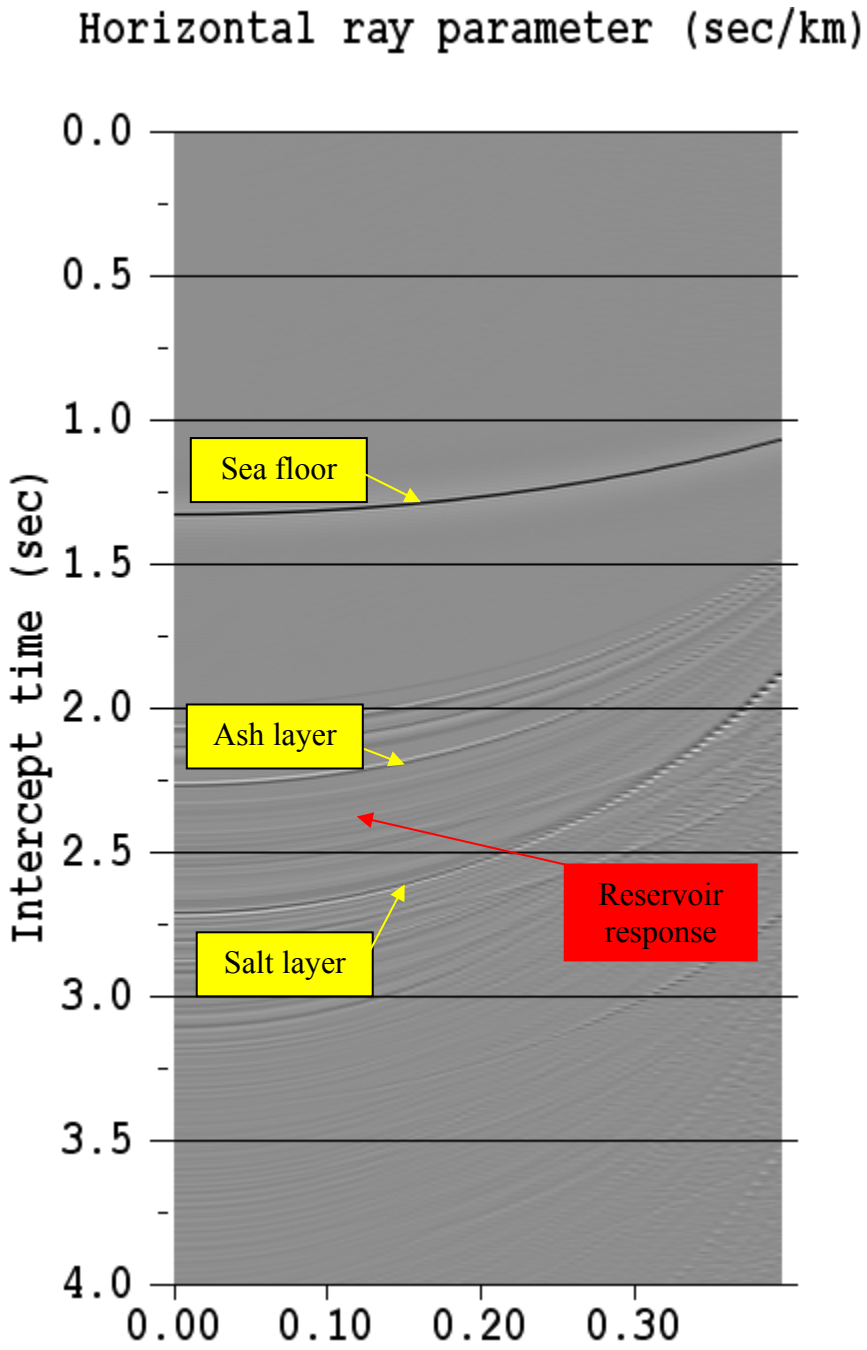

Figure 5.6: Plane-wave response of the 1D locally model in the middle of 2D reservoir for base survey (T0). The response was simulated by full elastic reflectivity algorithm for flat frequency of 0 to 75 Hz. Markers on the seismic data shows significant events associated with 2D model in Figure 5.5. No gain is applied to the data. For display purpose a band-pass filter of 5 to 65 Hz is applied.

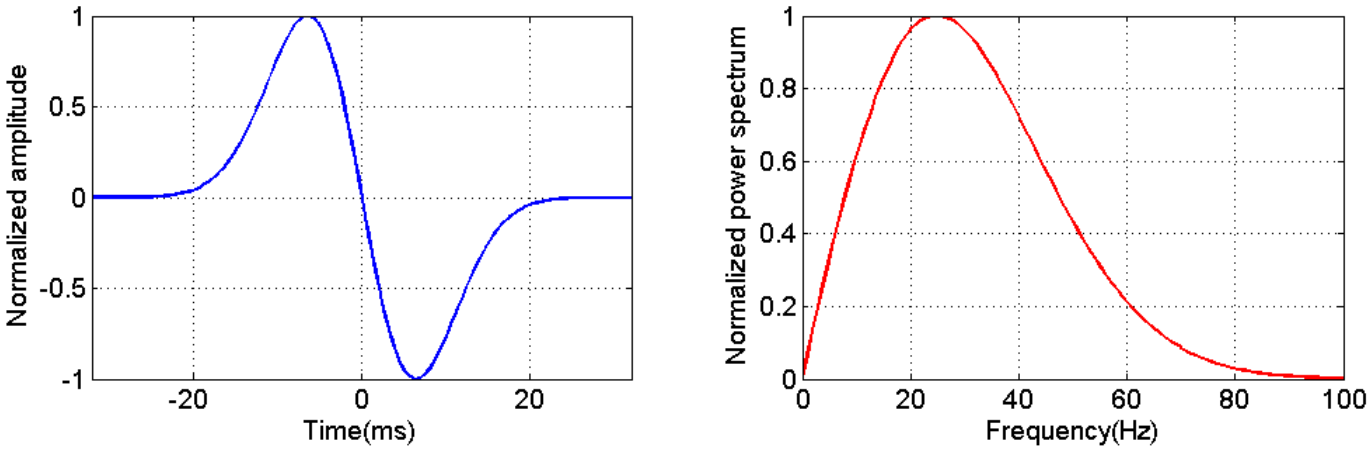

Figure 5.7: Normalized derivative of a Gaussian wavelet with a peak frequency of 35 Hz convolved with 1D and 2D plane-wave seismic data and used, as a source, to simulate 2D finite difference data.

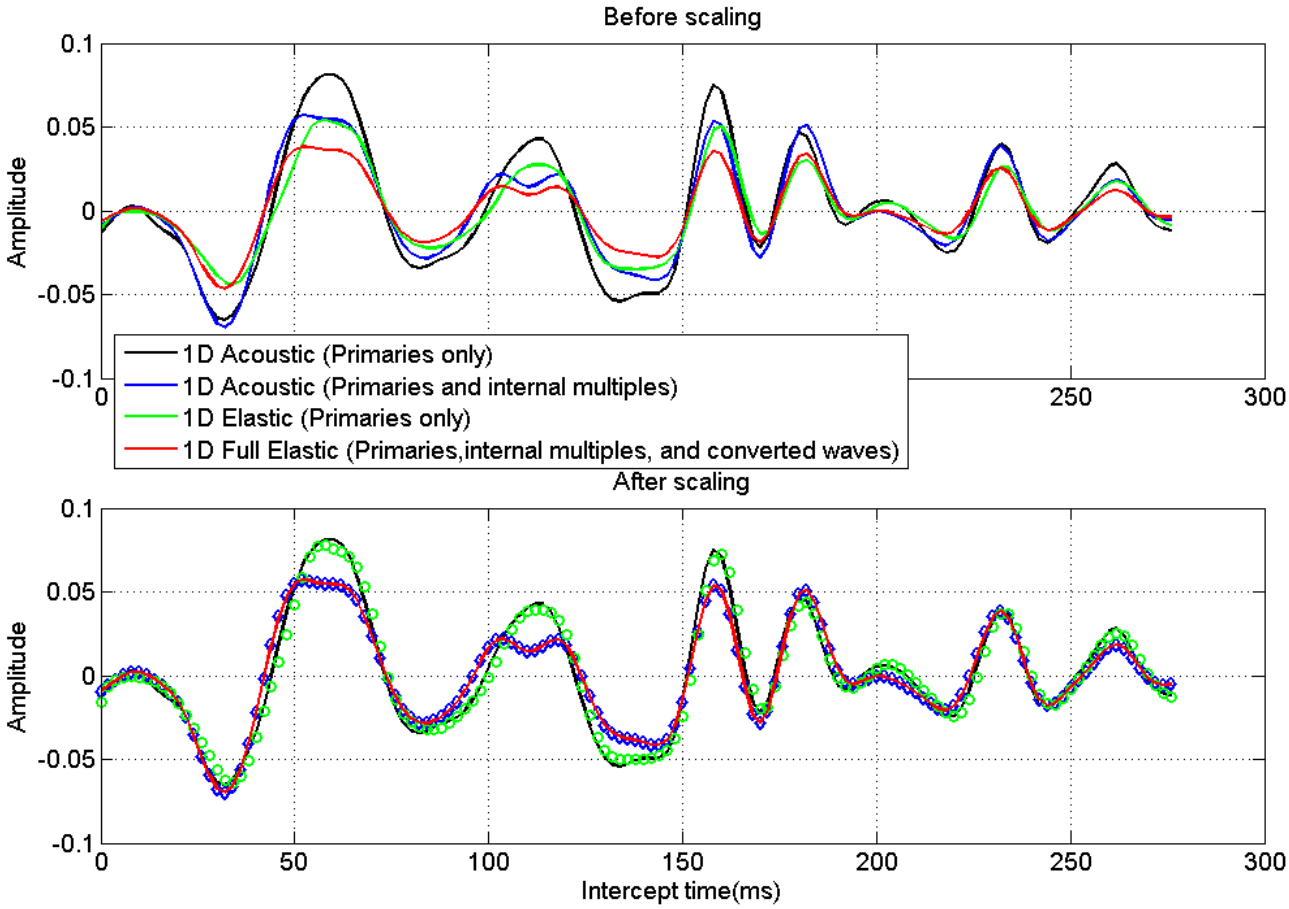

Figure 5.8: The scaling scheme used to tune 1D plane-wave seismic data computed from various algorithms.

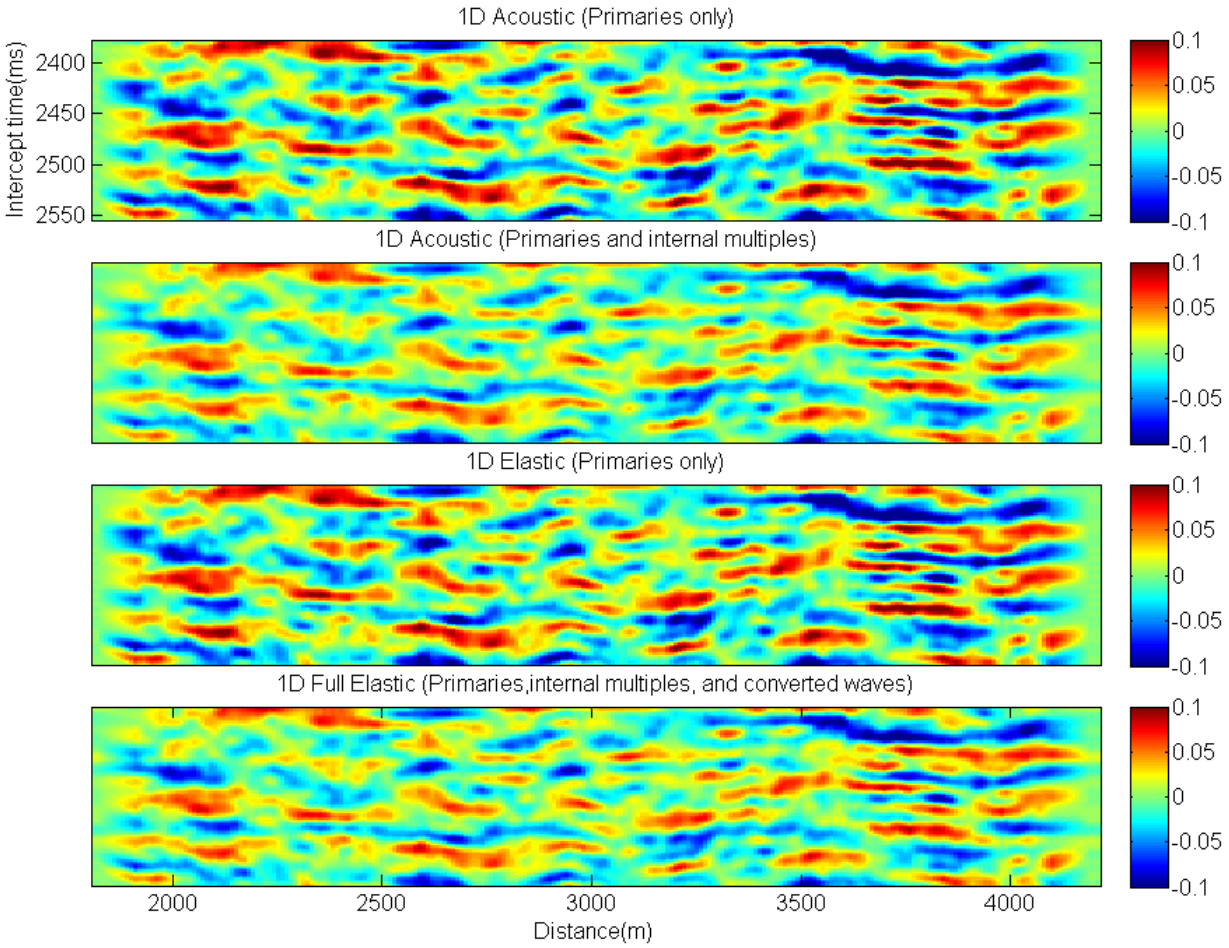

Figure 5.9: 1D plane-wave responses of the base survey (T0) at ray parameter (p=0 sec/km) computed by different seismic modeling methods.

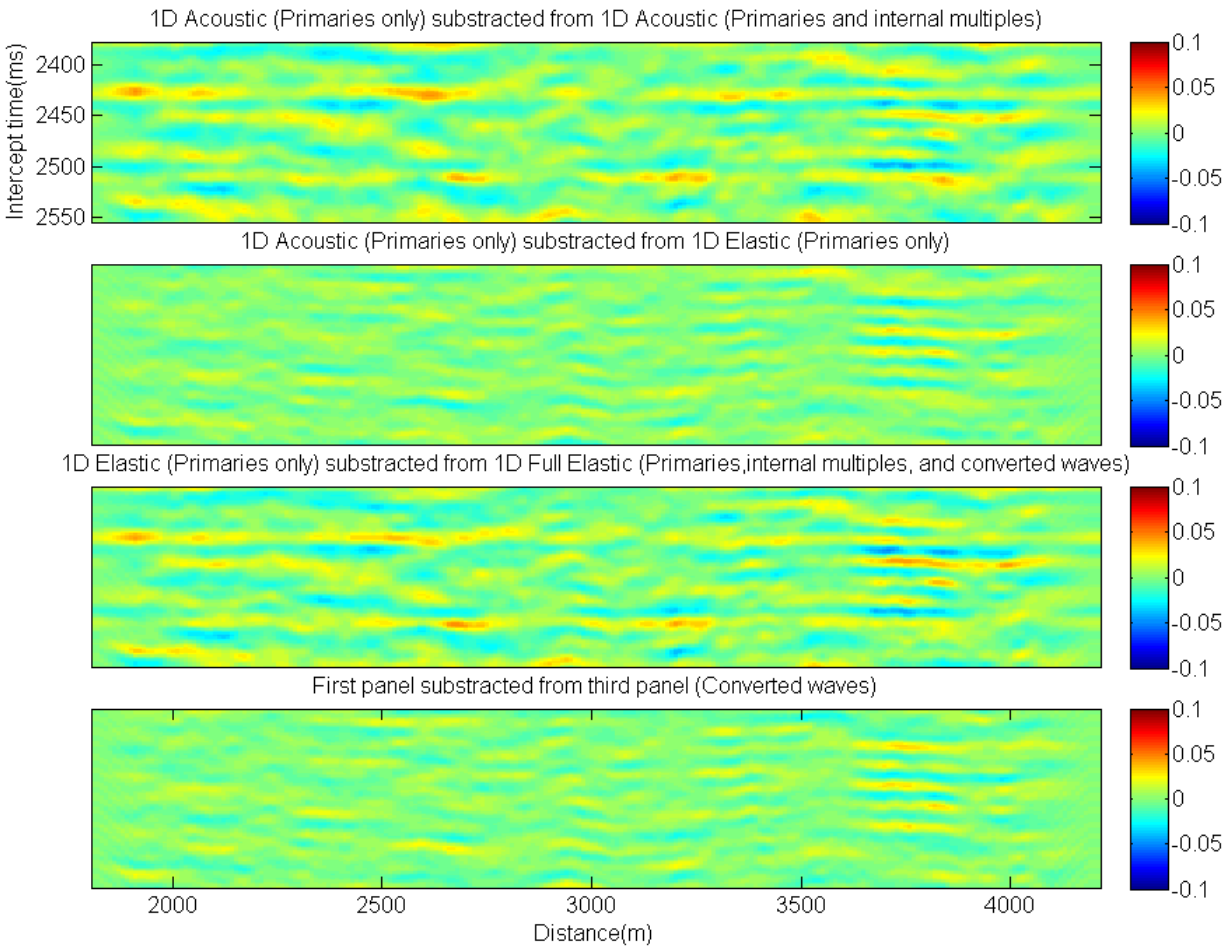

Figure 5.10: Residuals of 1D plane-wave responses of the base survey (T0) at ray parameter (p=0 sec/km) computed by different seismic modeling methods.

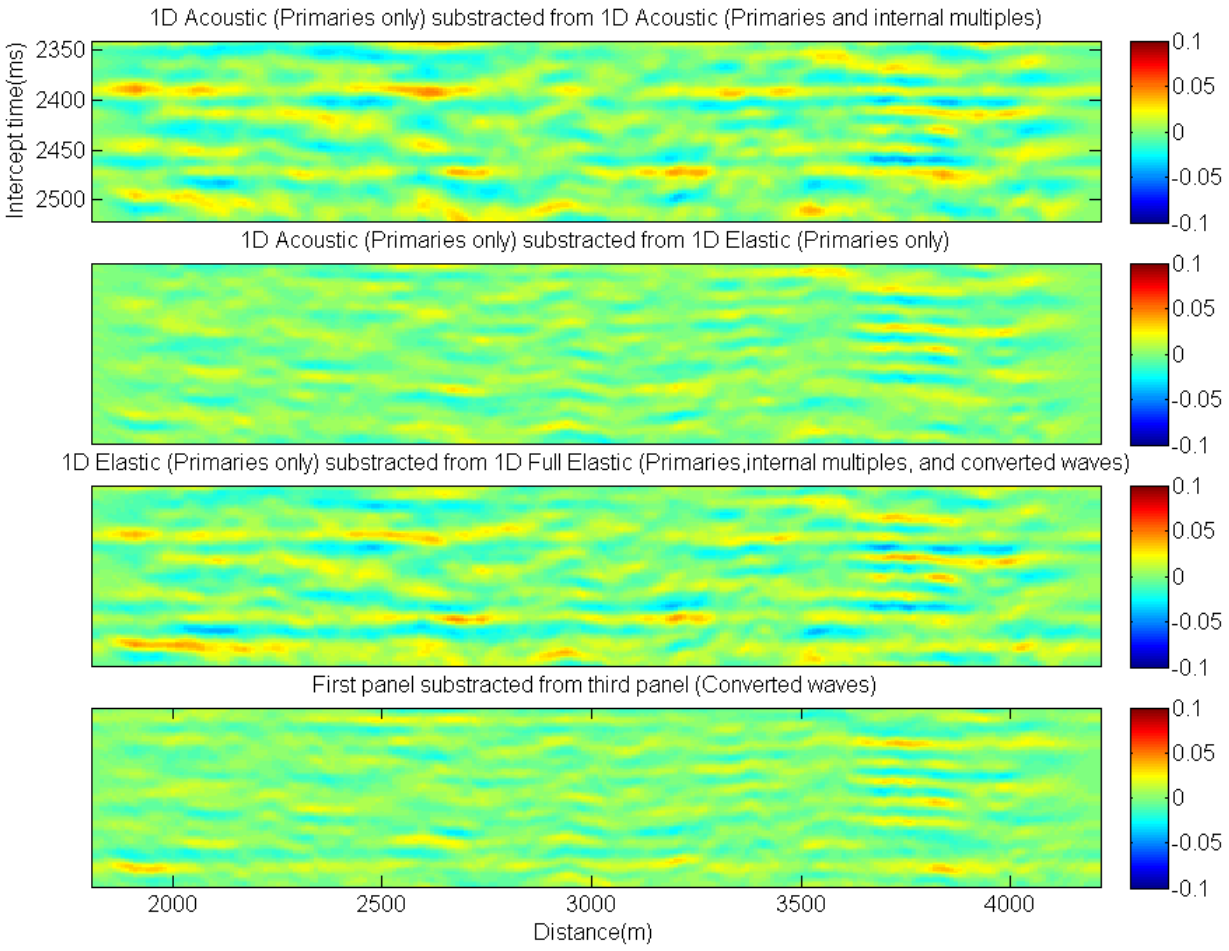

Figure 5.11: Residuals of 1D plane-wave responses of the base survey (T0) at ray parameter (p=0.1 sec/km) computed by different seismic modeling methods.

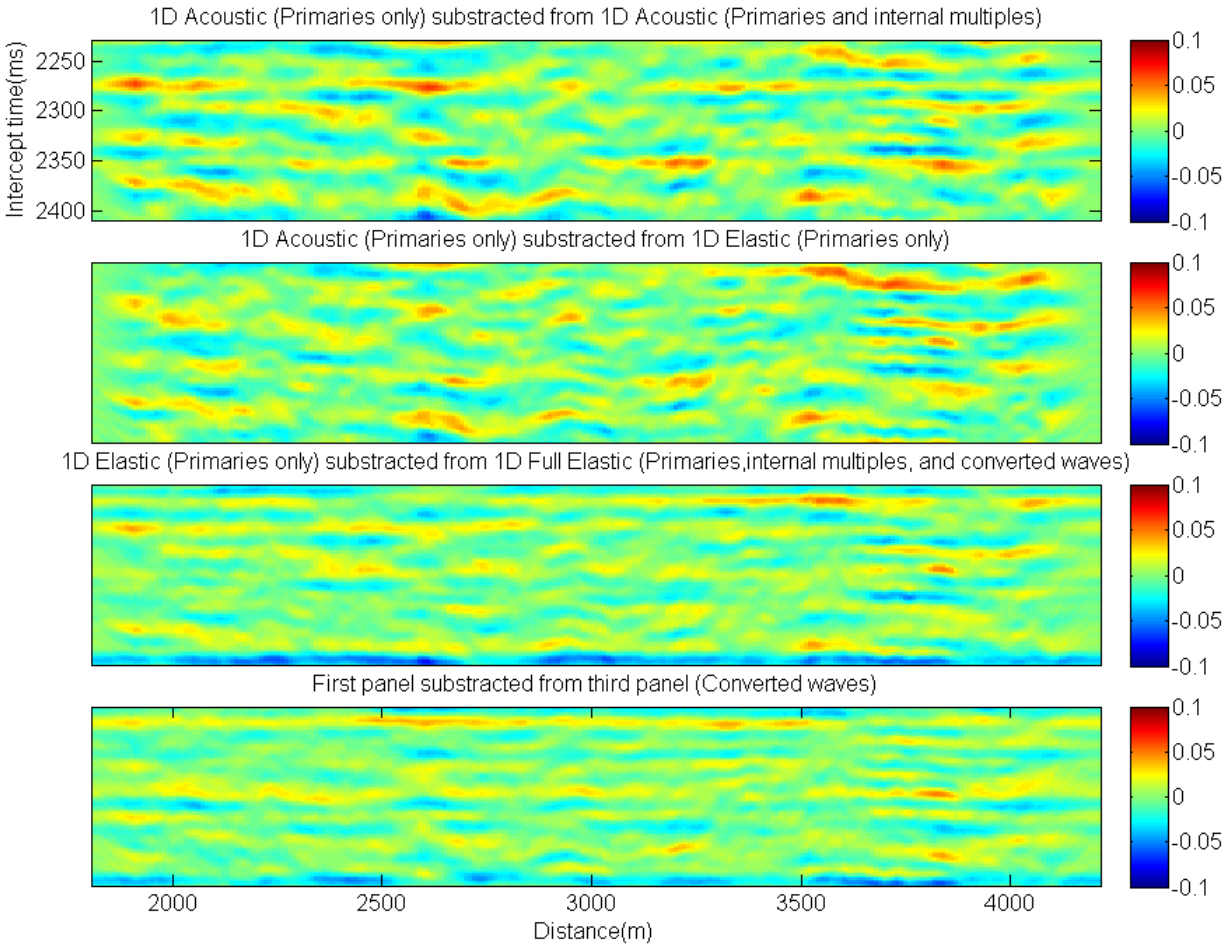

Figure 5.12: Residuals of 1D plane-wave responses of the base survey (T0) at ray parameter (p=0.2 sec/km) computed by different seismic modeling methods.

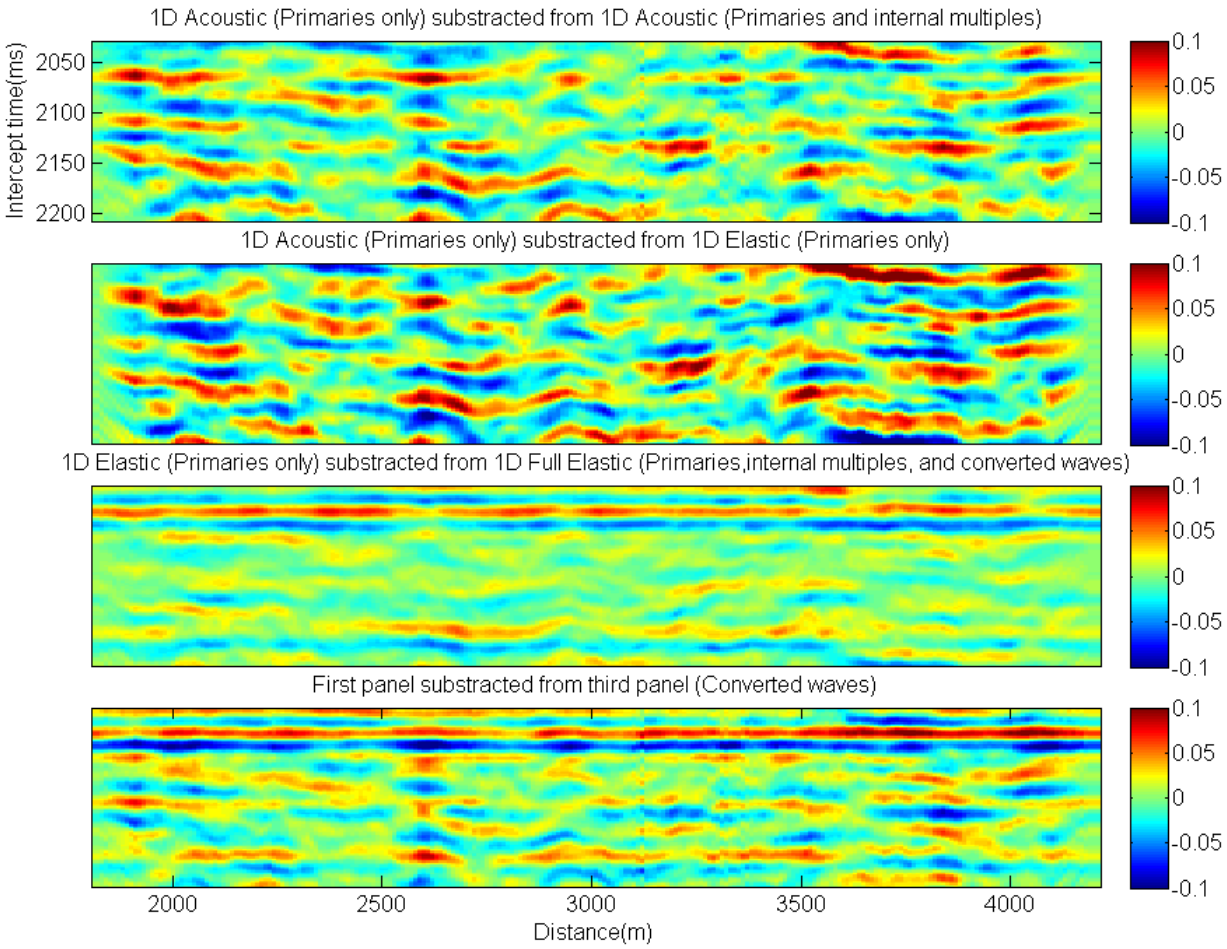

Figure 5.13: Residuals of 1D plane-wave responses of the base survey (T0) at ray parameter (p=0.3 sec/km) computed by different seismic modeling methods.

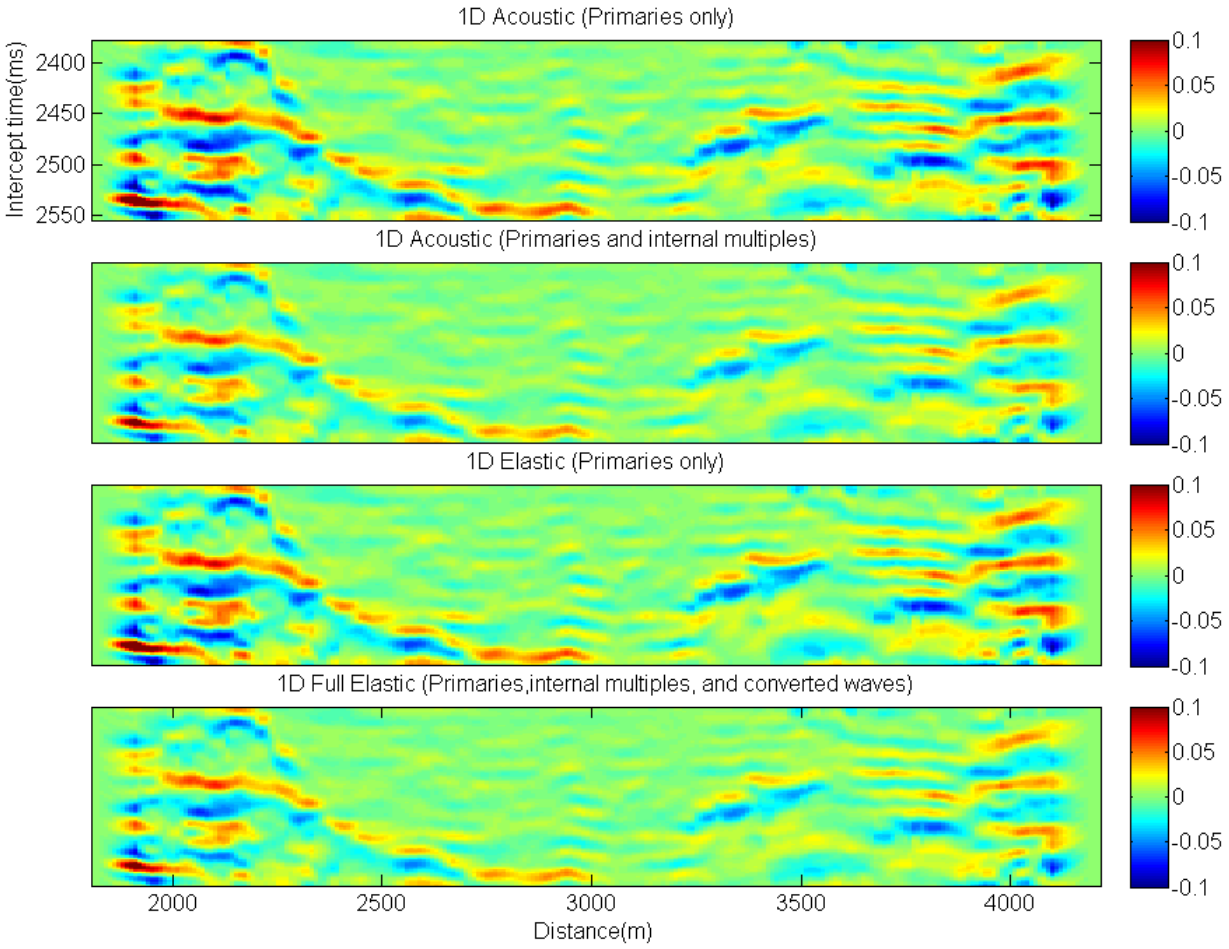

Figure 5.14: 1D plane-wave responses of the time-lapse (T5-T0), base survey is subtracted from monitor survey after 5 years of waterflooding, at ray parameter (p=0 sec/km) computed by different seismic modeling methods.

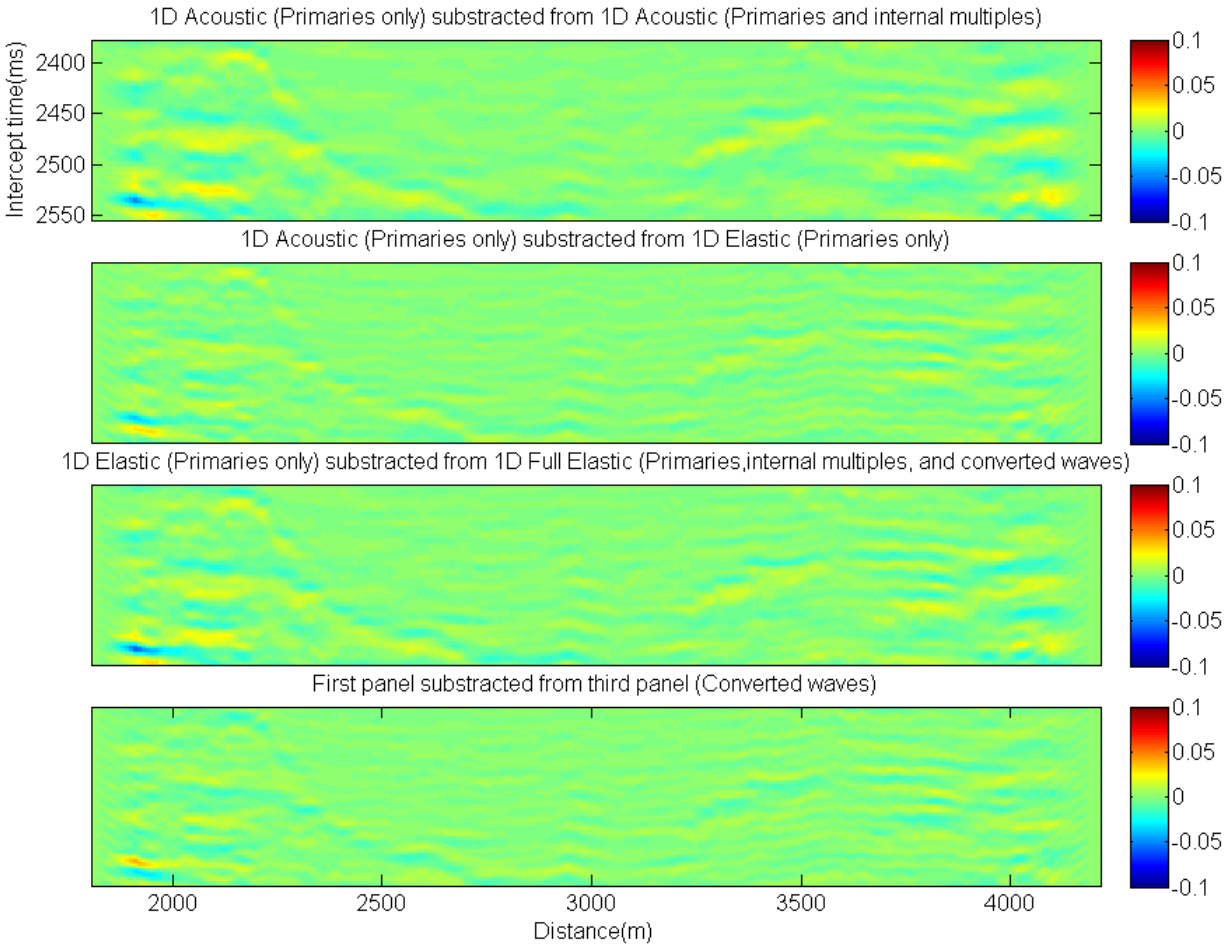

Figure 5.15: The residuals of 1D plane-wave responses of the time-lapse (T5-T0), base survey is subtracted from monitor survey after 5 years of waterflooding, at ray parameter (p=0 sec/km) computed by different seismic modeling methods.

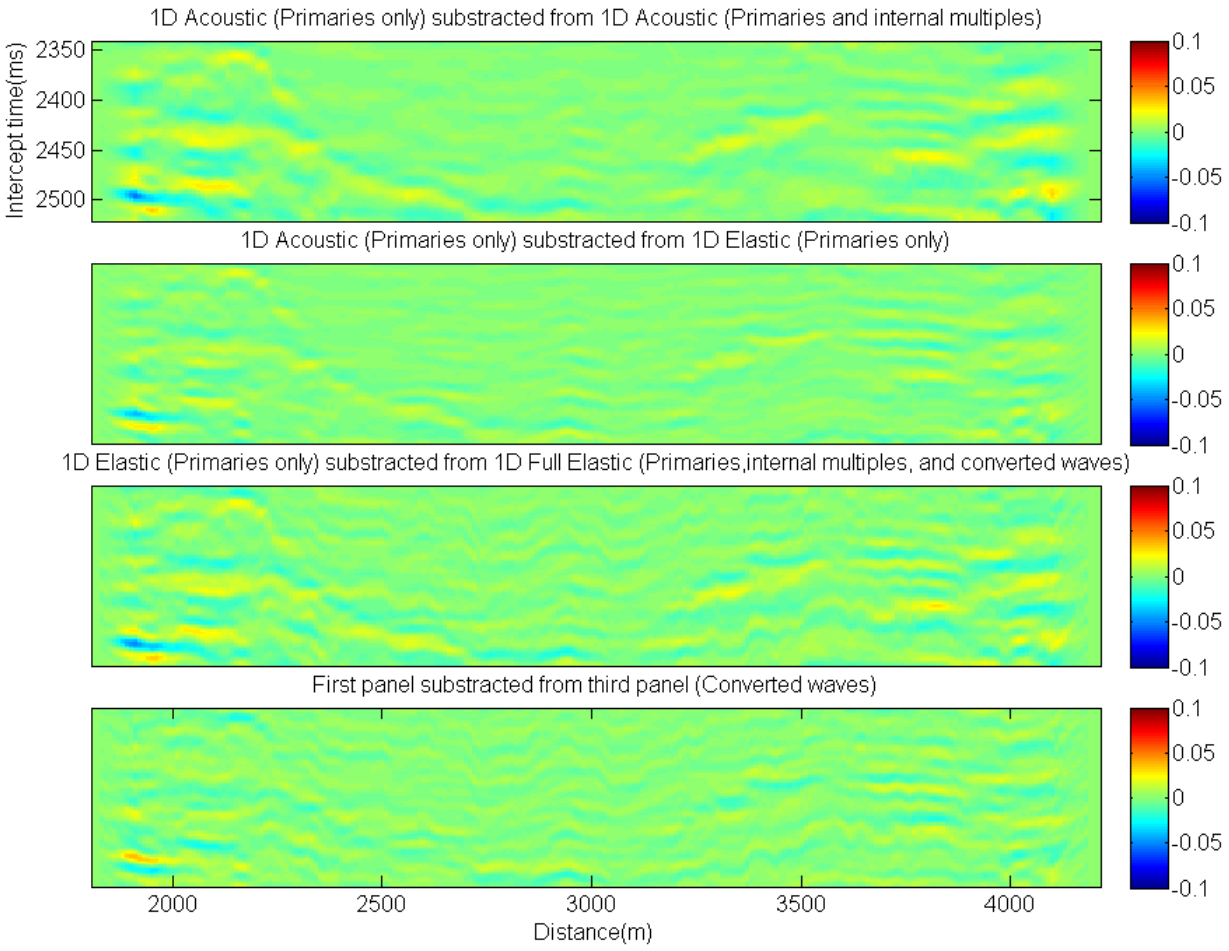

Figure 5.16: The residuals of 1D plane-wave responses of the time-lapse (T5-T0), base survey is subtracted from monitor survey after 5 years of waterflooding, at ray parameter (p=0.1 sec/km) computed by different seismic modeling methods.

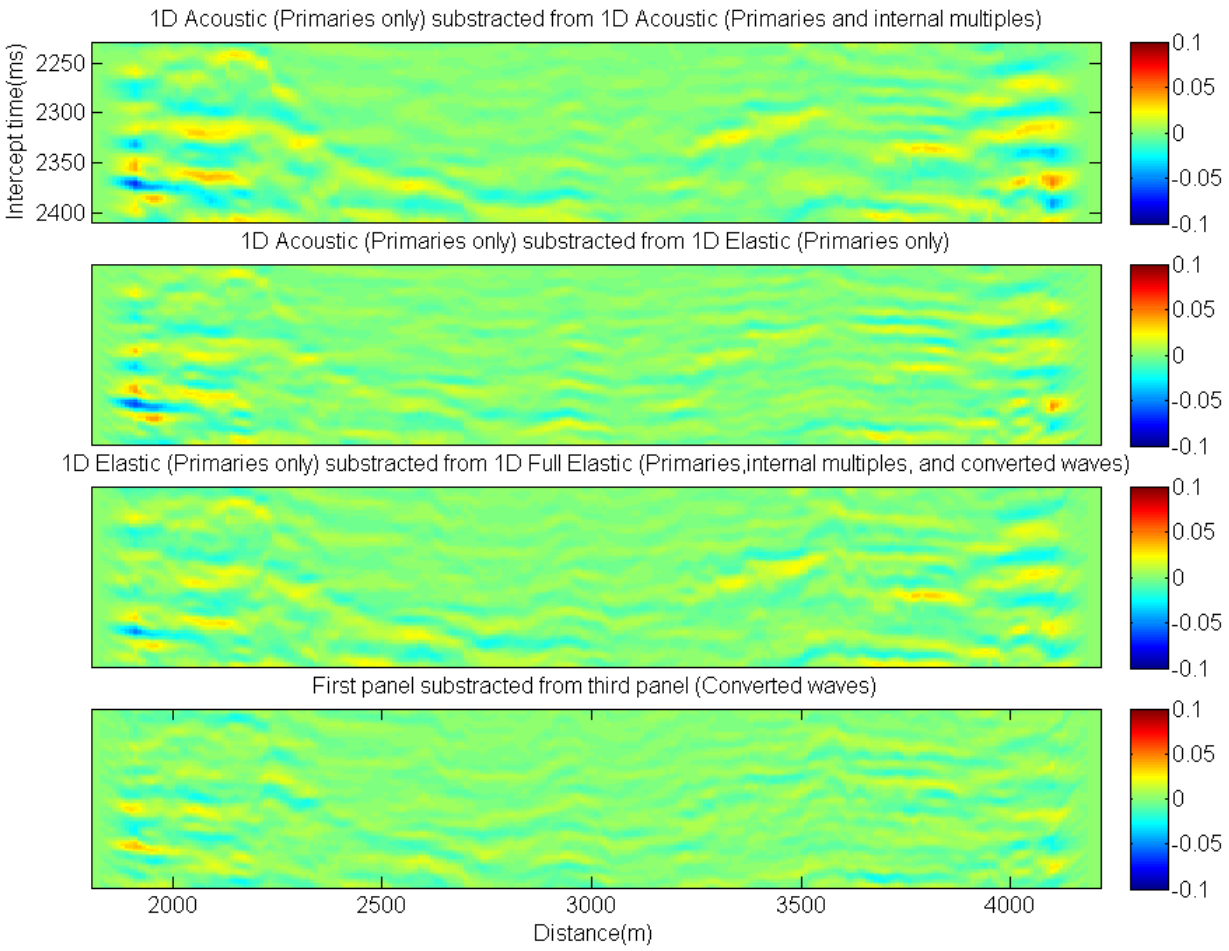

Figure 5.17: The residuals of 1D plane-wave responses of the time-lapse (T5-T0), base survey is subtracted from monitor survey after 5 years of waterflooding, at ray parameter (p=0.2 sec/km) computed by different seismic modeling methods.

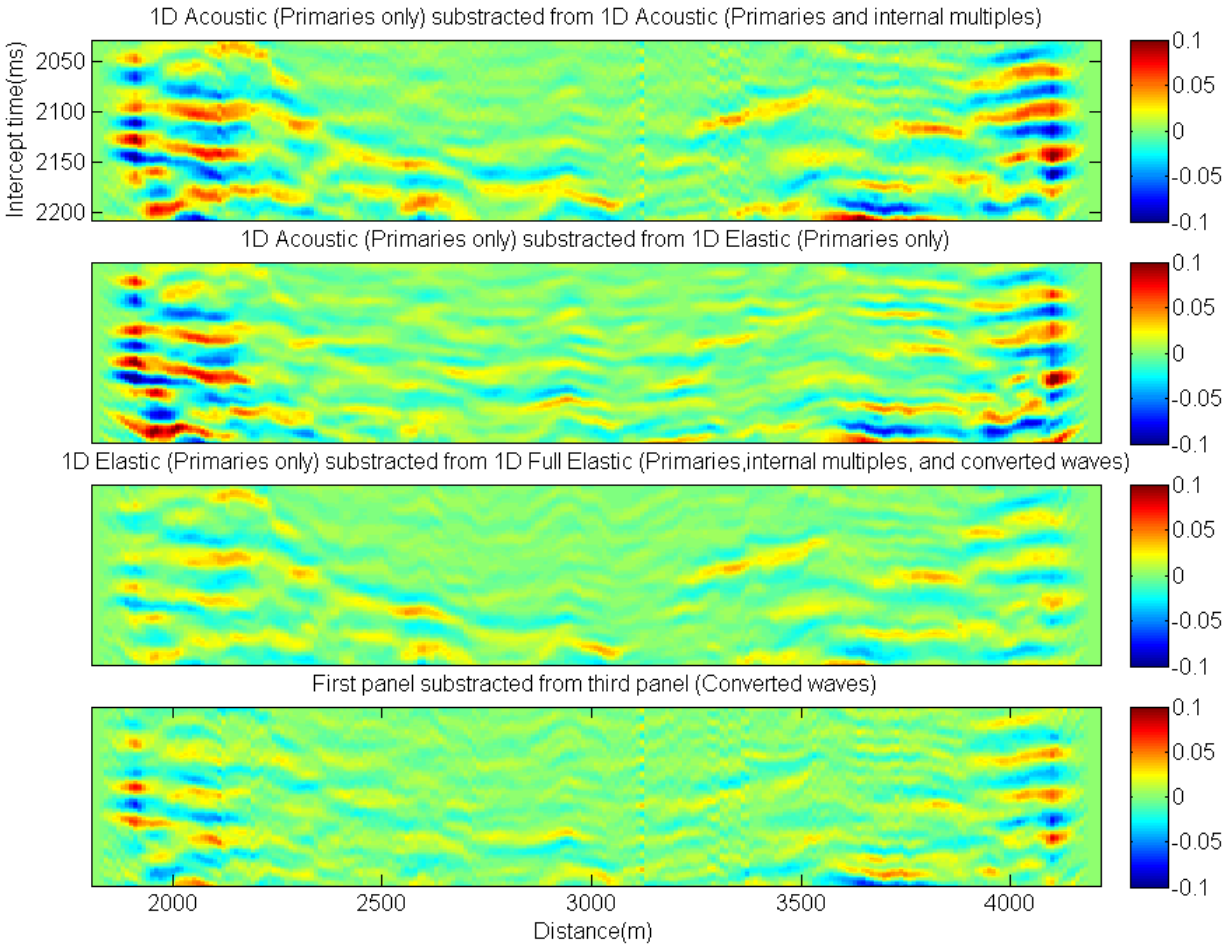

Figure 5.18: The residuals of 1D plane-wave responses of the time-lapse (T5-T0), base survey is subtracted from monitor survey after 5 years of waterflooding, at ray parameter (p=0.3 sec/km) computed by different seismic modeling methods.

Compute elastic reflection coefficients using full Zoeppritz equation for the cube of geological model at all X (x, y) positions, over depth z, and for all ray parameters (p), $\mathrm{RC}(\mathrm{X},\ \mathrm{z},\ \mathrm{p})$

Initialize the pressure wavefield, for all frequencies (ω) and all ray parameters (p), $P(X,\omega,p) = complex(0.,0.)$

- Loop over ray parameter
  - Loop over frequency
    - Loop over depth (from bottom to top)
      - Loop over X

        Apply local phase shift in frequency-space domain

        $P(X,\omega,p) = P(X,\omega,p) + RC(X,z,p)\times\exp(-i\omega\Delta u(X,z)\Delta z)$

        Add internal multiples if needed
      - End loop over X

      Space (X) to wavenumber (K_X) FFT
      - Loop over K_X

        Apply global phase shift in frequency-wavenumber

        $P(K_X,\omega,p) = P(K_X,\omega,p)\times\exp(-i\omega\Delta z\sqrt{\omega^2 u_{mean}^2 - K_X^2})$
      - End loop over K_X

      Wavenumber (K_X) to Space (X) FFT
    - End loop over depth
  - End loop over frequency
  - Loop over X

    Add surface multiples if needed

Frequency to intercept time (τ) FFT

Collect wavefield $P(X, \tau, p)$

- End loop over X

❖ End loop over ray parameter

Figure 5.19: A pseudo FORTRAN code for Split-step Fourier plane-wave (SFPW) seismic modeling.

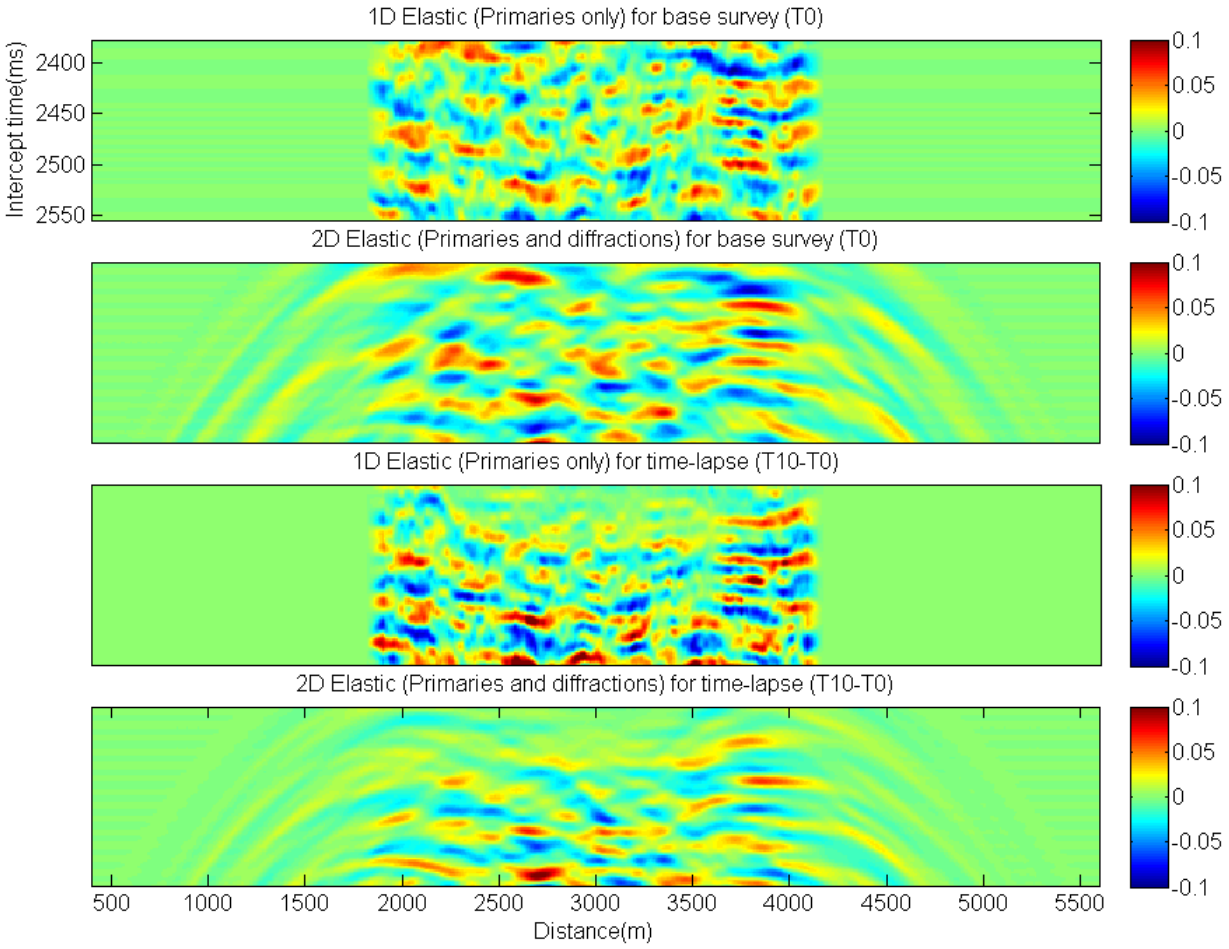

Figure 5.20: Plane-wave responses for base survey (T0) and time-lapse (T10-T0), associated with the base and the monitor survey after ten years of water flooding, at p= 0 sec/km. The first and the third panel are associated with 1D modeling and the second and forth panels are 2D modeling computed by SFPW algorithm.

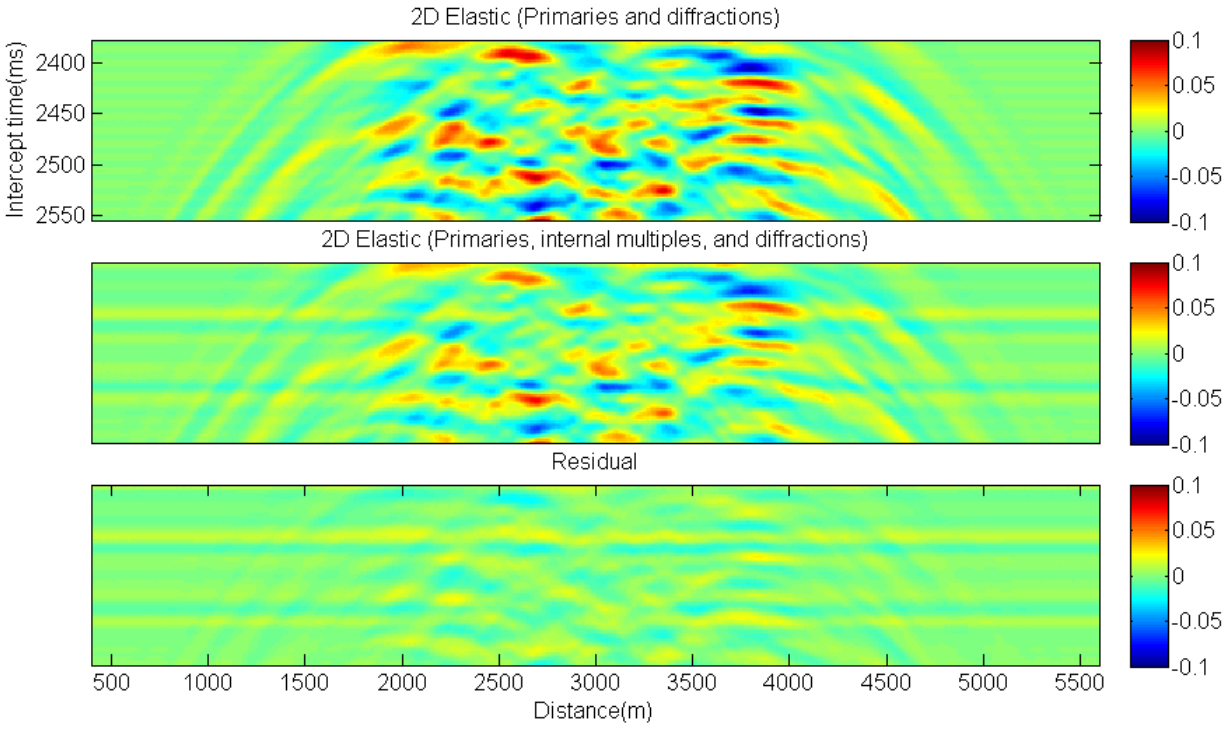

Figure 5.21: Plane-wave responses for base survey (T0), at p= 0 sec/km, without (first panel) and with (second panel) internal multiples. The third panel shows the residual of the first two panels, highlighting the internal multiples.

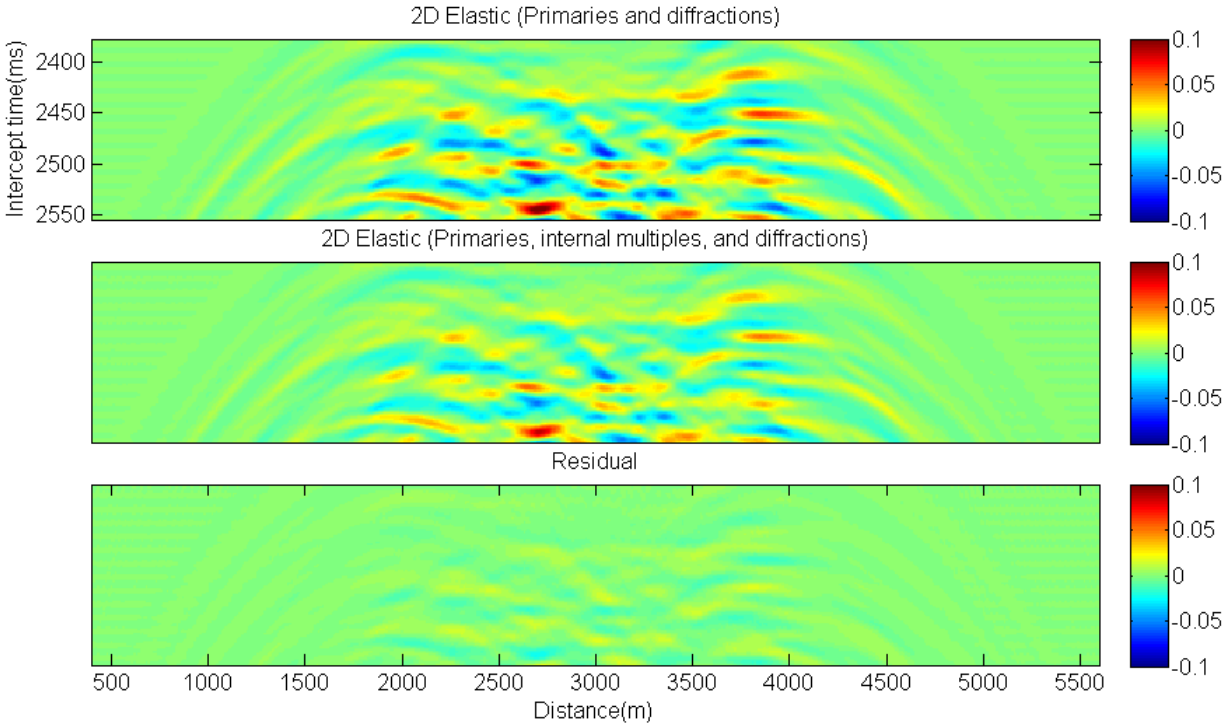

Figure 5.22: Plane-wave responses for time-lapse (T10-T0), associated with the base and the monitor survey after ten years of water flooding, at p= 0 sec/km, without (first panel) and with (second panel) internal multiples. The third panel shows the residual of the first two panels, highlighting the internal multiples.

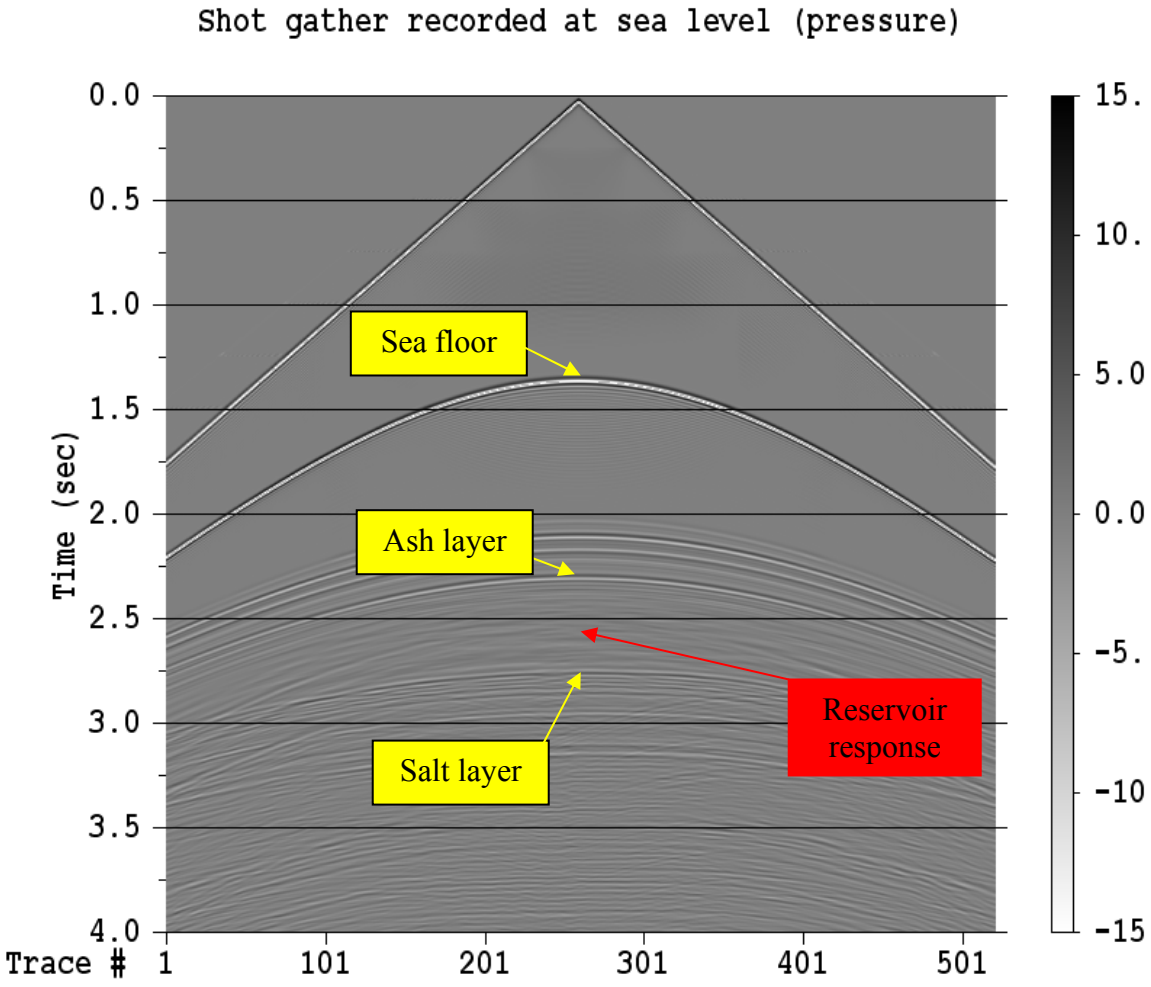

Figure 5.23: Finite difference shot gather located in the middle of 2D reservoir for base survey (T0). Pressure wavefield is displayed. Markers on the seismic data shows significant events associated with 2D model in Figure 5.5. For display purpose AGC of length 500 ms and band-pass filter of 5 to 65 Hz is applied.

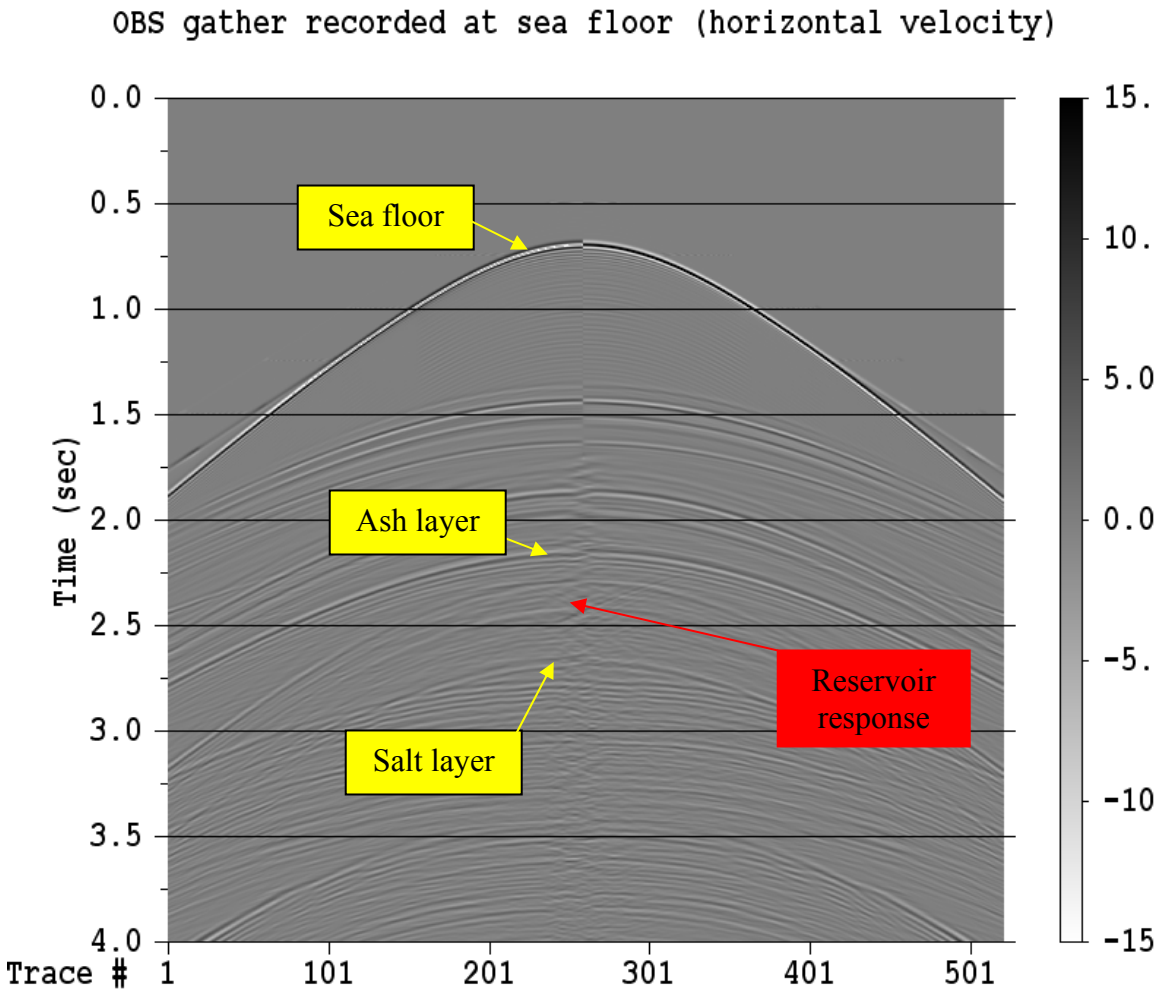

Figure 5.24: Finite difference OBS gather located in the middle of 2D reservoir for base survey (T0). Horizontal velocity wavefield is displayed. Markers on the seismic data shows significant events associated with 2D model in Figure 5.5. For display purpose AGC of length 500 ms and band-pass filter of 5 to 65 Hz is applied.

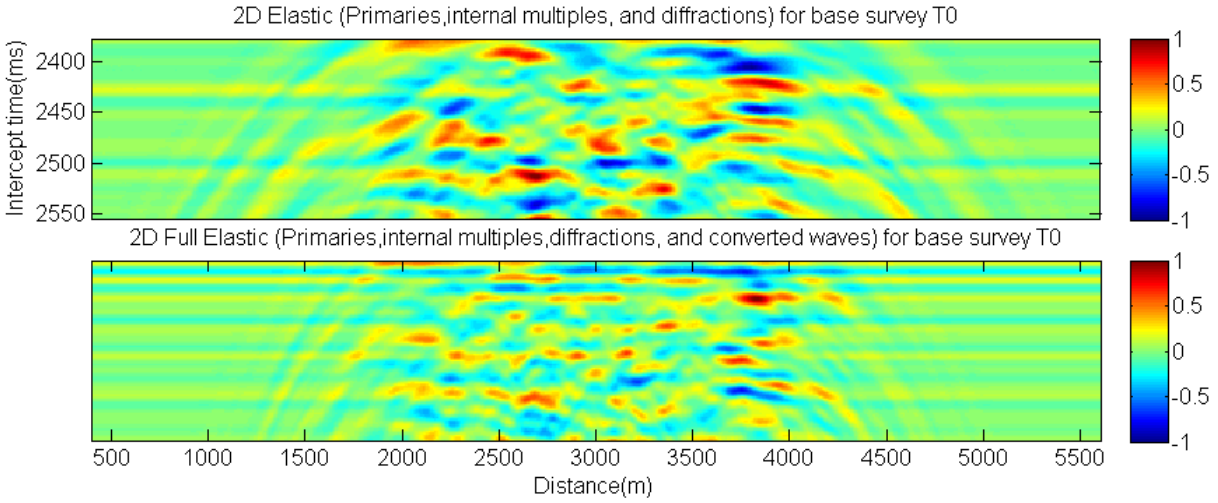

Figure 5.25: 2D Plane-wave (first panel) and Finite difference (second panel) responses of the base survey (T0) at p=0.0 sec/km.

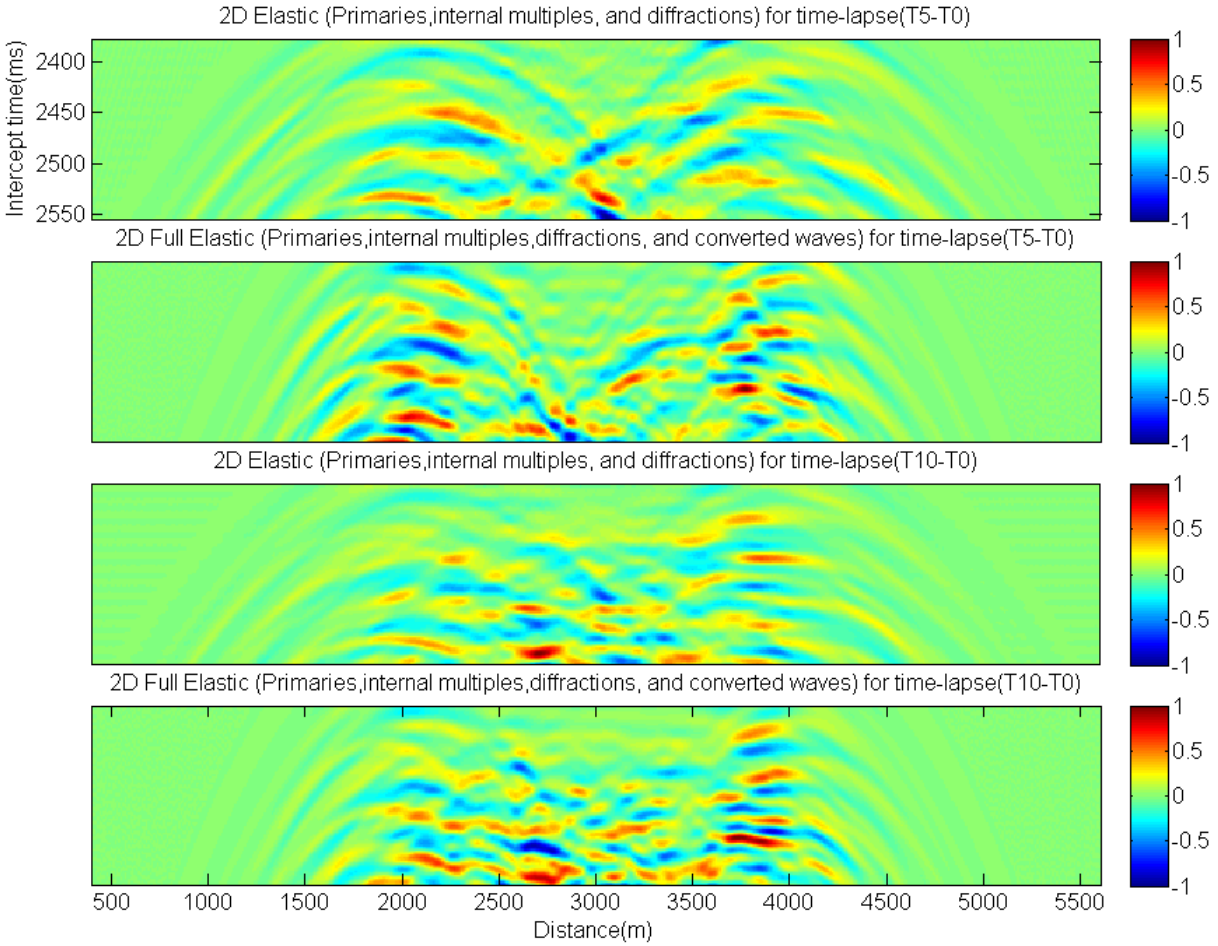

Figure 5.26: 2D Plane-wave (first and third panels after 5 and 10 years of waterflooding, respectively) and Finite difference (second and forth panels after 5 and 10 years of waterflooding, respectively) seismic responses at p=0.0 sec/km.

Chapter six: Petro-electric modeling aimed to simulate CSEM data for reservoir characterization and monitoring

This chapter is devoted to describing a petro-electric modeling of the reservoir under study for CSEM (controlled-source electromagnetic) time-lapse modeling. The reservoir model is launched into a reservoir simulator to predict the spatial distributions of water saturation and pore pressure due to an active waterflood scenario. Then, simulated static and dynamic reservoir properties provide the necessary input parameters for a rock physics model through which reservoir properties are converted to electrical resistivity. At the end of this chapter, CSEM time-lapse data are simulated by accurate modeling algorithms and the detectability of the corresponding signals are evaluated.

6.1 INTRODUCTION

This chapter appraises the ability of time-lapse CSEM (controlled-source electromagnetic) data to detect the changes in fluid saturation during waterflooding into a black oil reservoir. To do so, I simulate a poorly consolidated shaly sandstone reservoir based on a prograding near-shore depositional environment. To account for spatial distribution of petrophysical properties, an effective porosity model is first simulated by Gaussian Geostatistics. Dispersed clay and dual water models are then efficiently combined with other well-known theoretical and experimental petrophysical correlations to consistently simulate reservoir parameters including total porosity, directional permeabilities, shale content, initial water situation and pore pressure.

Next, the constructed reservoir model is subjected to numerical simulation of multi-phase fluid flow. A commercial reservoir simulator is employed to predict the spatial distributions of fluid pressure and saturation due to water injection into a black oil reservoir containing two phases: water and live oil. Finally, a geologically consistent rock

physics model, a modified Archie's equation for shaly sandstones called dual water, in conjunction with a fluid physics model, Arps' empirical equations, are utilized to simulate rock and fluid resistivity.

As a result, the comprehensive petro-electric model developed in this chapter can be efficiently utilized in sensitivity analyses of CSEM data to petrophysical properties and, ultimately, applied to reservoir characterization and monitoring research. As an example, I choose to present a time-lapse frequency domain CSEM feasibility study over the 2D reservoir model embedded in a 1D background resistivity model. Three sets of marine 2.5D CSEM data are simulated by a parallel adaptive finite element algorithm. My analysis demonstrates that a detectable time-lapse signal after 5 years and a strong time-lapse signal after 10 years of waterflooding are attainable using current CSEM technology. In addition, multi-component and multi-frequency analysis of the time-lapse signal have been investigated using 1D CSEM modeling and compared against 2.5D modeling results.

6.2 BACKGROUND AND FORMULATION

CSEM has been recently applied to petroleum exploration as a direct hydrocarbon detector. The contrast between the electrical conductivity of hydrocarbon-saturated reservoir rocks and the surrounding water-saturated rocks at depth leads to an anomaly in measured magnetic and electric fields emitted in the vicinity of the sea floor by dipole electrical transmitters and recorded at ocean bottom receivers. Various successful applications have been addressed by several authors (e.g., Ellingsrud et al. 2002; Eidesmo et al. 2002).

Time-lapse CSEM data consists of two or more repeated surveys recorded at different calendar times over a depleting reservoir. The main objective is to detect and

estimate production-induced time-lapse changes in subsurface rock and fluid properties. In doing so, changes in observations, i.e., the amplitude and phase of magnetic and electric fields, or inverted attributes, e.g., rock resistivity, are often associated to changes in fluid saturation assuming a non-compacting isothermal reservoir. This technique has been addressed by several authors in the literature.

Wright et al. (2002) presented time-lapse transient EM surveys over a shallow underground gas storage reservoir with high porosity and showed that the data are repeatable enough to detect the reservoir and monitor the moving of gas-water contact due to gas injection and/or extraction in summer and winter, respectively. Lien and Mannseth (2008) conducted a feasibility study of time-lapse CSEM data to monitor the waterflooding of an oil reservoir. Utilizing 3D integral equation modeling, they found that time-lapse signals exhibit detectable changes even in the presence of measurement errors. Orange et al. (2009) further expanded the work by Lien and Mannseth (2008) by utilizing a 2D finite element modeling to simulate time-lapse CSEM data in response to several simplified waterflooding scenarios, including lateral and bottom flooding, and partial depletion. Through a set of 2D modeling studies, they showed that a data repeatability of 1-2% is required to detect the small time-lapse signals. Zach et al. (2009) conducted 3D time-lapse modeling by perturbing conductivity over a large reservoir (10*10 km^2) and reported anomalies of 30% to 50% changes in relative amplitudes of base and monitor surveys. They mentioned that these relatively strong time-lapse signals as well as different shapes of fronts can be monitored considering 5% repeatability for time-lapse surveys. Black et al. (2009) modeled time-lapse CSEM response over a realistic geologic model for simplified flood geometry without fluid flow simulation and rock physics modeling. They showed that marine CSEM data are able to locate the

position of the oil-water contact if the field is normalized by the background, bathymetry, and salt dome effects.

No reservoir simulation and rock physics modeling was performed in the above-mentioned studies; instead, they all consider direct perturbation of electrical-conductivity. In 2009, PGS (Petroleum Geo-Services) published a time-domain EM repeatability experiment over the North Sea Harding field. Fluid flow simulation and resistivity modeling by Archie's equation for clay-free sandstone were combined by integral equation modeling to simulate EM data. They concluded that the production-induced time-lapse changes in reservoir resistivity would be observable provided that a signal to noise ratio of greater than 100, i.e., 40dB, is obtained (Ziolkowski et al. 2010).

Here, I first generate a 2D geological reservoir model showing the realistic spatial distribution of petrophysical parameters. Fluid flow simulation and a geologically consistent rock physics model are then employed to convert the petrophysical properties of the shaly sandstone to electrical resistivity. The representative time-dependent resistivity model developed here shows the accurate front geometry during a waterflooding to enhance oil recovery. To simulate the surrounding rocks, I embed the reservoir into a 1D background resistivity model correlated with a P-wave velocity log. Finally, I numerically acquire 1D and 2.5D time-lapse CSEM data over the reservoir to assess the value of EM data in monitoring of a waterflooding scenario. To the best of my knowledge, no such comprehensive study has been reported in the open technical literature.

6.3 CONSTRUCTING A SYNTHETIC RESERVOIR MODEL

6.3.1 Geological reservoir model

A stacked sand-rich strandplain reservoir architecture has been considered in this study to simulate a realistic geological framework. Strandplains are mainly marine-dominated depositional systems generated by seaward accretion of successive, parallel beach ridges welded onto the subaerial coastal mainlands. They are inherently progradational features and present on wave-dominated microtidal coasts (Tyler and Ambrose 1986; Galloway and Hobday 1996). This sand-rich beach-ridge reservoir architecture is inferred to be originally deposited as a clay-free geobody. However; due to post-depositional diagenesis, dispersed clay is produced and it is the main factor reducing porosity and permeability of the reservoir. Figure 6.1 displays a three dimensional distribution of effective porosity generated using a Gaussian Simulation technique. This model, called SPE comparative solution project (Christie and Blunt, 2001), is a large geostatistical model widely used in research in reservoir simulation, seismic and controlled-source electromagnetic (CSEM) modeling, etc. (e.g., Liang et al. 2010). I work with the top 35 layers of the model which is representative of the Tarbert formation, a part of the Brent sequence of middle Jurassic age and one of the major producers in the North Sea. By changing the grid size and imposing smoothness, I modify this model to meet the objectives of this research. Next, I will assign geologically consistent petrophysics information and add facies characterization to develop a more realistic reservoir model comparable to complicated models in the petroleum industry. The model is described on a regular Cartesian grid. The model size is 220*60*35 in X (east-west), Y (north-south), and Z (depth) directions, respectively. The grid size is 10*10*10 meters, so the model dimensions are 2200m by 600m by350m. Figures 6.2 illustrate cross-sections of the porosity cube in different directions.

The reservoir consists of three facies (Figure 6.3). Facies A is a fine grained sandstone with mean grain size distribution of 80 μm. This facies simulates a low porous and permeable sandstone reservoir with high clay content. Facies C is a course grained sandstone with mean grain size distribution of 500 μm. This facies is associated with a sandstone with high porosity and permeability and low clay content. Facies B is a transition facies between facies A and C and corresponds to a medium grained sandstone with mean grain size distribution of 250 μm. It is worth noting that a strong correlation between grain size and clay content is reported by several authors (e.g., Saner et al. 1996), so this knowledge has been accordingly incorporated into the model by assigning clay-dependent grain sizes to the three facies, i.e., the higher the clay content, the lower the mean grain size distribution.

6.3.2 Petrophysics model

The geological model described above is used as the basic model in which petrophysical properties are populated assuming a meaningful petrophysics model. A petrophysics model includes a set of the theoretical and experimental correlations among various sets of petrophysical properties. The model is required to be validated using available well log and core data. Here, the effective porosity model is first generated using Gaussian geostatistics and shale content and total porosity models are then computed assuming a dispersed clay distribution (Thomas and Stieber 1975; Marion et al. 1992), (Figure 6.4a). Horizontal permeabilities in the X and Y directions are equal and calculated based on the extension of the dispersed clay model for permeability introduced by Revil and Cathles 1999 (Figure 6.4b and 6.4c). It is worth mentioning that permeability fields depend on porosity, shale content, grain size distribution, and the degree of cementation ; subsequently facies A, B, and C are assigned different trends in

permeability-shale content and permeability-porosity domains based on their grain sizes. The vertical permeability field is taken as 25% of the horizontal permeability field for the entire reservoir. It is worth mentioning that joint relationship of permeability and resistivity has been taken into account by assigning three different cementation factors to three facies.

So far, the effective and total porosities, shale content and directional permeabilities are modeled using geostatistics and theoretical correlations according to dispersed clay distribution. Next, I should initialize the reservoir for water saturation and pore pressure. An experimental correlation (Uden et al. 2004; Spikes et al. 2007) between water saturation and shale content is combined with the dual water model (Best 1980; Dewan, 1983; Clavier, 1984) to compute clay bound water (Swb), effective water saturation (Swe), total water saturation (Swt), and oil saturation (So) (Figure 6.4d). Initial reservoir pore pressure is simulated assuming a linear hydrostatic gradient from the top to the bottom of the reservoir. Figure 6.5 summaries the distribution of petrophysical properties for a 2D cross section in the middle of the 3D reservoir. Figure 6.6 shows the histogram of petrophysical properties for the entire reservoir volume. Table 6.1 shows the petrophysical properties of the three facies within the reservoir.

Now, a complete set of dynamic and static reservoir parameters have been generated and will be used to launch a reservoir simulation and to predict time-dependent subsurface distributions of water saturation, pore pressure, and surface well production data.

6.3.3 Reservoir simulation

Fluid flow simulation combines three fundamental laws governing fluid motions in porous media. These laws are based on conservation of mass, momentum, and energy

(Aziz and Settari 1976). In this research, a commercial finite difference reservoir simulator, Eclipse 100, is utilized to replicate a waterflood enhanced oil recovery on a black-oil 2D reservoir containing oil, soluble gas, and water. The reservoir has no natural water drive. In addition, because of the high pressure conditions no gas is produced in the reservoir. Thus, solution gas is the only drive mechanism forcing oil to be produced. This drive is so weak that implementation of water injection is required to enhance oil recovery. The other reason for selecting a water-flood is to provide some insights into potential water-floods in deepwater reservoirs where seismic and CSEM data are the primary and sometimes the only source of data.

As discussed earlier in developing the petrophysical model, the effective porosity model is constructed via Gaussian simulation. The relationships among petrophysical properties including porosity, permeability, and shale content are theoretically derived assuming the dispersed clay distribution. Then an experimental correlation combined with the dual water theoretical model is employed to obtain the initial water saturation from shale content. Finally a linear hydrostatic pressure gradient is selected to initialize the reservoir pore pressure distribution. The same grid block dimensions used to generate the geological model, i.e. a square 10 by 10 meters, are used to simulate fluid flow; hence mathematical upscaling was not necessary.

The capillary pressure data, the relative permeability curves, and PVT (pressure, volume, and temperature) properties of reservoir fluids are borrowed from the well-known SPE 9th (Killough 1995) model (Figure 6.7) and slightly modified to meet research objectives. As shown on the capillary pressure and relative permeability curves, the value of water saturation at which water starts to flow, i.e. irreducible water saturation is 0.15 and this term for oil is called residual oil saturation and equals 0.12. In practice, irreducible water saturation and the corresponding capillary pressures are strongly clay-

dependent in shaly sandstones, but here for the sake of modeling ease I assume a single capillary pressure curve and the constant irreducible water saturation is true for the entire reservoir. The Pressure below which the dissolved gas releases from oil, i.e. bubble point, is 2000 psi.

For a period of 10 years, the waterflood schedule is simulated by using two injectors at the corners and one producer in the middle of the 2D reservoir (Figure 6.8). In this period, saturations and pressures values for each reservoir grid block are exported after each year. Collecting this database allows us to analyze the sensitivity of the corresponding rock resistivity and CSEM data to a wide range of changes in saturation. Figure 6.8 shows the snapshots of water saturation and pore pressure distributions for the initial reservoir state and after production at different calendar times. With the start of production/injection, oil is replaced by water near the injectors and a portion of mobile oil will be extracted by the producer. Increasing the time, more oil will be replaced with water, hence; more oil will be produced. In other words, behind the waterfronts, the water saturation is increasing monotonically towards the injectors, meaning more oil is gradually displaced as more water is injected. In addition, one can clearly see that the behavior of the pressure front is very different from that of the waterfront. In fact, pressure has a wave motion like behavior and propagates very fast, but water has a mass bulk movement and moves slowly.

Figure 6.9 illustrates surface reservoir simulation outputs, i.e., production data, for a period of 10 years throughout the reservoir life. Water injectors perforate the entire 350 meters of reservoir thickness and are set to a constant water rate of 400 STB/Day. The only producer located in the middle of reservoir also perforates the whole reservoir thickness and is initially set to a constant oil rate of 750 STB/Day. The reservoir initially starts producing oil with a plateau of 750 STB/Day. During this period, volumetric

average pressure of the reservoir increases from 3200 to 3920 psi. After 2650 days, this rate is not affordable for the reservoir, so production strategy is intentionally changed to a constant bottom hole pressure (BHP) of 2600 psi for the producer. From this point the oil rate will decrease and a significant pressure drop is observed. The reservoir always produces above the bubble point pressure, i.e., 2000 psi; consequently, no gas is produced within the reservoir. However, dissolved gas will be released from live oil at the surface and gas will be produced with a similar production trend as oil. A slight water production occurs from the beginning up to 2000 days of production, but it increases significantly afterward. CPU time for running 10 years of simulation of the 2D reservoir is 240 seconds.

Constructing a realistic reservoir model with spatial variations of petrophysical properties and simulating varying scenarios for the changes in water saturation due to the designed waterflood, I will be able to compute the spatial distributions of rock resistivity using the rock-fluid physics model described in the following section.

6.3.4 Rock and fluid physics model

Using rock physics modeling, one can transform the petrophysical properties of a reservoir to rock resistivity, which can then be used to simulate CSEM data. This process is an essential step in any inversion project aimed at estimating petrophysical properties. In CSEM reservoir monitoring, fluid flow simulation, rock-physics, and CSEM forward modeling can be effectively combined to simulate CSEM data and, ultimately, to predict reservoir properties trough an inversion algorithm.

Porosity in clastic rocks is controlled by two main factors. The first one is sedimentation, i.e., porosity variation resulting from variations in sorting and clay content. The second factor is diageneses, i.e., porosity reduction due to pressure solution,

compaction, and cementation (Avseth et al. 2005). Here, I deal with a strandplain geological architecture filled with poorly consolidated shaly sandstone. As described in the petrophysics model, the clay distribution is dispersed or pore-filling. The corresponding porosity-clay model was introduced by Thomas and Stieber (1975) and further developed by Marion et al. (1992) and Yin, (1992). As mentioned earlier, the reservoir is originally deposited as a clay-free geobody, however; due to post-depositional diagenesis, dispersed clay is produced and it is the main factor reducing porosity and permeability of the reservoir.

Archie' equation (Archie 1942) has been widely used in the geosciences community to relate petrophysical properties of reservoir rocks to electrical resistivity. However, this theory is not valid in shaly sandstones due to the excess conductivity of clay. Through the evolution of well log interpretation, several shaly-sand resistivity models have been developed for different types of clay distribution, i.e., dispersed and laminated clays. Among these models, Waxman-Smits model (1968) and dual water models (Best 1980; Dewan, 1983; Clavier, 1984) are more applicable for dispersed clay distributions. In this study, I use the dual water model because several of its parameters can be computed from well logs (Dewan, 1983) and it can be efficiently combined with the dispersed clay model. Formation water resistivity depends on salinity and temperature. I use Arps' empirical equation (Arps, 1953) to calculate the free and bound-water resistivity. Appendix C summarizes the rock and fluid model employed. Figure 6.10 summarizes the rock physics model employed. Panel (a) shows the effect of changes in porosity at constant water saturation on rock resistivity. As expected based on Archie's equation, resistivity decreases by increasing porosity. Panel (b) displays the effect of saturation at constant porosity or clay content on rock resistivity. Resistivity decreases by

increasing water saturation because of the conductivity of saline water. Panel (c) illustrates the joint effect of porosity and saturation on rock resistivity.

It is worth mentioning that the corresponding petro-elastic model for the reservoir can be efficiently simulated by combining the Thomas and Stieber petrophysics model (1975), the Dvorkin-Gutierrez rock physics model (2002), the fluid physics model (Batzle & Wang 1992), and a modified Gassmann theory (Dvorkin et al. 2007) for shaly sandstones. The joint modeling of the elastic and electrical properties of reservoir rocks will lead to the consistent forward modeling algorithms for joint inversion of seismic and CSEM data. Further applications of using the petro-elastic model is presented in chapter two where seismic rock and fluid physics templates are investigated to discriminate between the effects of changes in fluid saturation and pressure during a waterflooding scenario (Shahin et al. 2010b). Figure 6.11 compares the seismic and CSEM rock physics modeling in terms of their time-lapse signals due to changes in effective water saturation. Rock resistivity (Rt) changes significantly, about 100%, but elastic parameters including P-wave velocity (Vp), S-wave velocity (Vs), and density (Rho) are all less affected, e.g., at most 14% (See Shahin et al. 2010b and chapter two for further sensitivity analyses of other elastic parameters with respect to fluid saturation and pressure).

Finally, to replicate the surrounding offshore sedimentary basin in which the reservoir is embedded, a 1D resistivity model is generated by correlating the P-wave velocity and resistivity based on the modified Faust equation by Hacikoylu et al. (2006). A resistivity of 0.33 ohm-m is appended to the first 1km of the model, representing the overlying conductive ocean.

Figure 6.12 illustrates three resistivity logs extracted from the middle of the 2D reservoir in the vicinity of the producer. These are related to the base case (t0) before waterflooding and two monitor surveys (t05 and t10, i.e., after 5 and 10 years of

waterflooding, respectively). As expected, resistivity decreases as injected saline water replaces oil. The waterfront is clearly mapped on resistivity logs. Note that the absolute values of the resistivity, less than 10 ohm-m, are significantly lower than that of the simple "canonical" reservoir considered in many previous studies (e.g., Constable and Weiss, 2006; Key, 2009), in which reservoirs of 100 ohm-m electrical resistivity and 100 m thickness are investigated. This fact is due to the excess conductivity of clay and makes my reservoir seemingly a relatively hard-detectable exploration target. However it is also worth noting that CSEM is predominantly sensitive to the resistivity-thickness product of the reservoir (e.g., Constable and Weiss, 2006). While the reservoir considered here has a resistivity of only 10 ohm-m, its thickness of 300 m results in a resistivity-thickness product only about a factor of three lower than for the canonical reservoir, therefore making it a good exploration target. Now, the key question is whether or not the reservoir is a difficult target for monitoring purposes.

Figure 6.13 displays the percentage of time-lapse changes in effective water saturation and the associated changes in rock resistivity and seismic acoustic impedance. Here, for any parameter the base survey value is subtracted from that of the monitor survey and then normalized using that of the base survey. For plotting of the changes in resistivity, a minus sign is applied to have a consistent color display for flood geometry between saturation, acoustic impedance, and resistivity models. As confirmed in Figure 6.11, resistivity is much more sensitive to water saturation than acoustic impedance and that is why CSEM data are potentially more powerful than seismic data to monitor waterflooding. Of course, I must keep in mind that CSEM data have less vertical resolution than seismic reflection data due to its diffusive nature.

6.4 CSEM MODELING

The underlying physics of the EM field is governed by Maxwell's equations which are the mathematical formulation of the laws explaining the interaction of electric and magnetic fields. Throughout the history of CSEM technology, various algorithms have been developed to analytically and/or numerically solve Maxwell's equations for different earth structures. Depending on the complexity of the earth model and computer resources, one can select a suitable algorithm for the problem at hand. Here I explore the use of 1D and 2.5D CSEM modeling of the time-lapse reservoir simulations.

6.4.1 One-dimensional CSEM modeling

The most widely used earth model in petroleum exploration is a horizontally-stratified geo-electric model representing a typical conductive sedimentary basin in which a resistive reservoir is embedded. The corresponding approach computing the response of dipoles embedded in such a media is called one-dimensional forward modeling and is well studied in the open technical literature, e.g., Chave and Cox (1982), Flosadottir and Constable (1996). To simulate frequency domain CSEM data, here I perform numerical 1D forward modeling using the algorithm described in Key (2009). In this experiment, I employ three sets of resistivity logs (Figure 6.12) at the vicinity of the producer in the middle of a 2D reservoir. As mentioned earlier, these logs are related to a base (t0) and two monitor surveys (t05 and t10). Figure 6.14 displays the 1D CSEM data associated with the base survey (t0) using inline, crossline, and vertical dipole transmitters all located 20 m above the seabed. The absolute phase and amplitude of the electric and magnetic fields for a single frequency of 0.25 Hz are simulated on sea-floor detectors at different orientations, i.e., inline, crossline, and vertical field components. Note that amplitude responses of CSEM data are larger than the present-day receiver noise floor almost the entire offset coverage. Noise floor is around 10^{-15} V/Am2 and 10^{-18} T/Am for

electric and magnetic fields, respectively (Constable and Weiss, 2006; Hoversten et al. 2006). In general, as demonstrated by previous studies, e.g., Um and Alumbaugh (2007) and Key (2009), employing multi-component and multi-frequency measurements in interpretation and inversion of CSEM data will lead to better reservoir characterization.

Figure 6.15 shows the 1D CSEM time-lapse changes in response to waterflooding after 10 years between the base survey (t0) and monitor survey (t10) illustrated in Figure 6.12. Inline, crossline, and vertical dipole transmitters are employed. As before, the absolute amplitude and phase of the electric and magnetic fields for a single frequency of 0.25 Hz are simulated on sea-floor detectors for different field components. Similar to the model in Figure 6.12, amplitude of the CSEM data for the base survey are subtracted from that of the monitor survey and then normalized using that of base survey. This is called the percentage amplitude ratio. For illustration of phase, the difference between base and monitor surveys are displayed as phase difference in degree. When comparing different transmitters, the weakest anomalies are associated with crossline transmitter; inline and vertical transmitters have almost the same size of anomaly that are significantly greater than for the crossline transmitter. These observations suggest that inline transmitter should be the best option for CSEM reservoir monitoring, because it shows the strongest anomaly and its data acquisition is cheaper and more practical than other transmitter configurations. This finding is in general agreement with previous CSEM studies documenting superior resolution of the inline transmitter (e.g., Constable and Weiss, 2006; Key, 2009). Detailed analysis of the anomaly shapes for inline transmitter suggest that inline electric and crossline magnetic field components have relatively semi-symmetry trends around the centered range, i.e. 10 km, while the vertical electric field monotonically increase with increasing offset between transmitter and receivers. For the crossline transmitter, inline magnetic, crossline electric, and vertical

magnetic field components all show semi-symmetry trends around the centered range. Finally for vertical transmitter, all field components, i.e., inline electric, crossline magnetic, and vertical electric field components monotonically increases as offset increases and they all closely follow one another. This fact suggests that the discrimination of field components associated with a vertical transmitter in the time-lapse frequency-domain CSEM is very restricted. In other words, field components collected from vertical transmitters provide dependent data for both amplitude and phase and in particular for the phase information. Furthermore, given its large anomaly size and the practical efficiency of collecting inline data, I restrict my analyses to inline transmitter recording inline electric and crossline magnetic field components for the reminder of modeling in this chapter.

Figure 6.16 illustrates 1D CSEM time-lapse changes in response to waterflooding after 5 and 10 years. Here I employ an inline transmitter and simulate inline electric, crossline magnetic, and vertical electric field components for a single frequency of 0.25 Hz. As expected, the anomalies corresponding with 10 years of waterflooding are significantly higher than those related to 5 years of waterflooding.

Figure 6.17 displays the frequency analysis for 1D CSEM time-lapse changes in response to 5 and 10 years of waterflooding. For both the amplitude ratio and phase difference, higher frequencies lead to larger time-lapse anomalies at shorter offsets. However, much of large anomaly at high frequencies is where the data are below the noise levels (not shown here). Besides, the higher frequency, the smaller the anomalies in mid to far offset due to EM attenuation. Note that my observations are consistent with the frequency analysis for CSEM exploration in previous studies, e.g., Um and Alumbaugh (2007).

It is worth mentioning that the large time-lapse anomalies reported in all the above 1D modeling (0-40% in amplitude ratio and up to 100 degree in phase difference) can be easily monitored considering a time-lapse repeatability of 1-5% as reported in the literature, e.g., Orange et al. (2009) and Zach et al. (2009). I note that 1D anomalies in CSEM exploration are significantly higher than those modeled for the same 2D and 3D reservoirs, as reported by other authors, e.g., Um and Alumbaugh (2007) and Orange et al. (2009). Now the key question for this study is whether or not the same statement is true for 1D versus 2D and 3D time-lapse anomalies.

6.4.2 2.5D CSEM modeling

One-dimensional CSEM modeling is an accurate approach to model layered sedimentary basin and it can be readily used to design survey parameters and to obtain prior knowledge about water depth, target depth, and sediment resistivity (Constable and Weiss, 2006 & Zach and Frenkel 2009). Many offshore sedimentary basins, however; are so structurally complicated that they can not be modeled by 1D modeling algorithms. To overcome this problem, many forward modeling approaches; integral equations, finite difference and finite element, have been introduced to evaluate numerical approximations of Maxwell's equations for complex earth structures. Integral equation methods can provide fast and accurate simulation of CSEM data for compact 3D geo-bodies embedded in a 1D layered background (Zhdanov 2009). On the other hand, finite difference and finite element methods are powerful in simulating the CSEM data in complex 3D structures where integral equation method requires tremendous computer resources due to large matrices involved (Zhdanov 2009). Recently, CSEM has been known as a complementary method for seismic. Subsequently, structural details interpreted from seismic can be used to constrain the CSEM data; resulting in joint interpretation and

inversion of CSEM-Seismic data to extract elastic and electrical properties of petroleum reservoirs, Hoversten et al. (2006) and Hu et al. (2009). Finite difference methods, e.g., Newman and Alumbaugh (1995), limited to regular grid implementations, are used to include complex structural details obtained from seismic data. On other hand, finite element methods with flexible grid implementations, e.g. triangular meshing, are more powerful than finite difference to include structural details from seismic data interpretation. However, obtaining accurate results with flexible and fully unstructured triangular grids from finite element methods is costly especially in 3D structures mainly due to the representation of irregular grids in computer memory. To summarize, depending on the amount of structural constrains, available computer resources, and the complexity of the earth model, one can select either of these methods to simulate the CSEM data.

In this chapter, I utilize a recently developed (Key and Ovall, in revision) finite element code to simulate frequency domain 2.5D CSEM data, i.e., an EM source emits a 3D field into a 2D conductivity structure. This is a parallel goal-oriented adaptive finite element code using a new approach over the method proposed earlier in Li and Key (2007), which makes the optimal use of the several recently developed algorithms to enhance the performance of the finite element methods. A fully unstructured triangular element grid is implemented to handle earth structures with any level of complexity. A sparse-directly matrix factorization method is used to rapidly solve the linear system with multiple right hand-side vectors associated with multiple EM transmitters. Finally, an automated adaptive algorithm is employed to refine grids iteratively starting from a coarse grid network to a denser one until a user-specified degree of accuracy is obtained.

To simulate the production-induced CSEM response of the reservoir, I implement a 2.5D modeling over the 2D reservoir embedded into the 1D background. In this

experiment, I employ 41 inline transmitters, located 20 meters above the sea bed, and 41 receivers, located on the sea bed, all equally spaced every 500 meters. The adaptive finite element procedure is used to refine the triangular element grid until the solutions achieved an estimated accuracy of 1% or better. Figure 6.18 illustrates the starting and final refined model grid created by triangular meshing over the entire model. Note that the unstructured grid employed can easily incorporate different scales of heterogeneities in the background and reservoir sections, leading to an optimized grid network for the finite element algorithm which doesn't require a massive number of finely spaced grid elements, a limitation of rectangular structured grids employed in finite difference methods. Next, the inline electric and crossline magnetic field components are computed for a single frequency of 0.25 Hz. Finally, amplitude ratios and phase differences between the base and monitor surveys are calculated. Figure 6.19 and Figure 6.20 show the corresponding time-lapse anomalies for the magnetic and electric field components, respectively. The 2D anomalies are significantly weaker than the 1D anomalies, as expected due to the finite-width of the resistive 2D reservoir. Considering a time-lapse repeatability for real data that is likely to be at best about 1-2% using currently available nodal CSEM receivers and a deep-towed transmitter, the anomaly associated with 5 years of waterflooding (3-4% anomaly in amplitude ratio) would be just detectable, but the one corresponding to 10 years of waterflooding (6-10% anomaly in amplitude ratio and up to 10 degree in phase) should be measureable with existing CSEM survey technology. Future improvements to acquisition technology for time-lapse monitoring, such as permanently deployed sensors or sea-bottom cable systems might reduce the measurement uncertainties, particularly those associated with navigation of the transmitter, to well below 1%, making this 2D anomaly an appreciable target for monitoring purposes. It is worth noting that during these time-lapse surveys cumulatively

1330000 and 2290000 Stock Tank Barrels (STB) of oil and 1100000 and 1890000 Million Standard Cubic Feet (MSCF) of gas is produced due to injection of 1440000 and 2900000 STB of water after 5 and 1o years, respectively. This information in conjunction with other parameters, e.g., reservoir depth, water depth, reservoir lithology type, oil-gas-water electrical properties, etc., can be used to develop criterion for detectability of other reservoirs located at comparable conditions.

The results presented in this study suggest that for a realistic reservoir to be monitored at a short time lag, less than 5 years, a repeatability of 1-5% or even less is required for the basic CSEM measurements. As reported by Orange et al. (2009), this is likely to be impractical using the current CSEM technology which employs free-falling receivers and towed streamers. Besides, several other factors can ruin the small time-lapse signals. Some of the major ones are errors in positioning of transmitters and receivers, inhomogeneous near surface, effect of time-varying ocean conductivity, and changes in onsite field instruments during production. All these issues have to be addressed and appropriately modeled in order to make the time-lapse CSEM more appealing for reasonable time intervals through the reservoir's life.

6.5 SUMMARY AND CONCLUSIONS

The geologically consistent petro-electric model developed in this chapter explicitly relates petrophysical properties to rock resistivity. As a model, it can be generalized to other geological scenarios and, ultimately, applied to quantitative CSEM reservoir characterization and monitoring. In addition, this model is well-suited for elastic modeling aimed to simulate seismic data.

As an example of application, I simulate three sets of 2D resistivity models corresponding to the initial reservoir state, after 5 years, and 10 years of waterflooding

into a black oil reservoir. Then a base and two monitor time-lapse CSEM surveys are simulated via accurate numerical algorithms. 2.5D CSEM modeling demonstrates that a detectable time-lapse signal after 5 years and a strong time-lapse signal after 10 years of waterflooding are attainable with the careful application of currently available CSEM technology. In contrast, 1D CSEM data acquired at the middle of reservoir exhibits relatively strong time–lapse signals for both monitor surveys. These observations demonstrate that 1D modeling of a 2D reservoir can be misleading and results in the overestimation or under prediction of the time-lapse signal and the associated swept oil in the waterflooding enhanced recovery.

The results presented in this study clearly show that repeatability of CSEM measurements for monitoring of producing reservoirs are extremely important at large time intervals, 10 years, but they are limited at desired time intervals, less than 5 years, through the entire reservoir history. Furthermore, factors restricting the repeatability of CSEM measurements, e.g., errors in positioning of transmitters and receivers, inhomogeneities in the near surface, effect of time-varying ocean conductivity, and changes in field instruments during production have to be addressed properly to preserve these relatively small time-lapse signals. Finally, more detailed and 3D time-lapse CSEM synthetic modeling-inversion and time-domain CSEM simulation will shed light on complications probably not seen in my 2.5D frequency domain analyses.

Table 6.1: Facies petrophysical properties associated with the synthetic reservoir model.

Facies	Total porosity	Effective porosity	Shale volume	Effective water saturation	Mean grain size (micron)	Horizontal permeability (mD)
A	0.11–0.18	0.01–0.12	0.25–0.34	0.45–0.62	80	0.37–10
B	0.18–0.25	0.12–0.22	0.15–0.25	0.27–0.45	250	68–1400
C	0.25–0.37	0.22–0.37	0.0–0.15	0.15–0.27	500	6800–91000

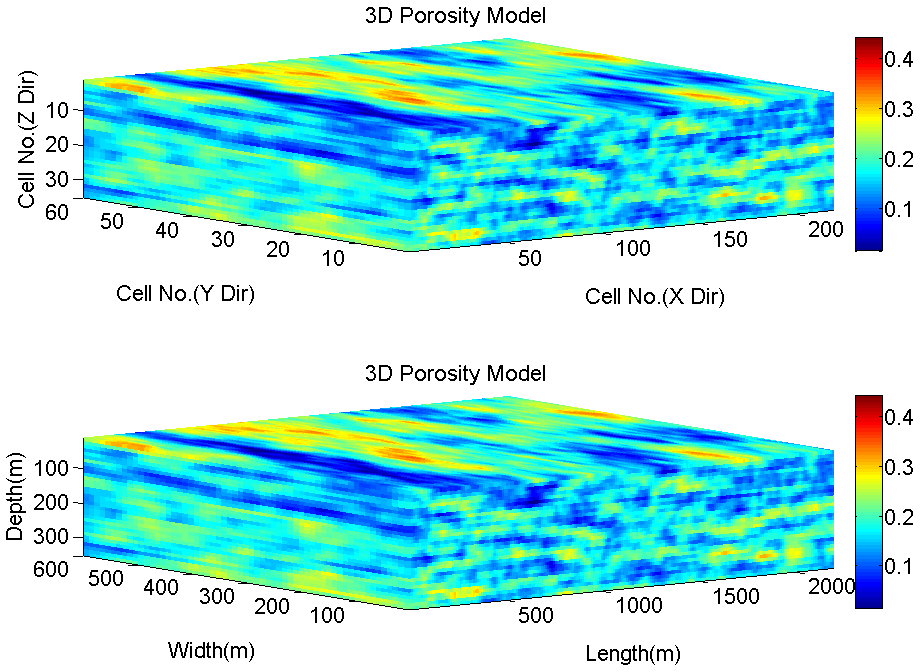

Figure 6.1: 3D distribution of effective porosity model (Christie and Blunt, 2001) associated with synthetic geologic model used for the numerical simulation of seismic and multi-phase fluid-flow. The model is described on a regular Cartesian grid. The model size is 220*60*35 cells in X (east-west), Y (north-south), and Z (depth) directions, respectively (top panel). The grid size defining the cells is 10*10*10 meters, so the model dimension is 2200m*600m*350m (bottom panel).

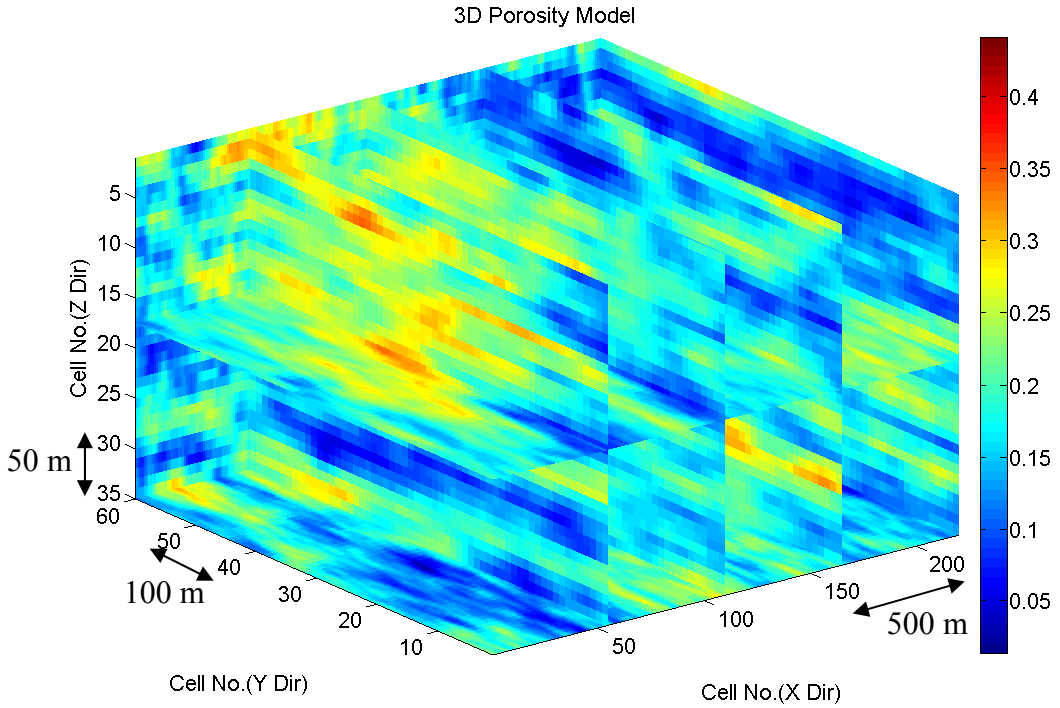
3D Porosity Model
Cell No.(Z Dir)
5
10
15
20
25
30
35
50 m
60
50
40
30
20
10
100 m
Cell No.(Y Dir)
50
100
150
200
500 m
Cell No.(X Dir)
0.4
0.35
0.3
0.25
0.2
0.15
0.1
0.05

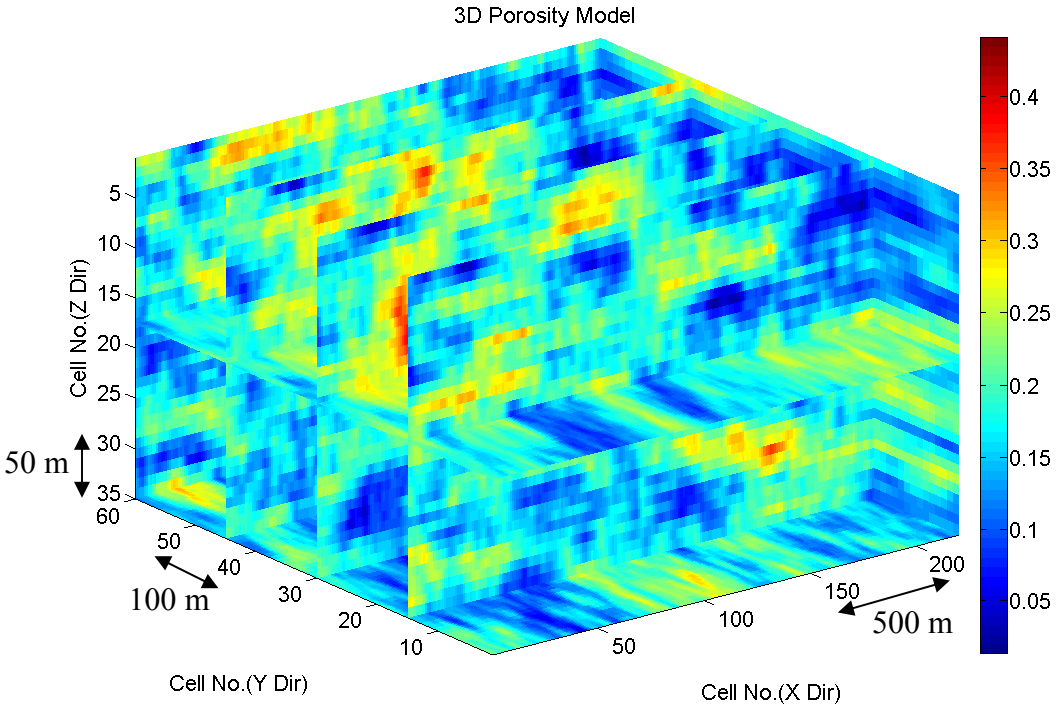
3D Porosity Model
Cell No.(Z Dir)
5
10
15
20
25
30
35
50 m
60
50
40
30
20
10
100 m
Cell No.(Y Dir)
50
100
150
200
500 m
Cell No.(X Dir)
0.4
0.35
0.3
0.25
0.2
0.15
0.1
0.05

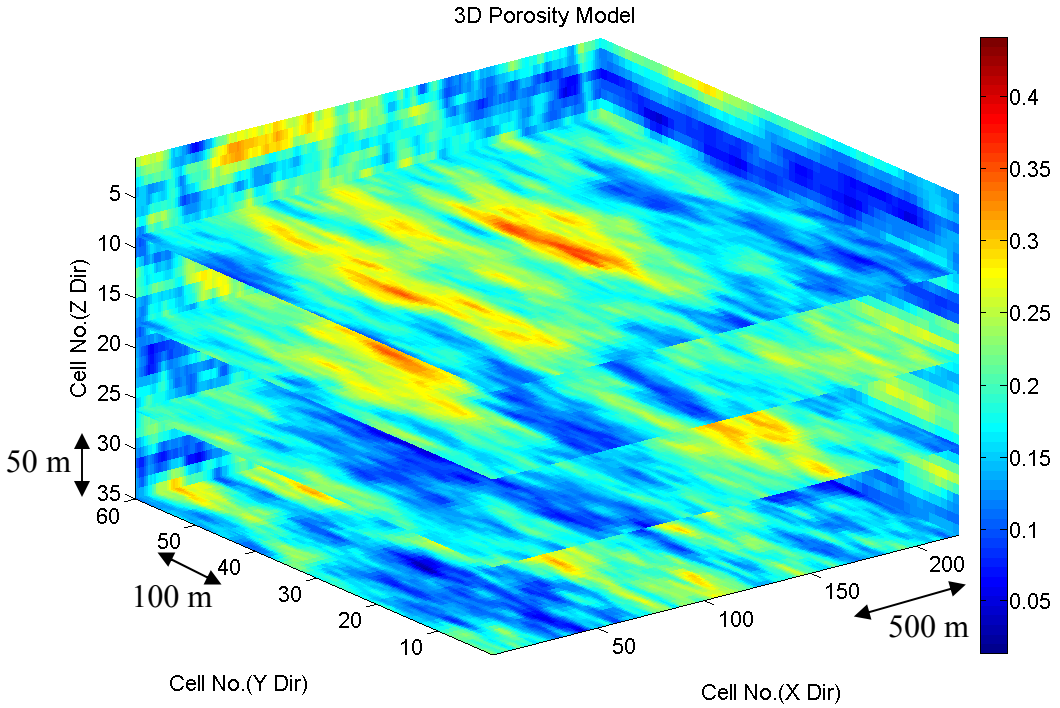

Figure 6.2: Three directional cross-sections of 3D effective porosity model in Figure 2.1.

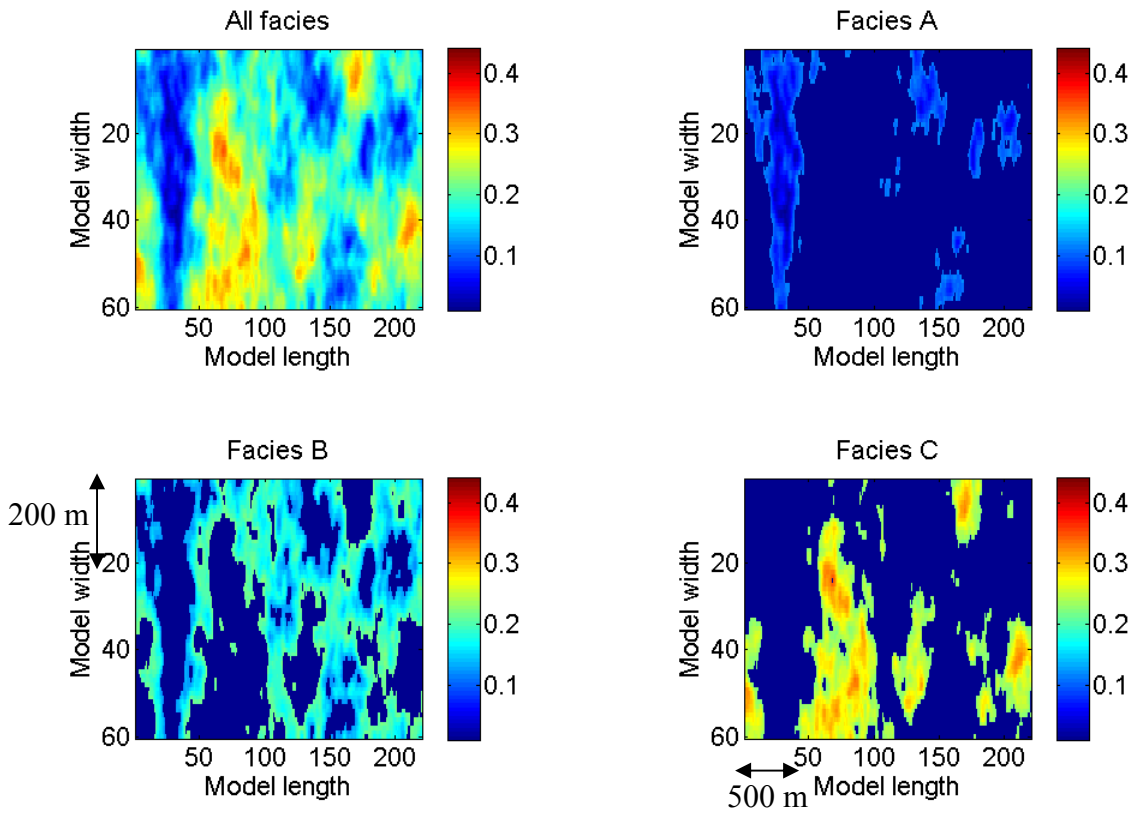

Figure 6.3: Map view of petrophysical facies A, B, and C overlaid on 2D distribution of effective porosity model. Grid numbers are used to show reservoir dimensions in two horizontal directions.

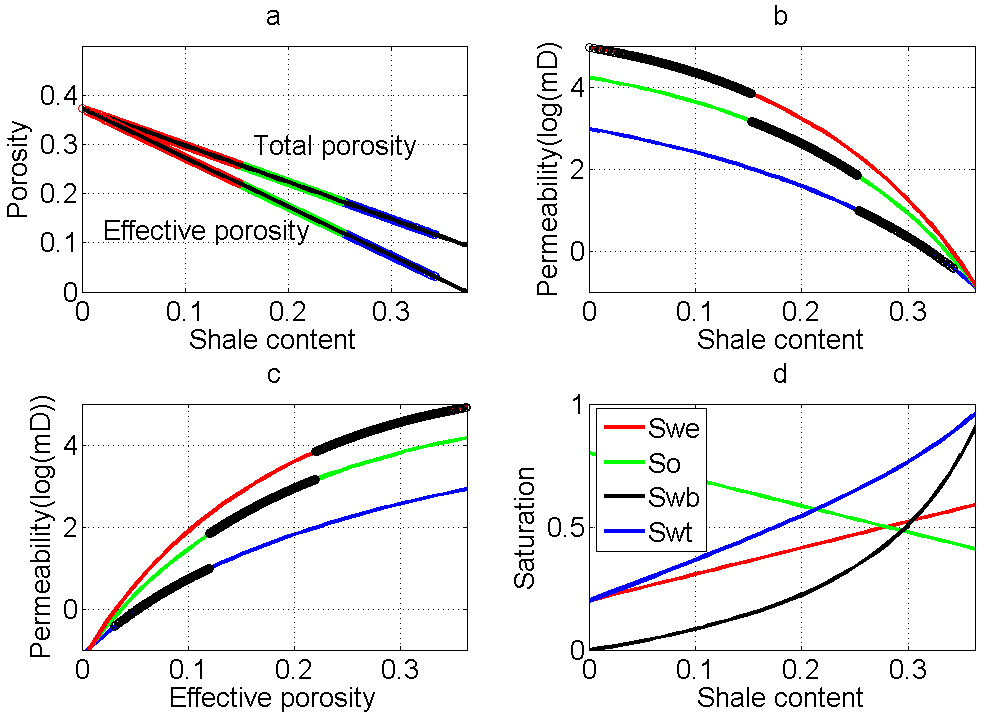

Figure 6.4: Petrophysics model. Panel a shows the dispersed clay model for porosity reduction due to increasing of clay. Panel b dispalys horizontal permeability versus shale content. Panel c is permeability vs. effective porosity. In panels a,b, and c, three colors are associated with three facies A(in blue), B(in green), and C(in red). Black dots in panels b and c are projected reservoir points . Panel d shows fluid saturations vs. shale content. Swe, So, Swb, and Swt are effective water saturation, oil saturation, caly bound water saturation, and total water saturation, respectively.

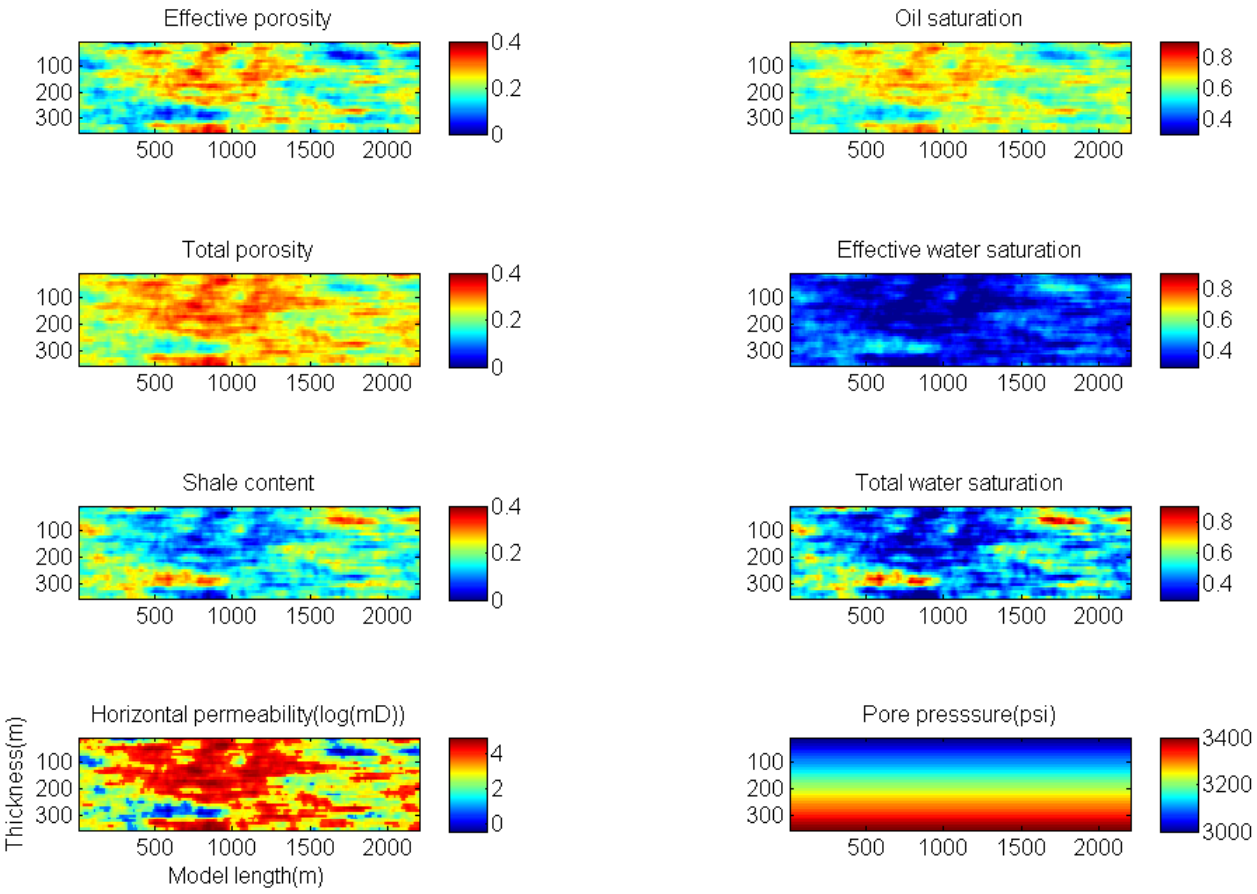

Figure 6.5: Distribution of petrophysical properties for a 2D cross-section in the middle of the 3D reservoir.

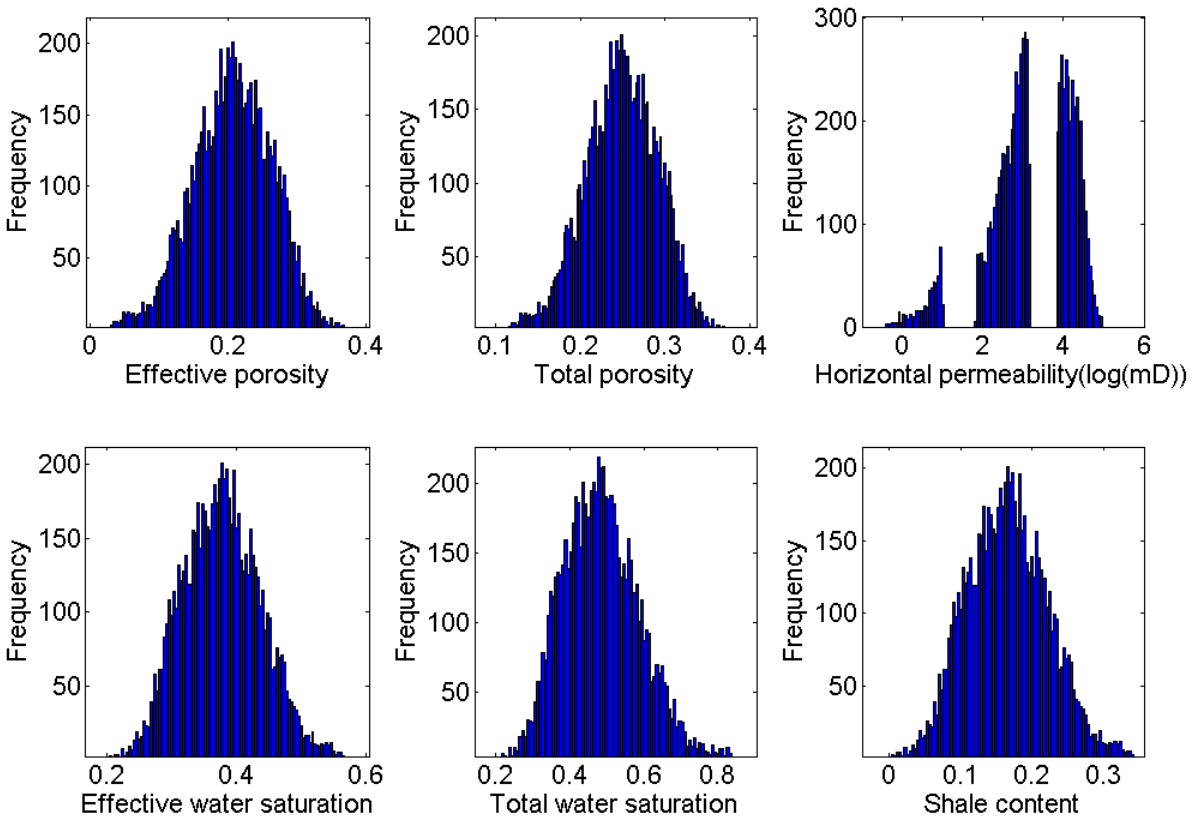

Figure 6.6: Histogram of the petrophysical properties. Petrophysical facies are overlapped in all domains except in permeability domain where three distinct facies are separated.

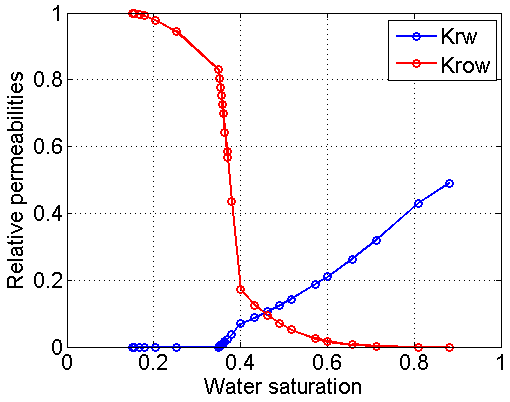
Krw
Krow
Relative permeabilities
Water saturation

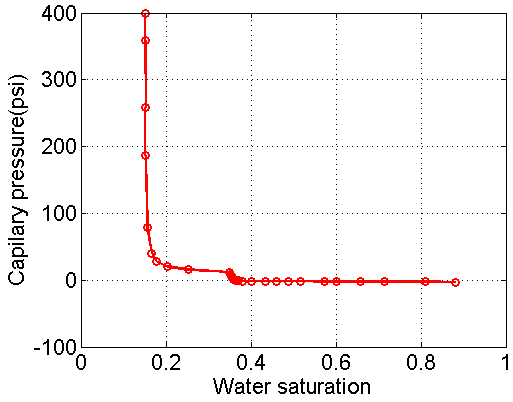
Capilary pressure(psi)
Water saturation

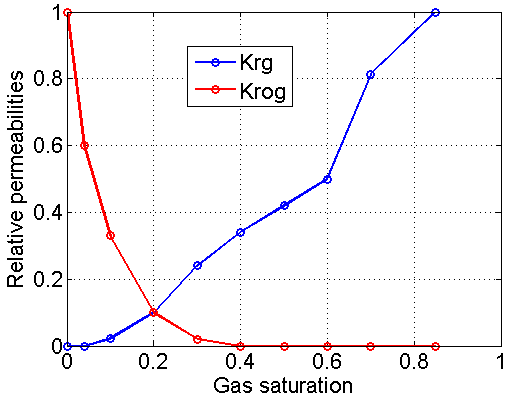
Krg
Krog
Relative permeabilities
Gas saturation

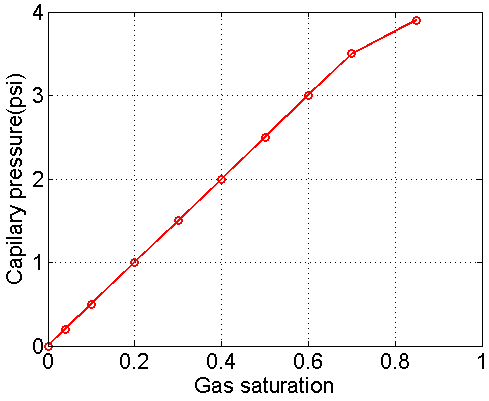
Capilary pressure(psi)
Gas saturation

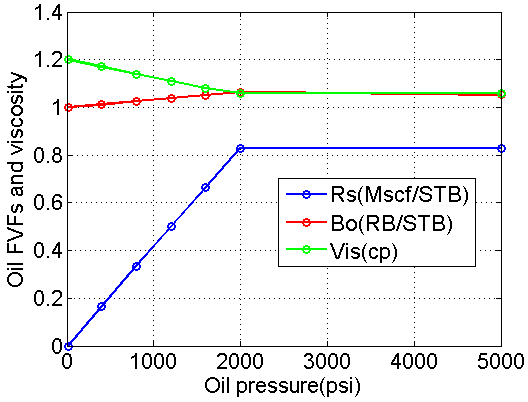
Rs(Mscf/STB)
Bo(RB/STB)
Vis(cp)
Oil FVFs and viscosity
Oil pressure(psi)

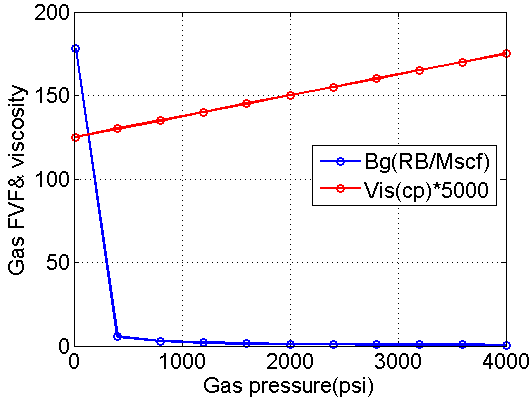
Bg(RB/Mscf)
Vis(cp)*5000
Gas FVF& viscosity
Gas pressure(psi)

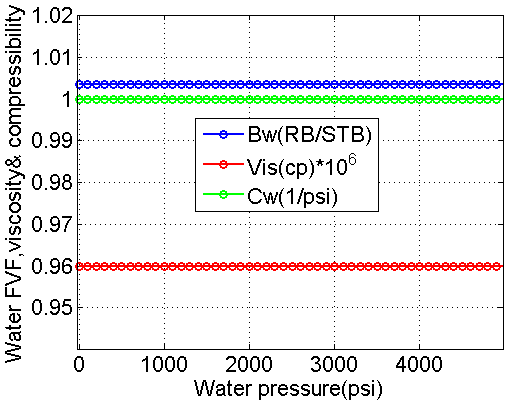

Figure 6.7: The capillary pressures data, the relative permeability curves, and PVT properties of reservoir fluids. FVF stands for Formation Volume Factor.

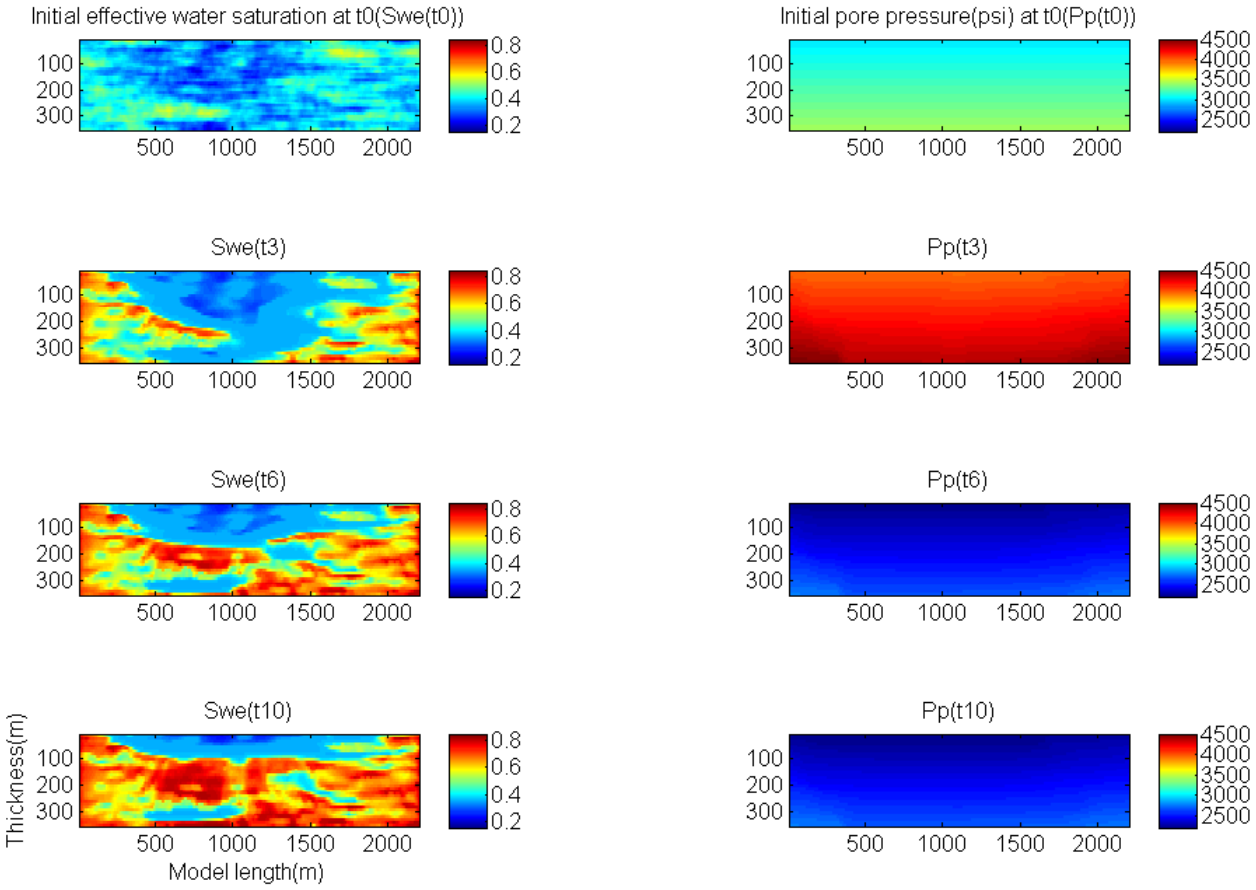

Figure 6.8: Snapshots of effective water saturation and pore pressure (psi) distributions at initial reservoir state (t0) and after production at different calendar times (three(t03), six (t06), and 10(t10) years).

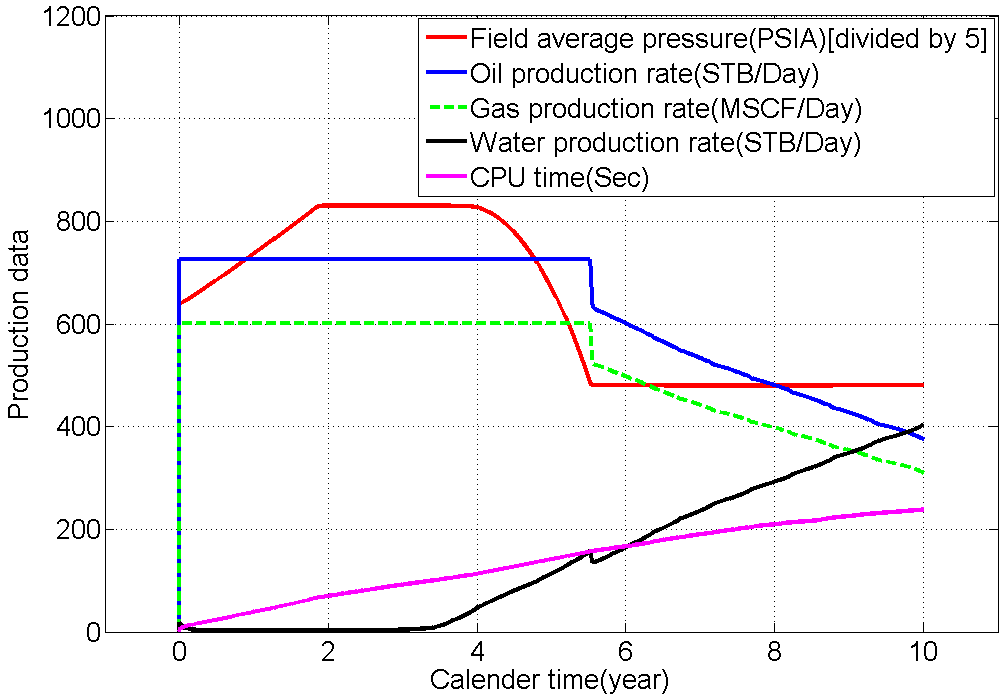

Figure 6.9 Surface reservoir simulation outputs, i.e., production data, for a period of 10 years of waterflooding to enhance oil recovery.

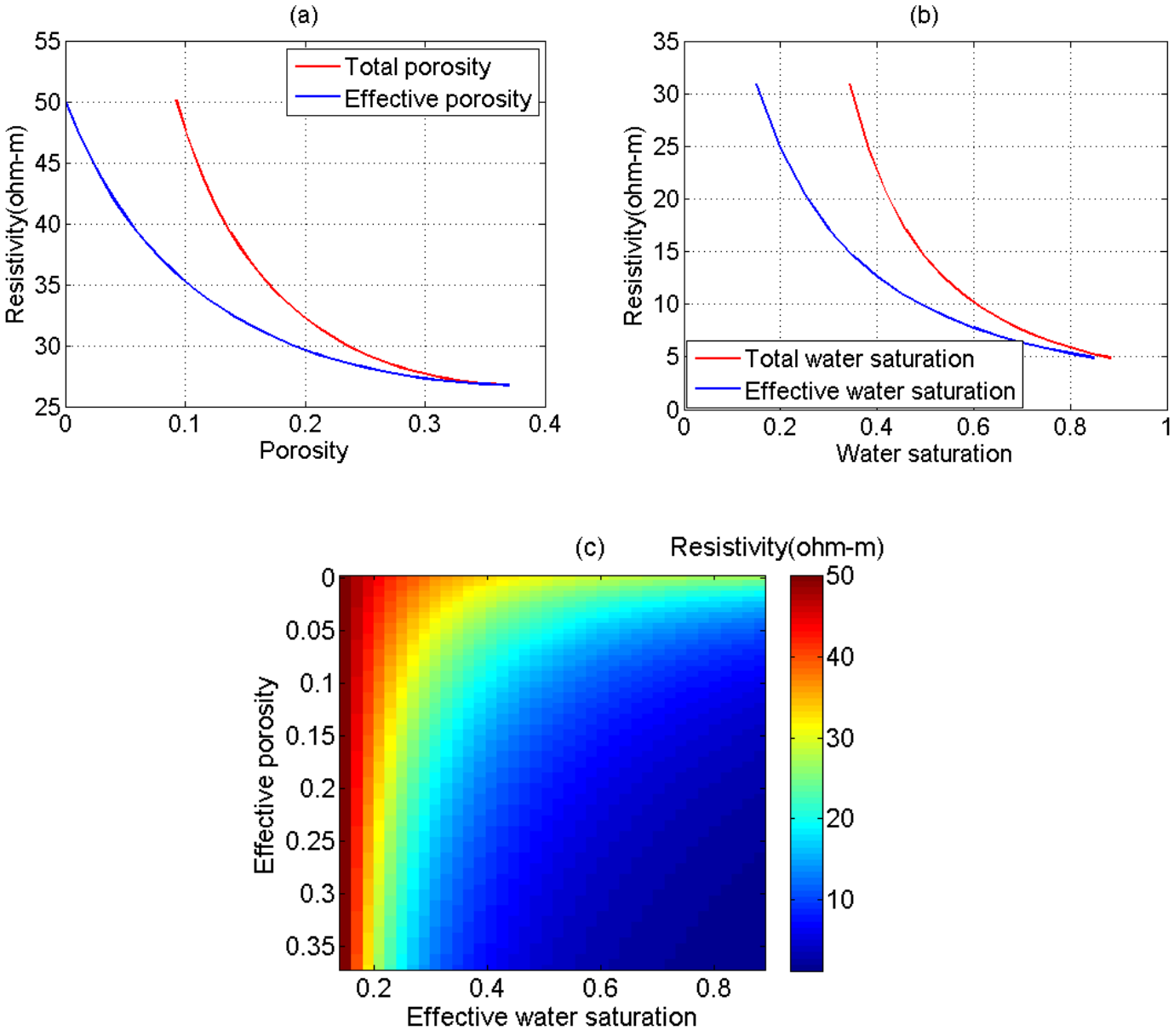

Figure 6.10 Rock physics model displaying the effects of porosity (Panel a), saturation (Panel b), and joint porosity-saturation (Panel c) on rock resistivity.

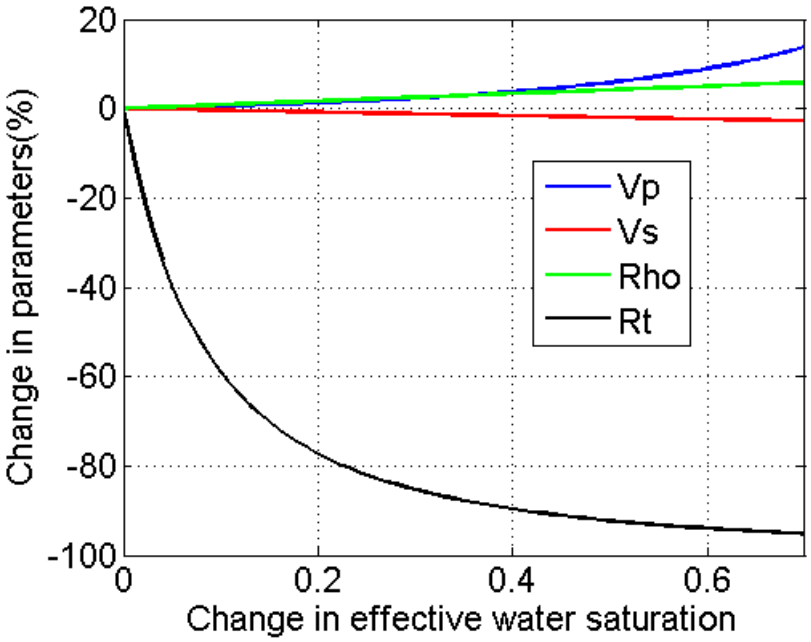

Figure 6.11 Comparison of seismic and CSEM rock physics model in terms of time-lapse signal due to changes in effective water saturation. Elastic parameters including P-wave velocity (Vp), S-wave velocity (Vs), and density (Rho) are less affected than rock resistivity (Rt).

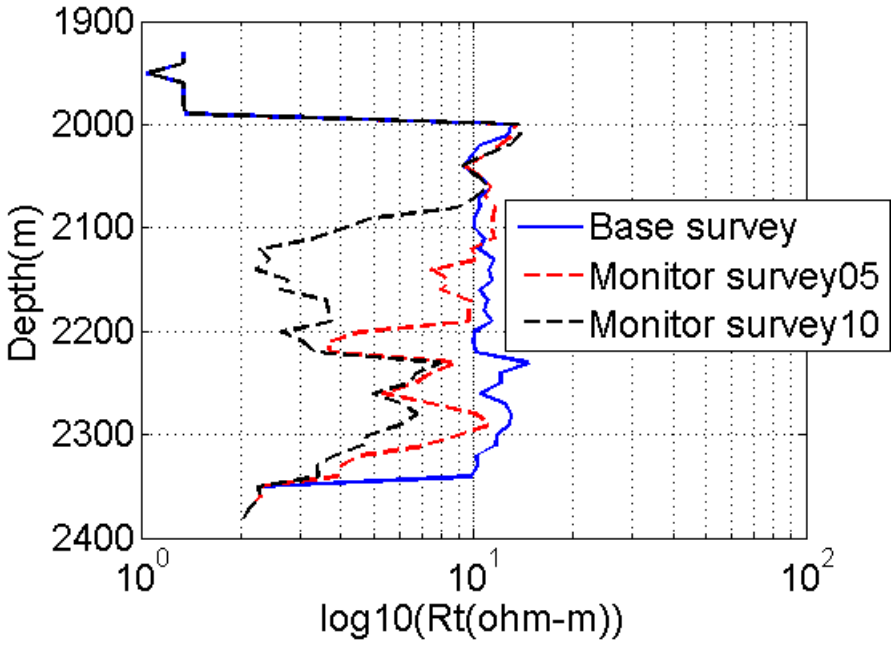

Figure 6.12: Resistivity logs extracted from the middle of the 2D reservoir for base survey (in blue), the first monitor survey after 5 years of water flooding (dashed red), and the second monitor survey after 10 years of waterflooding (dashed black).

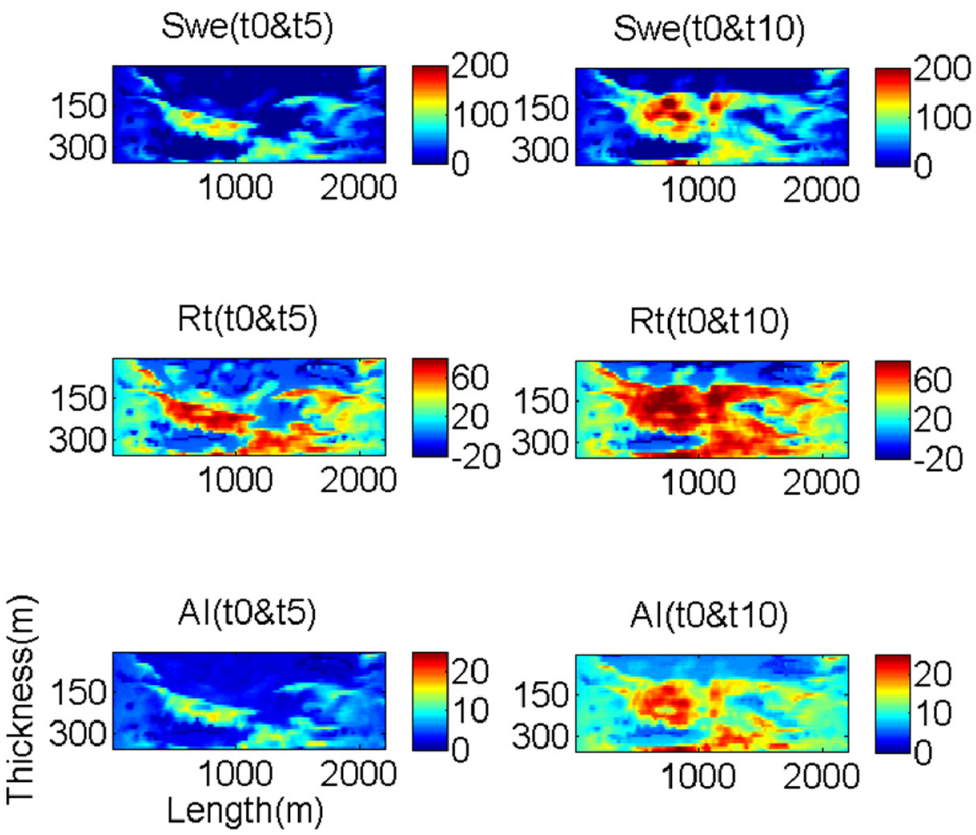

Figure 6.13: Time-lapse percentage changes in effective water saturation and the associated changes in electrical resistivity and seismic acoustic impedance for the first monitor survey(left column) and the second monitor survey(right column) after five and 10 years of water flooding, respectively. X and Y axes are the same for all panels and they are reservoir length and thickness in meters, respectively. Each panel is color-coded for the corresponding attribute. As mentioned in text, a minus sign is applied on the resistivity to have a consistent color display for flood geometry between saturation, acoustic impedance, and resistivity models.

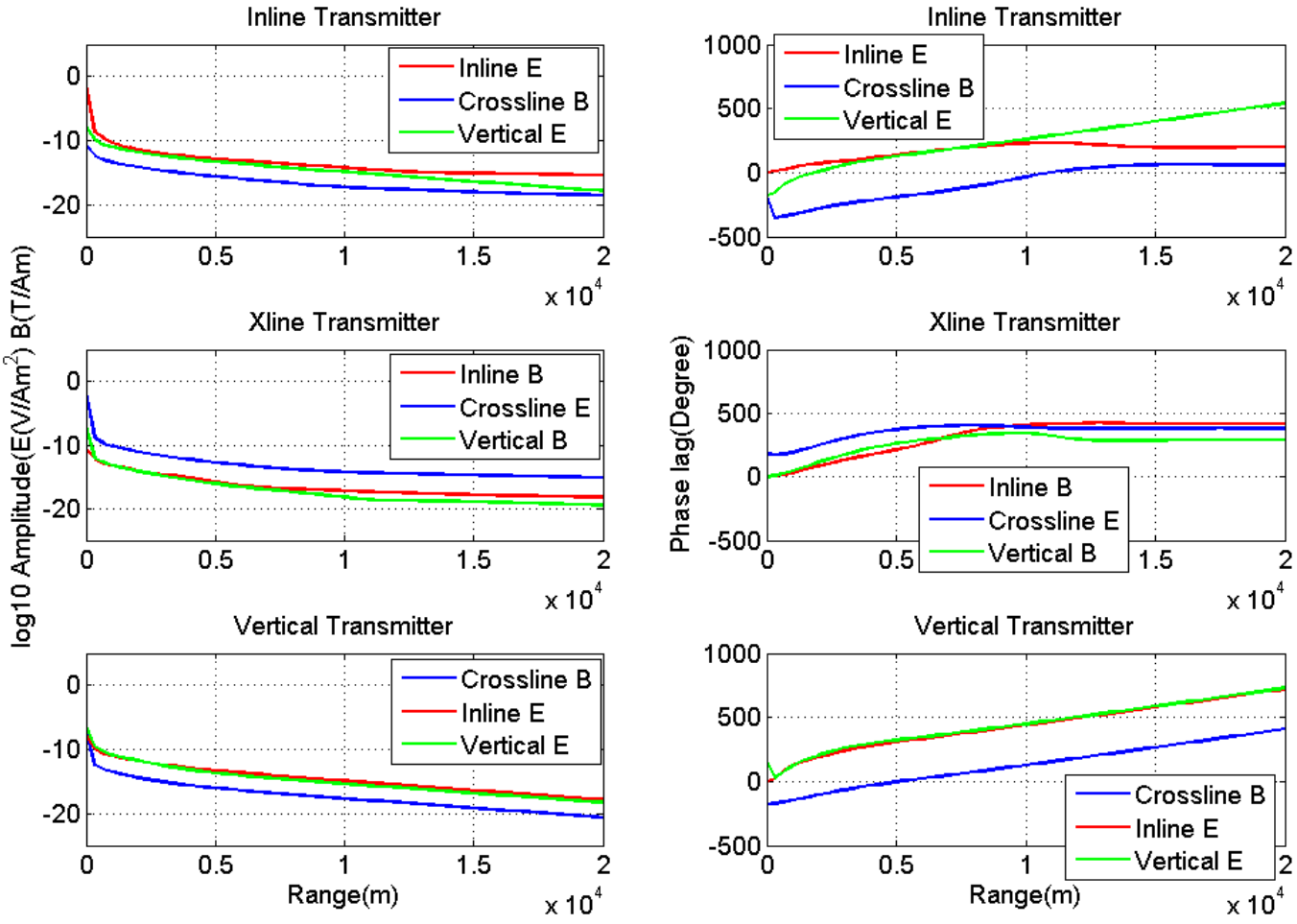

Figure 6.14: 1D CSEM data associated with the base survey (t0) illustrated in Figure 6.12. The absolute amplitude (left column) and phase (right column) of the electric and magnetic fields for a single frequency of 0.25 Hz are simulated on sea-floor detectors. The horizontal axis is the same for all panels and it is range or offset between transmitter and receivers in meters. Each panel is labeled for the corresponding transmitter's orientation and color legends show three field components associated with each transmitter.

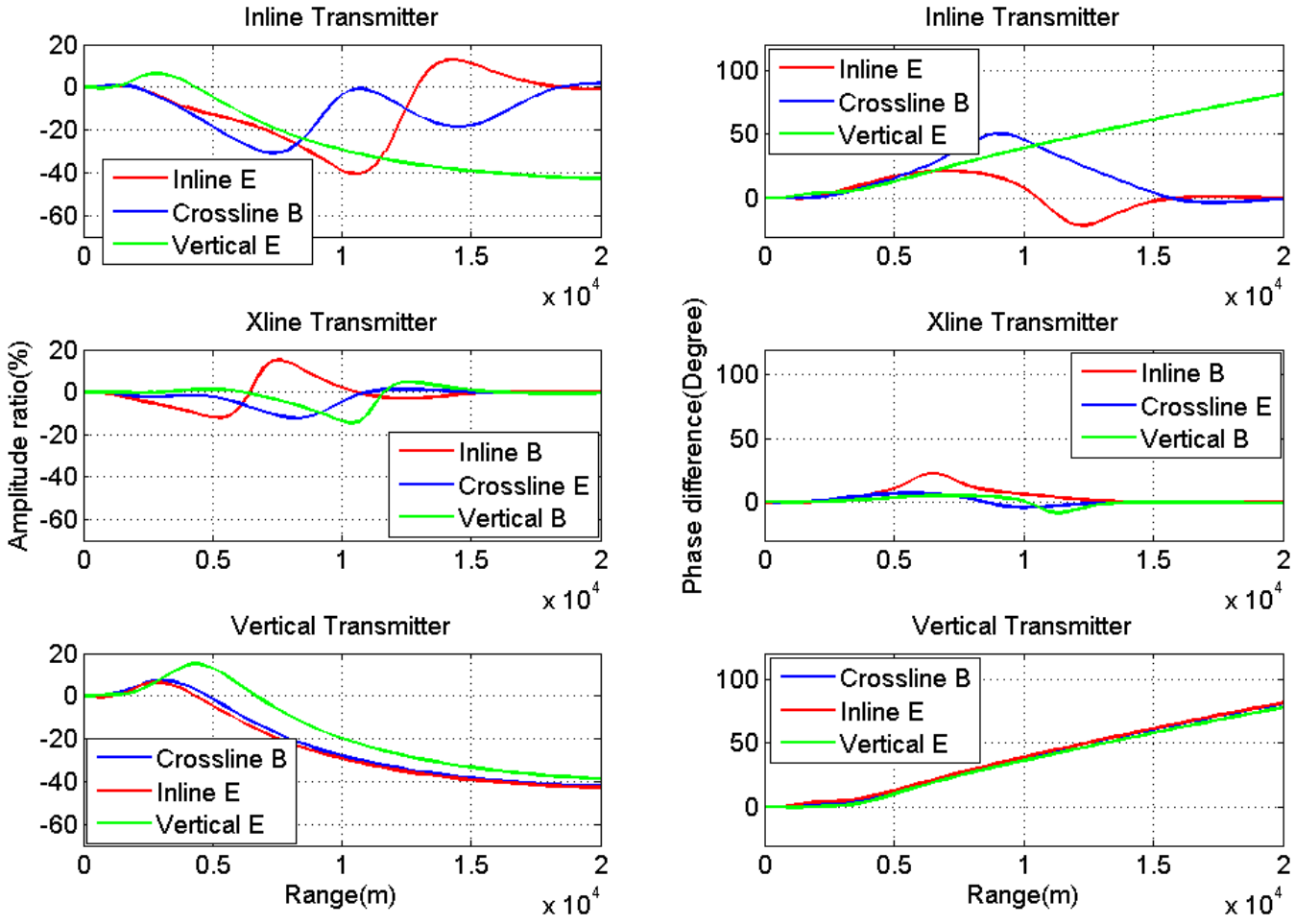

Figure 6.15: 1D CSEM time-lapse changes in response to waterflooding after 10 years between the base survey (t0) and monitor survey (t10) illustrated in Figure 6.12. The amplitude ratio in percent (left column) and phase difference in degree (right column) of the electric and magnetic fields for a single frequency of 0.25 Hz are simulated on sea-floor detectors. The horizontal axis is the same for all panels and it is range or offset between transmitter and receivers in meters. Each panel is labeled for the corresponding transmitter's orientation and color legends show three field components associated with each transmitter.

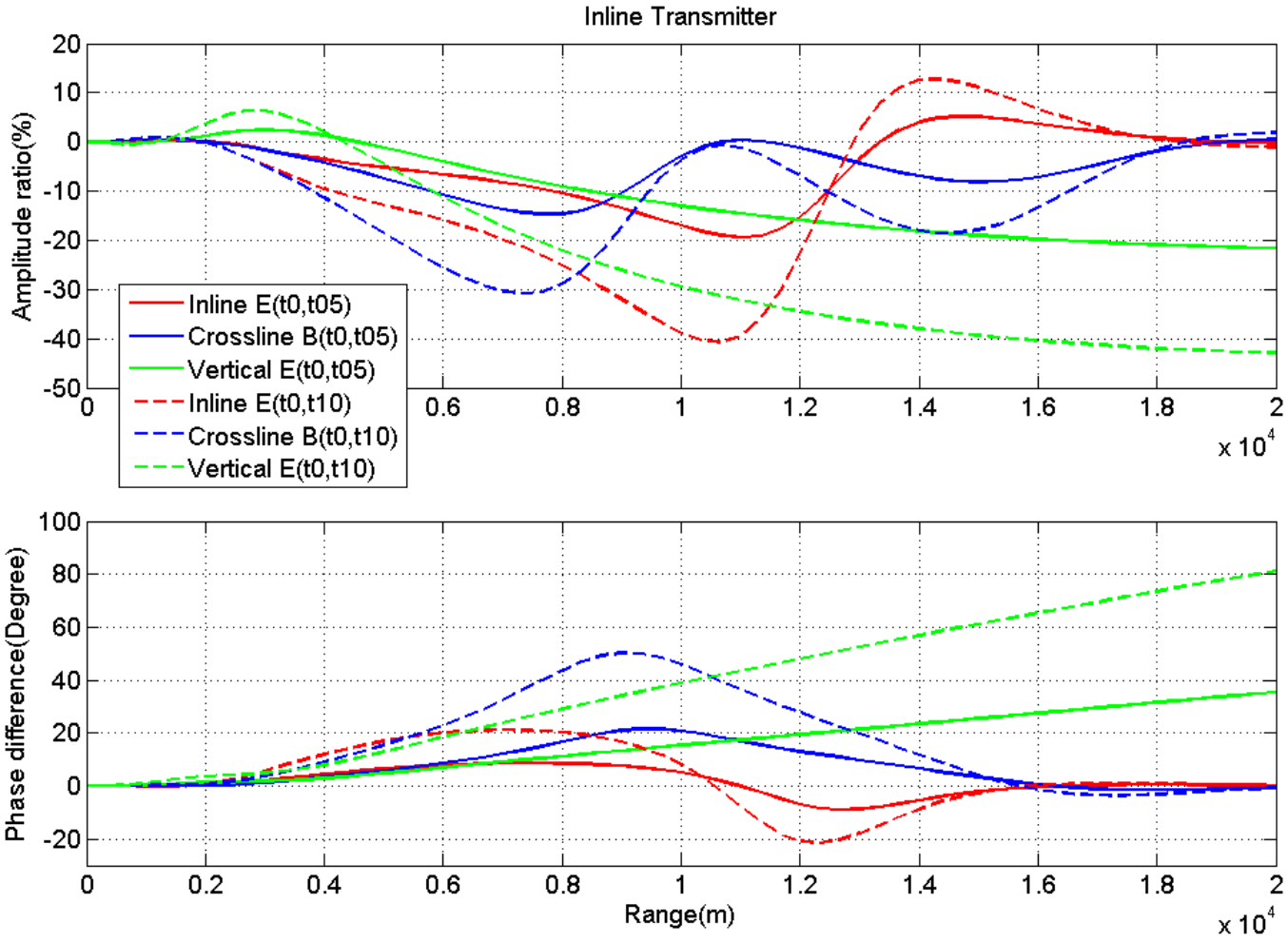

Figure 6.16: 1D-CSEM time-lapse changes in response to waterflooding after 5 years (solid lines) and 10 years (dashed lines). Inline transmitter is employed and inline electric (in red), crossline magnetic (in blue), and vertical electric (in green) fields simulated for a single frequency of 0.25 Hz. The top panel is the amplitude ratio (in percent), and the bottom panel is the phase difference (in degree) between base and monitor surveys. The horizontal axis is range or offset between transmitter and receivers in meters.

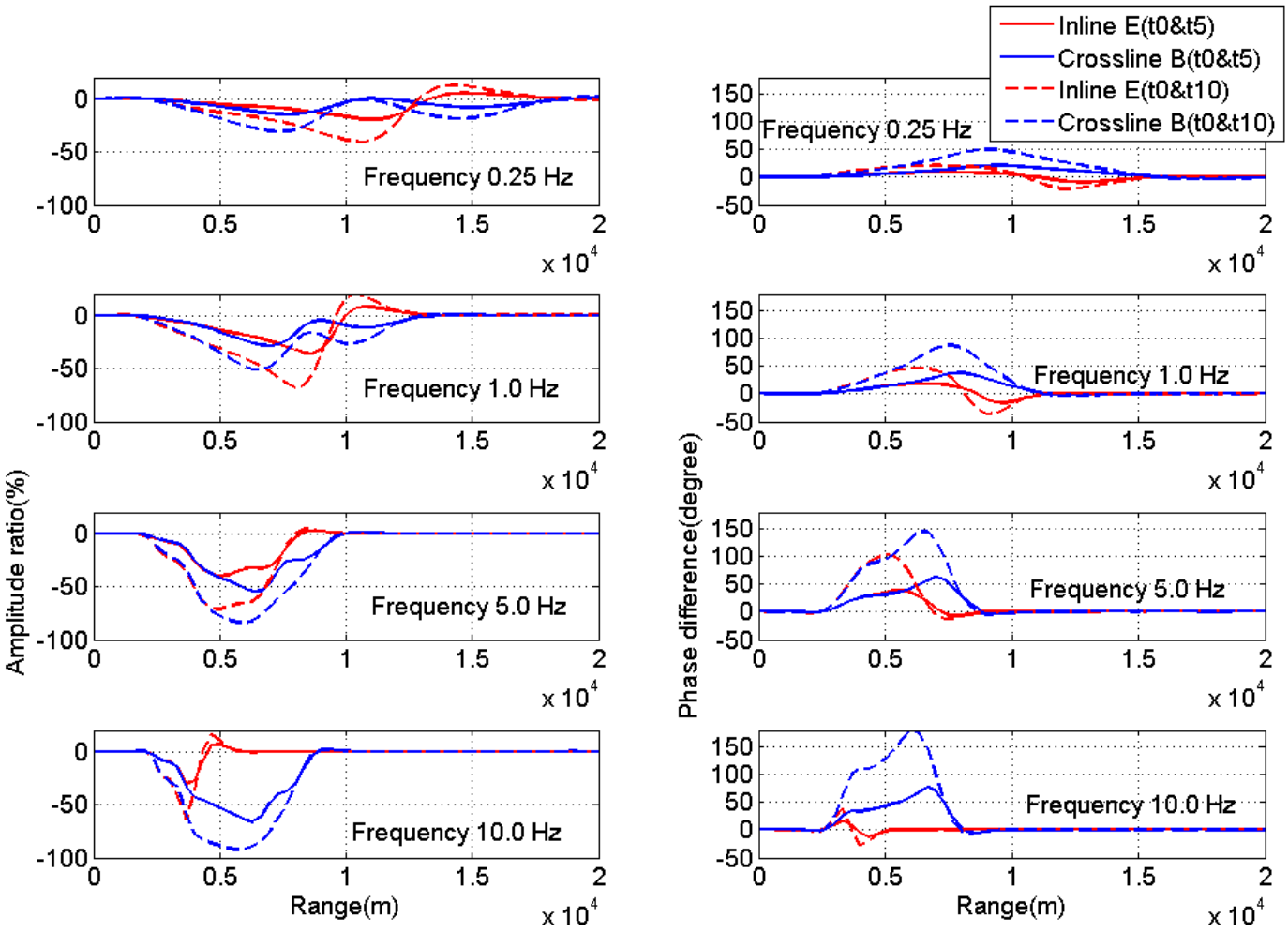

Figure 6.17: Frequency analysis for 1D CSEM time-lapse changes due to waterflooding after 5 and 10 years in solid and dashed line, respectively. The amplitude ratio in percent (left column) and phase difference in degree (right column) of the inline electric (in red) and crossline magnetic (in blue) field components for inline transmitter of 0.25 Hz frequency are displayed. The horizontal axis is the same for all panels and it is range or offset between transmitter and receivers in meters.

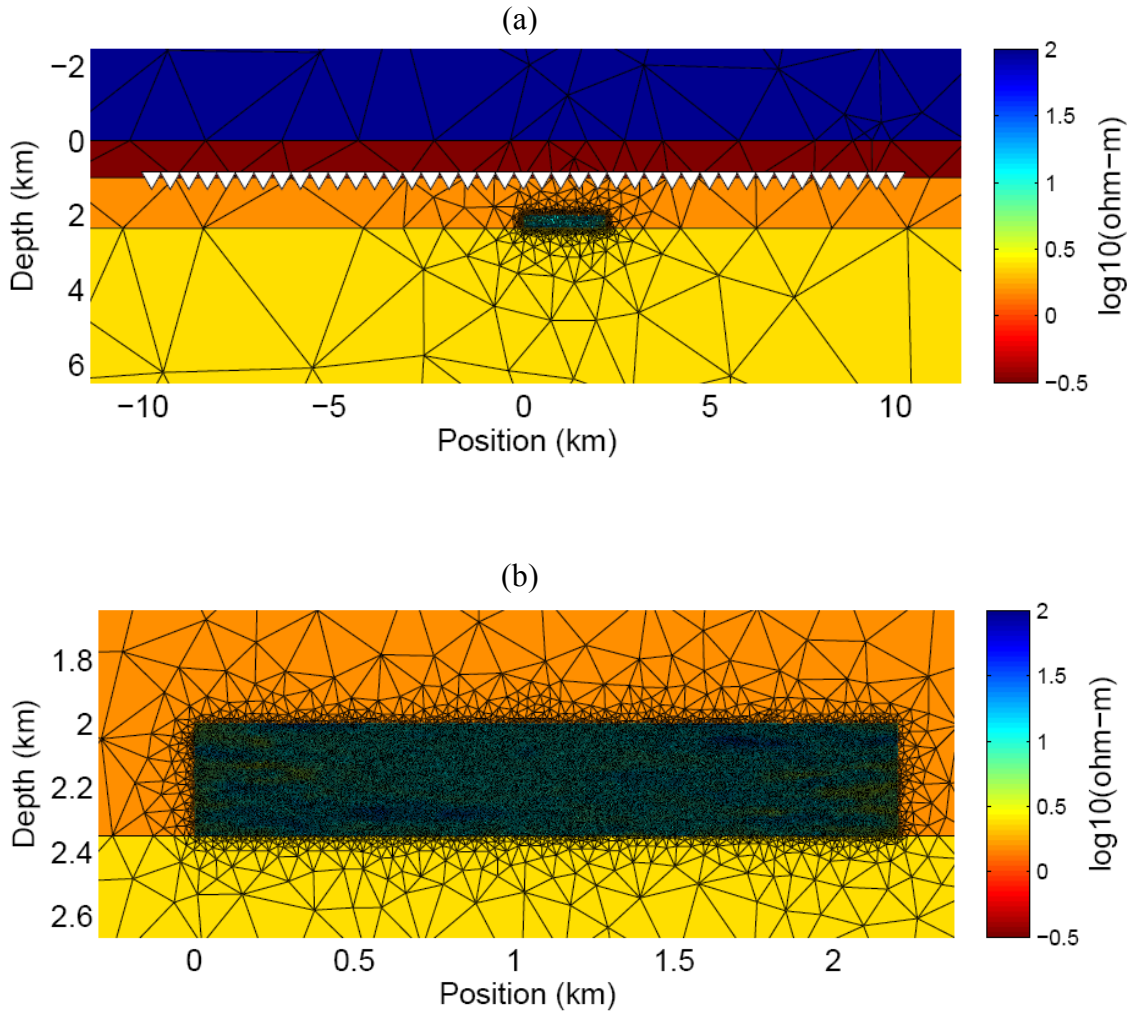

Figure 6.18: The coarse starting grid (a) and the final refined gird (b) created by triangular meshing over the 2D reservoir model embedded into 1D background.

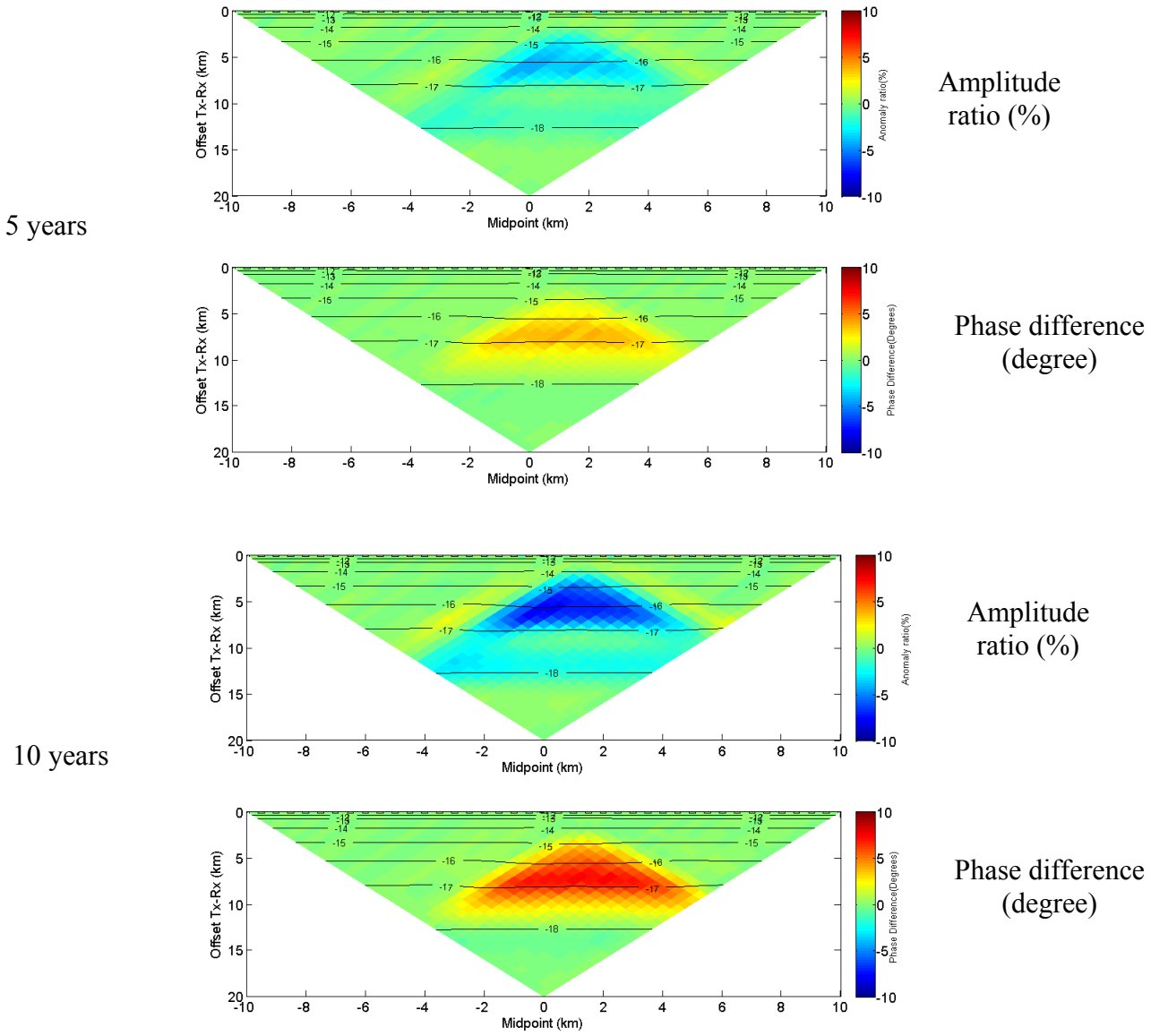

Figure 6.19: 2.5D CSEM time-lapse response of crossline magnetic field in midpoint-offset geometry. From top, the first and the second panels are related to the amplitude ratio (%) and the phase difference (degree) after 5 years of waterflooding, respectively. Third and fourth panels correspond to the amplitude ratio (%) and the phase difference (degree) after 10 years of waterflooding, respectively. The contour lines in all panels are the field amplitude (log10) of the base survey and show that the anomalies are present above the present day receiver noise floor of 10^{-18} T/Am.

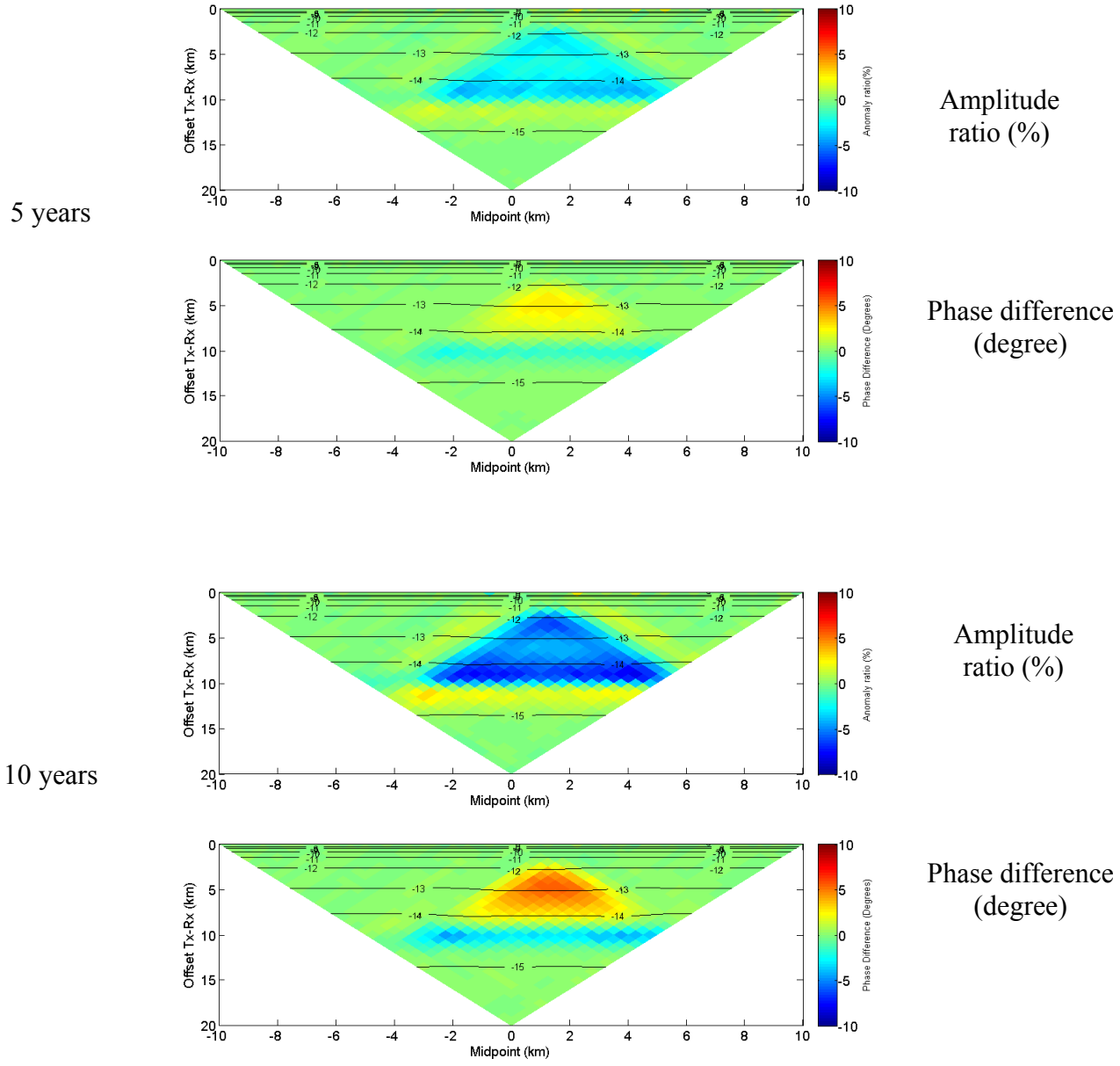

Figure 6.20: 2.5D CSEM time-lapse response of inline electric field in midpoint-offset geometry. From top, the first and the second panels are related to the amplitude ratio (%) and the phase difference (degree) after 5 years of waterflooding, respectively. Third and fourth panels correspond to the amplitude ratio (%) and the phase difference (degree) after 10 years of waterflooding, respectively. The contour lines in all panels are the field amplitude (log10) of the base survey and show that the anomalies are present above the present day receiver noise floor of 10^{-15} V/Am^2.

Chapter seven: Conclusions, recommendations, and future work

A geologically consistent petro-electro-elastic model developed in chapter 2 and 6 explicitly relates petrophysical properties to elastic and electrical parameters. It can be generalized as a model for other geological scenarios and, ultimately, applied to quantitative seismic and controlled-source electromagnetic (CSEM) reservoir characterization and monitoring. As an example of seismic applications, a sensitivity analysis is performed in chapter 2, and its results are validated by the developed reservoir model. Sensitivity analysis demonstrates that crossplotting of acoustic impedance (AI) vs. shear impedance (SI) is the most useful crossplot to quantitatively separate saturation and pressure changes. It is also shown that saturation patterns are detectable in most of the time-lapse scenarios because of the high percentage of change in water saturation, up to 100 percent. Pressure patterns are also well detected in most of the time-lapse scenarios in particular when notable pressure changes exist between the base and monitor surveys. The percentage in pressure change is often lower than of that of the saturation change in my waterflooded reservoir. Consequently, saturation patterns are more likely to be detected than pressure patterns. However, this does not necessarily mean that pressure patterns in time-lapse scenarios with lower change in percentage of pressure are less predictable. As I demonstrate, a small pressure change (less than 1%) is well detectable in some scenarios but it is not visible in others depending on the reservoir pressure state. I show that imperfections exist in both saturation and pressure patterns and they appear in different forms such as mix-scattering and misallocated points preventing monotonic patterns. Some factors causing this phenomenon are the interaction of saturation and pressure, diffusive nature of the pressure front, and rapid change in pressure due to the production operations. Imperfections in saturation patterns can be also addressed by a

pressure factor. The behavior of the pressure front during the waterflooding is very different from that of the water front. The distinct pressure behavior results in rapid iso-pressure equilibrium and makes the pressure and saturation patterns less predictable.

In chapter 3, I show that time-lapse cross-plots of changes in multi-component (MC) reflection coefficients (RCs) versus changes in traveltimes due to production leads to a separation between saturation and pressure and may have the capacity to quantitatively estimate and discriminate dynamic reservoir properties. In addition, I propose an effective statistical approach to estimate the detectability of a known production plan using MC seismic data. Time-lapse cross plot itself, single, and joint probability detectors help us to understand the efficacy of P-SV and SH-SH seismic time lapse data along with conventional P-P time-lapse reflectivity data. The results of applying the proposed approach on three different synthetic reservoirs, consolidated, poorly consolidated and medium consolidated sandstones, are consistent with my intuition regarding the detectability of fluids within different reservoir types: e.g., fluids within a reservoir with higher porosity are more likely detectable than fluids within a reservoir with lower porosity. This part of study suggests that fluid flow detection by seismic data is significantly limited for consolidated sandstone reservoirs. However, the detection is plausible for poorly to medium consolidated reservoirs in the present of realistic seismic noise level. In these cases, conventional P-P seismic data is dominant in amplitude change compared to converted P-SV and pure SH-SH seismic data. P-P data reflects the changes in fluid saturation and pore pressure, however; the main player is the saturation effect. SH-SH seismic data capture most the pressure information using traveltimes portion of pre-stack data. P-SV seismic data is the weakest detector in terms of time-lapse amplitude, but its traveltime shows an intermediate trend between P-P and SH-SH seismic data. Finally, my observations suggest that in a waterflooding scenario,

SH-SH and P-SV reflectivity data provide valuable information, if detectable changes in pore pressure accompany changes in water saturation. In contrast, P-SV and SH-SH reflectivity data are less valuable, if changes in water saturation within the reservoir are the only or dominant production-induced effects on seismic reflectivity data.

The examples presented in chapter 4 illustrate the sensitivities of MC seismic (P-P, P-SV, and SH-SH) traveltimes and RCs to water saturation and pore pressure. For the sensitivity of traveltimes to water saturation, the absolute intercept is greatest for P-P, smallest for P-SV, and intermediate for SH-SH. In addition, the absolute value of gradients is greatest for P-P, smallest for SH-SH, and intermediate for P-SV. For the sensitivity of traveltimes to pressure, the absolute intercept is greatest for SH-SH, smallest for P-P, and intermediate for P-SV. Here, the absolute value of gradients is greatest for SH-SH, smallest for P-SV, and intermediate for P-P. By analyzing the sensitivity of RCs at the reservoir top and OWC to water saturation, I found that the absolute value of amplitudes at all angels is greatest for P-P, smallest for P-SV, and intermediate for SH-SH. In addition, the absolute values of AVO gradients at reservoir top and OWC can be expressed in a descending order by (P-SV, SH-SH, P-P) and (P-P, P-SV, SH-SH), respectively. For the sensitivity of both interfaces, reservoir top and OWC, to pressure angle-dependent relations are extracted. At reservoir top and for the incident angels of 0-20, 20-28, and greater than 28 degrees, the absolute values of amplitudes can be expressed in a descending order by (SH-SH, P-P, PSV), (SH-SH, P-SV, P-P), and (P-SV, SH-SH, P-P), respectively. At OWC, the sensitivities of RCs to pore pressure are strictly angle-dependent. My observations suggest that in a waterflooding scenario, SH-SH and P-SV reflectivity data provide valuable information at the reservoir top and OWC, if detectable changes in pore pressure accompany changes in water saturation. In contrast, P-SV and SH-SH reflectivity data are less valuable, if

changes in water saturation within the reservoir are the only or dominant production-induced effects on seismic reflectivity data.

In the seismic section of this dissertation in chapter 5, I investigate the ability of different seismic modeling techniques to detect changes in reservoir properties due to waterflooding into a black oil reservoir. To do so, I simulate a poorly consolidated shaly sandstone reservoir model based on a prograding near-shore depositional environment. To account for the spatial distribution of petrophysical properties, an effective porosity model simulated by Gaussian geostatistics is employed. This model, called SPE comparative solution project (Christie and Blunt, 2001), is a large geostatistical model widely used in research in reservoir simulation, seismic and controlled-source electromagnetic (CSEM) modeling, etc. (e.g., Liang et al. 2010). Dispersed clay and dual water models are then efficiently combined with other well-known petrophysical correlations to consistently simulate other reservoirs. Next, the constructed reservoir model is subjected to numerical simulation of multi-phase fluid flow to predict the spatial distributions of pore pressure and water saturation due to water injection into a black oil reservoir. A geologically consistent stress-sensitive rock physics model, followed with modified Gassmann fluid substitution for shaly sandstones, is then utilized to simulate the seismic elastic parameters. I insert the petro-elastic model into a one-dimensional background elastic model simulating the surrounding offshore sedimentary basin in which the reservoir is embedded. Finally, I employ different seismic modeling algorithms, one-dimensional (1D) acoustic and elastic ray tracing, 1D full elastic reflectivity, 2D split-step Fourier plane-wave (SFPW), and 2D stagger grid explicit finite difference, to simulate seismic waves propagated through the model and recorded at sea level and on the sea floor. A base and two monitor surveys associated with 5 and 10 years of waterflooding are simulated and the corresponding time-lapse signatures are analyzed

at different reflection incident angles. My analyses demonstrate that internal multiples in the flooded zones partially subtract out due to time-lapse differencing, so they are less significant in monitoring applications than in actual reservoir characterization. I also found that for time-lapse seismic modeling, acoustic modeling of an elastic medium is a good approximation up to ray parameter (p) equal to 0.2 sec/km (reflection incident angle 24 degrees at reservoir top at depth 2 km),. But, at p=0.3 sec/km, (reflection incident angle 38 degrees), differences between elastic and acoustic wave propagation is the more dominant effect compared to internal multiples. Here, converted waves are generated with significant amplitudes compared to primaries and internal multiples. I demonstrate that time-lapse modeling of the reservoir using split-step Fourier plane-wave (SFPW) approach is very fast compared to finite difference (FD), 100 times faster for my case here. It is capable of handling higher frequencies than FD. It provides an accurate image of the waterflooding process comparable to FD. Consequently, it is a powerful alternative for time-lapse seismic modeling.

In the CSEM section of this dissertation in chapter 6, I first generate a 2D geological reservoir model showing the realistic spatial distribution of petrophysical parameters. Fluid flow simulation and a geologically consistent rock physics model are then employed to convert the petrophysical properties of the shaly sandstone to electrical resistivity. The representative time-dependent resistivity model developed here shows the accurate front geometry during a waterflooding to enhance oil recovery. To simulate the surrounding rocks, I embed the reservoir into a 1D background resistivity model correlated with a P-wave velocity log. Finally, I numerically acquire 1D and 2.5D time-lapse CSEM data over the reservoir to assess the value of EM data in monitoring of a waterflooding scenario. I simulate three sets of 2D resistivity models corresponding to the initial reservoir state, after 5 years, and 10 years of waterflooding into a black oil

reservoir. Then a base and two monitor time-lapse CSEM surveys are simulated via accurate numerical algorithms. 2.5D CSEM modeling demonstrated that a detectable time-lapse signal after 5 years and a strong time-lapse signal after 10 years of waterflooding were attainable with the careful application of currently available CSEM technology. In contrast, 1D CSEM data acquired at the middle of reservoir exhibit relatively strong time–lapse signals for both monitor surveys. These observations demonstrate that 1D modeling of a 2D reservoir can be misleading and results in the overestimation or under prediction of the time-lapse signal and the associated swept oil in the waterflooding enhanced recovery. The results presented in this study clearly show that repeatability of CSEM measurements for monitoring of producing reservoirs are extremely important at large time intervals, 10 years, but they are limited at desired time intervals, less than 5 years, through the entire reservoir history. Furthermore, factors restricting the repeatability of CSEM measurements, e.g., errors in positioning of transmitters and receivers, inhomogeneities in the near surface, effect of time-varying ocean conductivity, and changes in field instruments during production have to be addressed properly to preserve these relatively small time-lapse signals. Finally, more detailed and 3D time-lapse CSEM synthetic modeling-inversion and time-domain CSEM simulation will shed light on complications probably not seen in my 2.5D frequency domain analyses.

The development of the petro-electro-elastic model is based on the dispersed clay distribution in the reservoir pore volume. An extension of the current work will be the generation of a model with layered distribution of clay and then perform seismic and CSEM sensitivity and feasibility studies and finally compare their results with the dispersed model.

The comprehensive petro-electro-elastic model developed in this dissertation can be efficiently utilized in sensitivity analyses of seismic and CSEM data to petrophysical properties and, ultimately, applied to reservoir characterization and monitoring research. In this context, inversion of seismic data to elastic properties or even direct inversion to petrophysical properties are the next logical steps. Joint inversion of seismic and CSEM data may lead to better estimation of the petro-elastic-electric reservoir properties and results in lower uncertainties in the estimated properties compared to the properties estimated from seismic or CSEM alone.

Finally, seismic and CSEM reservoir history matching will be the ultimate application of the developed petro-electro-elastic model .The preparation of the static reservoir model with attached petrophysical facies, model parameterization techniques, accounting for spatial continuity of petrophysical properties, and model updating techniques are some of main concepts involved. Then, an efficient and robust optimization algorithm ,e.g., very fast simulated annealing, has to be developed to jointly invert pre-stack seismic gathers, CSEM data, production, and well data while honoring the facies architecture of the reservoir under study. The outcomes will be the posteriori probability density functions for petrophysical properties. The stochastic reservoir production forecasts can be easily evaluated by initiating the reservoir simulator from different realizations of the posteriori probability density function of reservoir model parameters.

Appendix A: Equations for the petro-elastic model developed in chapter two

As described in the petrophysics model, the clay distribution is dispersed or pore-filling. The corresponding porosity-clay model was introduced by Thomas and Stieber (1975) and further developed by Marion et al. (1992) and Yin, (1992). Total and effective porosity in shaly-sand domain is calculated as follows:

$$\varphi_t = \varphi_{ss} - C_{sh}(1-\varphi_{sh}) \qquad C_{sh} \le \varphi_{ss} \tag{A.1}$$

$$\varphi_e = \varphi_t - \varphi_{sh} C_{sh} \tag{A.2}$$

Where, φ_t total porosity, φ_e effective porosity, φ_{sh} pure shale porosity, φ_{ss} clean sandstone porosity, and C_{sh} is the volumetric shale concentration of the rock. Dual water models (Best 1980; Dewan, 1983; Clavier, 1984) are applicable for dispersed clay distributions. In this study, I use the dual water model because several of its parameters can be computed from well logs (Dewan, 1983) and it can be efficiently combined with the dispersed clay model.

Effective elastic modulus of solid phase (grain material) is the arithmetic average of Reuss lower bound and Voigt upper bound (Hills' average moduli). Reuss lower bound is the harmonic average of the elastic moduli of individual components in solid phase. In contrast, Voigt upper bound is the arithmetic average of the elastic moduli of individual components in solid phase. Here, two solid phases are Quartz and Clay (Kaolinite), so number of components n=2, and bulk and shear moduli of the solid phases are computed as follows:

Reuss bounds: $\dfrac{1}{K_R} = \dfrac{f_c}{K_c} + \dfrac{1-f_c}{K_q} \qquad \dfrac{1}{G_R} = \dfrac{f_c}{G_c} + \dfrac{1-f_c}{G_q}$ (A.3)

Voigt bounds: $K_V = f_c K_c + (1-f_c)K_q \quad G_V = f_c G_c + (1-f_c)G_q$ (A.4)

Where fc is the clay fraction, Kc and Kq are the bulk moduli of clay and quartz, respectively. Gc and Gq are shear moduli of clay and quartz, respectively.

According to Hertz-Mindlin (1949) contact theory for clean sandstone, bulk and shear moduli of the clean sandstone are calculated as follows:

$$K_{ss} = \left[\frac{n_{ss}^2 (1-\phi_{ss})^2 G_q^2 P_{eff}}{18\pi^2 (1-\upsilon_q)^2} \right]^{\frac{1}{3}} \quad \text{(A.5)}$$

$$G_{ss} = \frac{5-4\upsilon_q}{5(2-\upsilon_q)} \left[\frac{3n_{ss}^2 (1-\phi_{ss})^2 G_q^2 P_{eff}}{2\pi^2 (1-\upsilon_q)^2} \right]^{\frac{1}{3}} \quad \text{(A.6)}$$

Where $n_{ss\ is}$ grain contact for clean sandstone (Murthy upper bound, 1982):

$$n_{ss} = 20 - 34\phi_{ss} + 14\phi_{ss}^2 \quad \text{(A.7)}$$

υ_q is the Poisson's ration for quartz:

$$\upsilon_q = \frac{3K_q - 2G_q}{6K_q + 2G_q} \quad \text{(A.8)}$$

Peff is the effective stress.

For the elasticity of pure shale end member, friable (uncemented) model based on the Hetrz-Mindlin contact theory (Dvorkin and Nor 1996) has been used:

$$K_{sh} = \left[\frac{n_{sh}^2 (1-\phi_{sh})^2 G_c^2 P_{eff}}{18\pi^2 (1-\upsilon_c)^2} \right]^{\frac{1}{3}} \quad \text{(A.9)}$$

$$G_{sh} = \frac{5-4\upsilon_c}{5(2-\upsilon_c)} \left[\frac{3n_{sh}^2 (1-\phi_{sh})^2 G_c^2 P_{eff}}{2\pi^2 (1-\upsilon_c)^2} \right]^{\frac{1}{3}} \quad \text{(A.10)}$$

Where $n_{sh\ is}$ grain contact for pure shale (Murthy upper bound, 1982):

$$n_{sh} = 20 - 34\phi_{sh} + 14\phi_{sh}^2 \quad \text{(A.11)}$$

υ_c is the Poisson's ration for pure shale (clay mineral):

$$\upsilon_c = \frac{3K_c - 2G_c}{6K_c + 2G_c} \tag{A.12}$$

For elastic moduli at critical clay content, I use the following Modified Hashin-Shtrikman lower bound (Dvorkin et al. 1999)

$$K_{cc} = \left[\frac{\phi_{ss}}{K_{sh} + \frac{4}{3}G_{sh}} + \frac{1-\phi_{ss}}{K_q + \frac{4}{3}G_{sh}} \right]^{-1} - \frac{4}{3}G_{sh} \tag{A.13}$$

$$G_{cc} = \left[\frac{\phi_{ss}}{G_{sh} + Z_{sh}} + \frac{1-\phi_{ss}}{G_q + Z_{sh}} \right]^{-1} - Z_{sh} \qquad Z_{sh} = \frac{G_{sh}}{6}\left(\frac{9K_{sh} + 8G_{sh}}{K_{sh} + 2G_{sh}} \right) \tag{A.14}$$

$$K_{dry} = \left[\frac{1 - \frac{C_{sh}}{\phi_{ss}}}{K_{ss} + \frac{4}{3}G_{ss}} + \frac{\frac{C_{sh}}{\phi_{ss}}}{K_{cc} + \frac{4}{3}G_{ss}} \right]^{-1} - \frac{4}{3}G_{ss} \tag{A.15}$$

$$G_{dry} = \left[\frac{1 - \frac{C_{sh}}{\phi_{ss}}}{G_{ss} + Z_{ss}} + \frac{\frac{C_{sh}}{\phi_{ss}}}{G_{cc} + Z_{ss}} \right]^{-1} - Z_{ss} \qquad Z_{ss} = \frac{G_{ss}}{6}\left(\frac{9K_{ss} + 8G_{ss}}{K_{ss} + 2G_{ss}} \right) \tag{A.16}$$

For the saturation pattern, I use Reuss lower bound or Wood's mixing law assuming uniform or homogenous (fine scale) saturation:

$$\frac{1}{K_f} = \frac{S_{wt}}{K_w} + \frac{S_o}{K_o} + \frac{S_g}{K_g} \tag{A.17}$$

Where, K_f bulk modulus of the mixture, K_w water's bulk modulus, K_o oil's bulk modulus, K_g gas's bulk modulus and S_{wt}, S_o, and S_g are water, oil, and gas saturations.

For fluid substitution, I use Gassmann for shaly sandstone (Dvorkin et al. 2007):

$$G_{sat} = G_{dry} \tag{A.18}$$

$$K_{sat} = \frac{K_s}{1 + Z^{-1}} \qquad Z = \frac{K_f}{\phi_e(K_s - K_f)} + \frac{K_{dry}}{K_s - K_{dry}} \tag{A.19}$$

Appendix B: Equations for the sensitivity analysis developed in chapter three

Here, I show how I numerically compute the full derivatives of reflections coefficients and traveltime with respect to water saturation and pore pressure. To do so, consider an interface between two elastic media, e.g., shale over sandstone. Each of these medium can be presented with its elastic properties including P&S-wave velocities (α and β) and density (ρ). If we use subscript 1 and 2 for the upper and lower media, then the following compact-form of equations are defined to represent the interface:

$$\gamma = \frac{\alpha_2}{\alpha_1} \quad \varepsilon = \frac{\beta_2}{\beta_1} \quad \eta = \frac{\rho_2}{\rho_1} \quad q_1 = \frac{\alpha_1}{\beta_1} \quad q_2 = \frac{\alpha_2}{\beta_2} \quad \sigma_1 = \frac{0.5q_1^{\,2} - 1}{q_1^{\,2} - 1} \quad \sigma_2 = \frac{0.5q_2^{\,2} - 1}{q_2^{\,2} - 1} \tag{B.1}$$

Where γ, ε, and η are contrasts over interface in P-wave velocity, S-wave velocity, and density, respectively. σ_1 and σ_2 are Poisson ratios in the upper and lower media. Following the notation of Rosa, (1976) and Gomez and Tatham (2007), angle-dependent (θ) reflection coefficient at the interface can be expressed as follows:

$$R = f(\gamma, \varepsilon, \eta, \sigma_1, \sigma_2, \theta) \tag{B.2}$$

Using the rock physics equations summarized in Appendix A, elastic properties of the reservoir unit (lower medium) and the corresponding contrasts between reservoir and overburden (upper medium) can be numerically related to water saturation (Sw) and pore pressure (Pp):

$$[\eta, \gamma, \varepsilon, \sigma_1, \sigma_2] = f(S_W, P_P) \tag{B.3}$$

Finally, the full-derivative of the reflection coefficients can be numerically approximated using one of the variants of the finite difference operators. Here, I use a 3rd-order operator to compute the derivatives:

$$\frac{\partial R_{\langle\theta\rangle}}{\partial S_W} = \lim_{\Delta S_W \to 0} \frac{R_{\langle\theta\rangle}(S_W + \Delta S_W) - R_{\langle\theta\rangle}(S_W - \Delta S_W)}{2 * \Delta S_W}$$

$$\frac{\partial R_{\langle\theta\rangle}}{\partial P_p} = \lim_{\Delta P_p \to 0} \frac{R_{\langle\theta\rangle}(P_p + \Delta P_p) - R_{\langle\theta\rangle}(P_p - \Delta P_p)}{2 * \Delta P_p} \tag{B.4}$$

Appendix C: Equations for the petro-electric model developed in chapter six

As described in the petrophysics model, the clay distribution is dispersed or pore-filling. The corresponding porosity-clay model was introduced by Thomas and Stieber (1975) and further developed by Marion et al. (1992) and Yin, (1992). Total and effective porosity in shaly-sand domain is calculated as follows:

$$\varphi_t = \varphi_{ss} - C_{sh}(1-\varphi_{sh}) \qquad C_{sh} \le \varphi_{ss} \tag{C.1}$$

$$\varphi_e = \varphi_t - \varphi_{sh} C_{sh} \tag{C.2}$$

Where, φ_t total porosity, φ_e effective porosity, φ_{sh} pure shale porosity, φ_{ss} clean sandstone porosity, and C_{sh} is the volumetric shale concentration of the rock.

Dual water models (Best 1980; Dewan, 1983; Clavier, 1984) are applicable for dispersed clay distributions. In this study, I use the dual water model because several of its parameters can be computed from well logs (Dewan, 1983) and it can be efficiently combined with the dispersed clay model. Based on this model, electrical conductivity or inverse of rock resistivity (Rt) is computed as follows:

$$\frac{1}{R_t} = \frac{\phi_t^m S_{wt}^n}{a}\left[\frac{1}{R_w} + \frac{S_{wb}}{S_{wt}}\left(\frac{1}{R_{wb}} - \frac{1}{R_w}\right)\right] \tag{C.3}$$

Where a, m, n are tortuosity factor, cementation factor, and saturation exponent, respectively. S_{wb} and S_{wt} are clay bound water saturation and total water saturation, respectively and are computed using equations C.4 and C.5:

$$S_{wb} = \frac{C_{sh}\phi_{sh}}{\phi_t} \tag{C.4}$$

$$S_{wt} = S_{wb} + \frac{S_{ws}\phi_e}{\phi_t} \tag{C.5}$$

R_w and R_{wb} are free and bound-water resistivity which depends on salinity and temperature. I use Arps' empirical equation (Arps, 1953) to calculate these quantities:

$$Rw = \left[0.0123 + \frac{3647.5}{NaCl(ppm)^{0.995}} \right] * \left[\frac{81.77}{T(oF) + 6.77} \right] \qquad \text{(C.6)}$$

Where the concentration of NaCl in particle per million (ppm) and temperature (T) in Fahrenheit degree are required to compute fluid resistivity.

References

Aki, K., and P. G. Richards, 2002, Quantitative seismology: W.H. Freeman and Company.

Anderson, T., Zachariassen, E., Hoye, T., Meisingset, H. C., Otterlei, C., van Wijngaarden, A.J., Hatland, K., Mangeroy, F., 2006, Method of conditioning the reservoir model on 3D and 4D elastic inversion data applied to a fluvial reservoir in the North Sea, SPE 100190

Andersen, C.F., Grosfeld, V., Wijngaarden, A.J., Haaland, A.N., 2009, interactive interpretation of 4d prestack inversion data using rock physics templates, dual classification, and real-time visualization, the leading edge august 2009, interpreter's corner

Angelov, P., J., Spetzler, K., Wapenaar, 2004, Pore pressure and water saturation variations: Modification of Landrø AVO approach: 74th Annual International Meeting, SEG Expanded Abstracts

Archie, G.E., 1942, Electrical resistivity of log as an aid in determining some reservoir characteristics, Trans.: AIME, paper D

Arenas, E., van Kruijsdijk, C., Oldenziel, T., 2001, Semi-automatic history matching using the pilot point method including time-lapse seismic data, paper SPE 71634 presented at the SPE Annual Technical Conference and Exhibition

Azecott, R., (ed.), 1992, Simulated annealing: Parallelization techniques, John Wiley and Sons, Inc., New York

Aziz, K., and Settari, A., 1979, Petroleum reservoir simulation: Applied Science Publishers LTD, London.

Avseth, P., Mukerji, T., and Mavko, G., 2005, Quantitative seismic interpretation, Cambridge Univ. Press.

Avseth, P., Mukerji, T., Jorstad, A., Mavko, G., and Veggeland, T., 2001, Seismic reservoir mapping from 3-D AVO in a North Sea turbidite system: Geophysics, 66, 1157–1176

Bachrach, R., 2006, Joint estimation of porosity and saturation using stochastic rock-physics modeling, Geophysics, vol. 71, no. 5, p. O53-O63

Batzle, M., Wang, Z., 1992,Seismic properties of pore fluids, Geophysics 57, 1396.

Becker, E. B., Carey, G. F., & Oden, J. T., 1981. Finite Elements, an Introduction, vol. 1, UT Austin.

Behrens, R., et al. 2002, 4D seismic monitoring of water flux at Bay Marchand: The practical use of 4D in an imperfect world, SPEREE, 410

Best, D.L., Gardner, J.S., and Dumanoir, J.L., 1980, A computer-processed wellsite lo interpretation, SPE 9039

Bilgeri, D. and Ademeno, E. B., 1982, Predicting of abnormally pressured sedimentary rocks, Geophysical Prospecting, Vol. 30, 608-621.

Biot, M. A., 1956, Theory of propagation of elastic waves in a fluid-saturated porous solid, I: Low-frequency range; II: higher frequency range, J. Acoustic. Soc. Am. 28, 168–191.

Black, N. and Zhdanov, M.S., 2009, Monitoring of hydrocarbon reservoirs using marine CSEM method: 79th Annual International Meeting, SEG, Expanded Abstracts, 850-853.

Blangy, J.P., 1994, AVO in transversely isotropic media: Geophysics, 59, 775-781.

Brevik, I., 1999, Rock model based inversion of saturation and pressure changes from time-lapse seismic data, SEG Expanded Abstracts 18, 1044.

Buland, A., and H. Omre, 2003, Bayesian linearized AVO inversion: Geophysics, 68, 185–198.

Buland, A., and H Omre, 2003c, Joint AVO inversion, wavelet estimation and noise level estimation using a spatially coupled hierarchical Bayesian model: Geophysical Prospecting, 51, 531–550.

Buland, A., O. Kolbjornsen, and H. Omre, 2003, Rapid spatially coupled AVO inversion in the Fourier domain: Geophysics, 68, 824–836.

Buland, A., Ouair, Y., EI. 2006, Bayesian time-lapse inversion, Geophysics, 71, 43-48

Caers, J., Hoffman,T., Strebelle, S., and Wen, X.,H., 2006, Probabilistic integration of geologic scenarios, seismic, and production data- a west Africa turbidite reservoir case study, The Leading Edge , Interpreter's corner, March 2006.

Calvert, R. [2005] Insights and methods for 4D reservoir monitoring and characterization, SEG EAGE distinguished instructor short course.

Castagna, J.P., Batzle, M.L., and Eastwood, R.L. 1985, Relationship between compressional wave and shear wave velocities in clastic silicate rocks: Geophysics, Vol. 50, No. 4, pp. 571-581.

Castagna, J., P. and Backus M., M., 1999, fifth edition, Offset Dependent Reflectivity-Theory and Practice of AVO (Investigations in Geophysics, Vol 8)

Castro, S., Caers, J., Otterlei, C., Hoye, T., Anderson, T., Gomel, P., 2006, A probabilistic integration of well logs, geological information, 3D/4D seismic and production data: Application to the Oseberg Filed, SPE 103152

Cerveny, V., 1982, “Expansion of a plane wave into Gaussian beams: Studia geoph. et geod. 26. 120-131.

Cerveny, 2001, “Seismic ray theory”, Cambridge University Press.

Chapman, C., 2004, “Fundamentals of Seismic Wave Propagation”, Cambridge University Press.

Chave, A., and C. Cox, 1982, Controlled electromagnetic sources for measuring electrical-conductivity beneath the oceans. 1. Forward problem and model study: Journal of Geophysical Research, 87, no. NB7, 5327–5338.

Choudhary, M.K., Yoon, S., and Ludvigsen, B.E., 2007, Application of Global Optimization Methods for History Matching and Probabilistic Forecasting - Case Studies, SPE 105208

Christie, M. A., and M. J. Blunt, 2001, Tenth society of petroleum engineers comparative solution project: A comparison of upscaling techniques: Reservoir Simulation Symposium, SPE, 72469.

Chu, C., P.L., Stoffa, and R. Seif, 2009, “3D seismic modeling and RTM with parallel Fourier methods using non-blocking collective communications”, Expanded Abstracts, SEG

Clavier, C., Coates, G., Dumanoir, J., 1984, Theoretical and experimental bases for the dual water model for interpretation of shaly sands, SPE 6859

Cole, S., D., Lumley, M., Meadows, A., Tura, 2002, Pressure and saturation inversion of 4D seismic data by rock physics forward modeling: 72nd Annual International Meeting, SEG Expanded Abstracts

Connolly, P., 1999, Elastic impedance, The Leading Edge, 18, No. 4, 438–452

Cooper, M., et al., 1999, Foinaven active reservoir management: The time-lapse signal, SEG Expanded Abstracts 1640.

Constable, S., and C. J. Weiss, 2006, Mapping thin resistors and hydrocarbons with marine em methods: Insights from 1D modeling: Geophysics, 71, no. 2, G43–G51.

Contreras, A., C. Torres-Verdin, K. Kvien, T. Fasnacht, and W. Chesters, 2005, AVA stochastic inversion of pre-stack seismic data and well logs for 3d reservoir modeling: 67th Annual Conference and Exhibition, EAGE, Extended Abstracts, F014.

Contreras, A., C. Torres-Verdin, and T. Fasnacht, 2006, AVA simultaneous inversion of partially stacked seismic amplitude data for the spatial delineation of lithology and fluid units of deepwater hydrocarbon reservoirs in the central Gulf of Mexico, Geophysics, Vol. 71, No. 4, P. E41–E48

Contreras, A., C. Torres-Verdin, and T. Fasnacht, 2007, Sensitivity analysis of data-related factors controlling AVA simultaneous inversion of partially stacked seismic amplitude data: Applications to deepwater hydrocarbon reservoirs in the central Gulf of Mexico, Geophysics, Vol. 72, No. 1, P. C19–C29

Debeye, H., E. Sabbah, and P. van der Made, 1996, Stochastic inversion: 66th Annual International Meeting, SEG, Expanded Abstracts, 1212–1215.

Dewan, J.T., 1983, Essentials of modern open-hole log interpretation, Tulsa, Oklahoma, PennWell Books

Dey, A. K., Sacchi, M. D., Gisolf, A., 2006, High resolution reservoir rock properties via joint pre-stack seismic amplitude inversion, SEG Expanded Abstracts 25, 2156.

Deutsch, C.V. and Cockerham, 1994, P.W., Geostatistical modeling of permeability with Annealing Cosimulation (ACS), SPE 28413

Deutsch, C.V. and Journel, A.G, 1998, GSLIB: Geostatistical Software Library and Users Guide, second edition. New York City: Oxford U. Press.

Diebold, J.B., and Stoffa, P.L., 1981, The travel time equation, tau-p mapping, and inversion of common midpoint data, Geophysics, Vol. 46, p. 238-254.

Dong, Y. and Oliver, D., S., 2005, Quantitative use of 4D seismic data for reservoir description, SPE Journal, 84571

Dong, Y. and Oliver, D., S., 2008, Reservoir simulation model updates via automatic history matching with integration of seismic impedance change and production data, International Petroleum Technology Conference, IPTC 12550

Duffy, J., and Mindlin, R.D. 1957, Stress-strain relations and vibrations of a granular medium: J. Appl. Mech. Vol. 24, pp. 585-593

Dvorkin, J., Nur, A., 1996, Elasticity of high-porosity sandstones: Theory for two North Sea data sets, Geophysics, Volume 61, Issue 5, pp. 1363-1370 (September-October 1996)

Dvorkin, J., Gutierrez, M., 2002, Grain sorting, porosity, and elasticity, Petrophysics, Volume 43, No. 3, pp. 185-196

Dvorkin, J., Mavko, G., and Gurevich, B., 2007, Fluid substitution in shaly sediments using effective porosity, Geophysics, Vol. 72, No. 3, P. 1-8

Schlumberger, Eclipse reference user manual 2006.2

Eidesmo, T., Ellingsrud, S., MacGregor, L.M., Constable, S., Sinha, M. C. , Johansen,S., Kong, F.N., and Westerdahl, H., 2002, Seabed Logging _SBL, A new method for remote and direct identification of hydrocarbon filled layers in deepwater areas: First Break, 20, 144–152.

Ellingsrud, S., Eidesmo, T., Johansen, S., Sinha, M.C., MacGregor, L.M., and Constable, S., 2002, Remote sensing of hydrocarbon layers by seabed logging _SBL_: Results from a cruise offshoreAngola: The Leading Edge, 21, 972–982.

Ertekin, T., Abou-Kassem, J.H., and King, G.R., 2001, Basic applied reservoir simulation, textbook Series, SPE, Richardson, Texas 7: 350-361

Evans, A.,C., Dankbaar, H., and Stammeijer, J., 2007, 3D and 4D seismic AVO inversion for updating the Schiehallion reservoir model and prediction of production effects, 2007, Edge 69th Conference and Exhibition- London, UK, 11-14 June 2007

Fatti, J.L, Smith, G.C, Vail, P.J, Strauss, P.J, Levitt, PR, 1994, Detection of gas in sandstone reservoirs using AVO analysis: A 3D seismic case history using the Geostack technique" Geophysics 59, 1362-1376.

Flosadottir, A., and S. Constable, 1996, Marine controlled-source electromagnetic soundings, 1. Modeling and experimental design: Journal of Geophysical Research, 101, no. B3, 5507–5517.

Fournier, F., 1989, Extraction of quantitative geologic information from seismic data with multidimensional statistical analysis: Part I, methodology, and Part II, a case study: 59th Annual International Meeting, SEG, Expanded Abstracts, 59, 726–733.

Francis, A. M., 2002, Deterministic inversion: Overdue for retirement?: PETEX Conference and Exhibition.

Frasier, C. W., 1970, Discrete time solution of plane P-SV waves in a plane layered medium, Geophysics, Vol. 35, p. 197-219.

Gal, D., J. Dvorkin, and A. Nur, 1998, A physical model for porosity reduction in sandstones: Geophysics, 63, 454–459

Gal, D., J. Dvorkin, and A. Nur, 1999, Elastic-wave velocities in sandstones with non-load-bearing clay: Geophysical Research Letters, 26, 939–942.

Galloway, W.E., and Hobday, D.K., 1996, Terrigenous clastic depositional systems: Applications to fossil fuel and groundwater resources, 2nd edition, Springer-Verlag Berlin Heidelberg New York

Gassmann, F. (1951). On Elasticity of porous media. Joint Translation by Kathy, Christine, John, and Jim version date: January 9, 1998, Stanford University.

Geertsma, J. 1961, Velocity-log interpretation: The effect of rock bulk compressibility: Soc. Pet. Eng., Vol. 1, pp. 235-248

Geertsma, J., and Smit, D.C., 1961, Some aspects of elastic wave propagation in fluid-saturated porous solids: Geophysics, Vol. 26, No. 2, pp. 169-181

Gomez, C., T., and Tatham R., H., 2007, Sensitivity analysis of seismic reflectivity to partial gas saturation, Geophysics 72, C45 (2007)

Goodway, B., Chen, T., and Downton, J., 1997, Improved AVO fluid detection and lithology discrimination using Lam´e petrophysical parameters; "$\lambda\rho$","$\mu\rho$", and "λ / μ fluid stack", from P and S inversions, SEG, Expanded Abstracts, 183–186.

Gosselin, O., Aanonsen, S.I., Aavatsmark, I., Cominelli, A., Gonard, R., Kolasinski, M., Ferdinandi, F., Kovacic, L., Neylon, K., 2003, History matching using time-lapse seismic (HUTS), SPE Annual Technical Conference and Exhibition, Denver, 84464

Gurevich, B., and J. Carcione, 2000, On Gassmann modeling of acoustic properties of sand-clay mixtures: Pure and Applied Geophysics, 157, 811–827

Haas, A., and O. Dubrule, 1994, Geostatistical inversion: A sequential method of stochastic reservoir modeling constrained by seismic data: First Break, 12, 561–569.

Hacikoylu, P.,Dvorkin,J., and Mavko, G., 2006, Resistivity-velocity transforms revisited: The Leading Edge, 25, 1006-1009.

Hamilton, E.L. 1971, Elastic properties of marine sediments: J. Geophys. Res., Vol. 76, No. 2, pp. 579-604

Hamilton, E.L. 1979, Vp/Vs and Poisson's ratios in marine sediments and rocks: J. Acoust. Soc. Am., Vol. 66, No. 4, pp. 1093-1101

Hamilton, E.L., Bachman, R.T., Berger, W.H., Johnson, T.C., and Mayer, L.A. 1982, Acoustic and related properties of calcareous deep-sea sediments: J. Sed. Pet., Vol. 52, No. 3, pp. 733-753

Hampson, D. P., Schuelke, J. S., and Quirein, J.A., 2001, Use of multiattribute transforms to predict log properties from seismic data, Geophysics, vol. 66, no. 1; p. 220–236

Han, D.H., 1986, Effects of porosity and clay content on acoustic properties of sandstones and unconsolidated sediments: Ph.D. dissertation, Stanford University

Han. D., Nur, A., and Morgan. D., 1986, Effect of porosity and clay content on wave velocity in sandstones: Geophysics, 51, 2093-2107

Huang, X., Meister, L., Workman, R., 1997, Reservoir characterization by integration of time-lapse seismic and production data, paper SPE 38695 presented at the SPE Annual Technical Conference and Exhibition

Hill, N.R., 1990, Gaussian beam migration, Geophysics. Vol. 55, p.1416-1428.

Hoffman, T., 2005, Geologically consistent history matching while perturbing facies, PhD dissertation, Stanford University.

Hoversten, G. M., F.Cassassuce, E. Gasperikova, G. A. Newman, J. Chen, Y. Rubin, Z. Hou, and D. Vasco, 2006, Direct reservoir parameter estimation using joint inversion of marine seismic AVA and CSEM data: Geophysics, 71, no. 3, C1–C13.

Hu, W., Abubakar, A., and Habashy, M., 2009, Joint electromagnetic and seismic inversion using structural constraints, Geophysics, Vol.,74, No., 6, P. R99-R109.

Ikelle, T., L., and Amundsen, L., 2005, Introduction to Petroleum Seismology, Investigations in Geophysics, Society of Exploration Geophysicists.

Ingber, L., 1989, Very fast simulated reannealing, Mathl. Comput. Modeling, 12, 8, 967-993

Ingber, L., 1993, Simulated annealing, practice versus theory, Statistics and Computing

Ingber, L. and Rosen, B., 1992, Genetic algorithm and simulated reannealing: A comparison, Mathl. Comput. Modeling, 16, 11, 87-100

Jin, L., Sen, M., K., Stoffa, P., L., Seif, R., K., 2007, Optimal model parameterization in stochastic inversion for reservoir properties using time-lapse seismic and production data, SEG Expanded Abstracts

Jin, L., P. L. Stoffa, M. K. Sen, R. K. Seif, and A. R. Sena, 2009, Pilot point parameterization in stochastic inversion for reservoir properties using time-lapse seismic and production data: Journal of Exploration Geophysics, 18, no. 1, 1–20.

Journel, A., 2002, Combining knowledge from diverse information sources: an alternative to Bayesian analysis, Mathematical Geology, 34(5), 573-598

Karazincir, M.H., and Gerrard, C.M., 2006, Explicit high-order reverse time pre-stack depth migration, Expanded Abstracts, SEG

Kennett, B.L.N., (1974) Reflections, Rays, and Reverberations, Bulletin of the Seismological Society of America 64, p. 1685-1696.

Kennett, B. L.N., 1979, Theoretical reflection seismograms for elastic media, Geophysical Prospecting, Vol.27, p. 301-321.

Kennett, B.L.N., 1980, Seismic wave in a stratified half space - II. Theoretical seismograms: Geophysical Journal of the Royal Astronomical Society, Vol.61, p. 1-10.

Kennett, B.L.N., 1985, Seismic wave propagation in stratified media, Cambridge University Press.

Kennett, B.L.N., and Kerry, N., 1979, Seismic wave in a stratified half space, Geophysical Journal of the Royal Astronomical Society, Vol.57, p. 557-583.

Key, K., 2009, 1D inversion of multicomponent, multifrequency marine CSEM data: Methodology and synthetic studies for resolving thin resistive layers: Geophysics, 74, F9–F20, 12.

Key, K. and J. Ovall, A parallel goal-oriented adaptive finite element method for 2.5D electromagnetic modeling, in revision for Geophysical Journal International

Khazanehdari, and J., Curtis, A., 2005, Quantitative time-lapse seismic analysis through pre-stack inversion and rock physics, SEG Expanded Abstracts 24, 2476

Killough, J.E., 1995, Ninth SPE comparative solution project: A Reexamination of Black-oil simulation: SPE, 29110, 135-147

Kirkpatrick, S., Gellatt, C. D., Jr., and Vecchi, M. P., 1983, Optimization by simulated annealing, Science, 220, 671-680.

Lafet, Y., Roure, B., Doyen, P., M., Buran, H., 2009, Global 4-D seismic inversion and time-lapse fluid classification, SEG Expanded Abstracts 28, 3830

Landa, J. L., Horne, R. N., 1997, A procedure to integrate well test data, reservoir performance history and 4-D seismic information into a reservoir description, paper SPE 38653 presented at the SPE Annual Technical Conference and Exhibition

Landro, M., 2001, Discrimination between pressure and fluid saturation changes from time-lapse seismic data, Geophysics, Vol.66, 836-844.

Landro, M., 2002, Uncertainties in quantitative time-lapse seismic analysis, Geophysical prospecting, Vol. 50,527-538

Landro, M., Veire, H., H., Duffaut, K., and Najjar, N., 2003, Discrimination between pressure and fluid saturation changes from marine multi-component time-lapse seismic data, Geophysics, Vol. 68, 1592-1599.

Landro, M., Solheim, O. A. Hilde, E., Ekren, B. O, and Stronen, L. H., 1999, Petroleum Geoscience, Vol. 5,213-226.

Landro, M., Kvam, Ø., 2002, Pore pressure estimation-what can we learn from 4D? CSEG Recorder September 2002

Lee, M. W. (2002). Biot–Gassmann theory for velocities of gas-hydrate bearing Sediments. Geophysics, 67, 1711–1719.

Lee, M. W (2003). Elastic properties of overpressured and unconsolidated sediments. US Geological Survey Bulletin b2214, p. 10.

Lee, M. W., 2003, Velocity ratio and its application to predicting velocities, U.S. Geol. Surv. Bull. 2197, 15 p

Li, R., Reynolds, A. C., and Oliver, D. S., 2003, History matching of three-phase flow production data, SPE Journal, Vol. 8, No. 4, pp 328–340.

Li, Y., and Key, K., 2007, 2D marine controlled-source electromagnetic modeling: Part 1- An adaptive finite-element algorithm: Geophysics, 72, WA51–WA62.

Liange, L., Abubakar, A., Habashy, T., Three-dimensional fluid-flow constrained crosswell electromagnetic inversion, SEG abstrcta, 2010

Lien, M., and Mannseth, T., 2008, Sensitivity study of marine CSEM data for reservoir production monitoring: Geophysics, 73, F151–F163.

Lumley, D. E., R. A., Behrens, Z., Wang, 1997, Assessing the technical risk of a 4D seismic project: The Leading Edge, Society of Exploration Geophysicist.

Lumley, D.E., et al., Meren field, Nigeria: A 4D seismic case study, SEG Expanded Abstracts, 1628.

Lumley, L., M., Meadows, S., Cole, D., Adams, 2003, Estimation of reservoir pressure and saturation by crossplot inversion of 4D seismic attributes: 73rd Annual International Meeting, SEG Expanded Abstracts.

MacBeth, C., Floricich, M., Soldo, J., 2006, Going quantitative with 4D seismic analysis, Geophysical Prospecting, 54, 303-317.

Macrides, C.G., Rademakers, M., Fournier, F., and Dequirez, P.Y., 2000, 2-D and 3-D lithostratigraphic interpretation of seismic data for characterization of the 'Unayzah formation in central Saudi Arabia, Saudi Aramco Journal Of Technology , Fall 2000, p. 17-33

Mahmoudian, F., and Margrave, G., 2004, Three parameter AVO inversion with PP and PS data using offset binning, SEG Expanded Abstracts 23, 240.

Mario, D., Nur, A., Yin, H., and Han, D., 1992, Compressional velocity and porosity in sand-clay mixtures, Geophysics, Vol., 57, No., 4, P., 554-563

Marsh, J.M., et al. 2001, The use of 4D seismic in reservoir management, EAGE 63rd, Conference and Technical Exhibition

Mavko, G., Mukerji, T., and Dvorkin, J., 2009, second edition, The Rock physics handbook-Tools for seismic analysis of porous media, Cambridge Univ. Press.

McCowan, D., and Brysk, H., 1989, Cartesian and Cylindrical Slant Stacks, in Paul L. Stoffa (ed.), Tau-p: A Plane Wave Approach to the Analysis of Seismic Data. p. 1-33

Mindlin, R. D., 1949, Compliance of elastic bodies in contact: Trans. ASME, A-259.

Mukerji, T., Avseth, P., Mavko, G., Takahashi, I., and Gonzalez, E., 2001b, Statistical rock physics: combining rock physics, information theory, and geostatistics to reduce uncertainty in seismic reservoir characterization: The Leading Edge, 20, 313–319

Mukerji, T., Jorstad, A., Avseth, P., Mavko, G., and Granli, J. R., 2001a, Mapping lithofacies and pore fluid probabilities in a North Sea reservoir: Seismic inversions and statistical rock physics: Geophysics, 66, 988–1001

Oldenburg, D., T. Scheuer, and S. Levy, 1983, Recovery of the acoustic impedance from reflection seismograms: Geophysics, 48, 1318–1337.

Ottesen, T., Magnus, I., JØrgensen, Vestergaard, L., and Stage, M., G., 2007,The 3D reservoir geological model-A hub for 4D seismic interpretation, Edge 69th Conference and Exhibition, 11-14

Orange, A., Key, K., and Constable1, S., 2009, The feasibility of reservoir monitoring using time-lapse marine CSEM: Geophysics, 74, F21–F29.

Ouenes, A., Bhagavan, S., Bunge, P.H., and Travis, B.J., 1994, Application of simulated annealing and other global optimization methods to reservoir description: Myths and Realities, SPE 28415

Ouenes, A., Meunier, G., Peke, V., and Lhote, I., 1992, Enhancing Gas Reservoir Characterization by Simulated Annealing Method (SAM), SPE 25023

Ouenes, A. and Saad N., 1993, A new, fast parallel simulated annealing algorithm for reservoir characterization, SPE 26419

Panda, M.N and Lake, L.W., Lake, 1993, Parallel Simulated Annealing for Stochastic Reservoir Modeling, SPE 26418

Parker, J., Bertelli, L., and Dromgoole, P., 2003, 4D seismic technology special issue, Petroleum Geoscince 9(1): 1-111

Pestana, R.C and P.L., Stoffa, 2009, Rapid expansion method (REM) for time-stepping in reverse time migration (RTM), SEG expanded abstract

Praston, L., Gouveia, W., 2002, Seismic simulations of experimental strata, AAPG Bulletin, V. 86, No. 1, pp.129-144

PGS, 2009, A Multi-Transient EM Repeatability Experiment over the North Sea Harding Field: A Publication of Petroleum Geo-Services Vol. 9, No. 8, August

Raymer, D. S., Hunt, E. R., and Gardner, J. S., 1980. An improved sonic transit time-to-porosity transform: Presented at 2lst Ann. Mtg., Sot. Prof. Well-log Anal., paper P

Revil, A., and Cathles, L.M., 1999, Permeability of shaly sands, water resources research, vol. 35, no. 3, P.516-662

Reynolds, E. B., 1970, Predicting overpresssured zones with seismic data, World Oil, Vol. 171, 78-82

Rosa, 1976, Extraction of elastic parameters using seismic reflection amplitude with offset variation: M.S. thesis, University of Houston.

Rothman, D. H., 1985, Non-linear inversion, statistical mechanics, and residual static estimation, Geophysics, 50, 2784-2796

Rothman, D. H., 1986, Automatic estimation of large residual statics correction, Geophysics, 51, 337-346

Russell, B.,H., Hedlin, K., Hilterman, F.,J., and Lines, L., R., 2003, Fluid-property discrimination with AVO: A Biot-Gassmann perspective, Geophysics 68, 29 (2003)

Rutleda, H., et al. 2002, Time-lapse elastic inversion at the Oseberg field, EAGE 64th, Conference and Technical Exhibition

Saner, S., Cagatay, M.N., and A1 Sanounah, A.M., 1996, Relationships between shale content and grain-size parameters in the Safaniya sandstone reservoir, NE Saudi Arabia, Journal of Petroleum Geology, vol. 19(3), July 1996, pp. 305-320

Sen, M., Gupta, A. D., Stoffa, P.L., Lake, W.L., Pope, G.A., 1995, Stochastic reservoir modeling using simulated annealing and genetic algorithms, SPE 24754-PA

Sen, M., Stoffa, P.L., 1995, Global optimization methods in geophysical inversion, New York: Elsevier

Sena, A., Sen, M., K., Stoffa, P.,L., Seif, R.,K., Jin, L., 2009, Joint inversion of time-lapse seismic and production data using VFSA with Local Thermal Regulation and pilot point parameterization, SEG Expanded Abstracts 28, 1810.

Shahin, A., Key, K., Stoffa, P., L., Tatham, R., 2010a, Time-lapse CSEM analysis of a shaly sandstone simulated by comprehensive petro-electric modeling , poster presented in 80th Annual International Meeting, Society for Exploration Geophysicists (SEG), Denver, Colorado.

Shahin, A., Tatham, R., H., Stoffa, P., L., Spikes, K., T., 2010b, Comprehensive petro-elastic modeling aimed at quantitative seismic reservoir characterization and monitoring, poster presented in 80th Annual International Meeting, Society for Exploration Geophysicists (SEG), Denver, Colorado. .

Shahin, A., Stoffa, P., L., Tatham, R., H., Sava, D., 2009, Multicomponent seismic time-lapse cross-plot and its applications, SEG Expanded Abstracts 28, 1227.

Shahin, A., Stoffa, P., L., Tatham, R., H., Sava, D., 2008, Sensitivity analysis of multicomponent seismic attributes to fluid content and pore pressure, SEG Expanded Abstracts 27, 247.

Simmons, J.L., and Backus, M.M., 1994, AVO modeling and the locally converted shear wave, Geophysics, Vol. 59, p. 1237-1248.

Smith, G.C, and Gidlow, P.M., 1987, Weighted stacking for rock property estimation and detection of gas: Geophys. Prosp. 35, 993-1014.

Spikes, K., Mukerji, T., Dvorkin, J., Mavko, G., 2007, probabilistic seismic inversion based on rock-physics models, Geophysics, Vol. 72, No. 5, p. 87-97.

Stephen, K.D., MacBeth, C., 2006, Reducing reservoir prediction uncertainty by updating a stochastic model using seismic history matching, SPE100295.

Stoffa, P.L., Buhl, P., Diebold, J.B., and Wenzel, F., 1981, Direct mapping of seismic data to the domain of intercept time and ray parameter-A plane wave decomposition, Geophysics, Vol. 46, p. 255-267.

Stoffa, P.L., Sen, M.K., Seifoullaev., R.K., Pestana, R.C., Fokkema, J.T., 2006, Plan-wave depth migration, Geophysics, Vol. 71, p. 261-272.

Stoffa, P., L., Sen, M.,K., 1992, Seismic waveform inversion using global optimization, J. of seismic exploration 1, pp. 9-27.

Stoffa, P.L. and R.C Pestana, 2009, Numerical solution of the acoustic wave equation by the rapid expansion method (REM) - A one step time evolution algorithm, SEG expanded abstract

Takahashi, I., 1999, Quantifying information and uncertainty of rock property estimation from seismic data: Ph.D. thesis, Stanford University

Technical Note: Colored, Deterministic & Stochastic Inversion, © 2003 Earthworks Environment & Resources Ltd. All rights reserved

Thomas, E.C., and Stieber, S.J., 1975, The distribution of shale in sandstones and its effect upon porosity, paper T in the 16th Annual Logging Symposium Transactions: Society of Professional Well Log Analysts

Thomson, W., 1950, Transmission of elastic waves through a stratified solid medium, Journal of Applied Physics, Vol. 21, p. 89

Tyler, N., Ambrose, W.A., 1986, Facies architecture and production characteristics of strand-plain reservoirs on north Markham-North Bay City Field, Frio formation, Texas, AAPG Bulletin, 70, 809-829

Tura, A., Lumley, D., E., 1998, Subsurface fluid-flow properties from time-lapse elastic-wave reflection data, SPIE Vol. 3453

Tura, A., and D. E., Lumley, 1999, Estimating pressure and saturation changes from time-lapse AVO data: 69th Annual International Meeting, SEG, Expanded Abstracts, 1655–1658

Uden, R., Dvorkin, J., Walls, J., Carr, M., 2004, Lithology substitution in a sand/shale sequence, Extended Abstracts, ASEG 17th Geophysical Conference and Exhibition, Sydney 2004.

Vanorio, T., Prasad, M., and Nur, A., 2003, Elastic properties of dry clay mineral aggregates, suspensions and sandstones, Geophysical. Journal Int. (2003) 155, 319–326

Varela, O., J., 2003, Stochastic inversion of pre-stack seismic data to improve forecast of reservoir production, PhD dissertation, The University of Texas at Austin

Vasco, D., W., Gupta, A., D., Bhrens, R., Condon, P., Rickett, J., 2004, Seismic imaging of reservoir flow properties: Time-lapse amplitude changes, Geophysics 69, 1425

Veire, H., H., Landro, M., 2001, Joint inversion of PP-and PS-seismic data, SEG Expanded Abstracts 20, 861

Veire, H., H., Borgos, H., G., and Landro, M, 2006, Stochastic inversion of pressure and saturation changes from time-lapse AVO data , Geophysics 71, C81 (2006)

Waggoner, J. R., 1998, 4D seismic, synergy, not just integration, of geophysics and engineering, paper SPE 50665 presented at the SPE European Petroleum Conference

Wait, J. R., 1982, Geo-electromagnetism:Academic Press.

Walker, G., Allan, P., Trythall, R., Parr, R., Marsh, M., Kjelstadli, R., Barkved, O., Johnson, D., Lane, S., 2006, Three case studies of progress in quantitative seismic-engineering integration, The Leading Edge, September 2006

Waxman, M.H., and Smits, L.J.M., 1968, Electrical conductivities in oil-bearing shaly sands: SPEJ, Trans., AIME, 243, 107-122.

Wood. A. B., 1941, A textbook of sound: Macmillan Publ. Co.

Wright, D., Ziolkowski, A., and Hobbs, B., 2002, Hydrocarbon detection and monitoring with a multicomponent transient electromagnetic (MTEM) survey: The Leading Edge 21, 852-864.

Wyllie, M.R.J., Gregory, A.R., and Gardner, G.H.F., 1958, An experimental investigation of factors affecting elastic wave velocities in porous media: Geophysics, Vol. 23, No. 3, pp. 459-493

Zach, J.J., Frenkel, M.A., Ridyard, 2009, 3D inversion-based interpretation of marine CSEM data, OTC 20289, Offshore Technology Conference, Houston, Texas, USA.

Zach, J.J., Frenkel, M.A., Ridyard, D., Hincapie, J., Dubois, B., and Morten, J.P., 2009, Marine CSEM time-lapse repeatability for hydrocarbon field monitoring: 79th Annual International Meeting, SEG, Expanded Abstracts, 820-823.

Zhang, F., Reynolds, A. C., 2002, Optimization algorithms for automatic history matching of production data," paper presented at the 8th European Conference on the Mathematics of Oil Recovery

Zhdanov, M., S., 2009, Geophysical electromagnetic: Theory and Methods. Methods in Geochemistry and Geophysics, 43. First Edition, Elsevier, The Netherland.

Ziolkowski, A., Parr, R., Wright, D., Nockles, V., Limond, C., Morris, E., and Linfoot, J., 2010, Multi-transient electromagnetic repeatability experiment over the North Sea Harding field, Geophysical Prospecting, doi: 10.1111/j.1365-2478.2010.00882.x

Vita

Alireza Shahin earned a diploma in mathematic and physics. In 1995, he entered the *Isfahan University of Technology*. Graduated with a mining exploration engineering degree in 1999, he started his master degree in petroleum exploration engineering at *Tehran University* in 2000. He received his master degree in 2002 when he started his career in *OEID*. In 2006, he entered the Graduate School at the *University of Texas at Austin.* As a graduate research assistant, he was employed by *GBDS* in summer and fall 2007 and by *Edger Forum* from fall 2007 to fall 2010. He did an internship with *SWIFT ENERGY* in summer 2008. He joined *BP* in 2011.

Permanent email: a.shahin@mail.com

This dissertation was typed by the author.